

# **New Fourier Transform Microwave Techniques for Dynamic Rotational Spectroscopy**

Kevin O'Connell Douglass  
Cranford, New Jersey

B.S., Marist College, 2001

A Dissertation presented to the Graduate Faculty of the University of Virginia in  
Candidacy for the Degree of Doctor of Philosophy

Department of Chemistry

University of Virginia  
May, 2007

Brook V. Job

Kevin Lehman

Fred Richardson

Thomas J. Mulligan  
D. Johnson

#### INFORMATION TO USERS

The quality of this reproduction is dependent upon the quality of the copy submitted. Broken or indistinct print, colored or poor quality illustrations and photographs, print bleed-through, substandard margins, and improper alignment can adversely affect reproduction.

In the unlikely event that the author did not send a complete manuscript and there are missing pages, these will be noted. Also, if unauthorized copyright material had to be removed, a note will indicate the deletion.



---

UMI Microform 3288058

Copyright 2008 by ProQuest Information and Learning Company.  
All rights reserved. This microform edition is protected against  
unauthorized copying under Title 17, United States Code.

ProQuest Information and Learning Company  
300 North Zeeb Road  
P.O. Box 1346  
Ann Arbor, MI 48106-1346

## Abstract

Towards the goal of studying intramolecular vibrational energy redistribution (IVR) and the dynamics that result, various laser-FTMW techniques have been developed and applied to a wide range of systems. The techniques described combine the advantages of pulsed lasers (high pulse power and wide tuning range) with the high sensitivity of Fourier transform microwave spectroscopy (FTMW). Two methods of performing FTMW rotational spectroscopy will be presented. These methods are based on either the well known Balle-Flygare narrowband cavity FTMW spectrometer or the recently developed broadband Chirped-Pulse FTMW spectrometer. Several measurements are presented that demonstrate the versatility and sensitivity of using a Balle-Flygare type narrowband cavity as detector for IR spectroscopy. A technique for background-free Laser-FTMW spectroscopy is also described and is demonstrated by measuring the UV-FTMW double resonance spectrum of the seven conformers of p-methoxyphenethylamine. The cavity spectrometer is also used to investigate the motionally narrowed rotational spectrum of trifluoropropyne at the overtone of the acetylenic C-H stretch and the conformational isomerization dynamics of pent-1-en-4-yne at the acetylenic C-H stretch fundamental. However, due to limitations of slow scan speed and skewed intensity information of the narrowband cavity method, new methods for performing rotational spectroscopy have been developed based on chirped pulse excitation. The new chirped-pulse FTMW (CP-FTMW) spectrometer measures the rotational spectrum from 7.5 to 18.5 GHz for each valve pulse. For equal sensitivity the CP-FTMW is ~18 times faster than the traditional Balle-Flygare cavity method. The full characterization of the CP-FTMW spectrometer for sensitivity, frequency accuracy, and comparison to the cavity based FTMW technique are demonstrated for pure and vibrationally excited state rotational spectroscopy. The advantages of the broadband CP-FTMW technique are used to investigate the conformational isomerization dynamics of cyclopropanecarboxaldehyde (CPCA) as a function of excitation energy (2670 – 3110 cm<sup>-1</sup>).

**TABLE OF CONTENTS**

I	Introduction and Background	1
	A. Intramolecular Vibrational Energy Redistribution	8
	B. Dynamic Rotational Spectroscopy	13
	References I	19
II	Narrow Band Cavity FTMW Spectroscopy	23
	A. FTMW Background Theory	23
	B. Vacuum Chamber and Pumping System	27
	C. Free Jet Expansion	30
	D. Fabry – Perot Cavity	31
	E. Microwave Pulse Generation and Detection	33
	F. Secondary Microwave Excitation	37
	G. Infrared Excitation	38
	H. Pulse Timing	43
	I. Problems Encountered	44
	References II	49
III	Narrow Band Cavity FTMW Spectroscopy:	
	Applications to Pure Rotational Spectroscopy	50
	A. Formic Acid Trimer	58
	B. Propiolic - Formic Acid Dimer	64

Conclusion	76
References III	77
Appendix 3-A	80
<b>IV FTMW based Detection for Laser Spectroscopy</b>	<b>86</b>
A. Spectrometer Performance:	
The Acetylenic C-H Stretch Spectra of	
1-butyne,tertbutylacetylene, and trimethylsilylyacetylene	90
B. Applications to IVR:	
The Fast IVR Dynamics of Cyclopropylacetylene	96
C. Measuring Vibrational Spectra of Conformers:	
4-fluorobutyne	102
D. Vibrational Dynamics of Weakly Bound Dimers:	
HCCH-NH <sub>3</sub> and CH <sub>3</sub> CCH-NH <sub>3</sub>	105
Conclusions	111
References IV	113
<b>V FTMW based Detection for Laser Spectroscopy:</b>	<b>118</b>
Enhanced Sensitivity and Applications to Electronic Spectroscopy	
A. Background Free Ground State Depletion	124
B. Electronic Spectrum of para-Methoxyphenethylamine	133
Conclusions	138
References V	141

VI	Techniques for Dynamics Rotational Spectroscopy	143
	A. IR-FTMW-cwMW Triple Resonance	144
	Summary	168
	B. IR-FTMW-pulsed MW Triple Resonance	172
	Conclusions	185
	References VI	189
VII	Cavity FTMW Spectroscopy:	
	Motional Narrowing of trifluoropropyne at 6550 cm <sup>-1</sup>	192
	A. Infrared-Microwave Double-Resonance Spectroscopy	197
	B. Infrared-pulsed MW-FTMW Triple-Resonance Spectroscopy	200
	Discussion	
	A. Analysis of the Homogeneous Eigenstate Rotational Lineshape	205
	B. Comparison to the Predicted Ensemble Normal-Mode Rotational Frequency Distribution	206
	C. Estimate of the IVR Rate in the Low-Frequency Normal Modes	216
	Conclusions	221
	References VII	223

VIII	Cavity FTMW Spectroscopy:	
	Conformational Isomerization Dynamics of Pent-1-en-4-yne	226
	A. Pure Rotational Spectrum	229
	B. Infrared Spectrum	232
	C. Dynamic Rotational Spectroscopy	235
	Discussion	
	A. Lineshape analysis	243
	B. Rate analysis	246
	Conclusions	248
	References VIII	251
IX	Principles of Chirped-Pulse Fourier Transform	
	Microwave Spectroscopy	253
	A. Phase Noise and Triggering	257
	B. Chirped Microwave Pulse Generation	262
	C. Free Space Molecular Beam Chamber	268
	D. Free Induction Decay Detection	271
	E. Apodization	275
	F. Sample Polarization	279
	i. Linear Sweep Excitation	279
	ii. Power Requirements for Broadband FTMW Spectroscopy	284
	Summary	286
	References IX	287

X	Broadband Rotational Spectroscopy: Applications to Pure Rotational Spectroscopy	291
	A. Experimental Performance	291
	B. Comparison to Balle-Flygare cavity FTMW spectrometer	299
	Conclusions	301
	References X	305
XI	Broadband Rotational Spectroscopy: Applications for Dynamics Rotational Spectroscopy	306
	A. IR-CP-FTMW and IR-cavity-FTMW	
	Double Resonance Comparison	308
	B. Dynamic Rotational Spectroscopy of CPCAs	310
	Conclusions	326
	References XI	335
XII	Concluding Remarks	336
	Future Experiments	337
	References XII	339

## Acknowledgements

First, I would like to thank Brooks for his dedication, insight, and enthusiasm. Without his constant help none of this work would be possible. I have learned so much over the years and I have grown as a person and as a scientist through his careful guidance and for that I thank him.

I also need to thank all the current and recent Pate lab members to which I am greatly indebted. Gordon, Brian, and Jason we really worked well together and I will be lucky to have colleagues in the future who are as dedicated or as fun to work with as you were. Steve and Pam I thank you for all your proof reading and scientific insight from the time domain perspective. I also really need to thank John, Hyun, Francis, and Yehudi for their help and guidance. Rick, I am grateful to you and Igor for all the help with the initial FTMW system set-up. Rick you have been instrumental in this whole process and I want to thank you for being a great mentor and I also need to thank you for all the spectra you helped assign.

To my family and friends, your support and encouragement has helped guide me through this process. Meg, Paul, and Grandma Flynn I want to thank you for reminding me of the important things in life. I also need to thank the entire Crum family who have always helped me laugh and relax during times of stress. Mom and Dad I don't think I can express how truly grateful I am for all the unwavering support and encouragement you have provided over the years. To my best friend and colleague, I thank my wife Pam for continually inspiring and encouraging me to be a better person and scientist.

## Chapter 1

### Introduction and Background

Understanding the dynamics of chemical reactions has long been a primary goal of physical chemists. The complete elucidation of reaction mechanisms has proven to be a daunting task for even the simplest systems. Research in the field of reaction dynamics has provided a wealth of knowledge which has resulted from an array of experimental techniques such as chemiluminescence<sup>1</sup>, crossed molecular beam experiments,<sup>2,3</sup> and chemical activation.<sup>4</sup> More recently with the advent of ultrafast lasers, the dynamics of bond breakage can now be probed on a femtosecond time scale.<sup>5</sup> These results for unimolecular reactions have allowed theory to be tested by providing a direct comparison between experimental rates of reaction and those predicted by statistical theory (such as Rice-Ramsperger-Kassel-Marcus or RRKM).

A major assumption of RRKM is that the vibrational degrees of freedom rapidly exchange energy and that the flow of vibrational energy is much faster than the chemical reaction.<sup>6</sup> The flow of vibrational energy through the normal modes of a molecule is known as intramolecular vibrational energy redistribution (IVR).<sup>7</sup> The process of IVR is responsible for the failure of bond selective chemistry for large molecules because the intramolecular energy is redistributed on a time scale much faster than a chemical reaction can take place. Therefore, IVR plays a fundamental role in the theories describing the rates of chemical reactions.

Traditionally, the dynamics of IVR have been characterized by the rate of energy flow out of an initially excited vibrational state or zeroth order bright state.<sup>7,8</sup> Both time<sup>9</sup> and frequency domain<sup>8</sup> techniques have been developed to measure the IVR lifetime of the bright state. The same information is contained in both measurements as governed by Fourier transform relations. For the single-color time-domain pump probe technique, a pump pulse vibrationally excites the molecules and the probe pulse measures the population of the excited state as a function of time. As IVR occurs population moves out of the initially excited state and into the rest of the normal modes of the molecule.

The single photon frequency domain technique measures the contribution of the bright state character in the various molecular eigenstates as a function of frequency. When IVR occurs, the frequency domain spectrum displays fragmentation of the bright state and typically has a Lorentzian lineshape. From frequency and intensity measurements of the fragmented pattern the survival probability or lifetime of the bright state can be calculated.<sup>10-13</sup> High resolution frequency domain molecular beam techniques are widely used. These techniques have been used to measure IVR rates of the hydride stretch for a variety of molecules, and have demonstrated the effects of mode specificity (OH vs CH even for the same molecule), heavy atom substitution, and low barrier torsional motion on “typical” IVR rates.<sup>8</sup>

MW-IR double resonance spectroscopy has been used to obtain eigenstate resolved infrared spectra consisting of purely homogenous IVR induced widths, which are not complicated by the overlap of different rotational states or isomers.<sup>8</sup> These double resonance techniques have a shared rotational level in the ground vibrational state, and

have the advantage that only infrared transitions resonant with the two monitored rotational levels are observed. This greatly simplifies the spectra and makes assignment straightforward. These techniques<sup>14-16</sup> have the ability to measure the IVR lifetime as a function of rotational state, which provides insight into the different coupling mechanisms (Coriolis vs. anharmonic) of the bright state to the other vibrational degrees of freedom.

Alternatively, IR-MW double resonance techniques have been demonstrated where the shared rotational level is in the vibrationally excited state.<sup>14,17-19</sup> A narrow linewidth cw-IR laser prepares a vibrationally excited single eigenstate and by scanning a microwave source the rotational spectrum of the vibrationally excited single eigenstate is obtained. Because the molecule is vibrationally excited, if vibrational energy flows through the molecule the resulting rotational spectrum appears to have a distribution of rotational transitions that reflects a distribution of the effective rotational constants.<sup>20,21</sup>

This distribution of the rotational constants results from vibrational energy moving in and out of bending, stretching, and other normal modes, which effectively changes the geometry and moments of inertia of the molecule on the time scale of rotation.<sup>17,19</sup> In this case instead of observing a single rotational transition a spread of rotational transitions are observed, and from the overall lineshape profile of this spectrum dynamical information about the time scale of IVR can be obtained. This type of spectroscopy is referred to as dynamic rotational spectroscopy (DRS).<sup>19</sup>

Information on the vibrational energy redistribution dynamics is obtained from the lineshape profile of the vibrationally excited single eigenstate rotational spectrum. The

lineshape analysis follows directly from the motional narrowing theories developed for NMR.<sup>22-25</sup> The general pattern known as "motional narrowing" and "coalescence" in NMR spectra occurs when the rate of exchange between two instantaneous resonance frequencies is comparable to their difference, and as a result the two peaks move together towards an average frequency. As the exchange rate is increased, coalescence into one broad line occurs, which progressively narrows with further increase of the rate. In dynamic rotational spectroscopy, the relevant exchange rate is the IVR rate. The basic principles and theory of DRS have been presented for systems with a fixed conformational geometry<sup>20</sup> and have also been extended to isomerizing systems.<sup>21;26</sup>

The information obtained from dynamical rotational spectroscopy (DRS) is qualitatively different than the measurement of the lifetime of the bright state.<sup>19;27</sup> The DRS technique uses rotational spectroscopy to probe the effects of vibrational energy flow dynamics on molecular structure. This approach is statistical and yields an 'average' IVR rate of all the vibrational states participating in the dynamics.<sup>19;20</sup> In contrast, measuring the bright state lifetime is limited because it is only one state out of possibly thousands in a single wavenumber of energy. The bright state lifetime only measures how long the energy remains localized in a single vibrational mode, while the single eigenstate rotational spectrum measures how fast vibrational energy is exchanged between the vibrational modes of the molecule on average.<sup>19</sup>

For molecules that can undergo conformation isomerization, analysis of the vibrationally excited single eigenstate rotational spectrum can be used to determine a conformational isomerization rate and corresponding collision free microcanonical rate

constant,  $k(E)$ .<sup>18,19</sup> Because DRS measures a microcanonical rate this provides direct test of statistical rate theories, such as RRKM.<sup>28</sup> It has been suggested that predictions for low barrier isomerization reactions and disassociation of weakly bound complexes are not well described by RRKM theory.<sup>6,29</sup> Gaining insight into the isomerization rate constant,  $k(E)$ , and its correlation with IVR will prove important in developing an understanding of low barrier unimolecular reactions.

The techniques developed to perform dynamic rotational spectroscopy are currently at their sensitivity limits. The need for higher sensitivity grows out of the complexity of the molecular dynamics. The signature of IVR in an IR spectrum is fragmentation of the single vibrational band into many. Because the total intensity is conserved, fragmentation can drastically reduce the intensity of the main feature. Typically, molecules with fast IVR have highly fragmented IR spectra resulting from interactions with the dense set of near resonant vibrational states.<sup>7,8,14,30-36</sup> An ability to quantitatively measure the weak features is important in determining the IVR survival probability.

As the IVR rate increases the ability to saturate the infrared transition decreases limiting the sensitivity for cw-IR methods. There are similar sensitivity problems for the excited state rotational spectrum. Complex IVR dynamics (which lead to conformation isomerization) result in a distribution of rotational transitions that may be spread over several gigahertz, with sensitivity again with the constraint of conservation of the total intensity.<sup>19</sup> A technique that employs high sensitivity for the measurement of rotational transitions will be crucial for studying such systems.

In the late 1970's the theory had been developed for performing microwave spectroscopy using time domain techniques similar to FT-NMR.<sup>37</sup> A few years later the well known Balle-Flygare<sup>38</sup> Fourier transform microwave spectrometer was developed which implemented a high Q cavity. Cavity based FTMW spectroscopy has demonstrated unparalleled sensitivity for the detection of microwave transitions.<sup>39-41</sup> The high sensitivity of the FTMW spectrometer is confirmed by measuring substitution structures in natural abundance. For example, Suenram et al. have demonstrated that <sup>18</sup>O<sup>13</sup>C<sup>34</sup>S, a species just 0.000094% natural abundance, can be observed with a signal-to-noise of 4.5 after 5000 averages (5 minutes) with a 1% sample concentration of OCS in Ne/He 80%/20% mixture.<sup>42</sup>

There have also been FTMW spectrometers based on waveguide design. Although, they suffer from lower sensitivity these spectrometers have demonstrated ability to measure up to a bandwidth of 50 MHz in a single measurement step.<sup>43</sup> The ability to observe a large bandwidth of the rotational spectrum may have advantages for laser based experiments where there are problems of searching for laser induced rotational transitions. These two complementary methods of FTMW spectroscopy will be explored for pure and dynamic rotational spectroscopy.

Techniques for DRS based on FTMW spectroscopy and pulsed laser excitation may have several advantages. An application of the FTMW technique for laser-MW double-resonance spectroscopy has previously been reported.<sup>44</sup> This method provides a rotational assignment of the electronic spectrum through laser-induced changes to the pure rotational signal monitored by FTMW spectroscopy. For DRS studies, implementation

of a pulsed IR laser source provides high pulse energy over a broad tuning range. The high pulse energy is necessary to compensate for the fragmented oscillator strength of the individual vibrational transitions (due to IVR), and the tuning range is used to easily scan large frequency ranges to identify all of the perturbing IR bands. A typical pulsed optical parametric oscillator/amplifier (OPO/OPA) laser is capable of pumping the fundamental and first overtone vibrational frequencies of the acetylenic C-H stretch ( $3330\text{ cm}^{-1}$  and  $6560\text{ cm}^{-1}$ ). The requirements of the pulsed laser for efficient excitation are that the linewidth must be on the order of the Doppler distribution of the pulsed free jet expansion (200 MHz for the acetylenic C-H stretch fundamental<sup>45</sup>) and yet still provide J selective excitation, i.e. Doppler width  $\leq \Delta\nu \leq B + C$ .

To perform dynamic rotational spectroscopy (DRS) using FTMW techniques and a pulsed IR laser, several steps are necessary to obtain the vibrationally excited rotational spectrum of a single molecular eigenstate. First, for the technique to stand alone it must be capable of measuring infrared spectra with rotational resolution. This is IR-FTMW double resonance with the shared level in the ground vibrational state. Secondly, with the infrared transition known the rotational spectra of the molecular eigenstates that are directly pumped by the laser can be measured. This is IR-FTMW double resonance where the shared level is in the vibrationally excited state. Lastly, IR-FTMW-MW triple resonance spectroscopy (the two shared rotational levels are in the vibrationally excited state) is used to obtain the rotational spectrum of a single molecular eigenstate.

The purpose of this thesis is to demonstrate new techniques based on FTMW spectroscopy and pulsed laser excitation which will provide viable and robust methods to

performing DRS with greater sensitivity over previous methods. In addition to developing more sensitive tools to perform DRS, widely applicable techniques for obtaining rotationally resolved vibrational or electronic spectra and a completely new method of measuring rotational spectra have been developed and may find related use in other areas of spectroscopy.

#### A. Intramolecular Vibrational energy Redistribution

Intramolecular energy flow has been studied extensively through high resolution IR spectroscopy.<sup>7;8</sup> The characteristic feature of vibrational energy flow in high resolution IR spectra is the fragmentation of a single rovibrational transition into a set of transitions often referred to as the IVR multiplet.<sup>7;8;14;30-33;35;36;46</sup> The dynamics that give rise to the IVR multiplet can be described using the standard model for IVR as depicted in Figure 1.1.<sup>11;13;47</sup>

The standard model for IVR begins with the description of the full molecular Hamiltonian, which is separated into a simple zeroth-order term,  $H_0$ , and an interaction term,  $W$ .

$$H = H_0 + W \quad (2.1)$$

$H_0$  is the molecular Hamiltonian of the normal-mode vibrations (Harmonic oscillator) and the distortable rotor.<sup>48;49</sup> For the general case the eigenfunctions of  $H_0$  are direct products of the vibrational wavefunctions and an asymmetric top wavefunction.

$$|\psi^{(0)}\rangle = |\vec{v}\rangle |J_{KaKc}\rangle = |v_1, v_2, \dots, v_{3N-6}\rangle |J_{KaKc}\rangle \quad (2.2)$$

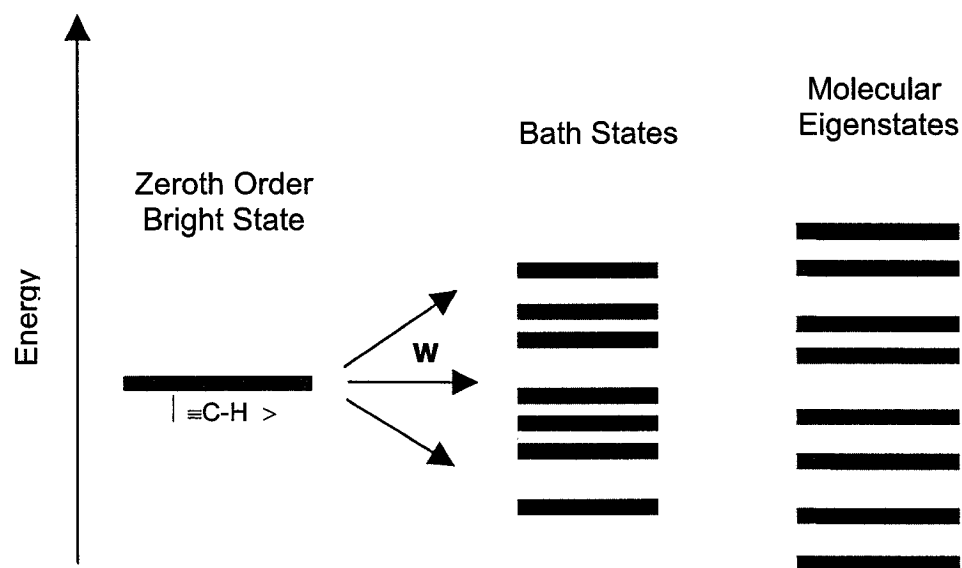


**Figure 2.1** The standard model for IVR is illustrated. The ‘bright’ zeroth order state has transition probability from the ground state. The ‘dark’ or bath states are nearby in energy and have zero transition probability from the ground state. The interaction, W, between the bright and bath states produces the set of molecular eigenstates. The intensity of each eigenstate in the observed spectrum is proportional to the amount of the bright state in the molecular eigenstate composition.

$W$  is the interaction term that couples eigenfunctions of  $H_0$  through anharmonic or rotationally mediated coupling (Coriolis, centrifugal).<sup>50</sup> The eigenfunctions of the full Hamiltonian are referred to as the exact molecular eigenstates. By completeness, the molecular eigenstates can be represented in the zeroth-order basis.

$$|\phi_i\rangle = c_b |\psi_b^{(0)}\rangle + c_1 |\psi_1^{(0)}\rangle + c_2 |\psi_2^{(0)}\rangle + \dots \quad (2.3)$$

Typically, only a single eigenfunction of  $H_0$  has appreciable intensity from the ground vibrational state in the energy region of the spectroscopic interest. This eigenfunction is called the bright state and carries all of the oscillator strength from the ground state. The remaining eigenfunctions are referred to the bath or dark states. The bath states are composed of various combinations and overtones of the zeroth order basis ( $3N-6$  normal modes) that are close in energy to the bright state.

In the ideal high resolution experiment eigenstate resolution is achieved.<sup>8;45;51-53</sup> In this case the intensity of each transition represents the character of the bright state in the particular molecular eigenstate ( $I_i \propto |c_{b_i}|^2$ ). The sum of the intensity for all eigenstates is equal to the intensity of the bright state in the zeroth-order basis set; this fixes the total intensity available to the eigenstates. The resulting spectrum of the molecular eigenstates is the IVR multiplet. The unperturbed frequency of the bright state can be calculated using an intensity-weighted average of the frequencies of the various eigenstates in the IVR multiplet.

Eigenstate resolved spectra have been largely obtained by using double resonance techniques.<sup>8;15;54</sup> These techniques offer simplification of the complicated spectra that

result from the fragmented oscillator (strength) and overlap of ro-vibrational transitions. Spectral simplification occurs through double resonance because a single transition is monitored while the second source is scanned, and thereby only transitions out of the monitored transition are observed. This effectively limits the number of observed transitions which makes observing weak nearby perturbations much easier because there is no overlap of the vibrational bands.

Eigenstate resolved spectra provide a means to measure the IVR rate of the bright state.<sup>7,8</sup> Using the frequency (energy) and relative intensity the survival probability of the bright state can be calculated using the following:<sup>12</sup>

$$P(t) = \left| \langle \Psi(t=0) | \Psi(t) \rangle \right|^2 = \left| \langle \psi_b^{(0)} | \Psi(t) \rangle \right|^2 = \sum_i \sum_j I_i I_j \cos\left(\frac{E_i - E_j}{\hbar} t\right) \quad (1.4)$$

Where  $I_i$  is the normalized intensity and  $E_i$  is the energy of the  $i^{\text{th}}$  state. From the probability decay the IVR rate ( $1/\tau_{\text{IVR}}$  lifetime  $\tau_{\text{IVR}}$ ) is obtained from the time it takes for unit probability at  $t=0$  to decay to a value of  $1/e$ . The survival probability is the same dynamic quantity obtained both from high resolution spectra and a single color pump-probe experiment.<sup>55,56</sup> However, high resolution spectra have the advantage of obtaining the rotational state dependence on the IVR rate.

An alternative approach to measuring the IVR lifetime is to use Fermi's Golden Rule,

$$\Gamma = 2\pi \langle W^2 \rangle \rho \quad (2.5)$$

where Fermi's Golden Rule states that the lifetime imposed linewidth is proportional to the product of the mean squared coupling of the bright state with the bath states and the

state density.<sup>8</sup> This assumes a dense manifold with near equally coupled levels.<sup>7</sup> The lifetime imposed linewidth,  $\Gamma$ , is the FWHM of the molecular eigenstate distribution (assumed to be Lorentzian). From the Fourier transform relation for a Lorentzian where  $\tau$  is the IVR lifetime of the bright state,

$$\tau = \frac{1}{2\pi \Gamma} \quad (2.6)$$

In terms of the Fermi Golden rule analysis, it was initially thought that increasing the state density would produce faster IVR rates. However, if the added states are weakly coupled then the IVR rate remains unchanged. It has been demonstrated for v=1 of hydride stretches that there is a certain IVR threshold at ~10 to 100 states per cm<sup>-1</sup>.<sup>57;58</sup> After this threshold has been exceeded the IVR rate and state density are largely uncorrelated.<sup>7;8</sup>

Although dynamical information has been obtained for a variety of molecules the results are largely restricted to describing only the bright state lifetime. The high resolution IR method does not answer the question: where and how fast does the vibrational energy flow after leaving the bright state? In addition to this, the bright state is only a single state while there are typically hundreds to thousands of states in a 1 cm<sup>-1</sup> energy region. This makes IVR lifetime measurements very specific; where perhaps a more general approach is needed to gain a broad understanding of IVR. To obtain more generalized information on the vibrational dynamics, spectroscopic techniques complementary to the high resolution methods are desirable.

## B. Dynamic Rotational Spectroscopy

The single-photon high resolution infrared spectrum can only measure the survival probability of the bright state, and a more complete understanding of the pathways of the nuclear dynamics is desirable. Pathways of nuclear dynamics can be understood in terms of the tier model for IVR,<sup>7,59-61</sup> depicted in Figure 2.2, which describes a hierarchy of coupling from the bright state to near-degenerate basis states. These basis states are in turn coupled to a further set of near-degenerate basis states. In some systems it is possible that the tiers represent different isomers, and the kinetics of the energy flow between the tiers corresponds to the isomerization rate. Therefore, obtaining tier dynamics or bath state dynamics from the frequency domain spectrum may be advantageous.

For the measurements described in this thesis the rotational spectrum is used to probe the molecular structure and the changes to that structure after vibrational excitation. Intramolecular energy flow dynamics can be obtained from the rotational spectrum of a vibrationally excited single eigenstate and is known as dynamic rotational spectroscopy (DRS).<sup>19</sup> A DRS experiment measures the rotational spectrum between the mixed molecular eigenstates at  $J$  and  $J+1$  as depicted in Figure 2.3 for highly mixed quantum states.<sup>62,63</sup> The energy flow dynamics are embedded in each single quantum state and typically several eigenstates are used to obtain an ensemble average.

The theories developed for NMR that describe “motional narrowing” and “coalescence”,<sup>22-25</sup> have been adapted to obtain dynamical information from the rotational spectrum. For NMR, coalescence describes the situation where a molecule has two or

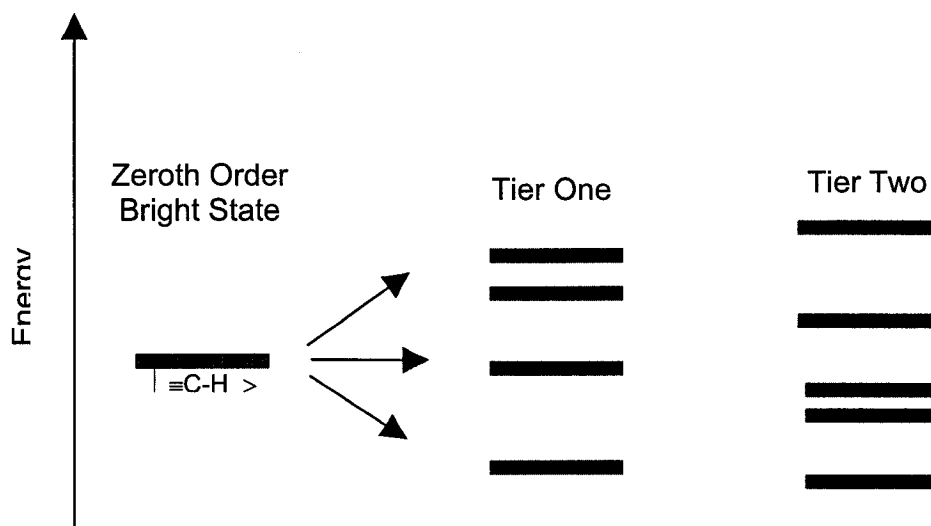


**Figure 2.2** The Tier model of IVR is illustrated. The zeroth order bright state is assumed to contain all of the transition probability from the ground state. Close in energy to the bright state is the 'dark' or bath states with no transition probability from the ground state. The bath states are divided into tiers which represent their physical importance. In a particular case the tiers can represent structures due to isomerization, and studying the energy flow between the tiers corresponds to an isomerization rate.

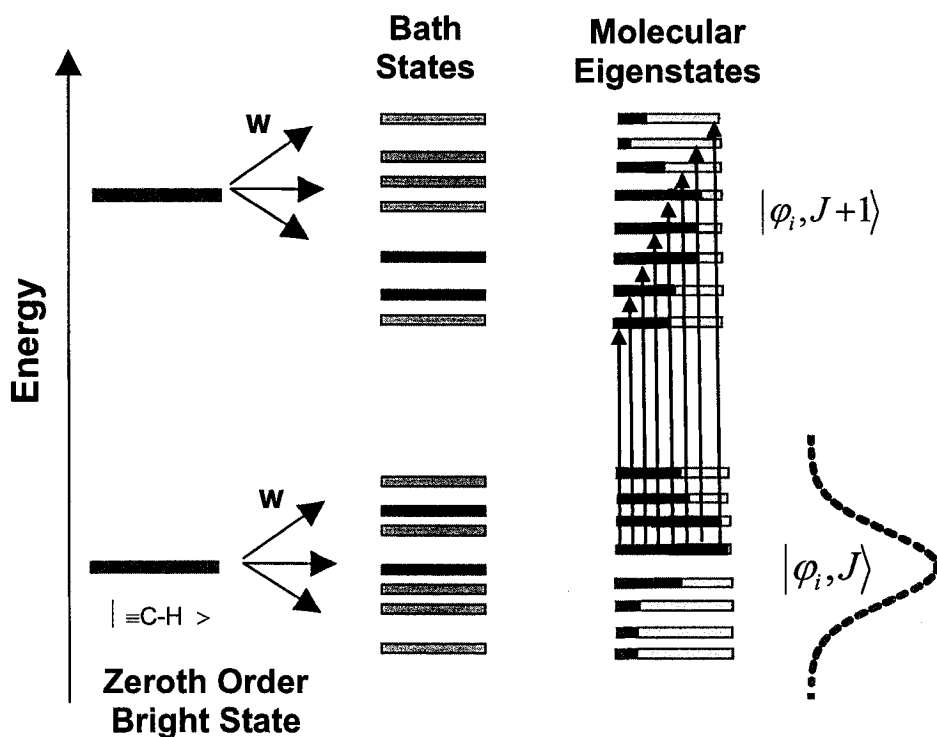


**Figure 2.3** This schematic level diagram illustrates the bright state coupling to the nearby bath states and creating a set of highly mixed molecular eigenstates. Rotational spectra are measured between the mixed molecular eigenstates at  $J$  and  $J + 1$ . Due to IVR the molecular eigenstates at  $J$  are not the same as those at  $J + 1$ . In contrast to rotational spectroscopy in the ground vibrational state many rotational transitions are observed that may originate from a single mixed molecular eigenstate as depicted on the right. Dynamical information is obtained from the overall lineshape profile of the rotational spectrum of the mixed molecular eigenstates. For most of the experiments described a pulsed IR laser is used and in this case all of the eigenstates under the bandwidth of the pulsed IR laser ( $\sim 600$  MHz, dotted red line) will be vibrationally excited.

more nuclei exchanging chemical environments. The molecule can jump between the two configurations if given enough energy to overcome the potential barrier.

Under the condition of infinitely slow exchange, the lineshape consists of two sharp lines. As the exchange rate increases the two lines broaden and begin<sup>20,21</sup> to move to an average position. Eventually the two peaks coalesce into a single broad peak. As the rate of exchange between the two configurations continues to increase, the spectrum narrows further.<sup>64</sup> This motional narrowing of the lineshape has been solved using the Bloch equations and can be used to determine the exchange rate between the two molecular configurations.<sup>64</sup>

In terms of IVR, motional narrowing can be observed in the vibrationally excited single molecular eigenstate rotational spectrum and is related to how fast vibrational energy flows through the molecule. This idea was first presented by Makarov.<sup>65</sup> This narrowing can be observed for a single stable conformer. In this case the exchange rate refers to energy exchange between vibrational states.<sup>19</sup> The lineshape analysis of the rotational spectrum is derived from the first and second moments of the spectrum.<sup>20</sup> The general expression for the  $n^{\text{th}}$  frequency moment is shown below:

$$\langle v^n \rangle = \frac{\sum_i I_i v_i^n}{\sum_i I_i} \quad (2.7)$$

The moments have been derived previously for the spectrum of a single molecular eigenstate with total angular momentum  $J$ .<sup>20,21</sup> The first moment is the center frequency which is determined by the expectation value of the rotational constant and the second moment, the width, is determined by the fluctuation (standard deviation) of the rotational

constant in the quantum state. Vibration–rotation interactions cause each normal mode basis state to have a different rotational constant, which results in a non-zero fluctuation. The rotational constant distribution is expected to be Gaussian based on measurements of the vibrational dependence on the rotational constant. If the “IVR exchange” rate is faster than the pure dephasing, the  $T_2$  time is lengthened and this leads to a narrowed spectrum.<sup>20</sup> An approximation for the observed width of the rotational spectrum in the strongly narrowed limit is given by the following.<sup>19</sup>

$$\Delta\nu_{obs} = \Gamma_{ROT} \frac{\Gamma_{ROT}}{\Gamma_{IVR}} = 2(J+1)\sigma_B \frac{2(J+1)\sigma_B}{2\pi\langle W^2 \rangle \rho} \quad (2.8)$$

From the width reduction, the average IVR rate can be determined. In the absence of IVR exchange narrowing the single eigenstate spectrum appears to have a Gaussian distribution, and in the limit of strong exchange narrowing the spectrum appear to have a Lorentzian lineshape.<sup>20</sup> The effective narrowing is largely controlled by the anharmonic coupling of vibrational states, and as the coupling increases the spectrum narrows.

Motional narrowing has been observed for propynol<sup>17</sup> and will be demonstrated trifluoropropyne using dynamic rotational spectroscopy. In these cases, motional narrowing was shown to occur at increasing  $K_a$  (where  $K_a$  is the projection of the total angular momentum  $J$  onto the a-principle-axis) values because of parallel Coriolis coupling due to the O-H rotor. These results demonstrate that the rotational spectrum of a single eigenstate is sensitive to different dynamics than the bright state lifetime measurement, which showed no dependence of the IVR rate on the  $K_a$  value. The DRS measurement contains information on bath state dynamics while the IR measurement

contains information on the bright state dynamics only.<sup>27</sup> Additionally, the IVR rate determined from DRS is an average over all participating vibrational state dynamics.

Recently, the theory and experimental methods for DRS have been developed to measure conformational isomerization rates.<sup>19</sup> The isomerization rate is obtained from the lineshape of the single eigenstate rotational spectrum by using the Bloch vector modified for chemical exchange.<sup>64</sup> The isomerization rate of a microcanonical ensemble is determined at a well-defined total energy and therefore there is direct relationship between the isomerization rate measured by DRS and that predicted by statistical rate theories, such as RRKM. Comparison of these experimental values and RRKM predictions has indicated that RRKM predicts a rate constant several orders of magnitude too fast.<sup>19</sup> RRKM theory has been successfully applied to disassociating systems and high barrier isomerization reactions,<sup>6</sup> but for low barriers isomerization reactions (i.e. conformation isomerization) RRKM has been shown to poorly describe these reaction rates.<sup>29;66</sup>

## Reference List

1. Polanyi, J. C., *Science* **1987**, *236*, 680.
2. Herschbach, D. R., *Angew.Chem.Int.Ed. Engl.* **1987**, *26*, 1221-1243.
3. Lee, Y. T., *Angew.Chem.Int.Ed. Engl.* **1987**, *26*, 939-951.
4. Oref, I.; Rabinovitch, B. S., *Acc.Chem.Res.* **1979**, *12*, 166-175.
5. Zewail, A. H., *J.Phys.Chem.A* **2000**, *104*, 5660-5694.
6. Baer, T.; Hase, W. L. *Unimolecular Reaction Dynamics: Theory and Experiments*; Oxford University Press: New York, 1996
7. Nesbitt, D. J.; Field, R. W., *J.Phys.Chem.* **1996**, *100*, 12735-12756.
8. Lehmann, K. K.; Scoles, G.; Pate, B. H., *Annu.Rev.Phys.Chem.* **1994**, *45*, 241-274.
9. Felker, P. M.; Lambert, W. R.; Zewail, A. H., *J.Chem.Phys.* **1985**, *82*, 3003-3010.
10. Freed, K. F. In *Radiationless processes in molecules and condensed phases*; Fong, F. K., ed. Springer-Verlag: New York, 1976; pp 23-168.
11. Bixon, M.; Jortner, J., *J.Chem.Phys.* **1968**, *48*, 715-726.
12. Jiang, X. P.; Brumer, P., *J.Chem.Phys.* **1991**, *94*, 5833-5843.
13. Freed, K. F.; Nitzan, A., *J.Chem.Phys.* **1980**, *73*, 4765-4778.
14. Takami, M.; Suzuki, M., *J.Chem.Phys.* **1980**, *72*, 4089-4098.
15. Fraser, G. T.; Pate, B. H.; Bethardy, G. A.; Perry, D. S., *Chem.Phys.* **1993**, *175*, 223-236.
16. Kerstel, E. R. Th.; Lehmann, K. K.; Gambogi, J. E.; Yang, X.; Scoles, G., *J.Chem.Phys.* **1993**, *99*, 8559-8570.
17. Green, D.; Holmberg, R.; Lee, C. Y.; McWhorter, D. A.; Pate, B. H., *J.Chem.Phys.* **1998**, *109*, 4407-4414.
18. McWhorter, D. A.; Hudspeth, E.; Pate, B. H., *J.Chem.Phys.* **1999**, *110*, 2000-2009.
19. Keske, J.; McWhorter, D.; Pate, B. H., *Int.Rev.Phys.Chem.* **2000**, *19*, 363-407.
20. Pate, B. H., *J.Chem.Phys.* **1998**, *109*, 4396-4406.

21. Pate, B. H., *J.Chem.Phys.* **1999**, *110*, 1990-1999.
22. Anderson, P. W., *J.Phys.Soc.Japan* **1954**, *9*, 316-339.
23. Anderson, P. W.; Weiss, P. R., *Rev.Mod.Phys.* **1953**, *25*, 269-276.
24. Kubo, R.; Tomita, K., *J.Phys.Soc.Japan* **1954**, *9*, 888-919.
25. van Vleck, J. H., *Phys.Rev.* **1948**, *74*, 1168-1183.
26. Keske, J. C. *Dynamic Rotational Spectroscopy*. PhD Dissertation, 2002.
27. Keske, J. C. and Pate, B. H., *Annu.Rev.Phys.Chem.* **2000** *19*, 363.
28. Robinson, P. J.; Holbrook, K. A. *Unimolecular Reactions*; Wiley-Interscience: New York, 1972.
29. Leitner, D. M.; Wolynes, P. G., *Chem.Phys.Lett.* **1997**, *280*, 411-418.
30. Kerstel, E. R. Th.; Lehmann, K. K.; Mentel, T. F.; Pate, B. H.; Scoles, G., *J.Phys.Chem.* **1991**, *95*, 8282-8293.
31. Lee, C. Y.; Pate, B. H., *J.Chem.Phys.* **1997**, *107*, 10430-10439.
32. Dolson, D. A.; Holtzclaw, K. W.; Moss, D. B.; Parmenter, C. S., *J.Chem.Phys.* **1986**, *84*, 1119-1132.
33. McIlroy, A.; Nesbitt, D. J., *J.Chem.Phys.* **1994**, *101*, 3421-3435.
34. Parmenter, C. S.; Stone, B. M., *J.Chem.Phys.* **1986**, *84*, 4710-4711.
35. Li, H.; Miller, C. C.; Philips, L. A., *J.Chem.Phys.* **1994**, *100*, 8590-8601.
36. Perry, D. S.; Bethardy, G. A.; Wang, X., *Ber.Bunsenges.Phys.Chem.* **1995**, *99*, 530-535.
37. McGurk, J. C.; Mäder, H.; Hofmann, T.; Schmalz, T. G.; Flygare, W. H., *J.Chem.Phys.* **1974**, *61*, 3759-3767.
38. Balle, T. J.; Flygare, W. H., *Rev.Sci.Instrum.* **1981**, *52*, 33-44.
39. Legon, A. C., *Annu.Rev.Phys.Chem.* **1983**, *34*, 275-300.
40. Arunan, E.; Dev.S.; Mandal, P. K., *Appl.Spectrosc.Rev.* **2004**, *39*, 131-181.
41. Xu, Y., Wijngaarden, J. van, and Jäger, W., *Int.Rev.Phys.Chem.* **2005**, *24*, 301-338.

42. Suenram, R. D.; Grabow, J. U.; Zupan, A.; Leonov, I., *Rev.Sci.Instrum.* **1999**, *70*, 2127-2135.
43. Ekkers, J.; W.H.Flygare, W. H., *Rev.Sci.Instrum.* **1976**, *47*, 448-454.
44. Nakajima, M.; Sumiyoshi, Y.; Endo, Y., *Rev.Sci.Instrum.* **2002**, *73*, 165-171.
45. de Souza, A. M.; Kaur, D.; Perry, D. S., *J.Chem.Phys.* **1988**, *88*, 4569-4578.
46. Bethardy, G. A.; Wang, X.; Perry, D. S., *Can.J.Chem.* **1994**, *72*, 652-658.
47. Stannard, P. R.; Gelbart, W. M., *J.Phys.Chem.* **1981**, *85*, 3592-3599.
48. Herzberg, G. *Molecular Spectra and Molecular Structure II. Infrared and Raman Spectra of Polyatomic Molecules*; Van Nostrand Reinhold: New York, 1945
49. Papousek, D.; Aliev, M. R. *Molecular Vibrational-Rotational Spectra*; Elsevier: New York, 1982
50. Lawrence, W. D.; Knight, A. E. W., *J.Phys.Chem.* **1988**, *92*, 5900-5908.
51. McIlroy, A.; Nesbitt, D. J., *J.Chem.Phys.* **1990**, *92*, 2229-2243.
52. Pate, B. H.; Lehmann, K. K.; Scoles, G., *J.Chem.Phys.* **1991**, *95*, 3891-3916.
53. Miller, C. C.; Philips, L. A.; Andrews, A. M.; Fraser, G. T.; Pate, B. H.; Suenram, R. D., *J.Chem.Phys.* **1994**, *100*, 831-839.
54. Keske, J. C.; B.H.Pate, *Chem.Phys.Lett.* **2001**, *342*, 51-57.
55. Wynne, K.; Hochstrasser, R. M., *Chem.Phys.* **1995**, *193*, 211-236.
56. Khundkar, L. R.; Zewail, A. H., *Annu.Rev.Phys.Chem.* **1990**, *41*, 15-60.
57. Kim, H. L.; Kulp, T. J.; McDonald, J. D., *J.Chem.Phys.* **1987**, *87*, 4376-4381.
58. McDonald, J. D.; Stewart, G. M., *J.Chem.Phys.* **1981**, *75*, 5949.
59. Muthukumar, M.; Rice, S. A., *J.Chem.Phys.* **1978**, *69*, 1619-1625.
60. Kay, K. G.; Rice, S. A., *J.Chem.Phys.* **1972**, *57*, 3041-3047.
61. Heller, E. J.; Rice, S. A., *J.Chem.Phys.* **1974**, *61*, 936-946.
62. Stone, J.; Thiele, E.; Goodman, M. F., *J.Chem.Phys.* **1981**, *75*, 1712-1727.

63. Keske, J. C.; Pate, B. H., *Annu.Rev.Phys.Chem.* **2000**, *51*, 323-353.
64. Slichter, C. P. *Principles of Magnetic Resonance*; Springer: New York, 1996.
65. Makarov, A. A., *Opt..Spektrosk., USSR* **1987**, *62*, 697-699.
66. Leitner, D. M.; Levine, B.; Quenneville, J.; Martinez, T. J.; Wolynes, P. G., *J.Phys.Chem.A* **2003**, *107*, 10706-10716.

## Chapter 2

### Narrow Band Cavity FTMW Spectroscopy

#### Introduction

We have recently built a Balle – Flygare type Fourier Transform Microwave (FTMW) spectrometer based on the recent design of the NIST spectrometer.<sup>1</sup> This spectrometer was chosen for its excellent sensitivity in obtaining rotational spectra and for its compact size. The spectrometer is designed to operate from 8 to 26 GHz. The lower frequency limit is due to the diffraction losses whereas the upper frequency bound is limited by electronics only. The spectrometer has been designed to have FTMW – MW double resonance and IR-FTMW-MW triple resonance capabilities. These capabilities are necessary to study intramolecular dynamics. The various components of the spectrometer will be described in detail along with the necessary excitation and detection schemes.

#### A. FTMW Background Theory

As an extension to previous molecular-beam high-resolution spectroscopy techniques for performing dynamic rotational spectroscopy (DRS) new techniques are presented based on Fourier transform microwave (FTMW) spectroscopy. The theory of FTMW spectroscopy was established in the late 1970's<sup>2</sup> and developed into the well known Balle-Flygare FTMW spectrometer.<sup>3</sup> Since that time many technological advances have led FTMW spectroscopy to achieve unrivaled sensitivity that has revitalized the

field of rotational spectroscopy.<sup>4</sup> Rotational spectroscopy is largely responsible for structural determination of van der Waals complexes,<sup>5-7</sup>, and a quantitative understanding of barriers to internal rotation.<sup>8-11</sup> Pulsed molecular beam methods were incorporated to achieve rotational cooling ( $\sim 2$  K) which provides spectral simplification. The addition of a Fabry-Perot build up cavity is the major component for achieving high sensitivity.

Flygare and McGurk have presented the theoretical foundations for FTMW spectroscopy.<sup>2</sup> Flygare later developed the FTMW theory incorporating the Fabry-Perot cavity and a pulsed supersonic expansion.<sup>3</sup> A relatively short microwave (MW) pulse (of length  $\tau$ , 1  $\mu$ s typical) is used to polarize the molecules in the active region of the FTMW cavity. This pulse aligns the dipoles of the molecules creating a macroscopic polarization which results in coherent emission. The emission of the molecules is recorded after the initial polarizing pulse has dissipated from the cavity. The emission is damped by the polarization relaxation time,  $T_2$  ( $T_2 \gg \tau$ ) and the emitted field appears as a free induction decay (FID).<sup>3</sup> The polarization relaxation time,  $T_2$ , is not necessarily associated with the energy relaxation of the system,  $T_1$ .  $T_2$  can be regarded as the phase memory time of the system.<sup>12</sup> Contributing factors to damping the  $T_2$  relaxation time are caused by transverse movement of molecules out of the cavity region and Doppler dephasing. Doppler dephasing results from molecules which were polarized with one phase move to a region in which they would have been polarized with a different phase.<sup>13</sup> The emitted electric field is measured directly and is proportional to the product of the transition moment,  $\kappa$ , population difference,  $\Delta N$ , number of molecules,  $M$ , and quality factor,  $Q_L$ .<sup>3</sup>

$$E(t) \propto \kappa \Delta N M \sqrt{Q_L} \quad (2.1)$$

The most critical component of the FTMW spectrometer for achieving high sensitivity is the Fabry-Perot cavity. For a radiating dipole placed between the two cavity mirrors an electric field can build up and enhanced by a  $\sqrt{Q}$  factor.<sup>3</sup> The cavity is designed to have a certain quality factor, Q, which is defined as the ratio of the energy stored to the power dissipated per cycle in the cavity.

The cavity Q can be estimated by assuming the only power dissipation is through reflection and diffraction. Reflection loss,  $\alpha_r$ , result from ohmic power dissipation due to the finite conductivity of the mirrors and can be calculated from the skin depth,  $\delta$ , and the wavelength,  $\lambda$ .<sup>3,1</sup>

$$\alpha_r = \frac{2\delta(2\pi)}{\lambda} \quad (2.2)$$

The skin depth is the distance into the material where the amplitude of an electromagnetic wave falls to 1/e of its value at the surface. For a good conductor the skin depth can be defined as the following:<sup>3</sup>

$$\delta = \sqrt{\frac{2}{\omega\mu\sigma}} \quad (2.3)$$

Where  $\omega$  is the angular frequency,  $\mu$  is the permeability of the material, and  $\sigma$  is the conductivity. For aluminum, at 10 GHz the skin depth is 850 nm. The fractional energy loss due to reflection losses at 10 GHz is  $3.5 \times 10^{-4}$  per cycle.

Diffraction losses are kept low by designing a cavity where the Fresnel number, N, is unity for the lowest frequency desired for the spectrometer. The Fresnel number is a

unitless quantity describing the type of diffraction (far field versus near field). For the UVA spectrometer the Fresnel number is 1 at 10 GHz. A Fresnel number of unity insures a high Q because a large fraction of the electric field amplitude is captured at any point by the mirror.<sup>1</sup>

$$N = \frac{a^2}{d\lambda} \quad (2.4)$$

The cavity mirrors have a radius of curvature of 30 cm, radius of 9.75 cm, a, and are separated by ~35 cm, d. The fractional energy loss due to diffraction,  $\alpha_d$ , can be calculated for a confocal arrangement with circular apertures for a given Fresnel number, N.<sup>1</sup>

$$\alpha_d = 16\pi^2 Ne^{-4\pi N} \quad (2.5)$$

The loss due to diffraction at 10 GHz is  $6 * 10^{-4}$  per cycle at 10 GHz. Taking into account reflection and diffraction losses the cavity Q can be estimated using the distance between the mirrors, d.<sup>1</sup>

$$Q = \frac{2\pi d}{\lambda(\alpha_r + \alpha_d)} \quad (2.6)$$

This equation provides an upper limit to the cavity Q because it does not take into account input and output coupling losses. At 10 GHz ( $\lambda \approx 3$  cm) the cavity Q is estimated to be  $7 * 10^4$ .

The Q can be measured by measuring the lifetime,  $\tau$ , of a MW pulse in the cavity or in the frequency domain by measuring the FWHM of the cavity linewidth,  $\Delta\nu$ , at a given frequency,  $\nu$ .<sup>3</sup>

$$Q_L = \tau 2\pi v = \frac{v}{\Delta v} \quad (2.7)$$

At 10 GHz the UVA FTWM cavity mode linewidth was fit to a Gaussian with a 0.963 MHz FWHM. This linewidth corresponds to a lifetime of 165 ns and a  $Q_L$  of  $10^4$ . The quality factor,  $Q_L$ , for the machine combines all the dissipative elements of the cavity such as reflection and diffraction,  $Q_c$ , input,  $Q_{c1}$ , and output coupling,  $Q_{c2}$ .<sup>3</sup>

$$Q_L = \left( \frac{1}{Q_c} + \frac{1}{Q_{c1}} + \frac{1}{Q_{c2}} \right)^{-1} \quad (2.8)$$

Because the electric field is detected there is a factor of 100 gain ( $\sqrt{Q}$ ) of the molecular emission signal corresponding to a factor of 100 improvement to the signal-to-noise ratio. This makes FTMW spectroscopy well suited to measuring weak transitions, which is a critical aspect of dynamic rotational spectroscopy.

## B. Vacuum Chamber and Pumping System

The vacuum chamber design is based on a 30 cm diameter sphere with five LF-ISO (NW200 MDC) flange ports. A sixth port is a 15 cm ASA flange which is mounted to a 15 cm ASA to 25 cm ASA flange adapter (MDC). The adapter is used to mount the chamber to a 25 cm water cooled baffle (Varian 330) and Diffusion pump (Varian VHS 10). The water cooled baffle is used to prevent diffusion pump oil from depositing on the IR multipass mirrors. The diffusion pump is backed by a mechanical pump and Roots blower system (Edwards E2M40 and H250). A 15 cm diameter fore line is used to connect the diffusion pump to the Roots blower system. Valves on the diffusion pump

and Roots blower system (Norcal ESV-2002-NWB) allow the system to be vented without also venting the fore line. This vacuum system provides a pumping speed of about 2000 l/s (estimated) with the water cooled baffle. The pumping speed is a factor of two faster than our previous vacuum system. This system typically achieves pressures around  $8 \times 10^{-6}$  Torr in about a half hour. The vacuum pressure is monitored with a thermocouple (Varian TC 0531) and ion gauge (Granville-Phillips Series 354).

The chamber, illustrated in Figure 2.1, is mounted on a moveable cart that contains rack mounts that house most of the electronics for the spectrometer. Attached to one of the ports on the chamber is a 20 cm arm that contains a Fabry-Perot cavity mirror mounted to a motorized translation stage (Aerotech ATS 03005). The motorized translation stage is controlled by an external motion controller (Aerotech Unidex 100M). The motion controller is connected to the translation stage through a hermetically sealed 25 pin connector (Cermaseal 14442-02W) that is welded into the end flange. This end flange also contains a hermetically sealed SMA connector that provides an input for MW radiation for the cavity mirror. Through software manipulation the motion controller is used to move the cavity mirror to find a cavity mode at a desired frequency. The other cavity mirror is fixed in place and is machined to form an integral end flange for the vacuum chamber. Both mirrors have a hole for placement of a pulsed nozzle and each mirror has two antenna one for broadcasting or receiving and the other for blocking non- $\text{TEM}_{00q}$  modes. In this way the machine can operate in either reflection or transmission mode. The top flange contains a 0.64 cm pipe and electrical feed-through for sample input and pulse control for the pulsed nozzle.

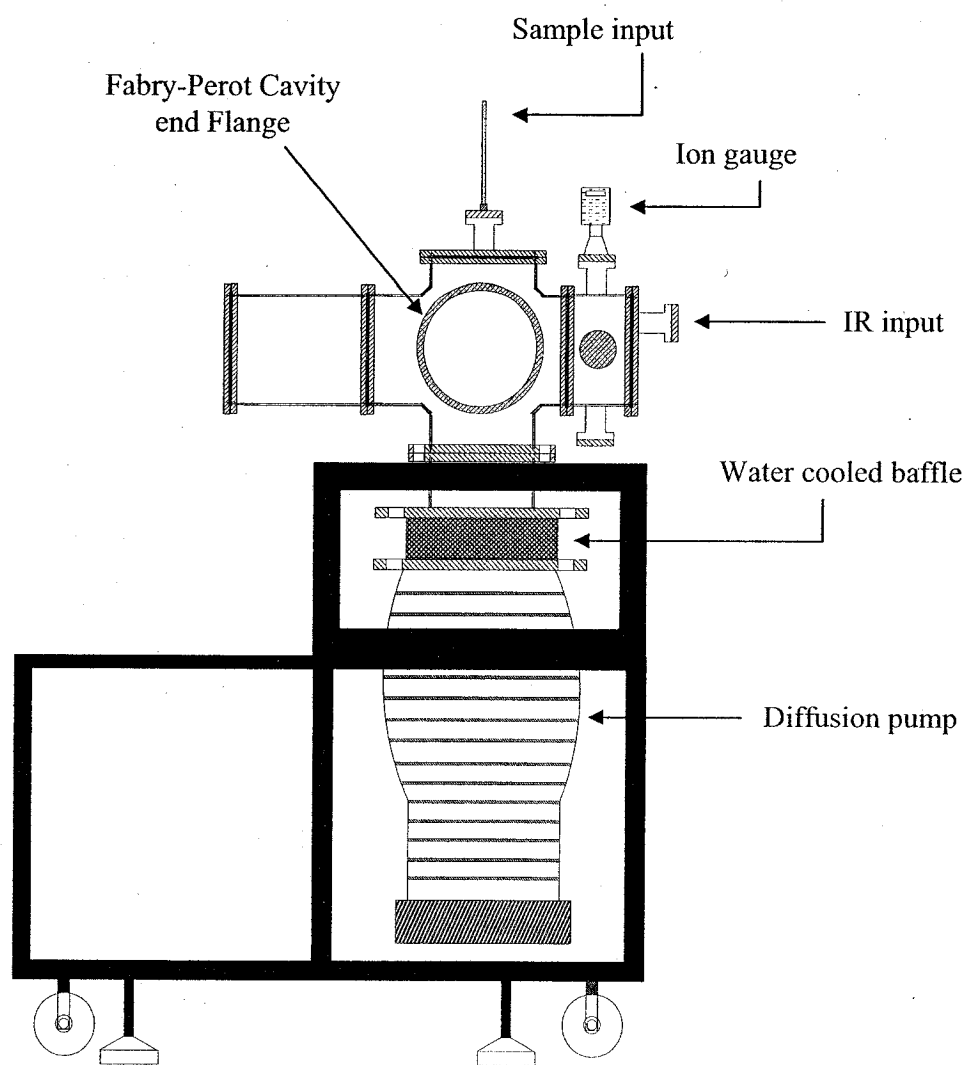


**Figure 2.1** The various components of the FTMW vacuum chamber are illustrated above.

A second 20 cm extension arm and a smaller 10 cm arm are attached to the remaining two ports of the chamber. The end flange of the smaller arm contains a 7 cm conflat flange that contains CaF<sub>2</sub> window for IR input. Both extension arms house the mounts for the infrared multipass mirrors.

### C. Free Jet Expansion

A pulsed valve (pulsed Series 9 General Valve) with 1 mm orifice is used for a molecular beam source. The pulsed valve is modified to incorporate a sample reservoir (few hundred  $\mu\text{L}$ ) for liquid samples with high boiling points ( $>100$  °C). A supersonic expansion is achieved which results in rotational cooling to 2-3 K (estimated from intensities of fit rotational spectra). There are two options for pulse valve placement, parallel or perpendicular. The nozzle tension of both perpendicular and parallel nozzles can be actively tuned to maximize the signal. A parallel nozzle placement has demonstrated narrower linewidth and stronger signals.<sup>14</sup> However, this geometry also leads to a Doppler doublet, where two peaks are observed split by their Doppler shift. Efficient IR excitation is achieved by having the nozzle close to the IR multipass. This is only feasible with the perpendicular nozzle geometry.

To provide room for optics and not to interfere with the cavity mode the pulsed valve is placed 8 cm above the cavity centerline. The laser intercepts the molecular beam directly after the nozzle, before the pulse expands in the radial direction. The pulsed valve is activated by a pulse driver (Iota One General Valve) and the relative timing and pulse duration are controlled with a TTL input. The backing pressure for experiments

varies with sample concentration. For most gas samples the backing pressure is about 5 psi for 0.1% - 0.5% sample concentrations. For liquid samples placed in the reservoir nozzle the backing pressure is kept low 1-2 psi.

#### **D. Fabry – Perot Cavity**

A cross section of the chamber illustrating the three excitation sources is illustrated in Figure 2.2. The Fabry - Perot cavity has mirrors with a 30 cm radius of curvature and a diameter 19.5 cm. The distance between mirrors is typically confocal at 35 cm between mirrors. The mirrors were sliced out of 20.54 cm diameter 5086 aluminum bar stock. Bar stock is used to minimize warping after machining. The 5 cm thick wafers are machined out roughly and then heat treated to reduce material stress. The mirrors are then machined using diamond turning techniques to obtain a surface quality of 15 - 20 nm (rms) with a deviation of the radius of curvature of  $<1 \mu\text{m}$ . It is important to keep the surface roughness below the skin depth in order to avoid a decrease in the effective surface conductivity.<sup>1</sup> This is important because the instrument sensitivity is dependent on the quality factor, Q, which in turn is dependent on the surface conductivity as described in equations 2.10 - 2.14.

One of the advantages of the FTMW is the large sample volume which is due to the large active region of the cavity. From the radius of curvature, R, and the distance between the mirrors, d, the active region at the centerline of the cavity can be calculated for a specific wavelength,  $\lambda$ .<sup>3</sup>

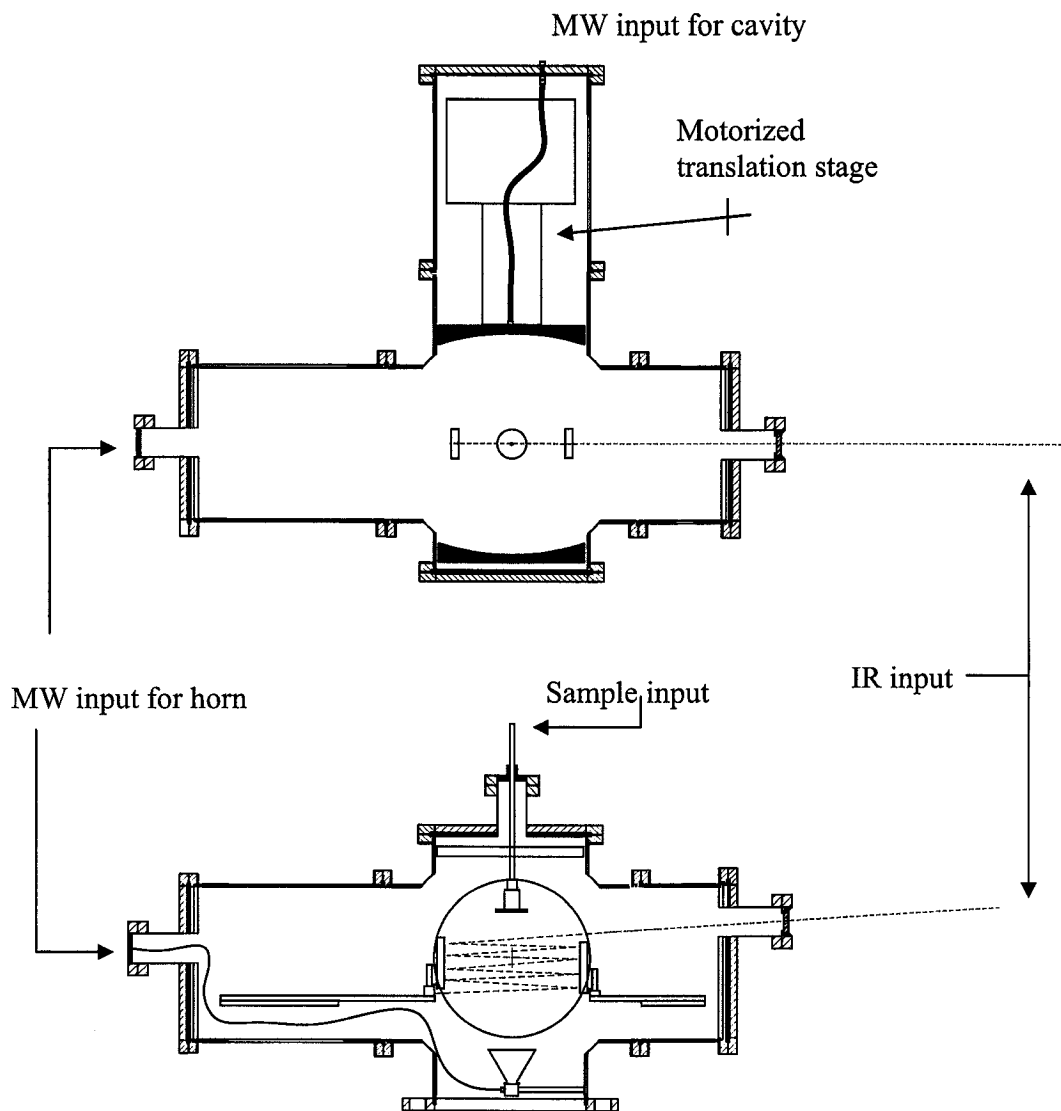


**Figure 2.2** A cross-section diagram of the FTMW chamber is illustrated above. The three excitation regions Fabry-Perot cavity, IR multipass, and standard gain horn are illustrated.

$$w_0 = \left( \frac{\lambda}{2\pi} [d(2R-d)]^{\frac{1}{2}} \right)^{\frac{1}{2}} \quad (2.9)$$

where  $w_0$  is the active region or beam waist radius. The beam waist is defined as the distance from the cavity centerline to where the electric field becomes  $1/e$  of its initial value. The total active region is  $2*w_0$  and at 17 GHz the beam waist of our machine is  $\sim 6$  cm.

### E. Microwave Pulse Generation and Detection

There are two systems to control the pulse timing and detection. The NIST setup is used for ground state scans only and has been described previously.<sup>1</sup> The block diagram for the FTMW setup, Figure 2.3, illustrates all of the components necessary for MW pulse generation and signal acquisition.<sup>1</sup> A new setup has been developed and will be described in detail. The new setup utilizes digital delay generators, an oscilloscope, and a data acquisition interface board (National Instruments DAQ-PAD 6020E) to set the pulses timing, detect the free induction decay, and set the cavity mode resonant to a desired frequency.

The source of the MW radiation is an HP8340B synthesizer (10 MHz-26.5 GHz, 15 dBm). The microwave switches, S1 and S3 are broad band (.5 - 26.5 GHz) single-pole-double-throw (SPDT) (Sierra MW Tech SM50071). Switch S2 is an rf switch (minicircuits zysw-2-50DR) that pulses 30 MHz into the single side band modulator (SSBM) (Miteq SM0226LCIA). The 30 MHz frequency offset is generated by a x3 active frequency multiplier (TCI FXA217-30) that inputs 10 MHz from the rubidium

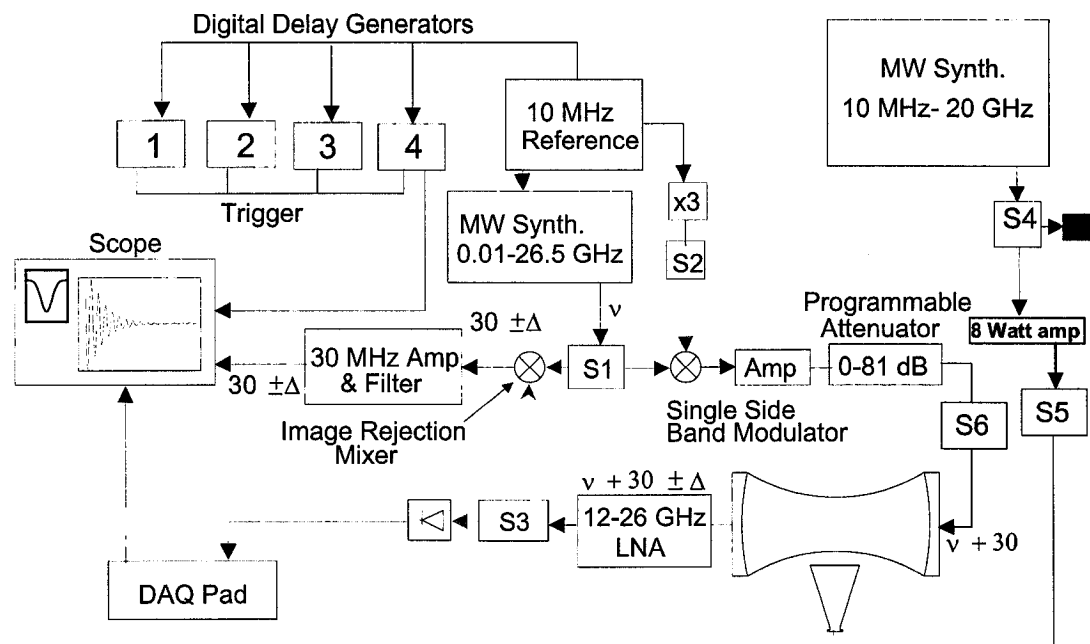


**Figure 2.3** The block diagram of the microwave circuit components is illustrated above.

oscillator frequency standard. The SSBM (2-26 GHz) is used to mix up 30 MHz from the output of the synthesizer. The cavity is set such that the resonant frequency is  $30 \text{ MHz} + \nu$ , where  $\nu$  is the synthesizer frequency. The  $30 \text{ MHz} + \nu$  is amplified (2-26 GHz 15 dBm gain, 10 dB max output Miteq ) and passes through two programmable attenuators (HP84904K and 84907K) before entering the cavity. The programmable attenuators are GPIB controlled through the HP11713A controller. The MW radiation is coupled into the cavity using a wire antenna made of semi-rigid coaxial cable.

On the detection side of the block diagram is a 12 – 18 GHz low noise amp (Miteq JS4-1200-2600-25-5P, 35 dB gain), switch S3, and image rejection mixer (Miteq IR0226LCIA). The image rejection mixer (IRM) detects only a single sideband which theoretically improves the signal-to-noise by a factor of 2 over a simple balanced mixer.<sup>14</sup> Rotational transitions on the order of the cavity bandwidth ( $\sim 2 \text{ MHz}$ ) are detected. A set of transitions can be detected  $\pm \Delta \text{ MHz}$  from the center frequency of the cavity. The IRM takes in the  $30 \text{ MHz} + \nu \pm \Delta$  from the molecular emission in the cavity and mixes with  $\nu$  from the synthesizer. The output of the IRM is a down converted signal centered at  $30 \text{ MHz}$  with  $\pm \Delta$  frequencies. The  $30 \text{ MHz}$  signal is amplified with a variable gain amplifier (Miteq VGC-3P-30/5BC,-4 to 62 dB gain), and filtered with a  $30 \text{ MHz}$  bandpass filter (Reactal 6B6-30-1.8S11). The  $30 \text{ MHz}$  signal is directly digitized with a 1 GHz bandwidth oscilloscope at 250 Msamples/s for a duration of  $20 \mu\text{s}$  (5000 pts, 4 ns/pt). The time domain signal is Fourier transformed to the frequency domain (4 kHz/pt) in real time and a Hamming windowing function is applied to remove Fourier

components due to truncation of the FID. The resulting linewidth is 75 kHz FWHM (nearly Gaussian). All active components are attached to water cooled copper blocks.

A single MW pulse and signal acquisition step consists of the following events; S1 and S3 switch to path A. and S2 opens sending a pulse into the SSBM from the synthesizer and the 30 MHz source. ‘A’ or ‘B’ refers to the possible paths depicted in the block diagram which is illustrated in Figure 2.3. The 30 MHz upconverted signal is amplified and attenuated in a way to optimize the signal. The MW pulse is coupled into the cavity with semi rigid cable acting as an antenna near the surface of the Fabry-Perot cavity mirror. The S2 switch closes and S1 and S3 then return to path b. allowing the emission signal to be coupled out of the cavity through a semi rigid coax antenna and enter the IRM with the synthesizer frequency. After time is allowed for the MW pulse to dissipate in the cavity (1- 3  $\mu$ s) the emission signal or free induction decay of the macroscopic polarization is detected. The machine is run at the 10 Hz repetition rate of the laser.

The cavity mode is found by using a lookup table to estimate the distance for the cavity mirror to move. The synthesizer is then set to sweep over this cavity position while switches S1 and S3 are set to path A. and switch S2 and S6 are held open. Switch S3 is connected to a Schottky power diode (Herotek DHM265AA) as the frequency is swept the output of the diode traces out the cavity mode shape. The cavity position is refined until a maximum is obtained. This typically takes 1 - 2 seconds for the entire mode-finding process. For the mode-finding process the oscilloscope through GPIB

control of the digital delay generators is used to ‘hold’ the switches to path A. The DAQ-PAD receives the MW sweep signal and the diode output.

For GPIB control of the various instruments using the oscilloscope an internet-to-GPIB adapter (AD007 National Instruments) or USB-GPIB adapter was used. Connecting the AD007 to the internet port on the oscilloscope and connecting the GPIB devices to the GPIB side of the adapter effectively enables the oscilloscope to make GPIB commands. Without a GPIB adapter the oscilloscope is only a listening device.

#### **F. Secondary Microwave Excitation**

A microwave standard gain horn (12-18 GHz) has been setup just above the water cooled baffle in the bottom part of the chamber. It was necessary to set the horn up in this fashion to achieve triple resonance because the multipass assembly is mounted in the center of the cavity. The horn is centered on the cavity axis, but now the polarization is perpendicular to the cavity polarization. The horn receives MW radiation using a 20 cm length of MW cable (Insulated Wire Inc. KPR-15-420-KPS) which is attached to 7 cm conflat flange that contains a hermetically sealed SMA feed-through. A second MW synthesizer (HP83752B) using a 15 cm length of MW cable is attached to the outside of the SMA feed-through. As illustrated in the block diagram, Figure 2.3, the horn can be set up to be pulsed using a single-pole-single-throw MW switch (same as above). An 8 watt amplifier (Microwave Power L0818-37) and a second SPST MW switch (American Microwave Corp. SW2184-1A) have been added to create high power MW pulses. The timing for this pulse is controlled through a digital delay generator.

### G. Infrared Excitation

A major hurdle for IR-FTMW spectroscopy is coupling the infrared light source to the FTMW spectrometer. A stable single-longitudinal-mode (SLM) nanosecond pulsed laser is used because the Doppler distribution exiting a pulsed jet for the acetylenic C-H fundamental is 200 MHz.<sup>15</sup> Having the bandwidth (600 MHz) of the pulsed laser on the order of the Doppler distribution ensures efficient pumping of all molecules exiting the pulsed nozzle source. At the same time the laser must be narrow enough for J selective excitation so that only a single J excited rotational state is created. Since the population of the rotational levels of the v=1 excited state is assumed to be zero, populating a single J in the excited state guarantees a large population difference between levels in the excited state. For this to be true the bandwidth of the laser must be less than the rotational level spacing of the molecule (B+C). A pulsed laser offers several other advantages such as fast scan rates, broad tunability, and high pulse energy. All of these aspects provide advantages for dynamical studies.

The IR laser system is an injection seeded Nd:YAG (Continuum Precision II 8000) laser that pumps a three stage, single longitudinal mode, OPO/OPA setup (Mirage 3000). A fraction of the 1064 nm light is converted to 532 nm light in an SHG crystal (KDP) before exiting the YAG laser. The YAG laser operates at a 10 Hz repetition rate with a pulse energy of 850 mJ per pulse (532 nm + 1064 nm). A diagram of the laser system is illustrated in Figure 2.4.

The Mirage utilizes optical parametric processes to generate tunable light from 1.45  $\mu\text{m}$  to 4.0  $\mu\text{m}$  and 710 nm to 840 nm. Optical parametric generation is an example

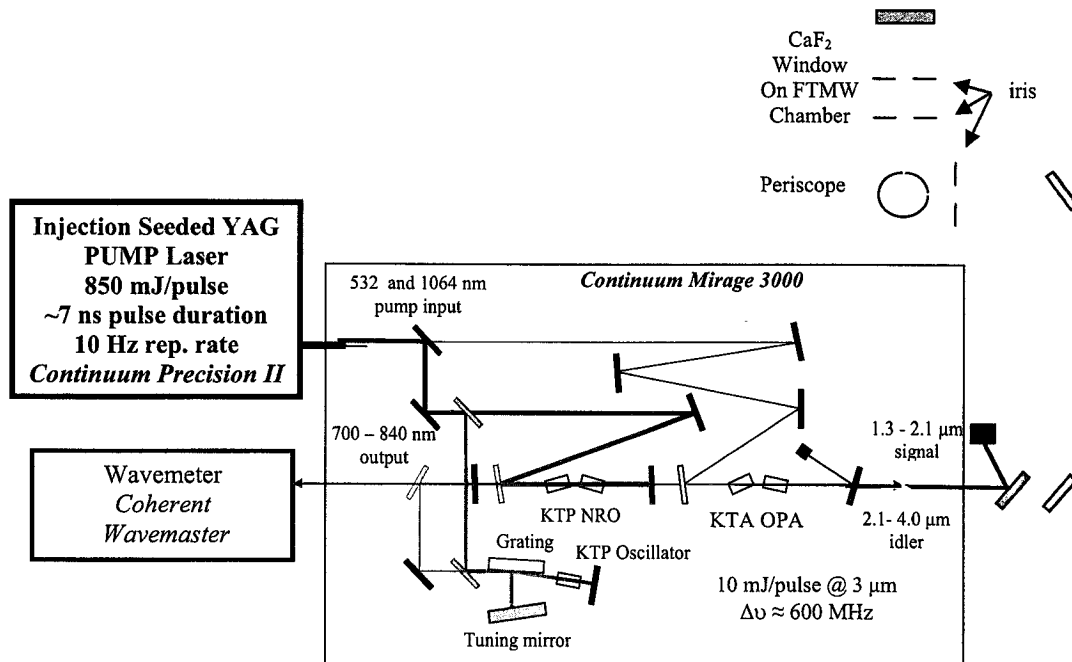


**Figure 2.4** The tunable IR laser system and optical setup is illustrated above.

pulse energy of 850 mJ per pulse (532 nm + 1064 nm). A diagram of the laser system is illustrated in Figure 2.4.

The Mirage utilizes optical parametric processes to generate tunable light from 1.45  $\mu\text{m}$  to 4.0  $\mu\text{m}$  and 710 nm to 840 nm. Optical parametric generation is an example of nonlinear 3-wave mixing process in which a photon of shorter wavelength is converted into two photons of longer wavelength. In a birefringent material such as potassium titanyl phosphate (KTP) optical parametric oscillation (OPO) or amplification (OPA) occurs when frequencies,  $\omega$ , of three photons conserve energy

$$\omega_p = \omega_s + \omega_i$$

and the wavevectors,  $\mathbf{k}$ , conserve momentum

$$\mathbf{k}_p = \mathbf{k}_s + \mathbf{k}_i$$

The subscripts refer to pump (p), signal (s), and idler (i). The idler is the low frequency component. Energy and momentum conservation are achieved by taking advantage of birefringent materials which have two indices of refraction. One index of refraction changes with propagation direction (angle). Angle tuning can be optimized to conserve energy and momentum or phase matching.

The Mirage laser consists of three nonlinear stages. The OPO or master oscillator (MO) is based on a grazing incidence grating resonator, and consists of four parts: rear mirror, KTP crystal, grating, and tuning mirror. Light enters the cavity with glancing incidence on a grating, passes through the KTP crystal and is reflected back to the grating by the rear mirror. Light that is reflected off the grating becomes the output beam while diffracted light propagates towards the tuning mirror and completes the cavity. The

cavity length is defined as the distance from the rear mirror to the grating plus the distance from the grating to the tuning mirror. The free spectral range is approximately 3 GHz. The tuning mirror angle controls the amount of diffracted light that is reflected back into the cavity to be further amplified by the KTP crystal. Lasing on other longitudinal modes is minimized by the phase matching requirement for the KTP crystal and the dispersion characteristics of the grating. However, to maintain SLM operation cavity length stabilization is implemented by monitoring the output pointing of the master oscillator (MO).

The master oscillator is pumped with 532 nm light and generates the seed beams for the non-resonant oscillator stage (NRO). The signal photon 710 – 840 nm and the idler photon  $2.12 \mu\text{m} - 1.45 \mu\text{m}$  from the MO are amplified in the NRO stage with the 532 nm pump photon. The optics at front end of the NRO reflect part of the idler while transmitting the signal and at the other back end the signal and pump are reflected and the idler is transmitted. The  $2.12 \mu\text{m}$  to  $1.45 \mu\text{m}$  idler photon becomes the seed for the final OPA stage which is pumped with 1064 nm light. This OPO stage was upgraded from KTP crystals to KTA (potassium titanyl arsenate) which have a much flatter power curve and comparable damage threshold. The 1064 nm photon is split into  $2.12 \mu\text{m} - 1.45 \mu\text{m}$  signal beam and  $2.12 \mu\text{m}$  to  $4.0 \mu\text{m}$  idler beam. Because both signal and idler exit the mirage a means to separate the beams is necessary. Initially a dichroic mirror was used, however was damaged by the high output power and was replaced with several silicon wafers at Brewster's angle. The laser pulse energy at  $3330 \text{ cm}^{-1}$  is 10 mJ/pulse, and at  $6560 \text{ cm}^{-1}$  is 25 mJ/pulse following the KTA upgrade.

### Optical Setup

The optical setup is depicted in Figure 2.4. The setup consists of four mirrors and four alignment irises. The first two mirrors are used to make the IR beam parallel to the laser table. The last two mirrors form a periscope to raise the beam height and angle the beam into the multipass. The periscope is arranged so the polarization of the 3  $\mu\text{m}$  idler beam is rotated 90 degrees and is parallel to the polarization of the FTMW cavity. The periscope assembly is mounted on a translation stage to allow for lateral translation of the IR beam across the multipass to maximize alignment with the molecular beam for maximum excitation. Initially a 2 m lens was used to weakly focus the IR beam. The lens was placed as close as possible to the input port for the IR light. Later experiments no lenses were used because there was no observed signal enhancement.

The laser frequency is measured with a wavemeter (Coherent Wavemaster) with an accuracy of 0.02  $\text{cm}^{-1}$ . The wavemeter is used to measure the frequency of the signal beam exiting the NRO cavity. The frequency of spectroscopic interest is the 3  $\mu\text{m}$  idler beam whose frequency is calculated using the 532 nm pump frequency and the NRO signal frequency.

### Multipass

The small beam waist of the Fabry-Perot cavity provides a good match for infrared excitation because there is typically a ~3% power loss per mirror bounce making efficient illumination of a large active region (>10 cm) difficult. The IR laser enters the machine through a  $\text{CaF}_2$  window and is directed into a plane parallel mirror assembly or multipass.

The multipass was designed so that the length (6 cm) was matched to the beam waist of the Fabry-Perot cavity so that a single laser pulse vibrationally excites a ‘plug’ of molecules that fills the active region of the cavity and is illustrated in Figure 2.2. The distance between the multipass mirrors is ~12.5 cm surface to surface. This distance is used to maximize the number of the IR crosses to approximately 14. The multipass assembly is centered on the cavity active region in order to be in a region of the molecular beam that has less collisional energy transfer and also to directly probe those molecules in the active region. In this design the nozzle was lowered slightly so that the exit of the pulsed nozzle was near the top of the multipass without interfering with the cavity mode.

#### **H. Pulse timing**

All of the pulse timing in the experiment is controlled by three digital delay generators (DG535 Stanford Research) 1. laser flash lamp and q-switch, 2. pulsed valve, 3. MW pulse and detection pulse. A fourth delay generator triggered on the zero crossing of the power line (60 Hz) and then divided down to 10 Hz was used as a trigger source for the other three pulse generators. Triggering on the power line knocked down the TTL pulse jitter greater than a factor of 2. All pulse generators and the MW synthesizers (HP 8340B and HP83752B) are locked to the same 10 MHz reference signal from the rubidium oscillator (Stanford Research PR S10). The oscilloscope begins digitizing the FID when the scope receives a TTL high from the digital delay generator and at the zero

crossing of the 10 MHz Rb oscillator signal. All of these techniques were implemented to achieve phase coherence in the time domain FID measurement.

### I. Problems Encountered

There has been an array of minor technical problems that have arisen over the course of developing FTMW-MW, IR-FTMW double resonance and IR-FTMW-MW triple resonance techniques. During the initial setup of the FTMW a strong 30 MHz spike was observed. The 30 MHz leak originated in the mixing step of the single side band modulator. The input power of the 30 MHz signal was too high going into the SSBM. The power of the 10 MHz signal before entering x3 frequency multiplier was reduced using 12 dB of attenuation (two 3 dB and 6 dB inline attenuators BWS3W2 and BWS6W2 Mini Circuits DC- 18 GHz). The 30 MHz spike was not observed after the attenuators were in place.

Phase coherence of the FID was not achieved until a fourth digital delay generator was added to the timing system and the oscilloscope signal acquisition was triggered with a two stage trigger on the zero crossing of the Rb oscillator and the TTL high detection pulse from the digital delay generator. The fourth digital delay generator was triggered on the zero crossing of the power line and knocked down to 10 Hz. All signals have been phase coherent since these changes were made. Under normal spectrometer conditions (10 averages) the phase of the FID compared to the 10 MHz reference has a standard deviation of 0.43 radians ( $\sim\pi/8$ ) or roughly 1/16th of a cycle.

During the initial double resonance experiments for propyne strong pickup of MW radiation was observed when monitoring the  $1_0-0_0$  transition in the cavity while pumping the  $2_0-1_0$  transition with the horn. This pickup originated from leakage around the SMA connectors leading up to the frequency doubler located inside the vacuum chamber. Because propyne is a symmetric top molecule the  $2_0-1_0$  frequency is almost exactly twice the  $1_0-0_0$  frequency, and the interference was coming from the frequency near the  $0-1$  transition that was not doubled. This pickup was eliminated by wrapping all connectors inside the chamber with MW absorbing foam (ECOSORB HR10 Emerson and Cumming MW products) and wrapping the foam in a layer of aluminum foil. There was no observed interference from the doubled light because there is a sharp cutoff frequency for the amplifier at 26 GHz, and the  $2_0-1_0$  frequency is  $\sim 35$  GHz.

Initially the spectrometer was operated with a lower throughput pumping system that consisted of a smaller diffusion pump (Varian VHS 6), water baffle (Varian 336), and mechanical pump (Douseal 1470). With this configuration strong rotational relaxation in the excited vibrational state was observed when the machine was run with a 10 Hz repetition rate. At this repetition rate  $1_0-0_0$  excited state transition was observed when the laser prepared vibrationally excited rotational levels up to  $J=5$  (through R(4)) as illustrated in Figure 2.5. There are two solutions to this problem. The first is to run at a 1 Hz repetition rate and the second is to upgrade the pumping system. For propyne and fluoropropyne a 1 Hz repetition rate was used. For later experiments the pumping system was upgraded, as described earlier, and the machine was run at the full 10 Hz repetition rate of the laser.

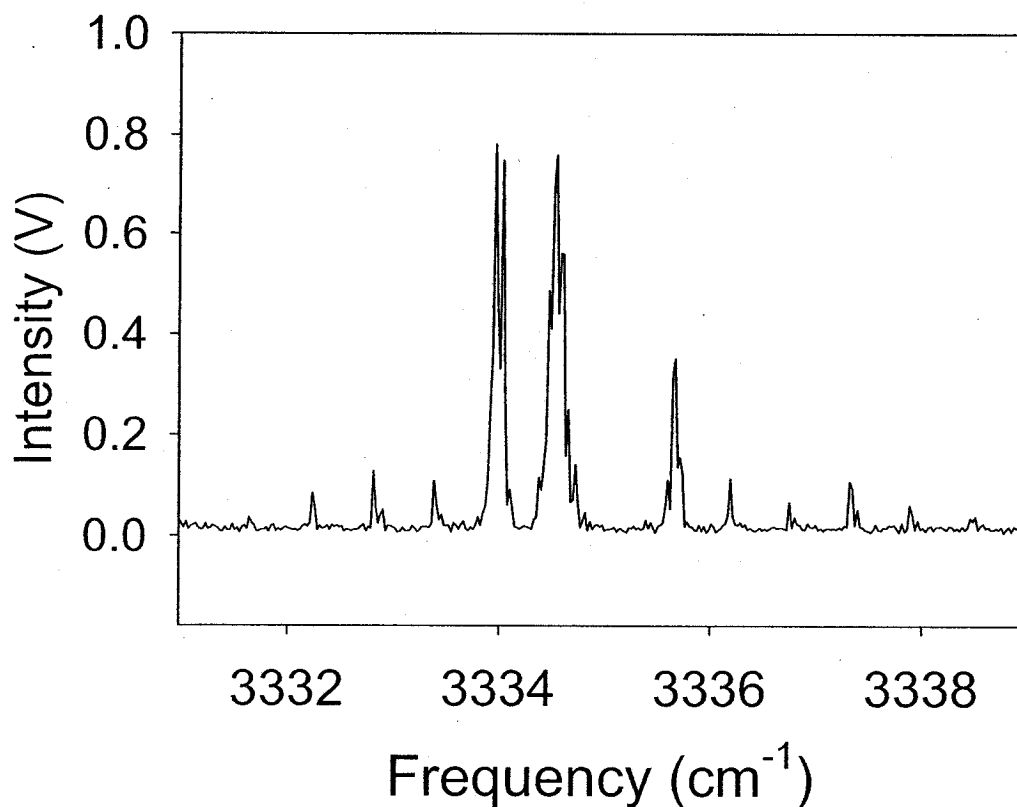


**Figure 2.5** The infrared spectrum above is obtained by monitoring the amplitude of the J=0-1 excited state transition. The only observable transitions should be those that prepare J=0 or J=1 in the vibrationally excited state, however here R(5) is observed due to rotational relaxation.

Initial experiments for propyne and fluoropropyne were performed with the multipass (9 cm) above the cavity axis. While this lead to strong upper state signals for propyne and fluoropropyne the corresponding infrared depletion signal was never greater than ~20%. The multipass was then mounted centered on the cavity axis and depletion signals of 100% were readily observed. With the multipass optics centered on the cavity axis and the nozzle lowered slightly the IR excitation occurs in an environment with fewer molecular collisions. This placement and the improved pumping system have eliminated collisional rotational energy transfer.

Signal enhancements were obtained for FTMW-MW double resonance spectroscopy by placing the horn polarization parallel to the cavity polarization. Similarly, IR polarization dependence of the signal amplitude was observed. The polarization of molecules by the IR laser is preserved when the molecules enter the FTMW cavity region. This effect is verified by monitoring the  $1_0-0_0$  upper state signal of propyne. When the laser is resonant with R(0) and the polarization of the laser is rotated to be parallel to the cavity a factor of two signal enhancement is observed. For P(1) no enhancement was observed because the laser can only populate J=0 M=0. For parallel polarizations the selection rules become  $\Delta M=0$ .<sup>16</sup>

For species with a small dipole moment a 1 watt amplifier (DBS MW DPB-0618N830) is placed after the small broadband low noise amplifier and before the attenuators as depicted in Figure 3.2 (AMP). The small amplifier is used to keep the 1 Watt amplifier in saturation. While monitoring a signal with the amplifier inline the noise increased drastically because the amplifier was amplifying ambient noise which

was entering the cavity during data collection. This noise was eliminated by placing a SPDT switch (Sierra Tech SM50071) with a 25 Watt terminator (ATM T2517) on the output of the programmable attenuators (S6 in Figure 3.2). The timing of the switch is the same for the polarizing MW pulse. This ensures no amplifier noise enters the cavity while detecting the FID.

## Reference List

1. Suenram, R. D.; Grabow, J. U.; Zupan, A.; Leonov, I., *Rev.Sci.Instrum.* **1999**, *70*, 2127-2135.
2. McGurk, J. C.; Schmalz, T. G.; Flygare, W. H., *Density Matix, Bloch Equation Description of Infrared and Microwave Transient Phenomena*; In Prigogine, I., Rice, S. A., eds., 1974
3. Balle, T. J.; Flygare, W. H., *Rev.Sci.Instrum.* **1981**, *52*, 33-44.
4. Arunan, E.; Dev.S.; Mandal, P. K., *Appl.Spectrosc.Rev.* **2004**, *39*, 131-181.
5. Legon, A. C., *Annu.Rev.Phys.Chem.* **1983**, *34*, 275-300.
6. Xu, Y., Wijngaarden, J. van, and Jäger, W., *Int.Rev.Phys.Chem.* **2005**, *24*, 301-338.
7. Leopold, K. R.; Fraser, G. T.; Novick, S. E.; Klemperer, W., *Chem.Rev.* **1994**, *94*, 1807-1827.
8. Gordy, W.; Cook, R. L. *Microwave Molecular Spectra*; John Wiley & Sons: New York, 1984
9. Herschbach, D. R., *J.Chem.Phys.* **1957**, *27*, 1420-1421.
10. Hershbach, D. R.; Swalen, J. D., *J.Chem.Phys.* **1958**, *29*, 761-776.
11. Landsberg, B. M.; Suenram, R. D., *J.Mol.Spectrosc.* **1983**, *98*, 210-220.
12. Slichter, C. P. *Principles of Magnetic Resonance*; Springer: New York, 1996.
13. Campbell, E. J.; Buxton, L. W.; Balle, T. J.; Keenan, M. R.; Flygare, W. H., *J.Chem.Phys.* **1981**, *74*, 829-840.
14. Grabow, J. U.; Stahl, W.; Dreizler, H., *Rev.Sci.Instrum.* **1996**, *67*, 4072-4084.
15. de Souza, A. M.; Kaur, D.; Perry, D. S., *J.Chem.Phys.* **1988**, *88*, 4569-4578.
16. Townes, C. H.; Schawlow, A. L. *Microwave Spectroscopy*; Dover Publications: New York, 1975.

## Chapter 3

### Narrow Band Cavity FTMW Spectroscopy: Applications to Pure Rotational Spectroscopy

An interest in studying prototypical hydrogen bonding systems such as complexes of carboxylic acids (in both ground and excited state) has lead to investigations into formic acid trimer (FAT) and propiolic acid – formic acid dimer (PFAD). The focus of this chapter is two fold, first to demonstrate the high sensitivity of the cavity FTMW spectrometer for detecting low abundance and low dipole moment species and second to lay the groundwork for future experiments where the aim will be to obtain dynamical information from the vibrationally excited state. Experiments on these systems complement the goals of current theoretical literature which are to model the structure of multiple hydrogen-bonded systems and to accurately predict the double proton transfer rate.

Formic acid monomer has two rotamers, *cis* and *trans*, both of which are well characterized by gas phase methods and are depicted in Figure 3.1.<sup>1,2</sup> Evidence for the cyclic eight member ring structure of formic acid dimer was first obtained by Pauling and Brockway<sup>3</sup>, and later revisited and verified for formic acid and other carboxylic acids with electron diffraction studies.<sup>4</sup> There also exists experimental evidence of *cis-trans* formic acid dimer from matrix isolation studies.<sup>5</sup> In contrast to gas phase studies the condensed phase investigations on the crystal structure of formic acid report that formic acid forms catemeric chains with the *trans* rotamer.<sup>6,7</sup> High pressure crystal structure studies indicate the presence of chains that consist of both *cis* and *trans* rotamers<sup>8</sup> and at

high temperature the crystal structure favors chains configured with the *cis* geometry.<sup>9</sup> There have also been a vast amount of solution phase studies with varying results. The most recent work using theoretical methods applied to experimental results emphasizes a hierarchical hydrogen bonding framework where at the lowest level clusters of 20-30 molecules are formed by O-H $\cdots$ O hydrogen bonds, the next tier is dominated by C-H $\cdots$ O hydrogen bonds which lead to short chain structures, and there is also some fraction of cyclic dimers.<sup>10</sup>

Several *ab initio* studies have focused on determining the cluster size at which an extended chain-like structure will become energetically favored over the formation of a series of rings or ring-like structures.<sup>11-14</sup> Theoretical studies looking at formic acid clusters of up to hexamer level have been performed.<sup>12</sup> Recent calculations using a polarization-consistent, pc,<sup>15</sup> basis set with density functional theory have been performed on formic acid trimer, tetramer, and pentamer.<sup>13;14;16</sup> The advantage of the pc basis set is to provide a systematic convergence to the basis set limit.<sup>15</sup> The three lowest energy conformers of formic acid trimer obtained by Roy et al. are illustrated in Figure 3.1.

Cyclic dimers of carboxylic acids are widely used as prototype systems to study double proton transfer because the hydrogen bonding is similar to that found between DNA base pairs and other biological systems such as enzymes.<sup>17-19</sup> These systems are also important because they can be readily studied with theoretical and experimental methods. There has been a great deal of theoretical work over the past several years that has focused on predicting the ground state tunneling splitting,  $\Delta_0$ , for formic acid

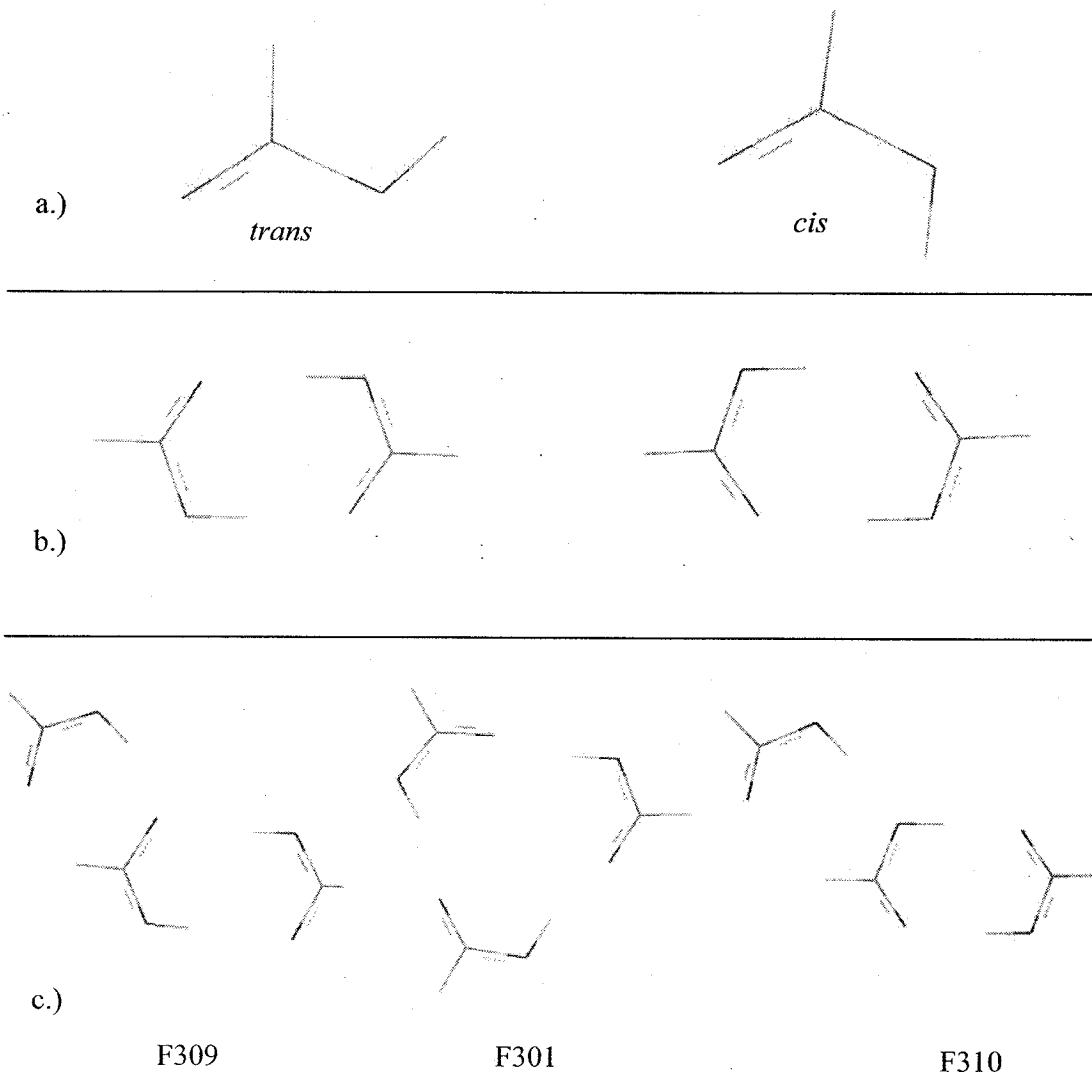


**Figure 3.1.** The above models illustrate a.) the two rotamers of formic acid, b.) the two tunneling configurations of formic acid dimer, and c.) the lowest energy conformers of formic acid trimer. The notation is from ref. 13.

dimer.<sup>20-30</sup>

Recently Madeja et al. experimentally determined the tunneling splitting for deuterated formic acid dimer ( $\text{DCOOH}_2$ ).<sup>31</sup> The two tunneling configurations of formic acid dimer (FAD) are illustrated in Figure 3.1. The high resolution infrared spectrum was obtained for the C-O stretch fundamental and tunneling rates for the ground state (86 MHz) and the vibrationally excited state (299 MHz) were determined. However, because of uncertainty in the intensity measurements the assignment may be reversed, i.e. the tunneling splitting may be smaller in the vibrationally excited state. The tunneling splittings that result from the two possible assignments are listed in Table 3.1.

The experimental determination of the tunneling splittings of deuterated FAD has greatly impacted the theoretical community as well as the general understanding of tunneling in acid dimers, as indicated in Table 3.1 which lists theoretically and experimentally determined values for  $\Delta_0$  (in chronological order). Most noticeably, there is a spread of the theoretically determined values prior to the measurement which span three orders of magnitude.(Refs 21-30) The major difference in the theoretical prediction by Shida et al. (Ref. 23 in Table 3.1) as compared to the others is in its accounting of the initial heavy atom motion that occurs as the monomers move towards each other followed by tunneling. This heavy atom motion causes the tunneling splitting to be much smaller than other systems that exhibit tunneling such as tropolone<sup>32</sup> or malonaldehyde (29,193 MHz and 647,046 MHz respectively).<sup>33</sup>

Among theorists there remains a dispute about the proper assignment of the high resolution deuterated FAD spectrum. The majority of the studies agree with the initial

Table 3.1. Theoretical and Experimentally Determined tunneling splitting values

		$\Delta_0 / \text{MHz}$	
	Ref.	$v=0$	$v=1^a$
$(\text{HCOOH})_2$	21	9000	
	22	27000	
	23	120	
	24	2700	
	25	3000	
	26	9000	
$(\text{DCOOH})_2$	27	63	
	28	441	129
	29	114	
	30	39	
	31 <sup>b</sup>	86	299
	c.	375	93

a. CO stretch ( $1244 \text{ cm}^{-1}$ )

b. experimental values

c. Alternate assignments from 31

assignment by Madeja et al. in which the tunneling rate increases with vibrational excitation. For example, the calculations by Mil'nikov et al. indicate an increase of the tunneling rate upon vibrational excitation, though these calculations were limited to energy regions below  $300\text{ cm}^{-1}$ .<sup>29</sup> Additional agreement of the initial experimental assignment comes from Luckhaus and Tautermann, who have calculated the tunneling splitting in the ground state only.<sup>30,34</sup> However, Smedarchina et al recommends reversal of the assignment based on their *ab initio* calculations and is the only theoretical work to perform calculations at the C-O stretch energy region ( $\sim 1250\text{ cm}^{-1}$ ).<sup>28</sup> The disagreements typically revolve around the number of approximations and the methods used. As such, the assignment remains ambiguous.

Microwave spectroscopy has a rich history of measuring weakly bound complexes,<sup>35-38</sup> and several heterodimers of carboxylic acids have been previously studied using microwave spectroscopy.<sup>39,40</sup> The aim of this chapter is to use microwave spectroscopy to determine the structure of the lowest energy conformer (with non-zero dipole moment) of formic acid trimer and also to unambiguously determine the tunneling rate for the ground state of the propionic - formic acid dimer. Rotational spectroscopy has previously demonstrated an advantage for measuring the tunneling splittings because the tunneling splitting can be fit to microwave precision.<sup>32,33</sup>

## Experimental

The experimental setup consists of a Balle-Flygare type Fourier transform microwave spectrometer<sup>41</sup> based on the recent NIST<sup>42</sup> design described in detail in the

previous chapter. The rotational spectra of formic and propiolic-formic acid dimer were measured using the NIST designed pulse timing, data acquisition electronics, and software. The spectrum was measured using the standard coaxial nozzle arrangement measured from 10 - 22 GHz with a 250 kHz step size (10 averages/step). The rotational spectra of propiolic acid<sup>43</sup> and formic acid<sup>1</sup> have been measured previously and serve as a starting point for this work.

The carrier gas (80/20 Ne/He) was flown over a steel sample cell placed outside the vacuum chamber which contained either pure formic acid or a 4:1 mixture of propiolic acid to formic acid. For both experiments the nozzle (General Valve series 9, 1 mm orifice) was heated to 50 °C. For pure formic acid this enhanced the intensity of the formic acid trimer rotational transitions and for the propiolic – formic experiments heating served to break up formic acid trimer which was observed by a reduction in the intensity of characteristic formic acid trimer rotational transitions. This both simplified the spectrum and increased the signal of the bound propiolic-formic acid complex. Propiolic acid (96%) and formic acid (99%) were purchased from Aldrich and used with no further purification.

FTMW-pulsed-MW double resonance spectroscopy was used to aid in the assignment of the pure rotational transitions, and to locate the much weaker tunneling-rotation transitions. A full discussion of double resonance techniques will be presented in Chapter 6 for applications in the vibrationally excited state. The timing was set up such that the second microwave pulse (~5 μs duration) followed directly (500 ns delay) after the cavity microwave pulse (4 μs duration). Figure 3.2 illustrates the sensitivity of the

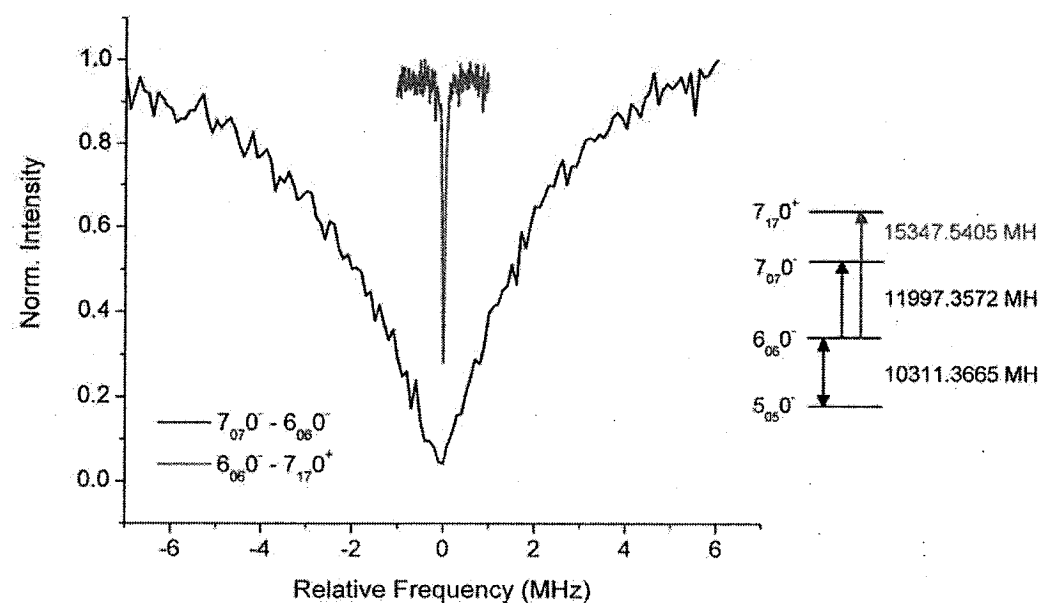


**Figure 3.2.** A FTMW-pulsed-MW double resonance spectrum is shown for the pure rotational transition  $7_{0^-} - 6_{0^-}$  (11997.3572 MHz, black) and the tunneling-rotation transition  $7_{17}^+ - 6_{0^-}$  (15347.5405 MHz, grey). The double resonance scans were obtained by monitoring the amplitude of the  $6_{0^-} - 5_{0^-}$  (10311.3665 MHz) rotational transition with the FTMW cavity while scanning the horn frequency across the desired rotational transition with 10 averages at each step and a step size of 100 and 10 kHz for pure and tunneling rotation transition, respectively. A 5  $\mu$ s MW pulse was used to destroy the coherence of the monitored transition using a source power of 7.3 Watts for both scans.

double resonance technique for the acid dimer complex in which nearly 100% signal modulation of the probe transition ( $5_{05}0^-$ - $6_{06}0^-$ ) is achieved when the second MW source is resonant with both the pure rotational transition ( $6_{06}0^-$ - $7_{07}0^-$ ) and the tunneling-rotation transition ( $6_{06}0^-$ - $7_{17}0^+$ ). This double resonance technique is analogous to the work by the Endo group where the second light source is used to destroy the coherence of the monitored rotational transition.<sup>44</sup>

Although double resonance was used to locate and check assignments, all transitions were re-measured in the standard coaxial cavity arrangement due to the difficulty of assigning the center frequency of these transitions. This dramatically reduced the RMS fit error (~factor of 5). A 1 Watt power amplifier (DBS) was used to amplify the cavity microwave pulse for optimal excitation of the low dipole moment tunneling-rotation transitions.

## Results

### A. Formic Acid Trimer

The observed rotational spectrum of formic acid trimer is shown in Figure 3.3. The spectrum is dominated by a-type and b-type transitions. The residual spectrum (grey) was generated by subtracting the assigned formic acid trimer transitions from the observed spectrum. The residual spectrum is dominated by formic acid monomer and only a few weak lines, which are most likely impurities from the sample-input line. This has led to the assignment of only a single species from the observed spectrum. The spectrum was analyzed using jb95 spectral fitting program and final fits were performed

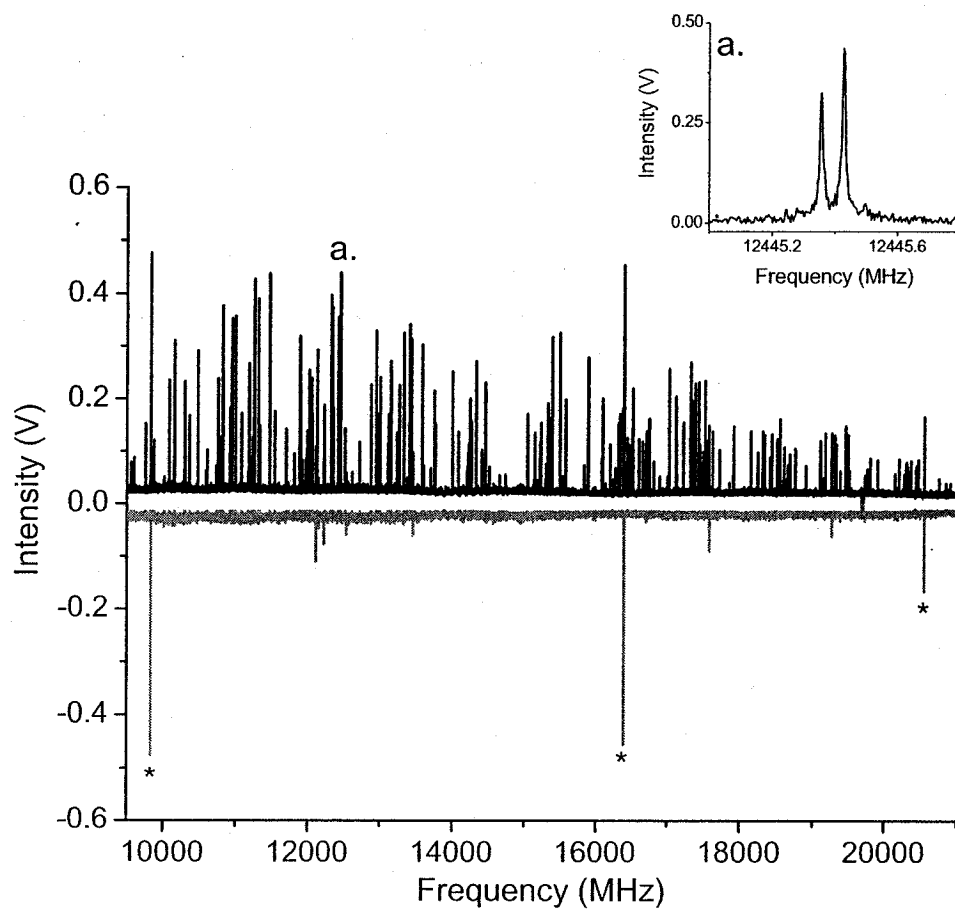


**Figure 3.3.** The pure rotational spectrum for formic acid trimer (black) and the residuals from the fit (grey) are shown. The remaining strong lines are due to formic acid monomer (\*). The inset (a.) illustrates the typical signal-to-noise ( $\sim 30:1$  with 10 averages per step) for an a-type transition ( $12_{012} - 11_{011}$  12445.3914 MHz).

Table 3.2. Formic Acid Trimer Rotational Constants

<b>Rotational Parameters</b>	
A / MHz	2936.512479(70)
B / MHz	595.071263(15)
C / MHz	495.260285(11)
$\Delta J$ / kHz	0.077755(26)
$\Delta JK$ / kHz	-0.28388(23)
$\Delta K$ / kHz	4.5351(36)
$\delta J$ / kHz	0.016812(12)
$\delta K$ / kHz	0.2900(12)
$\Delta I$ / amu Å <sup>2</sup>	-0.94542(3)
N lines	237
RMS /kHz	1.254

Table 3.3. Partial Transition List for Formic Acid Trimer

J'	K <sub>a</sub> '	K <sub>c</sub> '	J''	K <sub>a</sub> ''	K <sub>c</sub> ''	obs. (MHz)	obs - calc. (MHz)
8	1	8	7	0	7	9560.5683	0.0008
10	0	10	9	1	9	9598.5234	0.0003
9	2	8	8	2	7	9756.8846	-0.0007
9	4	6	8	4	5	9842.4978	-0.0006
9	4	5	8	4	4	9843.2790	0.0004
9	3	7	8	3	6	9851.6775	-0.0001
9	3	6	8	3	5	9879.2458	-0.0001
9	2	7	8	2	6	10083.5113	0.0002
9	1	8	8	1	7	10157.3354	-0.0002
3	2	2	2	1	1	10295.2572	0.001
10	1	10	9	1	9	10301.3685	0.001
9	1	9	8	0	8	10364.8177	-0.0004
10	0	10	9	0	9	10477.9895	-0.0002
11	2	10	11	1	11	10590.6632	-0.0008
3	2	1	2	1	2	10610.2804	0
11	0	11	10	1	10	10760.8076	-0.0002
11	3	8	11	2	9	10792.6474	0.0005
10	2	9	9	2	8	10824.7861	-0.0002
10	4	7	9	4	6	10942.2997	0.0008
10	4	6	9	4	5	10943.9813	-0.0012
10	3	8	9	3	7	10951.0536	-0.0004
10	3	7	9	3	6	10997.6981	-0.0013
10	3	7	10	2	8	11081.9910	0.0009
10	1	10	9	0	9	11180.8346	0.0003
12	2	11	12	1	12	11216.4752	-0.0009
4	2	3	3	1	2	11235.4244	-0.0002
10	2	8	9	2	7	11248.1158	-0.0012
10	1	9	9	1	8	11252.6549	-0.0018
11	1	11	10	1	10	11312.2759	-0.001
9	3	6	9	2	7	11332.4087	0.0011
11	0	11	10	0	10	11463.6508	-0.0015

using SPFIT.<sup>45</sup> The spectrum was fit with the Watson's A reduction Hamiltonian in the I<sup>r</sup> representation and the results of the fit are shown in Table 3.2 with an RMS error of 1.254 kHz using 237 transitions (122 a-type and 115 b-type). The fit includes transitions that range from J = 3 up to J = 20, and up to K<sub>a</sub> = 7. A partial line list is shown in Table 3.3 with the difference between observed and calculated transitions. The full line list is contained in Table 3.10 of Appendix 3A.

Theoretical calculations for formic acid trimer have recently been performed by Roy et al. which have determined the 13 lowest energy conformers using the B3LYP/pc2 level of theory. The geometry optimizations and relative energy calculations have been previously described in detail.<sup>13</sup> The rotational constants and relative energies for each of the 13 lowest energy conformers of formic acid trimer are shown in Table 3.4.<sup>46</sup> Species F309 (notation from Roy et al.) is the structure that best matches the experimental constants. The percent errors of the rotational constants (-0.41, 0.78, and 0.67 for A, B, and C respectively) are extremely small indicating excellent agreement between the calculated structure and the assigned species.

*Ab initio* calculations have shown that there are a vast number of possible formic acid trimer configurations, and yet only a single conformer is observed experimentally. The next lowest energy species F301 is not observable because its dipole moment is zero. *Ab initio* results estimate that species F310 is 2.02 kcal/mol higher in energy than the observed F309. Assuming population distributions from room temperature are maintained in the free jet expansion and a high barrier to isomerization (>1000 cm<sup>-1</sup>)<sup>47</sup>

Table 3.4. Formic acid trimer *ab initio* rotational constants and relative energies

Geometry*	Rotational Constants			Relative Energy / kcal/mol
	A / MHz	B / MHz	C / MHz	
F309	2948.5833	590.4815	491.9616	0
F301	1144.4327	1127.5207	567.9610	0.98
F310	3317.9324	546.1689	468.9710	2.02
F329	1979.4707	723.8978	530.0557	2.63
F332	1395.4206	949.2772	564.9518	3.75
F324	1314.7555	981.9939	562.1370	3.82
F303	1892.3080	954.9379	671.2757	4.27
F315	1531.4770	998.4168	606.8732	4.64
F336	2862.9668	493.9111	421.2400	5.19
F349	3524.8045	428.5095	382.0623	6.33
F302	5008.3097	395.7175	366.7405	7.47
F341	3378.8011	467.6868	410.8217	8.27
F311	2513.3621	504.9331	420.4624	8.57
Exp	2936.5124	595.0712	495.2602	

\*Geometry notation is from Ref. 13.

species F310 would be down a factor of ~30 which is close to the signal-to-noise limit of the spectrum. Therefore it is not unreasonable that only species F309 is observed. Furthermore, these results indicate the accuracy of the B3LYP/pc2 level of theory for predicting the structure of multiple hydrogen-bonded species such as formic acid trimer.

### B. Propiolic - Formic Acid Dimer

#### Rotational spectrum

A symmetric double well potential is used as a simplified potential energy surface to describe the concerted double proton tunneling motion in the propiolic – formic acid dimer. This well known problem splits the ground vibrational state into two energy levels; a lower symmetric ( $0^+$ ) and upper anti-symmetric ( $0^-$ ) level with an energy difference  $\Delta_0$ . As a result there are three distinct rotational spectra observed; two arising from pure rotational transitions ( $0^+ \rightarrow 0^+$  and  $0^- \rightarrow 0^-$ ) and one arising from the tunneling-rotational transitions ( $0^+ \rightarrow 0^-$ ). The three types of transitions are shown in Figure 3.4. The pure rotational transitions follow a-type selection rules because these transitions are symmetric and only connect symmetric or anti-symmetric rotational wave functions ( $K_a$  does not change). These transitions are observed as doublets where the  $0^+ \rightarrow 0^+$  transitions are separated from the  $0^- \rightarrow 0^-$  transitions by a few MHz. The tunneling-rotation transitions follow b-type selection rules, because these rotational wave functions are anti-symmetric and connect symmetric to anti-symmetric rotational wave functions ( $K_a$  changes).

The intensities of the a-type transitions must follow the spin statistics that result from having an equivalent pair of hydrogen nuclei with respect to a 180 degree rotation

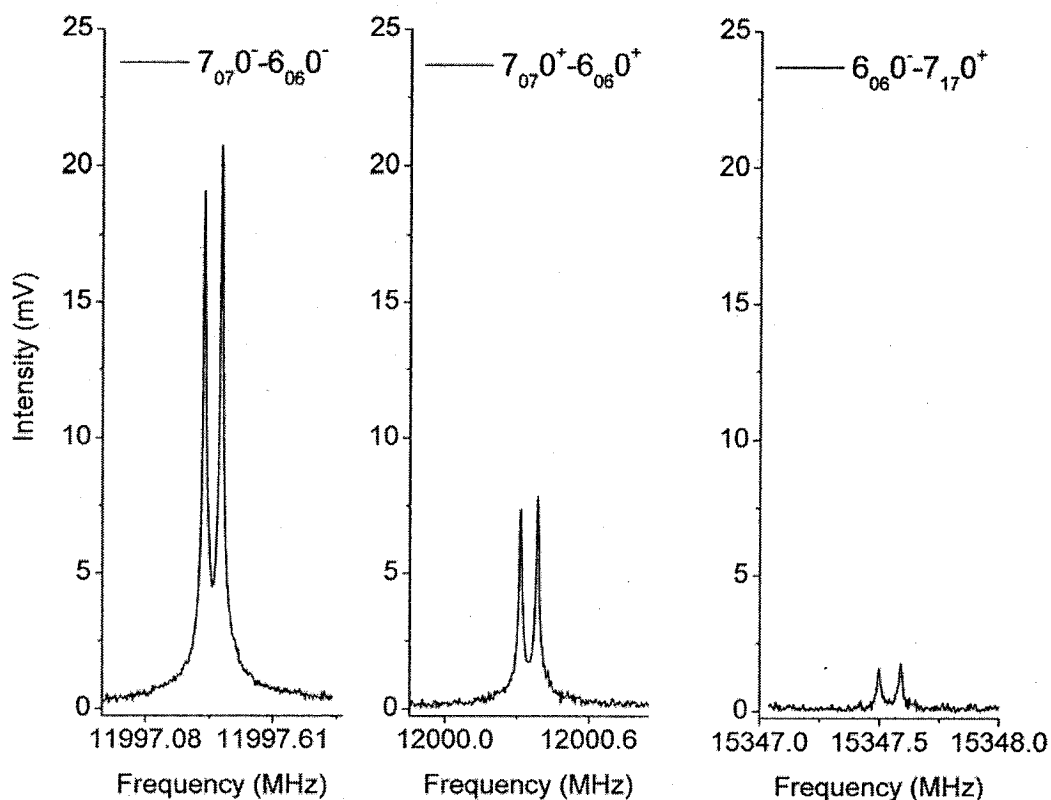


**Figure 3.4.** The  $0^-$  and  $0^+$  tunneling doublets for the  $7_{07}-6_{06}$  pure rotational transitions and the  $6_{06}0^- - 7_{17}0^+$  tunneling-rotation transition observed by FTMW spectroscopy are shown. The spectra were recorded with 400 signal averages at a 10 Hz repetition rate.

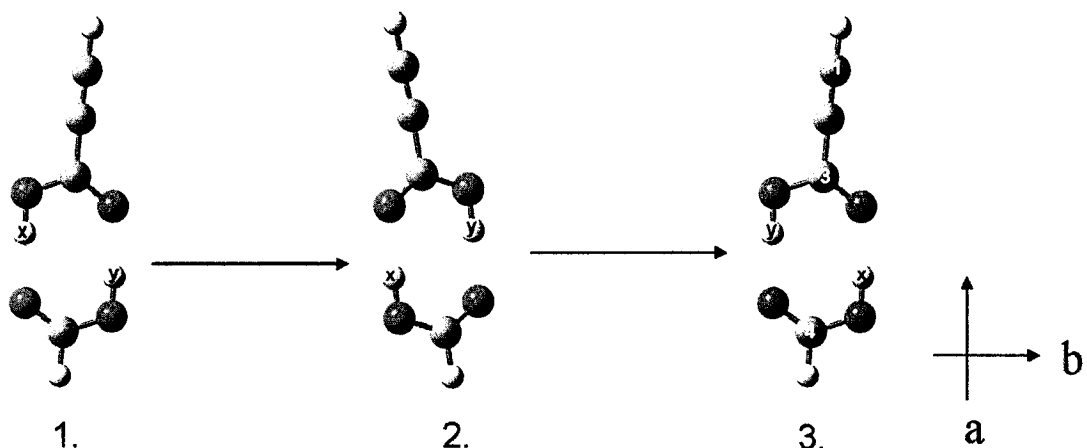


**Figure 3.5.** The conformations of the formic acid – propionic acid dimer species are illustrated relative to the principle axis orientation. The symmetric double proton transfer is shown (1.  $\rightarrow$  2.). 180 degree rotation about the a-principle axis (2. $\rightarrow$ 3. ) results in an exchange of hydrogen atoms with a structure that is isoenergetic with the initial structure (1.). The angle formed by the labeled carbons was used in the calculation of the axis switching constant,  $F_c$  (eq. 3).

about the symmetry axis. As depicted in Figure 3.5 for the propionic – formic acid dimer, tunneling followed by a 180 degree rotation results in exchange of the H nuclei. The hydrogen atoms obey Fermi-Dirac statistics which require the total wave function to be anti-symmetric. The total wave function is comprised of the electronic, vibrational, rotational, and spin wave functions and  $P$  is the permutation operator which exchanges the hydrogen atoms (x and y).

$$P_{xy} \Psi = \psi_e \psi_v \psi_r \psi_s = -\Psi \quad (3.1)$$

For hydrogen there are three symmetric spin functions (+) and one anti-symmetric spin function (-). This results in a 3:1 intensity ratio between  $0^+$  and  $0^-$  doublets when  $K_a$  is odd and 1:3 when  $K_a$  is even. Near the prolate rotor limit,  $K_a$  (even or odd) determines whether the rotational wave function is symmetric or anti-symmetric with respect to 180 degree rotation about the symmetry axis.<sup>48</sup> The 3:1 intensity ratio is observed in Figures 3.4 and 3.6. Figure 3.6 demonstrates the alternating 3:1 intensity pattern for even and odd values of  $K_a$  and shows good agreement between the observed and predicted intensities.<sup>49</sup>

From the rotational spectrum (10 - 23 GHz) 97 a-type pure rotational transitions from the  $0^+$  and  $0^-$  states and 23 b-type tunneling-rotation transitions were fit. The pure rotational transitions for the  $0^+$  and  $0^-$  states are listed in Table 3.6, and the tunneling-rotation transitions are listed in Table 3.7. The Hamiltonian used in the fit contains four terms,

$$H = H_{rot} + H_{cd} + H_{tun} + H_{int} \quad (3.2)$$

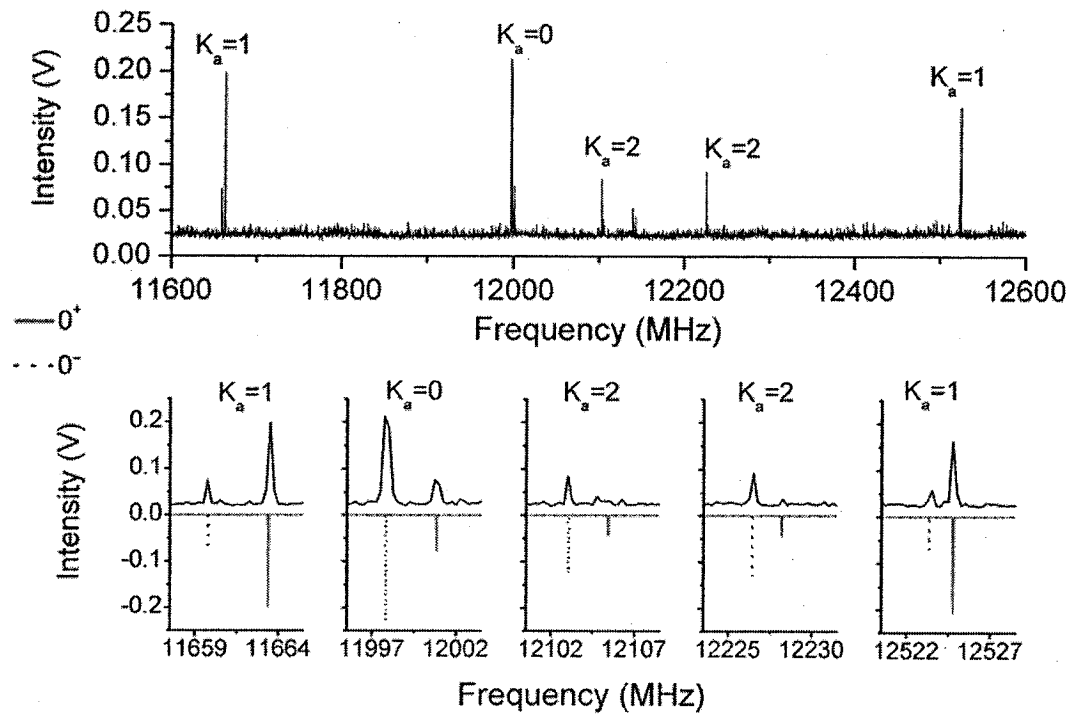


**Figure 3.6.** A 1 GHz section of the rotational spectrum of the propionic acid - formic acid dimer in the region of  $J = 7 \leftarrow 6$  is shown (top). The pure-rotational transitions (black) from the  $0^+$  and  $0^-$  states for different values of  $K_a$ , and a simulation (gray) of the spectrum using fit constants and predicted dipole moment are illustrated in the lower panels. The simulation accurately predicts the 1:3 intensity ratio observed for the  $0^+$  to  $0^-$  states (dotted) which alternate with even and odd values of  $K_a$ . The simulation was performed using SPCAT with a 1 K rotational temperature.

Table 3.6. Observed Pure Rotational Transitions of Propiolic-Formic Acid Dimer

J' Ka' Kc'	J"Ka"Kc"	0+ (MHz)	O-C (MHz)	0- (MHz)	O-C (MHz)
6 1 6	5 1 5	10003.3941	-0.0013	10000.3039	-0.0026
6 0 6	5 0 5	10313.7962	-0.0027	10311.3665	-0.0021
6 3 4	5 3 3	10402.4582	-0.0004	10400.4978	0.0012
6 3 3	5 3 2	10403.8586	-0.0009	10401.9091	0.0002
6 2 5	5 2 4	10380.9482	-0.0001	10378.8742	-0.0001
6 2 4	5 2 3	10458.0226	-0.0016	10456.3546	-0.0009
6 1 5	5 1 4	10743.0233	-0.0002	10741.8759	-0.0009
7 1 7	6 1 6	11662.9239	-0.0048	11659.295	-0.0011
7 0 7	6 0 6	12000.3513	0.0001	11997.3572	-0.0021
7 2 6	6 2 5	12105.4604	0.0018	12103.0212	0.0032
7 3 5	6 3 4	12139.6461	0.0002	12137.3823	0.0003
7 3 4	6 3 3	12142.7926	-0.001	12140.5558	0.0004
7 2 5	6 2 4	12227.7164	-0.0034	12225.9117	-0.0026
7 1 6	6 1 5	12524.2839	0	12522.9017	0.0014
8 1 8	7 1 7	13319.2408	-0.003	13315.0558	0.0008
8 0 8	7 0 7	13673.2542	-0.0012	13669.6409	-0.0012
8 2 7	7 2 6	13827.3761	0.0049	13824.5568	0.0022
8 3 6	7 3 5	13878.0919	-0.0009	13875.5378	0.0019
8 3 5	7 3 4	13884.3751	-0.0006	13881.873	0.0034
8 2 6	7 2 5	14008.4082	0.0013	14006.516	0.0006
8 1 7	7 1 6	14300.9177	-0.0001	14299.2751	0.0015
9 1 9	8 1 8	14972.1085	-0.0011	14967.3498	0.0006
9 0 9	8 0 8	15331.911	-0.0035	15327.6199	-0.0025
9 2 8	8 2 7	15546.3308	0.005	15543.1256	0.0028
9 4 6	8 4 5	15607.4235	0	15604.5357	-0.0035
9 4 5	8 4 4	15607.6094	0.0011	15604.7252	-0.001
9 3 7	8 3 6	15617.7545	-0.0013	15614.9174	0.0034
9 3 6	8 3 5	15629.2388	-0.0017	15626.4924	0.0012
9 2 7	8 2 6	15800.2836	-0.0024	15798.3497	-0.0029
9 1 8	8 1 7	16072.0041	-0.003	16070.0724	-0.0009
10 1 10	9 1 9	16621.3727	-0.0023	16616.026	0.0019
10 0 10	9 0 9	16976.487	0.0006	16971.4642	-0.0003
10 2 9	9 2 8	17261.9775	0.0073	17258.3772	0.0077
10 4 7	9 4 6	17346.1313	0.0008	17343.3701	-0.0023
10 4 6	9 4 5	17346.5309	0.0003	17342.9676	-0.0003
10 3 8	9 3 7	17358.5127	-0.0014	17355.3983	0.0037
10 3 7	9 3 6	17378.1195	-0.0013		
10 2 8	9 2 7	17602.7856	-0.0045	17600.8422	-0.0046
10 1 9	9 1 8	17836.5338	-0.0011	17834.276	-0.0013
11 1 11	10 1 10	18266.9709	-0.0013	18261.0081	0.0034
11 0 11	10 0 10	18607.9215	0.0007	18602.1249	-0.0009
11 2 10	10 2 9	18973.9732	0.0097	18969.9635	0.0103
11 3 9	10 3 8	19100.1717	0.0025	19096.7799	0.0026
11 3 8	10 3 7	19131.848	-0.0025	19128.7077	-0.0019
11 2 9	10 2 8	19414.5374	-0.0057	19412.5959	-0.0085
11 1 10	10 1 9	19593.3819	-0.0007	19590.7631	0.0022

Table 3.7. Observed Tunneling-Rotation Transitions of Propiolic-Formic Acid Dimer

J' K'a' Kc'	0 <sup>+</sup>	J"K'a"Kc"	0 <sup>-</sup>	Obs (MHz)	O-C (MHz)
2 0 2		3 1 3		10256.6695	0.0026
3 0 3		4 1 4		11744.0097	0.0017
9 0 9		8 1 8		11782.1772	-0.002
5 1 5		4 0 4		12605.4845	0.0039
4 0 4		5 1 5		13177.3073	0.0024
9 1 9		10 0 10		14327.1932	-0.0006
7 1 7		6 0 6		15347.5405	-0.0006
5 0 5		6 1 6		14562.7888	-0.0009
3 2 2		3 1 3		15510.0370	0.0117
6 0 6		7 1 7		15908.2888	0.0017
8 1 8		7 0 7		16669.4286	0.0029
6 1 6		5 0 5		13995.9800	-0.001
4 1 4		3 0 3		11168.1578	0.0055
6 2 4		6 1 5		14014.3900	-0.0036
5 2 3		5 1 4		14298.2450	-0.0013
6 1 5		6 2 4		14587.7950	-0.0036
5 1 4		5 2 3		14874.4650	-0.0016
7 1 6		7 2 5		14289.4250	-0.004
4 2 2		4 1 3		14556.7940	-0.0036
3 2 1		3 1 2		14778.1180	-0.0065
3 1 3		2 0 2		9677.7106	-0.0004
7 1 7		8 0 8		10319.4617	0.0013
2 1 1		2 2 0		15534.6948	0.0057

Table 3.8. Fit Constants for Propiolic-Formic Acid Dimer

	Pure Rotational	Rotation-Tunneling
0 <sup>+</sup> state		
A / MHz	6005.60(11)	6005.2896(28)
B / MHz	930.28(12)	930.5524(28)
C / MHz	804.0022(37)	803.99496(23)
ΔJ / kHz	-0.07426(55)	-0.07546(38)
ΔJK / kHz	-0.700(14)	-0.7010(61)
ΔJ / kHz	0.01070(60)	0.01042(40)
ΔI / amu Å <sup>2</sup>	1.173(70)	1.3335(16)
N lines	49	
0 <sup>-</sup> state		
A / MHz	6005.61(13)	6005.2753(28)
B / MHz	930.28(12)	930.5461(28)
C / MHz	803.9832(37)	803.99060(17)
ΔJ / kHz	-0.07656(55)	-0.07529(38)
ΔJK / kHz	-0.680(14)	-0.6966(63)
ΔJ / kHz	0.00825(59)	0.00874(38)
ΔI / amu Å <sup>2</sup>	1.188(70)	1.3330(16)
N lines	48	
ΔE /MHz	306.1(72)	291.4318(25)
F <sub>c</sub> /MHz	115.0(26)	120.688(59)
RMS /kHz	2.867	3.298
total lines	97	120

The first two terms represent the rotational and centrifugal distortion energies. The third term represents the energy difference between the  $0^+$  and  $0^-$  states (tunneling splitting)  $\Delta_0$ . The last term describes the tunneling-rotation interaction (axis switching),  $F_c$ , which connects the  $0^+$  and  $0^-$  states. The results to the fit are shown in Table 3.8 with a fit RMS error of 3.298 kHz. The proton tunneling splitting was determined to be 291.4318(25) MHz with a rotation-interaction constant 120.688(59) MHz. The fit was performed using SPCAT/SPFIT software.<sup>45</sup> The two columns in Table 3.8 represent the fits performed without (left) and with (right) the tunneling-rotation transitions.

*Ab initio* calculations at different levels of theory and basis set have been performed, and the pertinent constants and their percent deviations from the fit values are shown in Table 3.9. The deviation for the rotational constants A, B, and C of only a few percent are typical. *Ab initio* values of the axis switching constant,  $F_c$ , were calculated using the angle,  $\theta$ , formed by carbons 1, 3, and 4 (Figure 3.5), and the following relationship.<sup>50</sup>

$$F_c = (A - B) \cdot \sin(\theta) \quad (3.3)$$

The calculated values of the axis switching constant are in good agreement (deviations on the order of 10%) with the experimentally determined value.

### Dipole Moment Estimation

The difference in the widths observed for the FTMW-pulsed-MW double resonance spectra in Figure 3.2 indicate that the a-type pure rotational transition has a much larger dipole than the b-type tunneling-rotation transition because it is significantly more power broadened. An estimate of the dipole moment can be obtained from the intensity of a

Table 3.9. Propiolic-Formic Acid Dimer Theoretical Constants and Percent Errors

		A / MHz	% err	B / MHz	% err	C / MHz	% err	
HF	6-311++G**	6210.597	3.4	885.011	-4.9	774.6264	-4.9	
B3LYP	6-311+g	5803.313	-3.4	925.534	-0.5	798.2293	-0.5	
B3LYP	6-311++G**	5992.400	-0.2	920.193	-1.1	797.6981	-1.1	
MP2	6-311++G**	5964.061	-0.7	910.747	-2.1	790.0947	-2.1	
		$\mu_a / D$	$\mu_b / D$	$\mu_c / D$	$\mu_a/\mu_b$	$\theta$ (degrees)	Fc (MHz)	%err
HF	-0.61	0.10	0.00	-6.10	2.65	245.78	103.6	
B3LYP	-1.15	-0.13	0.00	8.85	1.35	114.89	-4.8	
B3LYP	0.80	0.10	0.00	8.00	1.48	131.23	8.7	
MP2	-0.80	-0.08	0.00	10.00	1.14	100.78	-16.5	

rotational transition.<sup>51</sup> The FTMW signal is proportional to the electric field of the microwave polarizing pulse at low electric fields. In the limit of a short microwave pulse, the signal for a rotational transition in a cavity microwave spectrometer has been shown to follow:<sup>41</sup>

$$\text{signal } \propto \frac{(1 - J_0(\kappa E \tau))}{\kappa E \tau} \quad (3.4)$$

where  $\tau$  is the duration of the microwave pulse,  $E$  is the electric field,  $J_0$  is a zero order Bessel function, and  $\kappa$  is proportional to the transition moment:

$$\kappa = \frac{|\langle a | \mu | b \rangle|}{2\hbar} \quad (3.5)$$

These relationships can be used to model the intensity of a microwave transition as a function of the square root of the microwave polarizing power to obtain the dipole moment,  $\mu$ . Figure 3.7 illustrates the signal dependence as a function of the electric field for the a-type pure rotational transition  $7_{16}0^+ - 6_{15}0^+$  and the b-type tunneling-rotation transition  $4_{04}0^- - 5_{15}0^+$ . These measurements were fit using equation (3.4) with a microwave pulse of 1  $\mu$ s and varying only  $\mu$ . The transition dipole matrix elements have been calculated for the a-type  $7_{16}0^+ - 6_{15}0^+$  and b-type  $4_{04}0^- - 5_{15}0^+$  (a-type 1.3 times larger than b-type). Due to tunneling, the tunneling-rotation transition signal is proportional to  $2^* \mu_b$ . These factors were used to calculate the ratio of  $\mu_a$  to  $\mu_b$  to be 11.2 in reasonable agreement with the values in Table 3.9.

The double proton transfer time for the ground state of PAFAD has been determined to be 1.715667(15) ns using the following relationship.<sup>52</sup>

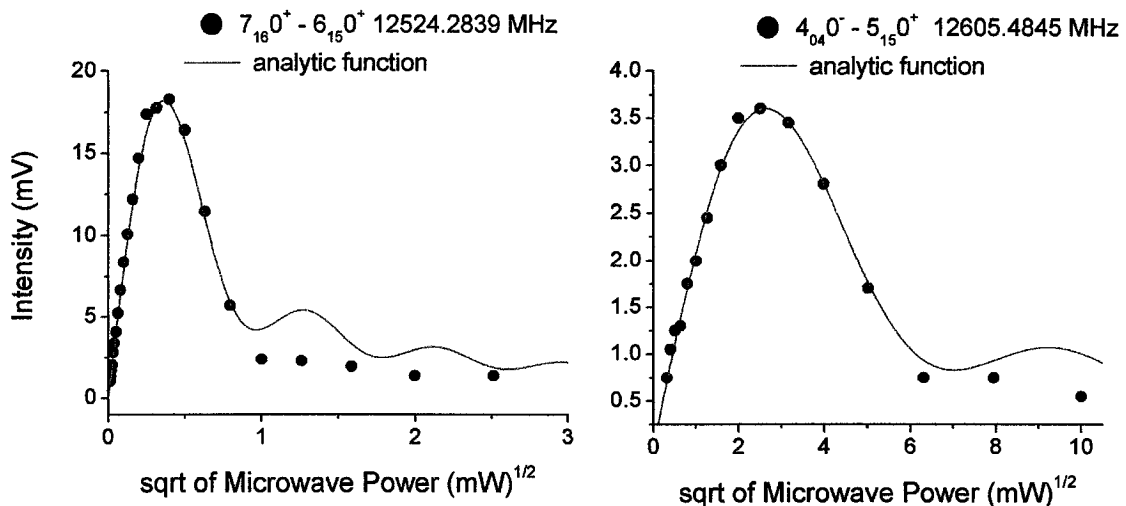


**Figure 3.7.** The above plots demonstrate the electric field dependence of the pure rotational transition  $7_{16}0^+ - 6_{15}0^+$  and the tunneling-rotation transition  $4_{04}0^- - 5_{15}0^+$  (points). These plots were obtained by measuring the peak intensity after 100 signal averages and stepping the microwave input power 2 dBm per step. The smooth line through the data points is an analytic function that gives the FTMW signal intensity as a function of electric field for a given microwave pulse duration.<sup>41</sup> The electric field dependence of the two different transitions is used to estimate the ratio of the  $\mu_a$  to  $\mu_b$  dipole moment.

$$\tau = \frac{1}{2\Delta_0} \quad (3.6)$$

The unambiguous determination of the double proton transfer time should aid theorists in accurately predicting the proton transfer time. The proton transfer time in formic acid dimer has been previously determined by Madeja et al. to be either 5.8 ns or 1.3 ns for the ground state. The calculations by Smedarchina et al. indicate that 1.3 ns transfer time is the proper assignment for the ground state which would result in very similar proton transfer times for the two systems (1.3 ns FAD and 1.7 ns PAFAD).<sup>28</sup>

### **Conclusion**

The aim of this chapter was to demonstrate the ability of the cavity-FTMW spectrometer for measuring low dipole moment and low abundance hydrogen bound species. The results of propionic formic acid demonstrate the type of dynamics possible in ground state. Measuring these challenging systems demonstrates that the cavity FTMW spectrometer will be well suited to measuring rotational spectra in the vibrationally excited state, which is necessary for dynamic rotational spectroscopy. As will be discussed in the following chapters the sensitivity for dynamical measurements is limited by the efficiency of population transfer to the excited state by the laser and once in the excited state the intensity may be spread over hundreds of rotational transitions.

## Reference List

1. Willemot, E.; Dangoisse, D.; Monnanteuil, N.; Bellet, J., *J.Phys.Chem.Ref.Data* **1980**, *9*, 59-160.
2. Winnewisser, M.; Winnewisser, B. P.; Stein, M.; Birk, M.; Wagner, G.; Winnewisser, G.; Yamada, K. M. T.; Belov, S. P.; Baskakov, O. I., *J.Mol.Spectrosc.* **2002**, *216*, 259-265.
3. Pauling, L.; Brockway, L. O., *Proc.Natl.Acad.Sci.U.S.A.* **1934**, *20*, 336-340.
4. Karle, J.; Brockway, L. O., *J.Am.Chem.Soc.* **1944**, *66*, 574-584.
5. Marushkevich, K.; Khriachtchev, L.; Lundell, J.; Räsänen, M., *J.Am.Chem.Soc.* **2006**, *128*, 12060.
6. Albinati, A.; Rouse, K. D.; Thomas, M. W., *Acta Crystallogr.B* **1978**, *34*, 2188.
7. Berkovitch-Yellin, Z.; Leiserowitz, L., *J.Am.Chem.Soc.* **1982**, *104*, 4052-4064.
8. Allan, D. R.; Clark, S. J., *Phys.Rev.Lett.* **1999**, *82*, 3464-3467.
9. Nahringbauer, I., *Acta Crystallogr.B* **1978**, *34*, 315.
10. Chelli, R.; Righini, R.; Califano, S., *J.Phys.Chem.B* **2005**, *109*, 17006-17013.
11. Stein, M.; Sauer, J., *Chem.Phys.Lett.* **1997**, *267*, 111-115.
12. Hermida Ramón, J. M.; Ríos, M. A., *Chem.Phys.* **1999**, *250*, 155.
13. Roy, A. K.; Thakkar, A. J., *Chem.Phys.Lett.* **2004**, *386*, 162.
14. Roy, A. K.; Thakkar, A. J., *Chem.Phys.* **2005**, *312*, 119.
15. Jensen, F., *J.Chem.Phys.* **2003**, *118*, 2459-2463.
16. Roy, A. K.; Thakkar, A. J., *Chem.Phys.Lett.* **2004**, *393*, 347-354.
17. Bell, R. P. *The Tunnel Effect in Chemistry*; Chapman and Hall: New York, 1980.
18. Hammer-Schiffer, S., *Acc.Chem.Res.* **2006**, *39*, 93-100.
19. Masgrau, L.; Roujeinikova, A.; Johannissen, L. O.; Hothi, P.; Basran, J.; Ranaghan, K. E.; Mulholland, A. J.; Sutcliffe, M. J.; Scrutton, N. S.; Leys, D., *Science* **2006**, *312*, 237-241.

20. Keller, J. W., *J.Phys.Chem.A* **2004**, *108*, 4610-4618.
21. Chang, Y.-T.; Yamaguchi, Y.; Miller, W. H.; Schaefer, H. F. I., *J.Am.Chem.Soc.* **1987**, *109*, 7245-7253.
22. Makri, N.; Miller, W. H., *J.Chem.Phys.* **1989**, *91*, 4026-4036.
23. Shida, N.; Barbara, P. F.; Alm  f, J., *J.Chem.Phys.* **1991**, *94*, 3633-3643.
24. Loerting, T.; Liedl, K. R., *J.Am.Chem.Soc.* **1998**, *120*, 12595-12600.
25. Ushiyama, H.; Takatsuka, K., *J.Chem.Phys.* **2001**, *115*, 5903-5912.
26. Vener, M. V.; K  hn, O.; Bowman, J. M., *Chem.Phys.Lett.* **2001**, *349*, 562-570.
27. Tautermann, C. S.; Loferer, M. J.; Voegle, A. F.; Liedl, K. R., *J.Chem.Phys.* **2004**, *120*, 11650-11657.
28. Smedarchina, Z.; Fernandez-Ramos, A.; Siebrand, W., *Chem.Phys.Lett.* **2004**, *395*, 339.
29. Mil'nikov, G. V.; K  hn, O.; Nakamura, H., *J.Chem.Phys.* **2005**, *123*, 074308-1-074308-9.
30. Luckhaus, D., *J.Phys.Chem.A* **2006**, *110*, 3151-3158.
31. Madeja, F.; Havenith, M., *J.Chem.Phys.* **2002**, *117*, 7162-7168.
32. Tanaka, K.; Honjo, H.; Tanaka, T.; Kohguchi, H.; Ohshima, Y.; Endo, Y., *J.Chem.Phys.* **1999**, *110*, 1969-1978.
33. Baba, T.; Tanaka, T.; Morino, I.; Yamada, K. M. T.; Tanaka, K., *J.Chem.Phys.* **1999**, *110*, 4131-4133.
34. Tautermann, C. S.; Voegle, A. F.; Liedl, K. R., *J.Chem.Phys.* **2004**, *120*, 631-637.
35. Legon, A. C., *Annu.Rev.Phys.Chem.* **1983**, *34*, 275-300.
36. Arunan, E.; Dev.S.; Mandal, P. K., *Appl.Spectrosc.Rev.* **2004**, *39*, 131-181.
37. Xu, Y., Wijngaarden, J. van, and J  ger, W. Microwave spectroscopy of ternary and quaternary van der Waals clusters. *Int.Rev.Phys.Chem.* **24**(2), 301-338. 2005.
38. Bauder, A., *J.Mol.Spectrosc.* **1997**, *408/409*, 33-37.
39. Costain, C. C.; Srivastava, G. P., *J.Chem.Phys.* **1964**, *41*, 1620-1627.

40. Martinache, L.; Kresa, W.; Vonmont, U.; Bauder, A., *Chem.Phys.* **1990**, *148*, 129-140.
41. Balle, T. J.; Flygare, W. H., *Rev.Sci.Instrum.* **1981**, *52*, 33-44.
42. Suenram, R. D.; Grabow, J. U.; Zupan, A.; Leonov, I., *Rev.Sci.Instrum.* **1999**, *70*, 2127-2135.
43. Lerner, R. G.; Dailey, B. P.; Friend, J. P., *J.Chem.Phys.* **1957**, *26*, 680-683.
44. Nakajima, M.; Sumiyoshi, Y.; Endo, Y., *Rev.Sci.Instrum.* **2002**, *73*, 165-171.
45. Pickett, H. M., *J.Mol.Spectrosc.* **1991**, *148*, 371-377.
46. Berden, G.; Meerts, W. L.; Kreiner, W., *Chem.Phys.* **1993**, *174*, 247-253.
47. Ruoff, R. S.; Klots, T. D.; Emilsson, T.; Gutowsky, H. S., *J.Chem.Phys.* **1990**, *93*, 3142-3150.
48. Townes, C. H.; Schawlow, A. L. *Microwave Spectroscopy*; Dover Publications: New York, 1975.
49. Kroto, H. W. *Molecular rotation spectra*; Wiley: New York, 1975.
50. Lehmann, K. K., *J.Chem.Phys.* **1991**, *95*, 2361-2370.
51. Xu, Y.; Jäger, W.; Djauhart, J.; Gerry, M. C. L., *J.Chem.Phys.* **1995**, *103*, 2827-2833.
52. Hollas, J. M. *High Resolution Spectroscopy*; Wiley, John & Sons, Inc.: New York, 1998.

## Appendix 3-A

Table 3.10. Full transition list for formic acid trimer.

J'	K <sub>a'</sub>	K <sub>c'</sub>	J''	K <sub>a''</sub>	K <sub>c''</sub>	obs. (MHz)	obs - calc. (MHz)
8	1	8	7	0	7	9560.5683	0.0008
10	0	10	9	1	9	9598.5234	0.0003
9	2	8	8	2	7	9756.8846	-0.0007
9	4	6	8	4	5	9842.4978	-0.0006
9	4	5	8	4	4	9843.2790	0.0004
9	3	7	8	3	6	9851.6775	-0.0001
9	3	6	8	3	5	9879.2458	-0.0001
9	2	7	8	2	6	10083.5113	0.0002
9	1	8	8	1	7	10157.3354	-0.0002
3	2	2	2	1	1	10295.2572	0.001
10	1	10	9	1	9	10301.3685	0.001
9	1	9	8	0	8	10364.8177	-0.0004
10	0	10	9	0	9	10477.9895	-0.0002
11	2	10	11	1	11	10590.6632	-0.0008
3	2	1	2	1	2	10610.2804	0
11	0	11	10	1	10	10760.8076	-0.0002
11	3	8	11	2	9	10792.6474	0.0005
10	2	9	9	2	8	10824.7861	-0.0002
10	4	7	9	4	6	10942.2997	0.0008
10	4	6	9	4	5	10943.9813	-0.0012
10	3	8	9	3	7	10951.0536	-0.0004
10	3	7	9	3	6	10997.6981	-0.0013
10	3	7	10	2	8	11081.9910	0.0009
10	1	10	9	0	9	11180.8346	0.0003
12	2	11	12	1	12	11216.4752	-0.0009
4	2	3	3	1	2	11235.4244	-0.0002
10	2	8	9	2	7	11248.1158	-0.0012
10	1	9	9	1	8	11252.6549	-0.0018
11	1	11	10	1	10	11312.2759	-0.001
9	3	6	9	2	7	11332.4087	0.0011
11	0	11	10	0	10	11463.6508	-0.0015
8	3	5	8	2	6	11536.6723	-0.0003
7	3	4	7	2	5	11692.9885	-0.0011
6	3	3	6	2	4	11804.3927	-0.0011
5	3	2	5	2	3	11877.4591	-0.0014
4	2	2	3	1	3	11880.8595	-0.0022
11	2	10	10	2	9	11887.7814	-0.0012
13	2	12	13	1	13	11890.2071	-0.0022
12	0	12	11	1	11	11893.9200	-0.0023
4	3	1	4	2	2	11920.6680	-0.0009
4	3	2	4	2	3	11966.8829	-0.0025
5	3	3	5	2	4	11983.9434	-0.0021

6	3	4	6	2	5	12013.5137	-0.0012
11	1	11	10	0	10	12015.1230	0.0016
11	5	7	10	5	6	12028.0019	-0.0021
11	5	6	10	5	5	12028.0781	0.0017
11	4	8	10	4	7	12043.8418	-0.0002
11	4	7	10	4	6	12047.1894	-0.0024
11	3	9	10	3	8	12050.2265	-0.0025
7	3	5	7	2	6	12060.0234	-0.0016
11	3	8	10	3	7	12124.6698	0.0002
5	2	4	4	1	3	12125.6269	0.0014
8	3	6	8	2	7	12128.2265	0.0007
9	3	7	9	2	8	12223.0193	0.0012
14	1	13	13	2	12	12229.8924	-0.0006
12	1	12	11	1	11	12319.7302	0.0015
11	1	10	10	1	9	12335.4939	0.0009
10	3	8	10	2	9	12349.2869	0.0011
11	2	9	10	2	8	12414.0134	0.0006
12	0	12	11	0	11	12445.3923	0.0008
11	3	9	11	2	10	12511.7339	0.0017
14	2	13	14	1	14	12608.9253	0.002
12	3	10	12	2	11	12714.7299	0.0015
12	1	12	11	0	11	12871.1986	0.0008
12	2	11	11	2	10	12945.5401	-0.0005
13	3	11	13	2	12	12962.1809	0.0014
6	2	5	5	1	4	12966.6985	0.0007
13	0	13	12	1	12	12999.7981	0.001
12	7	6	11	7	5	13108.7705	-0.0004
12	5	8	11	5	7	13127.3585	0.0017
12	5	7	11	5	6	13127.5226	0.0009
12	4	9	11	4	8	13147.1437	-0.0007
12	3	10	11	3	9	13148.5362	-0.0007
12	4	8	11	4	7	13153.3819	0
5	2	3	4	1	4	13231.4776	0.0015
14	3	12	14	2	13	13257.4092	0.0001
12	3	9	11	3	8	13261.5459	0.0023
13	1	13	12	1	12	13324.0674	0.0014
15	2	14	15	1	15	13369.2099	0.002
12	1	11	11	1	10	13404.0439	0.0013
13	0	13	12	0	12	13425.6044	0.001
12	2	10	11	2	9	13577.3504	0
15	1	14	14	2	13	13697.8346	0.0013
13	1	13	12	0	12	13749.8737	0.0014
7	2	6	6	1	5	13760.0690	-0.0002
13	2	12	12	2	11	13997.7993	0
16	3	14	16	2	15	14001.0532	0.0022
14	0	14	13	1	13	14081.6195	0.0001
13	5	9	12	5	8	14228.2327	-0.0005
13	5	8	12	5	7	14228.5842	0.0019

13	3	11	12	3	10	14245.2502	-0.0001
13	4	10	12	4	9	14252.1487	0
13	4	9	12	4	8	14263.1369	-0.0018
14	1	14	13	1	13	14325.6681	-0.0012
14	0	14	13	0	13	14405.8888	0.0004
13	3	10	12	3	9	14409.3946	-0.0005
17	3	15	17	2	16	14452.4669	-0.0007
13	1	12	12	1	11	14456.8048	0.0006
8	2	7	7	1	6	14507.9258	-0.0004
14	1	14	13	0	13	14649.9394	0.0011
6	2	4	5	1	5	14676.3436	0.0003
13	2	11	12	2	10	14734.8260	-0.0003
14	2	13	13	2	12	15044.3844	0.0012
16	1	15	15	2	14	15128.9058	-0.0005
15	0	15	14	1	14	15143.0894	-0.0009
17	4	13	17	3	14	15181.0073	0.0004
9	2	8	8	1	7	15213.4175	0.0011
3	3	1	2	2	0	15226.2475	-0.0003
3	3	0	2	2	1	15229.4331	0.0008
14	7	8	13	7	7	15301.2533	-0.0013
15	1	15	14	1	14	15324.9291	-0.0004
14	5	10	13	5	9	15330.7435	0.0008
14	5	9	13	5	8	15331.4369	-0.0005
14	3	12	13	3	11	15339.6127	-0.0001
14	4	11	13	4	10	15358.7103	-0.0006
14	4	10	13	4	9	15377.1810	-0.0006
15	0	15	14	0	14	15387.1400	-0.0002
14	1	13	13	1	12	15492.8879	0.0017
16	4	12	16	3	13	15530.5676	-0.0025
14	3	11	13	3	10	15568.6691	-0.0002
15	1	15	14	0	14	15568.9797	0.0002
15	4	11	15	3	12	15827.0791	0.0006
10	2	9	9	1	8	15880.8681	0.0011
14	2	12	13	2	11	15883.7978	0.0004
14	4	10	14	3	11	16069.5555	0.0012
15	2	14	14	2	13	16085.2137	-0.0004
16	0	16	15	1	15	16187.8972	-0.0011
7	2	5	6	1	6	16230.6881	0.0009
13	4	9	13	3	10	16261.0397	-0.0022
4	3	2	3	2	1	16310.1744	-0.001
16	1	16	15	1	15	16322.2252	0
4	3	1	3	2	2	16326.1998	0.0007
16	0	16	15	0	15	16369.7388	0.0012
15	7	8	14	7	7	16398.7993	-0.0019
12	4	8	12	3	9	16407.2993	0.0008
15	3	13	14	3	12	16430.8696	-0.0014
15	5	11	14	5	10	16434.9810	0.0001
15	5	10	14	5	9	16436.2935	0.0003

15	4	12	14	4	11	16466.5903	0.0006
15	4	11	14	4	10	16496.3813	-0.0005
16	1	16	15	0	15	16504.0649	0.0004
15	1	14	14	1	13	16512.3247	0.0013
11	4	7	11	3	8	16515.4594	-0.0006
17	1	16	16	2	15	16515.6547	-0.002
11	2	10	10	1	9	16515.9946	0.0017
10	4	6	10	3	7	16592.9379	0.0001
9	4	5	9	3	6	16646.6527	-0.002
8	4	4	8	3	5	16682.6214	-0.0006
12	4	9	12	3	10	16684.3460	-0.0006
11	4	8	11	3	9	16685.7386	-0.0006
13	4	10	13	3	11	16691.2425	-0.0025
10	4	7	10	3	8	16692.1253	-0.0008
9	4	6	9	3	7	16700.8811	-0.0003
7	4	3	7	3	4	16705.7796	-0.0004
8	4	5	8	3	6	16710.0608	0.0002
14	4	11	14	3	12	16710.3440	0.0007
7	4	4	7	3	5	16718.3675	-0.0008
6	4	2	6	3	3	16720.0139	0
6	4	3	6	3	4	16725.0843	-0.0008
5	4	1	5	3	2	16728.2678	0.0024
5	4	2	5	3	3	16729.9632	-0.0017
15	3	12	14	3	11	16738.8577	0
15	4	12	15	3	13	16746.0628	0.0009
16	4	13	16	3	14	16803.1955	-0.0026
17	4	14	17	3	15	16886.7638	-0.0009
15	2	13	14	2	12	17022.1700	-0.0019
16	2	15	15	2	14	17120.3183	0.0008
12	2	11	11	1	10	17126.0410	0.0004
17	0	17	16	1	16	17219.4081	-0.0013
17	1	17	16	1	16	17317.9061	-0.0008
17	0	17	16	0	16	17353.7361	-0.0002
5	3	3	4	2	2	17381.9939	0.001
5	3	2	4	2	3	17430.3454	-0.0001
17	1	17	16	0	16	17452.2341	0.0002
16	7	9	15	7	8	17497.3044	-0.0007
16	6	11	15	6	10	17513.7926	0.0002
16	6	10	15	6	9	17513.8610	-0.0009
16	1	15	15	1	14	17516.2868	-0.0004
16	3	14	15	3	13	17518.3024	0
16	5	12	15	5	11	17541.0250	0.0016
16	5	11	15	5	10	17543.3922	0
16	4	13	15	4	12	17575.4371	-0.0016
16	4	12	15	4	11	17621.7691	0.0008
13	2	12	12	1	11	17719.7983	0.001
8	2	6	7	1	7	17909.2259	0.0017
16	3	13	15	3	12	17918.2767	0.0001

16	2	14	15	2	13	18148.2121	0.0004
17	2	16	16	2	15	18149.8253	0.0016
18	0	18	17	1	17	18240.5245	0.001
14	2	13	13	1	12	18307.3760	-0.0003
18	1	18	17	1	17	18312.2861	-0.0001
18	0	18	17	0	17	18339.0215	0.0005
18	1	18	17	0	17	18410.7841	0.0003
6	3	4	5	2	3	18433.2138	-0.0013
17	1	16	16	1	15	18507.0672	-0.0006
6	3	3	5	2	4	18546.5242	-0.0003
17	3	15	16	3	14	18601.2390	-0.0012
17	6	12	16	6	11	18616.6453	-0.0009
17	6	11	16	6	10	18616.7840	-0.0006
17	5	13	16	5	12	18648.9167	-0.0012
17	5	12	16	5	11	18653.0242	-0.0029
17	4	14	16	4	13	18684.8073	0.0004
17	4	13	16	4	12	18754.5085	-0.0014
15	2	14	14	1	13	18899.7017	-0.0025
17	3	14	16	3	13	19104.0746	0.0012
19	1	18	18	2	17	19141.4554	0.0001
18	2	17	17	2	16	19173.9632	-0.0007
19	0	19	18	1	18	19253.6389	-0.0008
17	2	15	16	2	14	19260.3538	-0.0001
19	1	19	18	1	18	19305.6291	-0.0023
19	0	19	18	0	18	19325.4006	-0.0019
19	1	19	18	0	18	19377.3947	0.0004
7	3	5	6	2	4	19453.7735	0.0003
18	1	17	17	1	16	19487.7735	0.0016
16	2	15	15	1	14	19507.6973	-0.001
7	3	4	6	2	5	19680.7624	0.0006
18	5	14	17	5	13	19758.6776	0.0024
18	5	13	17	5	12	19765.5553	-0.0009
18	4	15	17	4	14	19794.1424	-0.0003
18	4	14	17	4	13	19895.8630	0.0026
17	2	16	16	1	15	20141.2359	0.0011
19	2	18	18	2	17	20193.0620	0.0026
20	0	20	19	1	19	20260.6870	0.0012
18	3	15	17	3	14	20292.5112	0
20	1	20	19	1	19	20298.1661	-0.0011
20	0	20	19	0	19	20312.6791	0.0017
18	2	16	17	2	15	20357.1166	0.0014
8	3	6	7	2	5	20432.9134	0.0023
19	1	18	18	1	17	20461.8157	0.0013
19	3	17	18	3	16	20751.3546	-0.0009
8	3	5	7	2	6	20840.6260	0
20	2	19	19	2	18	21207.5032	-0.0005
17	5	13	17	4	14	21289.6881	0.0053
21	1	21	20	1	20	21290.0788	0.002

9	3	7	8	2	6	21360.4225	0
20	1	19	19	1	18	21432.3794	-0.0011
19	2	17	18	2	16	21437.1001	-0.0001

---

## Chapter 4

### FTMW Based Detection for Laser Spectroscopy

#### Introduction

The second step towards performing dynamic rotational spectroscopy is to measure the IR spectrum and therefore the aim of this chapter is to demonstrate that the FTMW spectrometer can be used to obtain infrared spectra. The importance of this technique comes from the fact that frequency-domain techniques for molecular-beam vibrational spectroscopy are widely used to study molecular structure and dynamics. Common applications in molecular spectroscopy include the study of the structure and dissociation dynamics of weakly bound clusters,<sup>1-12</sup> the structure of conformational isomers in large polyatomic molecules,<sup>13-15</sup> and the intramolecular vibrational energy redistribution (IVR) dynamics of isolated molecules.<sup>16-24</sup> In general, structural information is derived from the origin and rotational structure of the vibrational bands and the dynamics are obtained from width measurements.

The technique of FTMW-detected IR-FTMW double-resonance spectroscopy contains several important features that are desirable in experimental techniques for molecular-beam vibrational spectroscopy: 1) high-detectivity for species at low concentrations in the molecular beam (e.g. weakly bound clusters), 2) high-sensitivity to measure weak transition moments (e.g. to find weak, perturbing vibrational bands in IVR studies), 3) reasonably high-resolution so that the rotational structure can be observed and

lifetime broadening can be detected, and 4) moderately fast scan rates so that large spectral regions can be examined to find new species (clusters and conformers) and distant perturbations. The capabilities of a Fourier transform microwave (FTMW) spectrometer coupled with a single-longitudinal-mode pulsed infrared (IR) laser will be applied to a variety of problems that can be addressed using molecular-beam vibrational spectroscopy. This work extends the range of applications for FTMW-detected laser spectroscopy from the previous demonstration of the technique for electronic spectroscopy.<sup>25</sup> The goal of this chapter is to illustrate these four important features and to prove that FTMW-detected vibrational spectroscopy is a viable technique.

A major strength of FTMW-detected IR spectroscopy is that it is intrinsically a double-resonance technique. By monitoring a single pure rotational transition, the rotational contour of the vibrational spectrum is greatly simplified. Spectral simplification results from species selectivity and from the fact that only transitions out of the monitored ground state transition are observed. This feature makes it possible to observe weak perturbations in the spectrum that lie under the rotational band contour even at the ultra-cold rotational temperatures found in molecular beams. This ability is especially important in IVR studies where these perturbations can determine the initial time scale for vibrational energy redistribution.<sup>24;26-29</sup> The spectral simplification also makes it possible to determine homogeneous spectral widths associated with IVR and dissociation even when the width is on the order of the rotational spacing. These features of the technique make it more suitable for dynamics studies than techniques like cavity ring down spectroscopy<sup>30-34</sup> or slit-jet FTIR spectroscopy.<sup>35</sup>

As discussed in more detail below, the FTMW-detected IR spectroscopy method is based on detecting the population change in a rotational level induced by the IR laser. The detection limit of our spectrometer requires excitation of about 0.1% of the molecules in one of the monitored rotational levels. This indirect detection method is similar to optothermal spectroscopy<sup>36,37</sup> and offers the important advantage that measurement sensitivity scales with laser power. For example, vibrational overtone spectroscopy can be performed if a suitably powerful laser system is available. To achieve good spectrometer sensitivity it is crucial that the laser interacts with as many of the molecules giving rise to the FTMW signal as possible. One implication of this condition is that the laser should excite the full Doppler width of the vibrational transition. This consideration limits the spectral resolution of the laser sources used for the spectroscopy. The resolution of this technique ( $\sim 0.03 \text{ cm}^{-1}$  in our spectrometer) is low compared to many of the techniques developed around cw laser systems.<sup>38-40</sup> However, by offering frequency scan rates that are significantly higher than the very high resolution, cw-laser IR spectrometers, the current design complements the strengths of these techniques.

## Experimental

The spectrometer configuration implemented is described in Chapter 2 in which the IR multipass is centered on the cavity beam waist and the use of the upgraded pumping system is employed. To achieve maximum excitation we have found the backing pressure needs to be kept low ( $\sim 2 \text{ psi}$ ) with sample concentrations on the order of 0.1%.

These conditions minimize clustering down the center line of the expansion where the laser pulse interacts with the sample.

As described by Nakajima *et al.*, there are two methods for obtaining FTMW-detected laser spectra. If the laser interacts with the molecular beam sample before the FTMW measurement is performed, then laser absorption is detected through the population changes in the pure rotational levels induced by laser excitation.<sup>25</sup> This measurement will be referred to as ground state depletion (GSD). Alternatively, the laser can interact with the molecular beam after the polarizing microwave pulse has been applied. In this case, laser excitation destroys the coherent rotational signal and the spectrum can be detected through changes to the rotational free induction decay (FID) at times after the laser pulse. This measurement will be referred to as the coherence method. In our implementation of the coherence method, the acquisition of the rotational FID begins after the laser pulse interacts with the sample. For GSD measurements the laser excitation pulse is fired 1  $\mu$ s before the polarizing MW pulse. For the coherence method the laser fires 5  $\mu$ s after the falling edge of the polarizing MW pulse and 1  $\mu$ s before the data acquisition trigger.

FTMW-detected IR spectra are obtained by monitoring the peak height of a pure rotational transition in the frequency domain as the laser is scanned. Typically, the lowest J rotational transitions in the working range of our spectrometer are chosen. This minimizes the population difference between the monitored levels, which results in large signal modulations for small changes in the population of either level. The baseline noise of these spectra is determined by the fluctuations in the ground-state signal. For 10

averages these spectra typically have a noise of 1% and for 100 averages the noise drops to 0.3%. Generally, initial fast scans are taken by continuously scanning the laser at  $10.8\text{ cm}^{-1}/\text{h}$  with 10 averages (effective  $0.003\text{ cm}^{-1}$  step size). Then slower scans ( $3.6\text{ cm}^{-1}/\text{h}$ ) with 100 averages (effective  $0.01\text{ cm}^{-1}$  step size) are taken to enhance the signal-to-noise ratio of features identified in the fast scan spectrum.

## Results

### A. Spectrometer Performance: The Acetylenic C-H Stretch Spectra of 1-butyne, tertbutylacetylene, and trimethylsilylacetylene

In this section the GSD and coherence approaches are compared in a measurement of the acetylenic C-H stretch vibrational spectrum of 1-butyne. The sensitivity of the spectrometer for overtone vibrational spectra is demonstrated for two other molecules: tertbutylacetylene and trimethylsilylacetylene. The infrared spectrum of 1-butyne in the region of the acetylenic C-H stretch fundamental measured using the GSD and coherence methods is shown in Figure 4.1. These spectra are obtained using a laser scan rate of  $3.6\text{ cm}^{-1}/\text{hr}$  and averaging 100 measurements of the  $1_{01}-0_{00}$  rotational transition at 8633.42 MHz.<sup>41</sup> There are two differences between the GSD and coherence measurements. The GSD spectrum gives rise to bidirectional signals while only signal depletions are observed in the coherence method. Because the FTMW signal is proportional to the population difference between rotational levels, the laser excitation step in the GSD measurement can either increase (excitation out of the  $1_{01}$  level) or decrease (excitation out of the  $0_{00}$  level) the FTMW signal. When the laser excites the

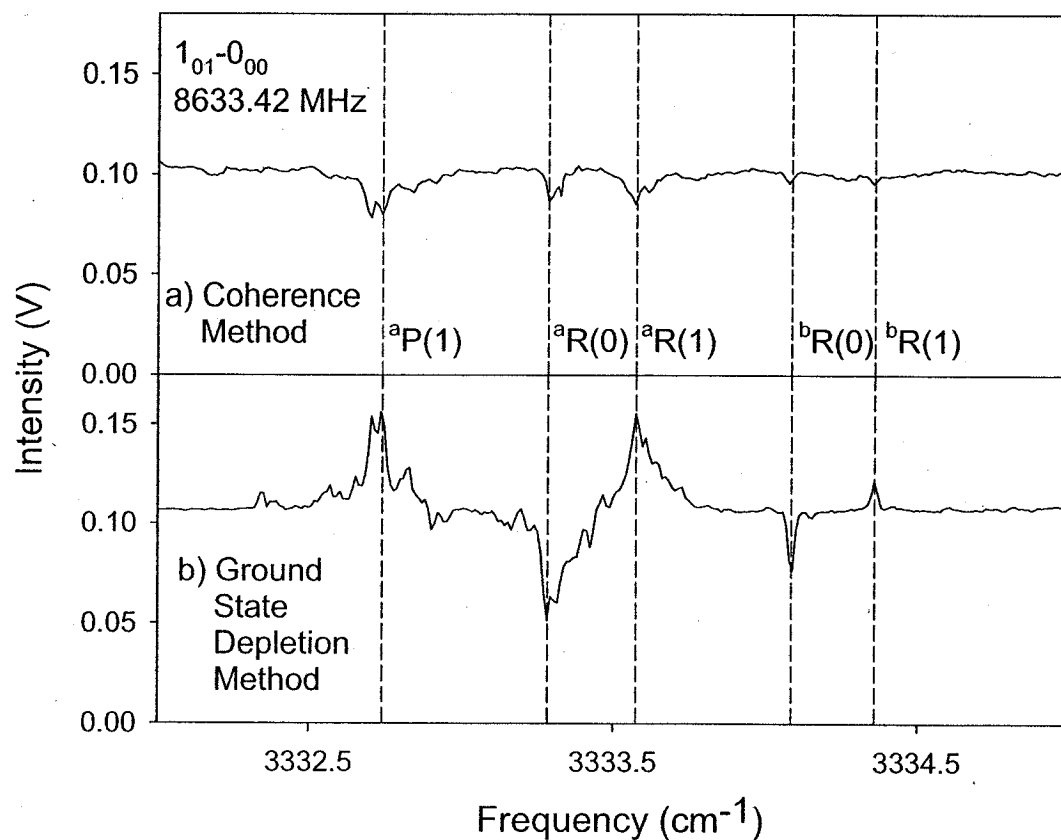


**Figure 4.1** A comparison of a) the coherence method and b) the ground state depletion method for measuring the acetylenic C-H stretch fundamental spectrum of 1-butyne is shown. Both of these measurements were taken while monitoring the  $1_{01}-0_{00}$  pure rotational transition at 8633.42 MHz. The dashed vertical lines show the positions of the more intense *a*-type vibrational transitions (<sup>a</sup>P(1), <sup>a</sup>R(0), and <sup>a</sup>R(1)), as well as two less intense *b*-type vibrational transitions (<sup>b</sup>R(0) and <sup>b</sup>R(1)).

sample after the coherent rotational excitation, the amplitude of the rotational FID is reduced for transitions out of either level so that all laser-induced transitions decrease the MW signal amplitude. As will be discussed below when the results on dimer spectra are presented, the unidirectional signals of the coherence methods are better suited to spectra where fast vibrational dynamics lead to extensive line broadening.

The second difference in the two methods is that the GSD signals are significantly stronger than those observed using the coherence technique. This difference is, in part, related to the multipass geometry used in the spectrometer. With this optics arrangement, the laser can only intercept a fraction of all molecules in the microwave cavity that give rise to the FTMW signal. Based on the signal levels observed in Figure 4.1 and other spectra measured in the Pate lab, we find that the laser excites at most 25% of the molecules that contribute to the FTMW signal. This geometric limitation means that largest MW signal depletion achievable using the coherence method is 25% of the FTMW signal. This limit provides good measurement sensitivity for the coherence method (about 75:1 signal-to-noise ratios can be achieved).

The same limit on the excitation efficiency can produce much larger GSD signals. At the typical rotational temperatures in the pulsed molecular beam ( $T_{\text{rot}} = 1\text{-}2 \text{ K}$ ), the fractional populations of the two rotational levels that give rise to a transition frequency of 12 GHz (a typical operating frequency used in these measurements) are 0.58 and 0.42 ( $\Delta P = 0.16$ ). If the laser excitation is rotationally selective then transitions occur from only one of the two rotational levels. In this case, excitation of 25% of the molecules in the lower energy rotational level leads to about equal populations in the two levels when

the polarizing microwave pulse is applied. Under these conditions, the FTMW signal will be reduced to zero by the laser excitation creating 100% modulation of the signal. For IR transitions that can be saturated, we typically observe complete signal modulation in our measurements. In general, the GSD method has a gain of  $1/\Delta P$ , which provides about a factor of 5 sensitivity enhancement over the coherence method under the typical operating conditions of our spectrometer.

The  $^3P(1)$  region of the 1-butyne spectrum obtained using the GSD method is shown in Figure 4.2. The spectrum consists of a set of spectral components spread over  $\sim 1 \text{ cm}^{-1}$ . This structure is caused by intramolecular vibrational energy redistribution (IVR) which is manifested by extensive local perturbations in the frequency-domain spectrum.<sup>23,24,29</sup> The high resolution spectrum of 1-butyne has been previously investigated.<sup>16,42</sup> Recently, this spectrum has been measured at high-resolution ( $0.0002 \text{ cm}^{-1}$ ) using our electric-resonance optothermal spectrometer<sup>43</sup> and this spectrum is shown with the FTMW-detected IR spectrum. Also shown in the Figure 4.2 is a convolution of the high-resolution spectrum with a Gaussian lineshape with width  $0.03 \text{ cm}^{-1}$  (FWHM) that demonstrates the spectrometer resolution.

One of the advantages of the FTMW-detected IR spectrometer is that the indirect detection method makes it possible to measure weak absorption spectra by increasing the laser power. We demonstrate that it is possible to measure double-resonance vibrational overtone spectra in Figure 4.3. This figure shows the double-resonance spectrum of the first overtone of the acetylenic C-H stretch of tertbutylacetylene and trimethylsilylacetylene. The tertbutylacetylene spectrum was observed monitoring the

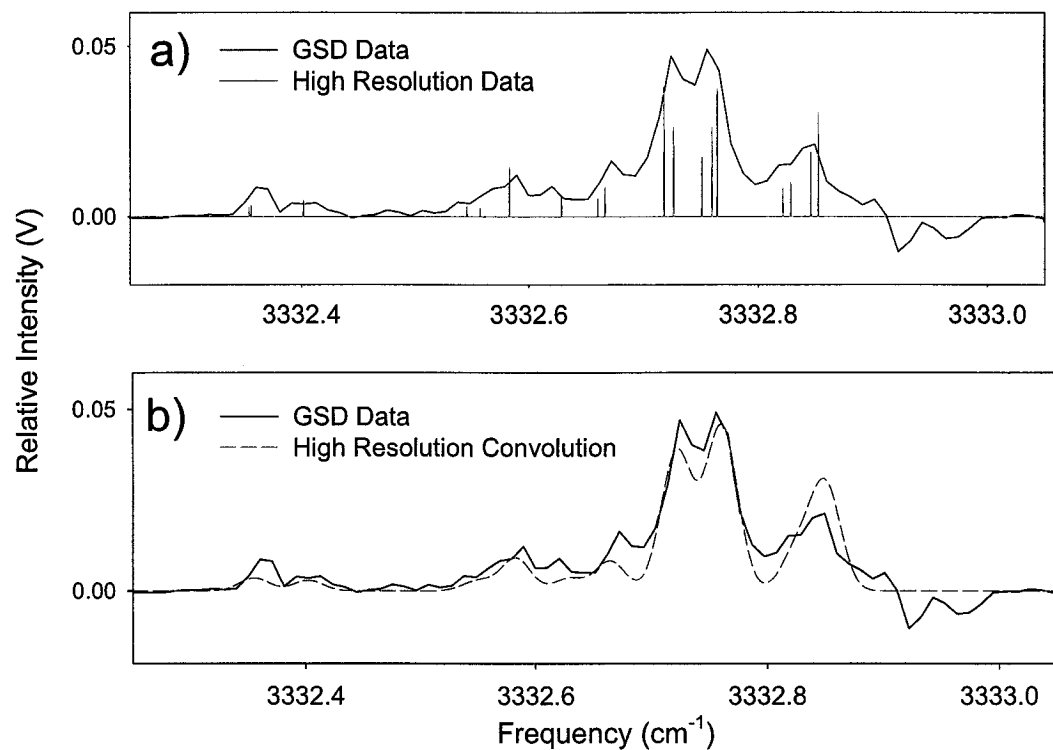


**Figure 4.2** a) A comparison of the GSD method using nanosecond infrared pulses ( $0.03 \text{ cm}^{-1}$  resolution) with high-resolution cw-infrared spectrum obtained by electric-resonance optothermal spectroscopy ( $0.0002 \text{ cm}^{-1}$  resolution) is shown. In both cases, the laser was scanned over the P(1) transition of 1-butyne. Note that the main spectroscopic features are present in both spectra. b) The convolution of the high-resolution spectrum using a Gaussian line shape of width  $0.03 \text{ cm}^{-1}$  (FWHM) is compared to the GSD spectrum.

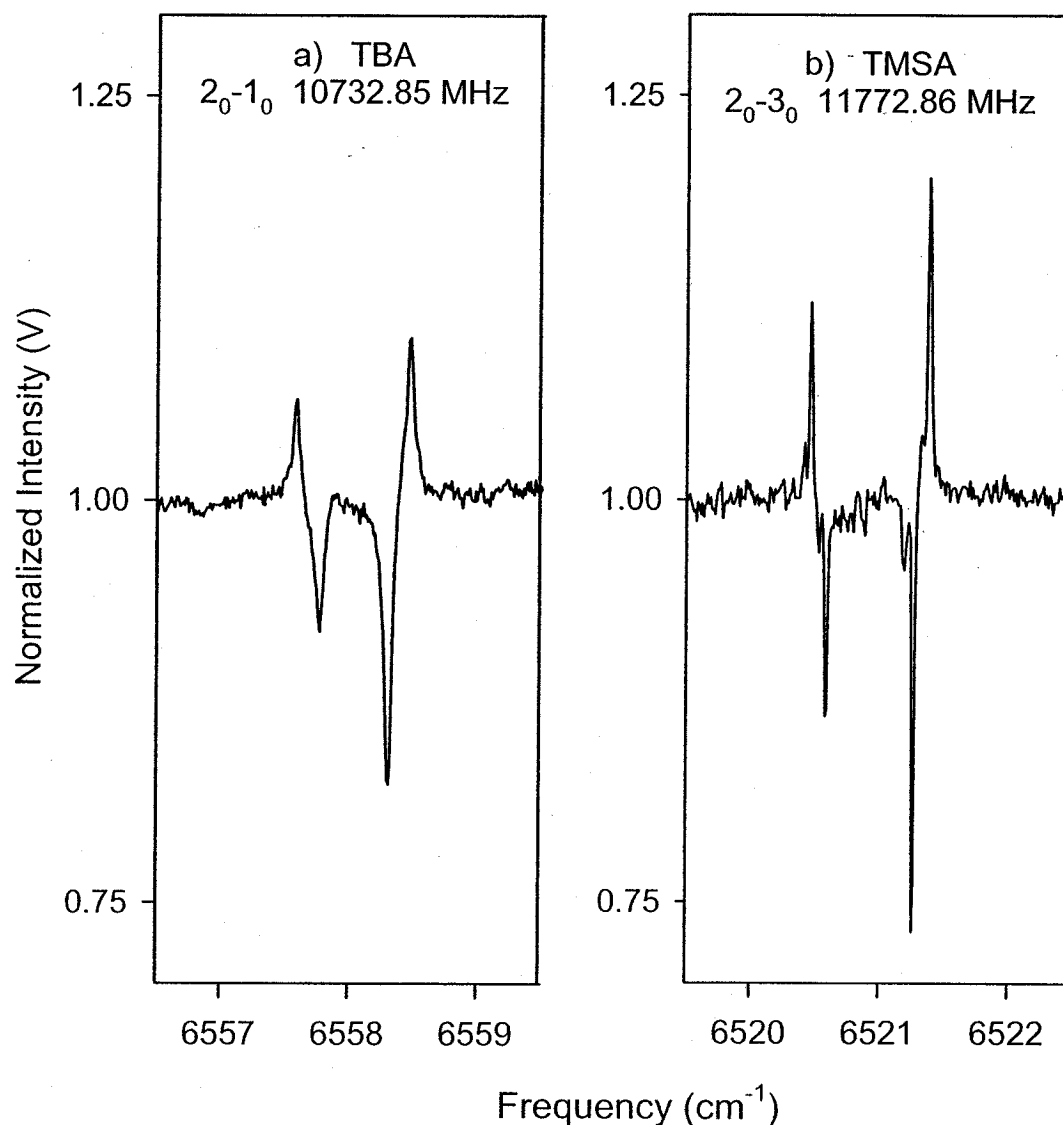


**Figure 4.3** The ground state depletion spectrum of the first overtone of the acetylenic C-H stretch of a) tertbutylacetylene (TBA) and b) trimethylsilylacetylene (TMSA) are displayed. The TBA spectrum was observed by monitoring the  $2_0-1_0$  rotational transition at 10732.85 MHz, while the TMSA spectrum was observed by monitoring the  $2_0-3_0$  rotational transition at 11772.86 MHz.

$2_0-1_0$  rotational transition at 10732.85 MHz<sup>44</sup> and the trimethylsilylacetylene spectrum was observed monitoring the  $2_0-3_0$  rotational transition at 11772.86 MHz. These spectra have been previously measured using high-resolution optothermal spectroscopy where their analysis is discussed.<sup>45</sup>

#### *B. Applications to IVR: The Fast IVR Dynamics of Cyclopropylacetylene*

The FTMW-detected IR spectroscopy method complements high-resolution techniques for studying intramolecular vibrational energy redistribution. As shown in Figure 4.2, this technique cannot compete with the highest resolution methods for measuring fully quantum-state-resolved vibrational spectra. However, it does have a strong advantage in its ability to rapidly scan large spectral ranges. This feature makes it well-suited for frequency-domain spectroscopy of molecules exhibiting fast IVR. As an example, the vibrational spectrum of cyclopropylacetylene (CPA) in the region of the acetylenic C-H stretch in Figure 4.4 is shown. This spectrum was obtained using 10 signal averages of the  $2_{02} - 1_{01}$  rotational transition at 13103.80 MHz<sup>46</sup> and a scan rate of 18 cm<sup>-1</sup>/hr. Fourteen vibrational bands in the region of the acetylenic C-H stretch fundamental have been identified. These perturbations are caused by anharmonic interactions because they appear in  $0_{00}$  vibrationally excited rotational state. These vibrational bands are shown in Figure 4.5 using 100 FTMW signal averages and a 3.6 cm<sup>-1</sup>/hr scan rate. The measured frequencies and relative intensities for the R(1) transitions are listed in Table 4.1.

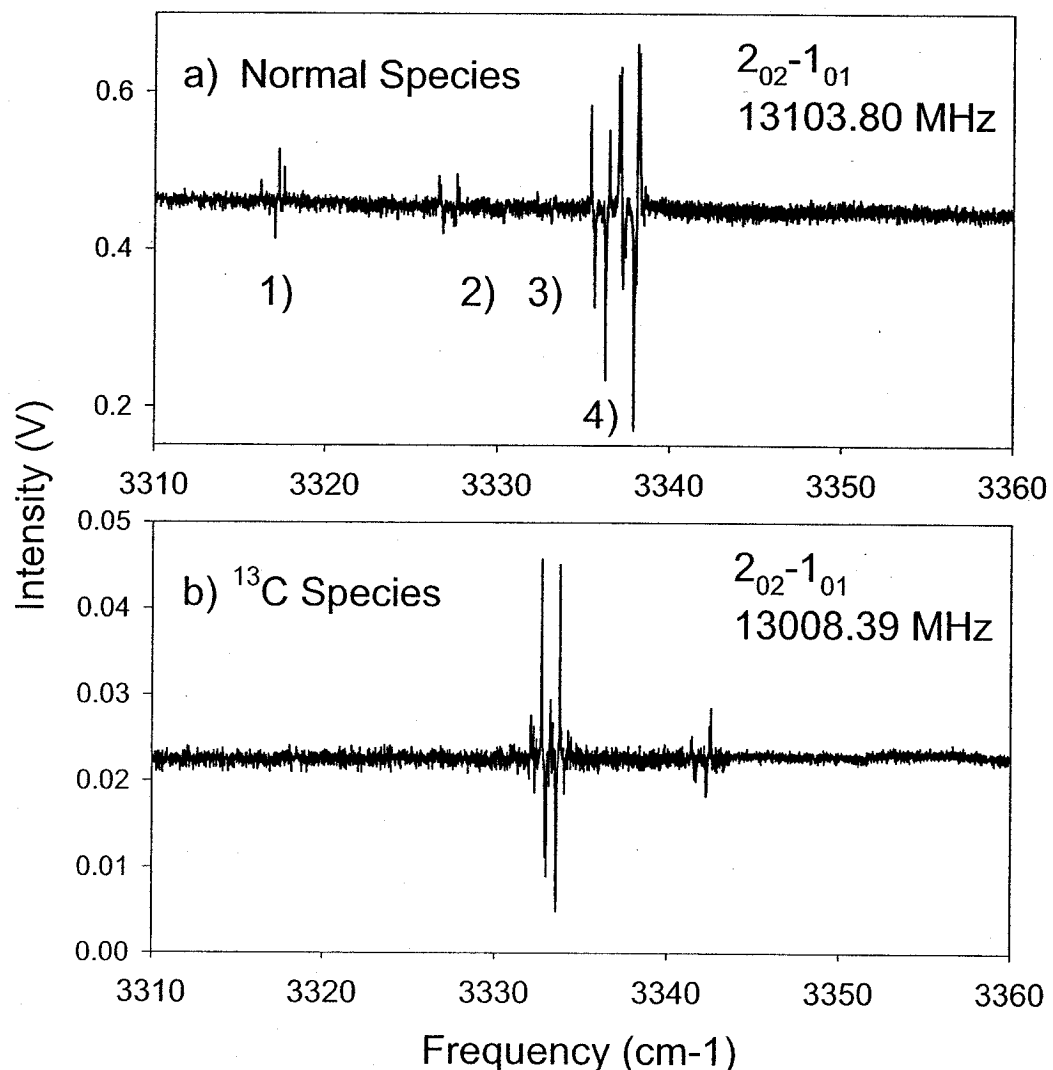


**Figure 4.4** The infrared spectrum of cyclopropylacetylene in the region of the acetylenic C-H stretch fundamental is shown for a) the normal species and b) the  $\text{cyclo-C}_3\text{H}_5-\text{C}^{13}\text{H}\equiv\text{CH}$  isotopomer. These spectra were obtained monitoring the  $2_{02}-1_{01}$  rotational transition at 13103.80 MHz (13008.39 MHz for the  $^{13}\text{C}$  species).

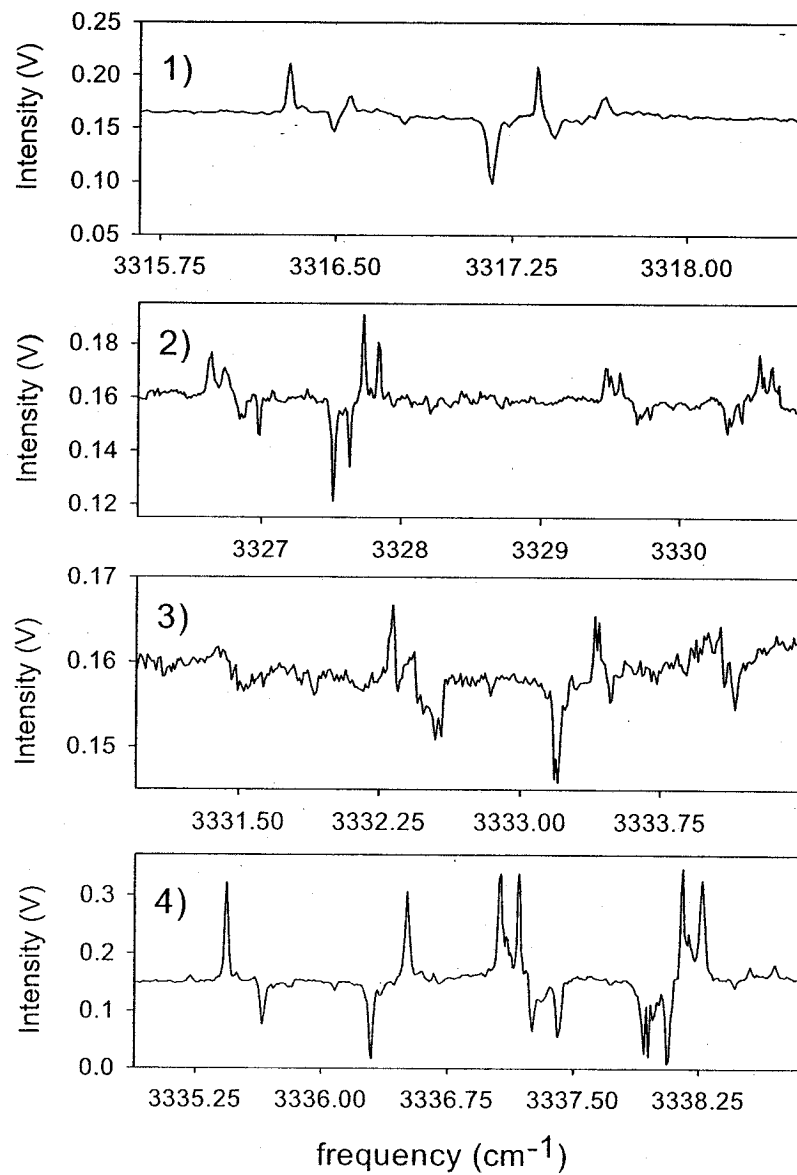


**Figure 4.5** The vibrational bands of the normal species of cyclopropylacetylene in the region of the acetylenic C-H stretch were measured at a slower scan rate ( $3.6 \text{ cm}^{-1}/\text{hr}$  vs  $10.8 \text{ cm}^{-1}/\text{hr}$  in Figure 4.4) with more signal averages (100 vs 10 in Figure 4.4). The vibrational transition frequencies and relative intensities measured in these slower scans are listed in Table 4.1. The numbering scheme corresponds to the observed transitions in the fast scan from Figure 4.4.

**Table 4.1.** CPA infrared absorbance frequencies and relative intensities are listed.

	Frequency (cm <sup>-1</sup> )	Relative Intensity
<b>CPA Normal Species R(2)</b>		
	3317.16	0.2601
	3317.24	0.0365
	3317.43	0.0797
	3327.51	0.1615
	3327.58	0.0273
	3327.65	0.1078
	3330.34	0.0537
	3330.37	0.0419
	3330.44	0.0357
	3336.32	1.0000
	3336.39	0.1829
	3337.94	0.9899
	3337.99	0.3171
	3338.07	0.9513
<b>CPA c-C<sub>3</sub>H<sub>5</sub>-<sup>13</sup>C≡CH P(1)</b>		
	3332.14	0.3357
	3332.27	0.1500
	3332.43	0.0929
	3332.73	1.0000
	3341.28	0.0500
	3341.41	0.0714
	3341.49	0.0571

Using the frequency and intensity information obtained from the FTMW-detected vibrational spectrum the initial time scale for IVR following coherent excitation of the acetylenic C-H stretch can be determined by performing a survival probability calculation.<sup>2,47-49</sup> This calculation is shown in Figure 4.6. At early times there are two time scales for the population decay of the acetylenic C-H stretch. The initial IVR rate occurs in 1 ps and corresponds to the main vibrational band structure in the spectrum of Figure 4.4. The second redistribution time scale is about 7 ps. This time scale corresponds to the frequency width of the more local perturbations in the individual bands shown in Figure 4.5.

The exceptionally fast initial IVR rate of cyclopropylacetylene is unusual for terminal acetylenes. A possible explanation for the fast IVR in this system is that resonant interaction with the C≡C stretch + 2 CH bend combination band provides a "doorway" for subsequent IVR to other near-resonant vibrational modes.<sup>42,50</sup> In most terminal acetylenes this interaction is off-resonance by about 40 cm<sup>-1</sup> with an anharmonic interaction of about 6.5 cm<sup>-1</sup>.<sup>51</sup> However, in cyclopropylacetylene and molecules with a vinyl acetylene structure this interaction tunes into resonance through lowering of the out-of-plane acetylenic C-H bend frequency.<sup>52,53</sup>

The sensitivity of FTMW spectrometers for low abundance species provides a new tool for elucidating IVR mechanisms. For cyclopropylacetylene the <sup>13</sup>C isotopes in natural abundance can be monitored to obtain IR spectra with nearly equal sensitivity to the normal species. The vibrational spectrum of *c*-C<sub>3</sub>H<sub>5</sub>-<sup>13</sup>C≡CH is shown in Figure 4.4.

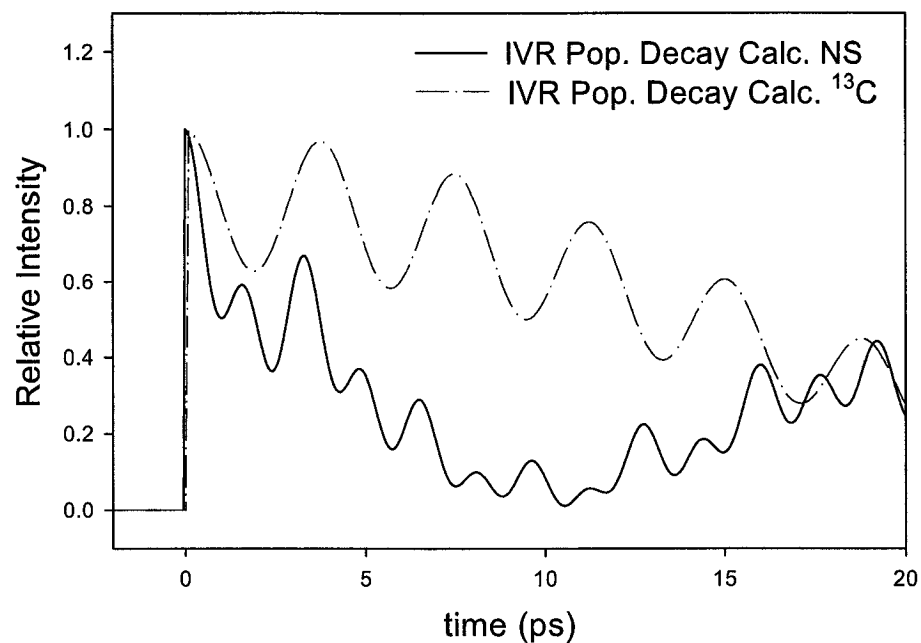


**Figure 4.6** IVR population decay of the normal species and the  $^{13}\text{C}$  isotopomer of cyclopropylacetylene calculated from the frequencies and intensities in the GSD spectrum (Table 5.1) are compared.

The measured frequencies and relative intensities are listed in Table 4.1. This spectrum was obtained using the same experimental conditions used for the normal species, while monitoring the  $2_{02}$ - $1_{01}$  rotational transition at 13008.39 MHz.<sup>54</sup> This isotopic substitution produces a large shift of the C≡C stretch normal-mode frequency ( $\nu \approx -50 \text{ cm}^{-1}$ ), but has negligible effect on the acetylenic C-H stretch ( $\nu \approx -1 \text{ cm}^{-1}$ ) and bend frequencies ( $\nu \approx -0.3 \text{ cm}^{-1}$ ). The frequency shifts were calculated using density functional theory (B3LYP) with the 6-31G(d) basis set.<sup>55</sup> Therefore, this substitution selectively detunes the main resonance. The survival probability calculation for the isotopomer is compared to that of the normal species in Figure 4.6. With the resonance detuned, the initial 1 ps IVR time scale found in the normal species is no longer observed. However, the second IVR time scale of about 10 ps persists. This IVR rate is still fast compared to other terminal acetylenes.<sup>24;26-28</sup> This result is interesting because the molecule has no internal rotors, which have previously been suggested to enhance IVR rates.<sup>56-58</sup>

### C. Measuring Vibrational Spectra of Conformers: 4-fluorobutyne

Molecular beam spectroscopy is well-suited to studies of molecular conformations because the rapid cooling in the free jet expansion can trap the conformers at near-room temperature populations.<sup>59</sup> The high-sensitivity and resolution of the FTMW spectrometer makes it possible to characterize the structures of large numbers of conformers in polyatomic molecules.<sup>60</sup> Using FTMW-detected IR spectroscopy it is possible to obtain conformationally selected, rotationally-resolved vibrational spectra of large molecules. These spectra are especially interesting for biological molecules where

new techniques have been developed to investigate conformational isomerization reactions following selective vibrational excitation.<sup>61</sup> The first results in this field of spectroscopy have shown that the reaction kinetics are strongly influenced by both the selection of conformational geometry and by the vibrational mode excited.<sup>62,63</sup>

Here we use FTMW-detected IR spectroscopy to measure the acetylenic C-H stretch fundamental spectrum of the less stable *gauche* conformer of 4-fluorobutyne. Despite the high sensitivity in our measurement of the vibrational spectrum of the *trans* conformer using an EROS spectrometer, we were unable to obtain the spectrum of the *gauche* conformer.<sup>64</sup> It was speculated that the inability to obtain this spectrum was caused by a combination of low abundance in the molecular beam and fast IVR dynamics for the non-planar conformer. The fast IVR hypothesis is supported by several other measurements of IVR rates from our lab.<sup>43,64</sup> The GSD measurements for the *trans* and *gauche* conformers are shown in Figure 4.7. The spectra were obtained by averaging 100 FTMW spectra and using a laser scan rate of 3.6 cm<sup>-1</sup>/hr. The 3<sub>03</sub>-2<sub>02</sub> rotational transition of the *trans* conformer was monitored at 13176.20 MHz, and the 1<sub>11</sub>-0<sub>00</sub> rotational transition of the *gauche* conformer was monitored at 13958.16 MHz. The line width of the spectral features in the *trans* conformer are spectrometer limited. The previous quantum-state-resolved EROS measurements were used to determine an IVR lifetime for the *trans* conformer of about 1 ns.<sup>64</sup> The GSD spectrum for the *gauche* conformer shows Lorentzian broadening by IVR of each rovibrational transition. For the isolated rotational features, we obtain a Lorentzian width of 2710(108) MHz corresponding to an IVR lifetime of the acetylenic C-H stretch of 58 ps. This IVR lifetime of the non-planar

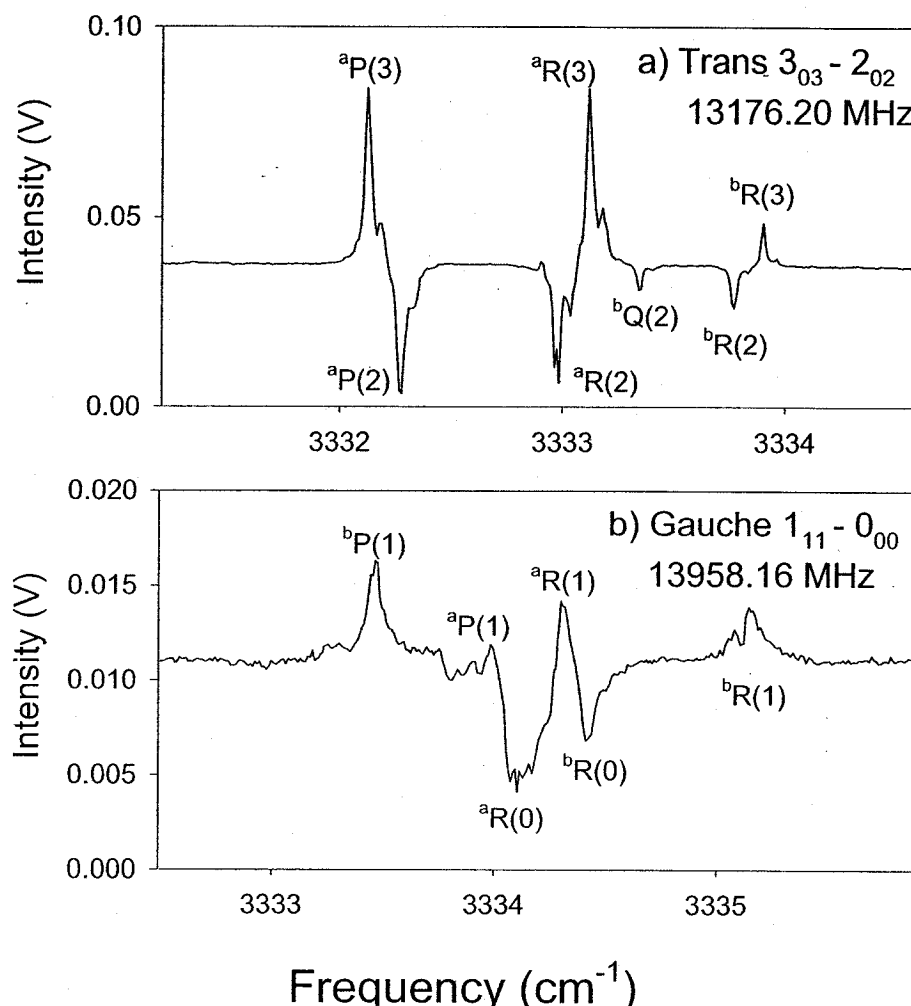


**Figure 4.7** The GSD spectra of the acetylenic C-H stretch fundamental of the *trans* (a) and *gauche* (b) conformers of 4-fluorobutyne are displayed. Although the population of the *gauche* conformer is roughly 9% of the population of the *trans* conformer at room temperature, the FTMW is able to obtain IR spectra of both conformers with comparable sensitivity. The  $3_{03}-2_{02}$  rotational transition of the *trans* conformer was monitored at 13176.20 MHz, and the  $1_{11}-0_{00}$  rotational transition of the *gauche* conformer was monitored at 13958.16 MHz. The *gauche* conformer shows Lorentzian broadening by IVR of each rovibrational transition.

conformer is about 17 times shorter than the *trans* conformer lifetime supporting the trend of faster IVR rates for nonplanar structures that we have previously described.<sup>43</sup>

#### D. Vibrational Dynamics of Weakly Bound Dimers: HCCH-NH<sub>3</sub> and CH<sub>3</sub>CCH-NH<sub>3</sub>

The last application of FTMW-detected IR spectroscopy we present is the measurement of vibrational spectra of weakly bound clusters. One aspect of the vibrational dynamics of weakly bound complexes that we are interested in is whether there is a fast IVR process that precedes dissociation of the complex. In this context, the IVR step causes population redistribution to other quasibound vibrational levels of the complex. If the IVR process is much faster than dissociation, then it would manifest itself as perturbations to the vibrational spectrum similar to those of cyclopropylacetylene in Figure 4.4. For dimers formed from two small monomers, like the acetylene-ammonia complex that is studied here<sup>65</sup>, these perturbing vibrational states would most likely involve excitation in the intermolecular vibrational modes. Despite the prevalence of IVR for large, single molecules, very few dimer systems have shown distinct perturbations suggesting that IVR into the intermolecular vibrational modes is weak.<sup>4;8;66-68</sup> However, the sensitivity of existing molecular-beam spectrometers used for dimer spectroscopy would make it difficult to detect weak perturbations far from the spectrum center.

We have reinvestigated the vibrational spectrum of the acetylene-ammonia complex in the region of the acetylenic C-H stretch using FTMW-detected IR spectroscopy. A rapid scan spectrum (18 cm<sup>-1</sup>/hr, 10 FTMW signal averages) is shown in Figure 4.8. This spectrum was obtained monitoring the 203-102 (J'Ka'F'-J''Ka''F'') rotational transition of

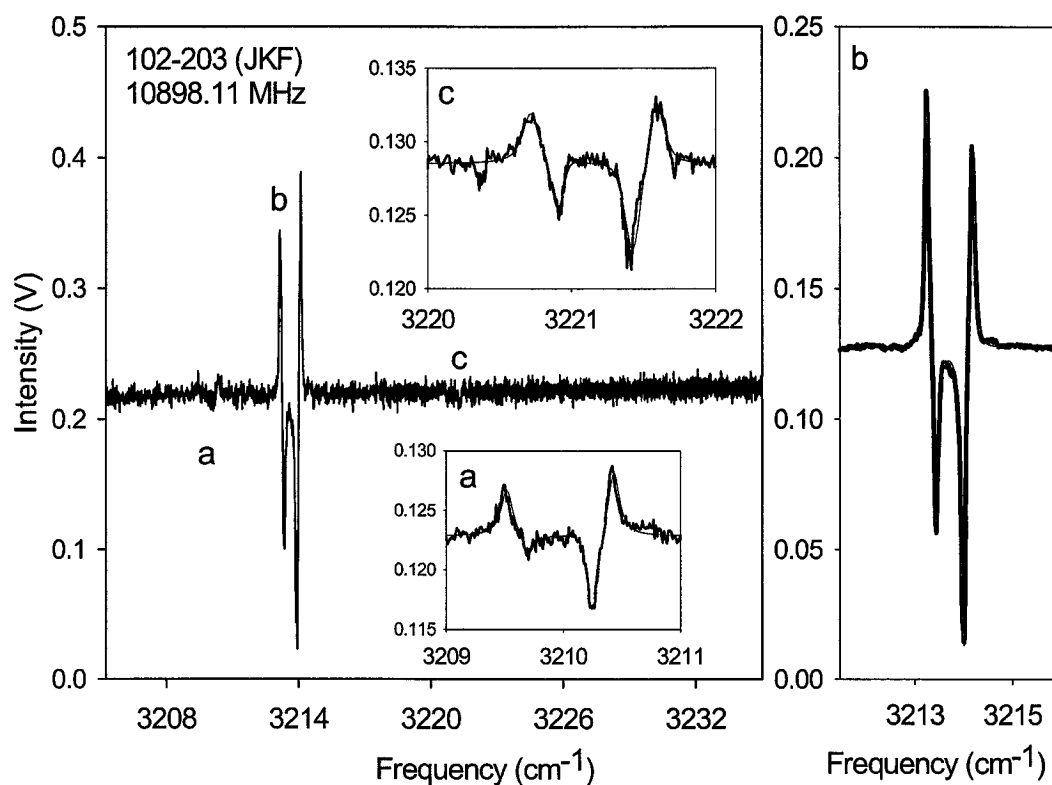


**Figure 4.8** A rapid scan ( $18 \text{ cm}^{-1}/\text{hr}$ , with five signal averages) infrared spectrum of the hydrogen bonded acetylenic C-H stretch fundamental region of the acetylene-ammonia complex is shown. The inset spectra were taken at slower ( $3.6 \text{ cm}^{-1}/\text{hr}$ , 100 signal averages) scan rates over the main absorption band (b) and two weakly coupled perturbing states (a and c). The 203-102 ( $J'K_a''F' - J''K_a''F''$ ) rotational transition was monitored at 10898.11 MHz. The spectra of the slower scans are fit to a sum of four pseudo-Voigt line shapes. The fit results are listed in Table 4.2.

the complex at 10898.11 MHz.<sup>69</sup> In this scan three new weak perturbations in the IR spectrum are detected. One perturbation appears in the wing of the main vibrational band. The other two perturbations are several wavenumbers from the position of the most intense spectral feature. Higher sensitivity scans of these vibrational bands using slower scan rates and more FTMW signal averages are also shown in Figure 4.8. The solid line through the data is a fit of the spectrum to the sum of four pseudo-Voigt line shapes.<sup>70</sup> This lineshape is accurate in the Lorentzian limit.

The values of the lineshape parameters are given in Table 5.2. In the pseudo-Voigt lineshape fit, the fraction of Lorentzian line shape was allowed to vary from 0.0 (a purely Gaussian line shape) to 1.0 (a purely Lorentzian line shape). This fraction is reported in Table 5.2 as the Lorentzian parameter. The uncertainty reported for the average linewidth ( $\Gamma_{\text{avg}}$ ) was obtained from the standard deviation of the four line widths fit for each rovibrational transition. The band origin and excited state rotational constant of the strongest band agree with those previously reported.<sup>69</sup> However, the line width of the strongest band is about 30% larger for our measurement, possibly indicating power broadening.

Observation of the new spectral features shows that there is a fast initial IVR step that leads to a partial redistribution of the acetylenic C-H stretch population. In this way, dynamics of the HCCH-NH<sub>3</sub> dimer are similar to the IVR dynamics of many terminal acetylenes where picosecond transient absorption spectroscopy has revealed an initial fast, restricted IVR process.<sup>26-28</sup> These spectra also provide information on the mode-

**Table 4.2.** The fit parameters for the GSD spectra of acetylene-ammonia (Fig. 4.8) and the propyne-ammonia spectrum (Fig. 4.9) are shown.

	NH <sub>3</sub> --HCCH <sup>a</sup>	NH <sub>3</sub> --HCCH <sup>b</sup>	NH <sub>3</sub> --HCCH <sup>c</sup>
$\nu_0$ (cm <sup>-1</sup> )	3209.88 (2)	3213.64 (2)	3221.08 (2)
B' (MHz)	2737 (6)	2743 (6)	2617 (9)
$\Gamma$ FWHM (MHz)	P(3) 3759 (414)	2518 (431)	3885 (594)
$\Gamma$ FWHM (MHz)	P(2) 3687 (905)	2632 (216)	2410 (246)
$\Gamma$ FWHM (MHz)	R(2) 2974 (162)	2782 (156)	3562 (222)
$\Gamma$ FWHM (MHz)	R(3) 3496 (306)	2680 (234)	3783 (402)
$\Gamma_{avg}$ FWHM (MHz)	3479 (354)	2653 (110)	3410 (680)
Lorentzian Parameter	P(3) 1.0	1.0	1.0
	P(2) 1.0	1.0	0.0
	R(2) 0.4	0.8	0.5
	R(3) 1.0	0.1	0.7
NH <sub>3</sub> --HCCCH <sub>3</sub>			
$\nu_0$ (cm <sup>-1</sup> )	3250.52 (2)		
B' (MHz)	1472 (1)		
$\Gamma$ FWHM (MHz)	P(5) 3789 (276)		
$\Gamma$ FWHM (MHz)	P(4) 3172 (234)		
$\Gamma$ FWHM (MHz)	R(4) 3921 (276)		
$\Gamma$ FWHM (MHz)	R(5) 2961 (210)		
$\Gamma_{avg}$ FWHM (MHz)	3461 (466)		
Lorentzian Parameter	P(5) 0.5		
	P(4) 1.0		
	R(4) 0.9		
	R(5) 1.0		

<sup>a, b, c</sup> correspond to their respective spectra from Fig. 4.8.

specificity of the dimer dissociation kinetics. Mode-specific dissociation rates are commonly observed in dimers formed from small monomer units and the rates correlate with the proximity of the normal-mode vibration to the intermolecular bond.<sup>10,68</sup> The relative intensity distribution of the observed vibrational bands shows that the main band has predominantly acetylenic C-H stretch character. Conversely, because the intensity of the perturbing bands is weak (about 3-5% of the total intensity), these vibrational states have little amplitude in the acetylenic C-H stretch coordinate. Because each monomer is small, it is expected that excitation in the large amplitude stretch and bend intermolecular modes is present in these vibrational states. This expectation is supported by the measured excited state rotational constants. For example, the rotational constant for the vibrational band centered at 3221.08 cm<sup>-1</sup> (labeled c in Figure 4.8) is significantly smaller than the ground state rotational constant suggesting excitation in the intermolecular stretching mode. Both of the weaker vibrational bands analyzed in Figure 4.8 and Table 5.2 have widths larger than the main band which has dominant acetylenic C-H stretch character. This result implies that the dimers with vibrational energy in other modes, most likely intermolecular modes, have a faster dissociation rate.

The acetylenic C-H stretch spectrum of the propyne-ammonia complex has also been measured. This spectrum has not been reported previously, although Botschwina has predicted the frequency shift of the acetylenic C-H stretch fundamental upon complexation as -93 cm<sup>-1</sup>.<sup>71</sup> The spectrum, shown in Figure 4.9, was obtained while scanning the laser at 3.6 cm<sup>-1</sup>/hr and averaging 100 measurements of the 506-405

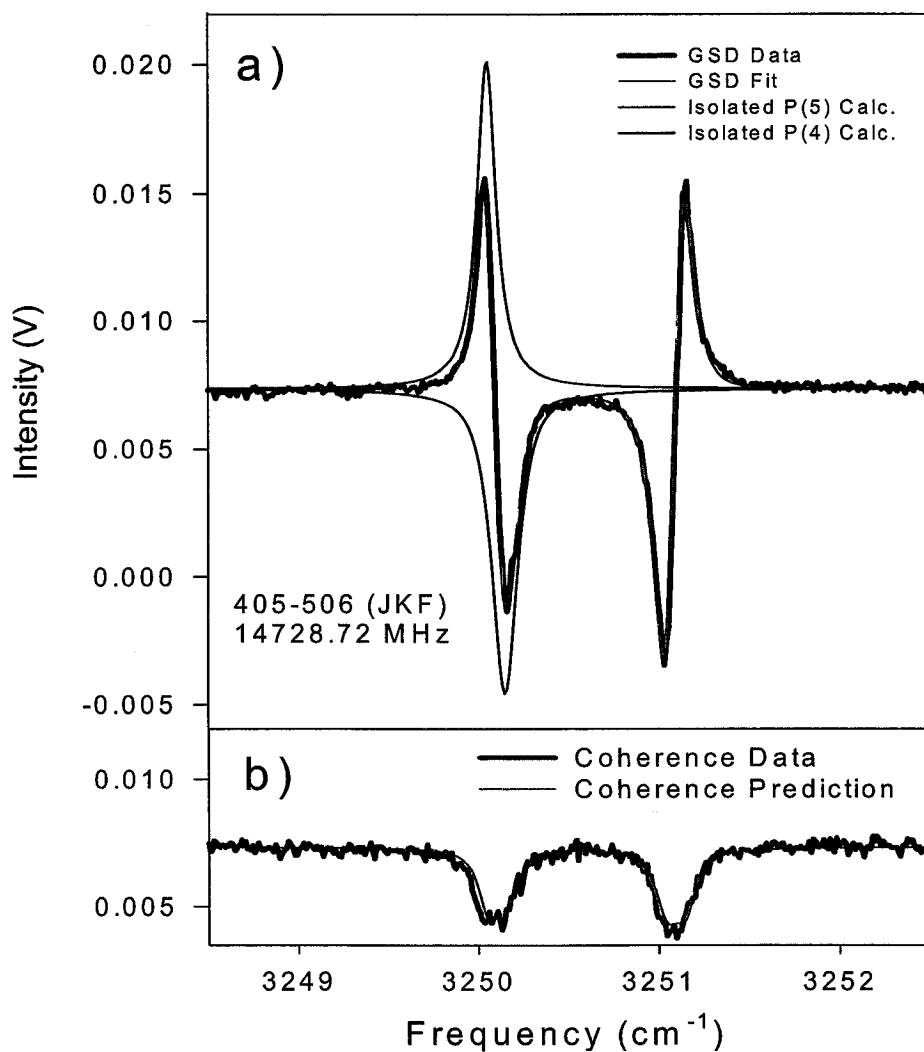


**Figure 4.9** a) The acetylenic C-H stretch fundamental spectrum of the propyne-ammonia complex is shown using the ground state depletion method. The 506-405 ( $J'K_a'F'-J''K_a''F''$ ) rotational transition was monitored at 14728.72 MHz. Pseudo-Voigt lineshape fits of the rovibrational transitions are superimposed on the spectrum. Because the peaks overlap in frequency, some cancellation of the signal occurs in the P- and R-branch regions of the spectrum. The individual spectral features of the P(4) and P(5) transitions obtained from the fit are shown by the dotted lines. b) The spectrum acquired using the coherence method is shown overlapped with the predicted spectrum obtained from the fit of the GSD spectrum. A factor of 5 sensitivity decrease for the coherence technique relative to the GSD method is included in the prediction. The parameters of the pseudo-Voigt line shape fits are listed in Table 4.2.

(J'Ka'F'-J''Ka''F'') rotational transition at 14728.72 MHz.<sup>72</sup> The band origin is observed at 3250.52 cm<sup>-1</sup> (-83 cm<sup>-1</sup> shift), in good agreement with the theoretical prediction. The bidirectional GSD spectrum was fit to obtain the band origin, excited state rotational constant, and the line width and these values are reported in Table 4.2. In this case, the line width of the spectrum is on the order of the rotational spacing leading to signal cancellation in the bidirectional GSD spectrum. The individual spectral features for the P-branch ro-vibrational transitions are shown in Figure 4.9 to illustrate this effect. This spectrum illustrates the major limitation of the GSD method: if the spectral broadening caused by the intramolecular dynamics greatly exceeds the rotational spacing, the GSD signal will be diminished due to its bidirectional nature. When broad features occur, the coherence method is expected to have better sensitivity. We have measured the CH<sub>3</sub>CCH-NH<sub>3</sub> spectrum using the coherence method and this spectrum is shown in Figure 4.9. The solid line through this spectrum is a prediction of the coherence method spectrum using the fit results of the GSD spectrum and the factor of 5 sensitivity decrease ( $1/\Delta P$ ) for the coherence technique relative to the GSD method. The excellent agreement between this signal prediction and the measurement shows that the spectral parameters obtained in the fit of the GSD spectrum are accurate.

### Conclusions

The main goal of this chapter has been to show that the FTMW spectrometer can be used as a detector for infrared laser spectroscopy. The spectrometer that results from coupling pulsed IR lasers to the compact FTMW design has several useful features for studies of vibrational dynamics. One set of advantages derives from the fact that a single

rotational transition is monitored by the FTMW spectrometer. This detection scheme provides species selectivity and spectral simplification through rotational double-resonance. The second set of advantages comes from the excellent sensitivity of the FTMW spectrometer to low abundance species. This makes it possible, for example, to obtain the vibrational spectra of high energy conformers, weakly bound complexes, and  $^{13}\text{C}$  isotopomers in natural abundance. The ability to perform spectroscopy on low abundance species provides a new method to understand the complex vibrational dynamics of large molecules. The spectrometer is shown to have good sensitivity in both GSD and coherence modes of operation. The GSD technique is about a factor of 5 more sensitive than the coherence technique in our design and is, therefore, the favored operation mode when the vibrational dynamics are slow. For fast vibrational dynamics, the bidirectional nature of the GSD signals makes it less suitable and the coherence method is preferred.

## Reference List

1. Hayman, G. D.; Hodge, J.; Howard, B. J., *Chem.Phys.Lett.* **1985**, *118*, 12-18.
2. Freed, K. F. In *Radiationless processes in molecules and condensed phases*; Fong, F. K., ed. Springer-Verlag: New York, 1976
3. Gough, T. E.; Mengal, M.; Rountree, P. A.; Scoles, G., *J.Chem.Phys.* **1985**, *83*, 4958-4961.
4. Suhm, M. A.; Farrell, J. T., Jr.; Ashworth, S. H.; Nesbitt, D. J., *J.Chem.Phys.* **1993**, *98*, 5985-5989.
5. Gruenloh, C. J.; Carney, J. R.; Arrington, C. A.; Zwier, T. S.; Fredricks, S. Y.; Jordan, K. D., *Science* **1997**, *276*, 1678-1681.
6. Robertson, E. G.; Simons, J. P., *Phys.Chem.Chem.Phys.* **2001**, *3*, 1-18.
7. Diken, E. G.; Robertson, W. H.; Johnson, M. A., *J.Phys.Chem.A* **2004**, *108*, 64-68.
8. Dayton, D. C.; Block, P. A.; Miller, R. E., *J.Phys.Chem.* **1991**, *95*, 2881-2888.
9. Kerstel, E. R. Th.; Lehmann, K. K.; Gambogi, J. E.; Yang, X.; Scoles, G., *J.Chem.Phys.* **1993**, *99*, 8559-8570.
10. Leopold, K. R.; Fraser, G. T.; Novick, S. E.; Klemperer, W., *Chem.Rev.* **1994**, *94*, 1807-1827.
11. Bacic, Z.; Miller, R. E., *J.Chem.Phys.* **1996**, *100*, 12945-12959.
12. Fraser, G. T.; Pine, A. S., *J.Chem.Phys.* **1989**, *91*, 637-645.
13. Brummel, C. L.; Mork, S. W.; Philips, L. A., *J.Chem.Phys.* **1991**, *95*, 7041-7053.
14. Hudspeth, E.; McWhorter, D. A.; Pate, B. H., *J.Chem.Phys.* **1997**, *107*, 8189-8192.
15. Green, D.; Hammond, S.; Keske, J.; Pate, B. H., *J.Chem.Phys.* **1999**, *110*, 1979-1989.
16. de Souza, A. M.; Kaur, D.; Perry, D. S., *J.Chem.Phys.* **1988**, *88*, 4569-4578.
17. McIlroy, A.; Nesbitt, D. J., *J.Chem.Phys.* **1989**, *91*, 104-113.
18. Pate, B. H.; Lehmann, K. K.; Scoles, G., *J.Chem.Phys.* **1991**, *95*, 3891-3916.

19. Go, J.; Perry, D. S., *J.Chem.Phys.* **1992**, *97*, 6994-6997.
20. Fraser, G. T.; Pate, B. H.; Bethardy, G. A.; Perry, D. S., *Chem.Phys.* **1993**, *175*, 223-236.
21. Gambogi, J. E.; Kerstel, E. R. Th.; Lehmann, K. K.; Scoles, G., *J.Chem.Phys.* **1994**, *100*, 2612-2622.
22. Lee, C. Y.; Pate, B. H., *J.Chem.Phys.* **1997**, *107*, 10430-10439.
23. Nesbitt, D. J.; Field, R. W., *J.Phys.Chem.* **1996**, *100*, 12735-12756.
24. Lehmann, K. K.; Scoles, G.; Pate, B. H., *Annu.Rev.Phys.Chem.* **1994**, *45*, 241-274.
25. Nakajima, M.; Sumiyoshi, Y.; Endo, Y., *Rev.Sci.Instrum.* **2002**, *73*, 165-171.
26. Yoo.H.S.; DeWitt, M. J.; Pate, B. H., *J.Phys.Chem.A* **2004**, *108*, 1348-1364.
27. Yoo.H.S.; DeWitt, M. J.; Pate, B. H., *J.Phys.Chem.A* **2004**, *108*, 1365-1379.
28. Yoo.H.S.; McWhorter, D. A.; Pate, B. H., *J.Phys.Chem.A* **2004**, *108*, 1380-1387.
29. Keske, J.; McWhorter, D.; Pate, B. H., *Int.Rev.Phys.Chem.* **2000**, *19*, 363-407.
30. O'Keefe, A.; Deacon, D. A. G., *Rev.Sci.Instrum.* **1988**, *59*, 2544-2551.
31. Romanini, D.; Lehmann, K. K., *J.Chem.Phys.* **1993**, *99*, 6287-6301.
32. Scherer, J. J.; Paul, J. B.; O'Keefe, A.; Saykally, R. J., *Chem.Rev.* **1997**, *97*, 25-51.
33. Ito, F.; Nakanaga, T., *Chem.Phys.Lett.* **2000**, *318*, 571-577.
34. Ito, F.; Nakanaga, T., *Chem.Phys.* **2002**, *277*, 163-169.
35. Schaal, H.; Haber, T.; Suhm, M. A., *J.Phys.Chem.A* **2000**, *104*, 265-274.
36. Gough, T. E.; Miller, R. E.; Scoles, G., *Appl.Phys.Lett.* **1977**, *30*, 338-340.
37. Callegari, A.; Merker, U.; Engels, P.; Srivastava, H. K.; Lehmann, K. K.; Scoles, G., *J.Chem.Phys.* **2000**, *113*, 10583-10596.
38. Green, D.; Holmberg, R.; Lee, C. Y.; McWhorter, D. A.; Pate, B. H., *J.Chem.Phys.* **1998**, *109*, 4407-4414.
39. Takami, M.; Suzuki, M., *J.Chem.Phys.* **1980**, *72*, 4089-4098.

40. Shimoda, K. *Laser Spectroscopy of Atoms and Molecules*; Plenum: New York, 1974.
41. Bestmann, G.; Dreizler, H., *Z.Naturforsch* **1985**, *40a*, 263-266.
42. McIlroy, A.; Nesbitt, D. J., *J.Chem.Phys.* **1990**, *92*, 2229-2243.
43. Engelhart, C.; Keske, J. C.; Rees, F. S.; Self-Medlin, Y. B.; Yoo, H. S.; Pate, B. H., *J.Phys.Chem.A* **2001**, *105*, 6800-6807.
44. Nugent, L. J.; Mann, D. E.; Lide, D. R., Jr., *J.Chem.Phys.* **1962**, *36*, 965-971.
45. Kerstel, E. R. Th.; Lehmann, K. K.; Mentel, T. F.; Pate, B. H.; Scoles, G., *J.Phys.Chem.* **1991**, *95*, 8282-8293.
46. Collins, M. J.; Britt, C. O.; Boggs, J. E., *J.Chem.Phys.* **1972**, *56*, 4262-4265.
47. Bixon, M.; Jortner, J., *J.Chem.Phys.* **1968**, *48*, 715-726.
48. Jiang, X. P.; Brumer, P., *J.Chem.Phys.* **1991**, *94*, 5833-5843.
49. Freed, K. F.; Nitzan, A., *J.Chem.Phys.* **1980**, *73*, 4765-4778.
50. Cupp, S. B.; Lee, C. Y.; McWhorter, D. A.; Pate, B. H., *J.Chem.Phys.* **1998**, *109*, 4302-4315.
51. Duncan, J. L.; McKean, D. C.; Nivellini, G. D., *J.Mol.Struct.* **1976**, *32*, 255-268.
52. Nyquist, R. A.; Potts, W. J., *Spectrochim.Acta* **1960**, *16*, 419-427.
53. Evans, J. C.; Nyquist, R. A., *Spectrochim.Acta* **1963**, *19*, 1153-1163.
54. Harmony, M. D.; Nandi, R. N.; Tietz, J. V.; Choe, J.-I.; Getty, S. J.; Staley, S. W., *J.Am.Chem.Soc.* **1983**, *105*, 3947-3951.
55. Frisch, M. J., Trucks, G. W., Sclegel, H. B., Scuseria, G. E., Robb, M. A., Cheeseman, J. R., Zakrzewski, V. G., Montgomery, J. A. Jr., Stratmann, R. E., Burant, J. C., Dapprich, S., Millam, J. M., Daniels, A. D., Kudin, K. N., Strain, M. C., Farkas, O., Tomasi, J., Barone, V., Cossi, M., Cammi, R., Mennucci, B., Pomelli, C., Adamo, C., Clifford, S., Ochterski, J., Petersson, G. A., Ayala, P. Y., Cui, Q., Morokuma, K., Malick, D. K., Rabuck, A. D., Raghavachari, K., Foresman, J. B., Cioslowski, J., Ortiz, J. V., Baboul, A. G., Stefanov, B. B., Liu, G., Liashenko, A., Piskoz, P., Komaromi, I., Gomperts, R., Martin, R. L., Fox, D. J., Keith, T., Al-Laham, M. A., Peng, C. Y., Nanayakkara, A., Challacombe, M., Gill, P. M. W., Johnson, B., Chen, W., Wong, M. W., Andres, J. L., Gonzalez, C., Head-

- Gordon, M., Replogle, E. S., and Pople, J. A. Gaussian 98, Revision A.7. Gaussian, Inc., Pittsburgh PA . 1998.
56. Bethardy, G. A.; Wang, X.; Perry, D. S., *Can.J.Chem.* **1994**, *72*, 652-658.
  57. Perry, D. S.; Bethardy, G. A.; Wang, X., *Ber.Bunsenges.Phys.Chem.* **1995**, *99*, 530-535.
  58. Parmenter, C. S.; Stone, B. M., *J.Chem.Phys.* **1986**, *84*, 4710-4711.
  59. Ruoff, R. S.; Klots, T. D.; Emilsson, T.; Gutowsky, H. S., *J.Chem.Phys.* **1990**, *93*, 3142-3150.
  60. Fraser, G. T.; Suenram, R. D.; Lugez, C. L., *J.Phys.Chem.A* **2001**, *105*, 9859-9864.
  61. Dian, B. C.; Longarte, A.; Zwier, T. S., *Science* **2002**, *296*, 2369-2373.
  62. Dian, B. C.; Longarte, A.; Winter, P. R.; Zwier, T. S., *J.Chem.Phys.* **2004**, *120*, 133-147.
  63. Evans, D. A.; Wales, D. A.; Dian, B. C.; Zwier, T. S., *J.Chem.Phys.* **2004**, *120*, 148-157.
  64. Keske, J. C.; Rees, F. S.; Suenram, R. D.; Pate, B. H., *Phys.Chem.Chem.Phys.* **2003**, *5*, 1599-1609.
  65. Fraser, G. T.; Leopold, K. R.; Klemperer, W., *J.Chem.Phys.* **1984**, *80*, 1423-1426.
  66. Oudejans, L.; Moore, D. T.; Miller, R. E., *J.Chem.Phys.* **1999**, *110*, 209-219.
  67. Farrell, J. T. Jr.; Suhm, M. A.; Nesbitt, D. J., *J.Chem.Phys.* **1996**, *104*, 9313-9331.
  68. Nesbitt, D. J., *Annu.Rev.Phys.Chem.* **1994**, *45*, 367-399.
  69. Hilpert, G.; Fraser, G. T.; Pine, A. S., *J.Chem.Phys.* **1996**, *105*, 6183-6191.
  70. Douglass, K. O. The equation for a single pseudo-Voigt lineshape is as follows.  
2004.
$$y(x) = y_0 + a \left[ c \left( \frac{1}{1 + \left( \frac{x - x_0}{b} \right)^2} \right) + (1 - c) e^{\left( -\frac{1}{2} \left( \frac{x - x_0}{b} \right)^2 \right)} \right]$$
  71. Schulz, B.; Botschwina, P., *Mol.Phys.* **1996**, *89*, 1553-1565.

72. Omron, R. M.; Hight Walker, A. R.; Hilpert, G.; Fraser, G. T.; Suenram, R. D., *J.Mol.Spectrosc.* **1996**, *179*, 85-93.

## Chapter 5

### FTMW Detected Laser Spectroscopy: Enhanced Sensitivity and Applications to Electronic Spectroscopy

#### Introduction

The previous chapter described two methods for measuring IR spectra using an FTMW spectrometer as a detector. These techniques are an extension from earlier microwave optical double resonance (MODR) spectroscopy developed by Lehmann and Coy in which they detected the ground state microwave (MW) absorption signal while pumping with a pulsed dye laser.<sup>1</sup> This technique was used to make rotational assignments to high overtone bands of ammonia in the visible region.<sup>2,3</sup> Endo's group applied this MODR technique to FTMW spectroscopy and demonstrated two methods for obtaining laser-FTMW spectra, which are referred to as ground state depletion (similar to MODR by Lehmann and Coy) and the coherence method.<sup>4</sup>

The previous chapter demonstrated the sensitivity of the ground state depletion and coherence techniques for a wide range of systems with applications to vibrational spectroscopy. For the most part these systems were gas phase samples with reasonably strong pure rotational signals and/or IR transition strengths. In order to study more challenging systems an increase in sensitivity is required. Additionally, this will demonstrate that FTMW detected laser spectroscopy is competitive with other techniques.

The major noise source for the ground state depletion (GSD) measurements is the shot-to-shot number density fluctuations of the pulsed nozzle and longer term drift of the

number density which leads to significant modulation of the baseline. The GSD and coherence methods may have significant problems for studying species generated from novel sources such as ablation, discharge, or even heated nozzles where shot-to-shot fluctuations are expected to increase.<sup>5</sup> The goal for sometime has been to develop a technique that removes these fluctuations and would therefore be background-free. New techniques will be demonstrated that achieve background-free detection of laser absorption. These techniques have been made possible by implementing a 2 Gs/s arbitrary function generator into the circuit of the cavity FTMW spectrometer.

As described in the previous chapter, advantages arise from the spectral simplification that occurs when performing IR-FTMW double resonance spectroscopy. This aspect enables the technique to obtain rotationally resolved vibrational or electronic spectra from a sample with a dense laser spectrum. This has advantages for studying systems that have a poorly defined rotational contour or when several conformers are present with overlapping spectra. There are also advantages for systems that are perturbed by IVR.

Another important aspect of this method is for electronic spectroscopy. Measuring the low resolution LIF spectrum has become widespread. Several double resonance methods have been developed to assign a particular LIF feature to a specific conformer.<sup>6;7</sup> High resolution rotationally resolved methods have also been established that determine the rotational constants in the ground and excited state which provides an unambiguous conformer assignment of the electronic spectrum.<sup>8;9</sup> However, high resolution methods

become difficult for weakly fluorescing molecules and for large systems where the spacing of the transitions is on the order of the linewidth for the experiment.

Methods based on microwave spectroscopy have advantages for assigning specific conformers to the low resolution LIF spectrum. By first measuring and assigning the rotational spectrum in the ground state the transitions of a specific species can be monitored and the UV laser scanned in the region of the LIF feature to determine conformer assignments. This will be demonstrated for para-methoxyphenethylamine (pMPEA), a biologically relevant molecule that has previously been studied using high resolution LIF methods.<sup>8</sup> Before the high resolution measurement significant controversy existed in the literature over the assignment of the LIF features to the specific conformers.<sup>10-13</sup>

### Experimental

The major aims of this work are to extend the laser-FTMW double resonance technique to electronic spectroscopy and to demonstrate the advantages of using a cavity FTMW spectrometer as a generic detector for laser spectroscopy. For UV-FTMW double resonance experiments visible light is generated by using the 532 nm output of the doubled Nd:YAG (Continuum II) laser to pump a dye laser (Coherent-Lambda Physik ScanMatePro 0.025cm<sup>-1</sup> linewidth). The output of the dye laser is doubled using a  $\beta$ -Barium Borate (BBO) crystal (Lambda Physik) to generate light in the UV. The typical output power is ~7mJ/pulse in the UV.

The laser dye used for the UV-FTMW double resonance experiments on phenylacetylene was Fluorescein and for experiments on pyridine and pMPEA

Rhodamine 6G was used. The electronic spectra of phenylacetylene<sup>14-17</sup>, pyridine<sup>18</sup>, and pMPEA<sup>10</sup> have previously been measured and are used here as benchmarks for the enhanced GSD technique.<sup>8,11-13</sup> The pure rotational spectra of phenylacetylene<sup>19</sup> and pyridine<sup>20,21</sup> have also been studied previously.

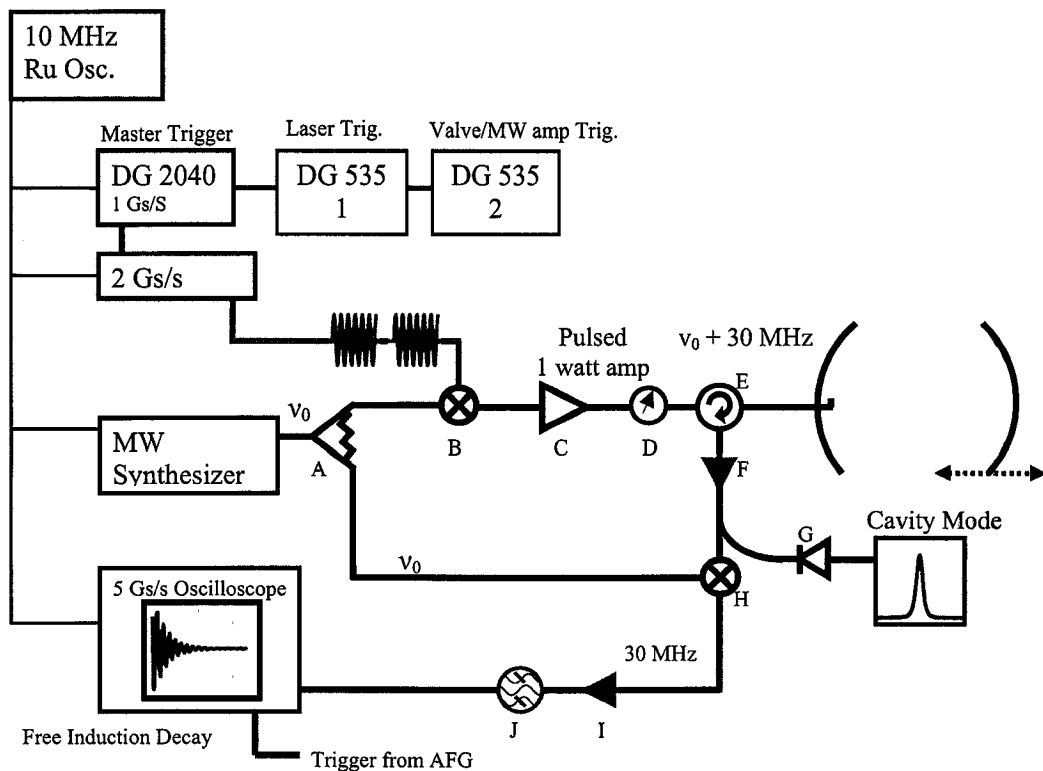
Steering of the UV beam was performed by using two pairs of uncoated UV grade fused silica prisms. The second pair of prisms (2.5 cm) were arranged to form a periscope to steer the UV beam into the molecular beam chamber. The wavelength of the dye laser was measured using a broadband beam sampler (BK7 Newport 10B20) placed before the frequency doubler to direct a portion of the visible light to the wavemeter (Coherent Wavemaster). A plane parallel multipass assembly inside the chamber was used for experiments on pyridine. For the experiments on phenylacetylene and pMPEA the UV beam was expanded with a negative lens and aligned coaxially with the pulsed nozzle.

The spectrometer used to perform background free ground state depletion is based on the Balle-Flygare<sup>22</sup> and NIST<sup>23</sup> cavity machine designs described in Chapter 2 with several modifications. The changes mainly encompass the pulse excitation scheme and more robust triggering source, while the vacuum chamber and pumping system remain the same. The changes reflect a design that uses the cavity machine as a laser detector. The circuit has been simplified for ease of use and the movement of the mirror is manually controlled. Also to reduce cost the mirrors have not been diamond turned however, by using a single coupling antenna the cavity Q remains high ( $\sim 10^4$ ).

The modified block diagram is illustrated in Figure 5.1. The triggering source for the experiment is a Data Pattern Generator (Tektronix DG2040) which has a 1 Gs/s sampling rate, low jitter (30 ps), and fast rising edge (150 ps) which are critical for achieving phase stability for averaging in the time domain. The DG2040 triggers the Arbitrary Function Generator (Tektronix AFG 3252). The AFG echoes the trigger from the DG2040 to trigger the oscilloscope (Tektronix TDS 5104). To achieve phase stability all components are phase locked to the rubidium oscillator at 10 MHz (Stanford FS725).

The main difference between the circuit in Figure 5.1 and the one illustrated in Chapter 2 is that the AFG is used as the 30 MHz source into the single sideband modulator. The AFG allows for complete control over phase, amplitude, pulse delay, and pulse duration for up to two pulses and all of these parameters are adjustable in real time from the front panel. The 2 Channel AFG has a feature which allows the second channel (or any arbitrary pulse) to be combined with the output of Channel 1. This feature allows for push button control of turning the pulse from Channel 2 on or off.

There were two methods for performing IR-FTMW double resonance spectroscopy described in the previous chapter based on the work of Endo's group and differed by the relative timing of the laser and microwave (MW) pulse.<sup>4</sup> For the coherence method the laser is fired after the polarizing MW pulse and detection of the rotational FID begins after the laser pulse is fired. A minor extension of Endo's dual gate method<sup>4</sup> is to trigger the scope a few microseconds before the laser pulse is fired and have two gates on the FID that are Fourier transformed; one before the laser and one after. This allows for an internal calibration of the signal fluctuations because for every valve pulse a laser on and



- A Power Divider (Omni Spectra 2-18 GHz)
- B Single Sideband Modulator (Miteq)
- C Pulsed Amplification Stage (2-26 Miteq amp – 10 dB attenuator – pulsed 1 Watt amp MW Power Inc.)
- D Manual step attenuator (0-69 dB) Wenchel
- E Circulator (Ditom DMCB018 6-18 GHz)
- F Low noise amplifier (Miteq AMF-5F-0800-1800-14-10P 8-18 GHz )
- G Power Detector (Herotek 6 -18GHz)
- H Standard Double Balanced Mixer (Miteq 5-20 GHz DM0520LW1)
- I RF Amp (Miteq DC-1 GHz AM1297)
- J 30 MHz Bandpass Filter (Reactel)

**Figure 5.1.** A schematic of the block diagram used to perform laser-FTMW double resonance spectroscopy is shown above. A typical measurement consists of splitting the power microwave synthesizer into two arms. The upper arm is mixed with the 30 MHz pulse output of the AFG in the single sideband modulator (SSBM). This adds 30 MHz and is the resonant cavity and molecular frequency. The output of the SSBM is amplified to 1 Watt then attenuated to achieve optimal excitation. The MW power passes through a circulator and is coupled into the cavity using a wire antenna. The FID is coupled with the same wire antenna and the circulator sends the reflected power to a low noise amp. The amplified output is down converted to 30 MHz using the second arm of the synthesizer and is subsequently amplified and filtered. The signal is digitized and Fourier transformed on the digital oscilloscope. The cavity mode is found by sweeping the synthesizer, setting the AFG for continuous 30 MHz output, and using a long TTL pulse to run the pulsed 1 Watt amp. The mode is optimized by minimizing the reflected power by adjusting the cavity mirror position.

laser off spectrum can be acquired. A schematic of this technique is illustrated in Figure 5.2, where a measurement consists of subtracting the laser on and laser off spectra for every valve shot as the laser scans. The coherence method has advantages for absorption features that are significantly broadened because there is cancellation of the transitions that come from the upper or lower rotational levels using the ground state depletion technique. This aspect was demonstrated in the previous chapter for the propyne-NH<sub>3</sub> complex.

#### A. Background Free Ground State Depletion

Although the dual gate coherence method is an improvement, overall the coherence method is much less sensitive than the ground state method (factor of ~5) and so techniques that are background free and have excitation similar to the ground state depletion method would be preferred. To achieve background-free laser detection, methods that employ a  $\pi/2$  MW pulse - laser pulse -  $-\pi/2$  MW pulse sequence have been developed. The first step is to maximize the ground state signal; for this, a 500 ns MW pulse is used and the MW power is varied to achieve optimal excitation with the cavity mode set exactly on resonance to the frequency of the rotational transition of interest. The next step takes full advantage of the capabilities of the AFG, and consists of turning on the second pulse which is delayed from the first MW pulse by 60 ns. The phase and amplitude of the second pulse are iteratively adjusted to eliminate the FID signal created by first pulse.

Cancellation of the first FID in theory can either be achieved using a second  $\pi/2$  or  $-\pi/2$  pulse. However, in practice only a  $-\pi/2$  pulse works effectively because rotational

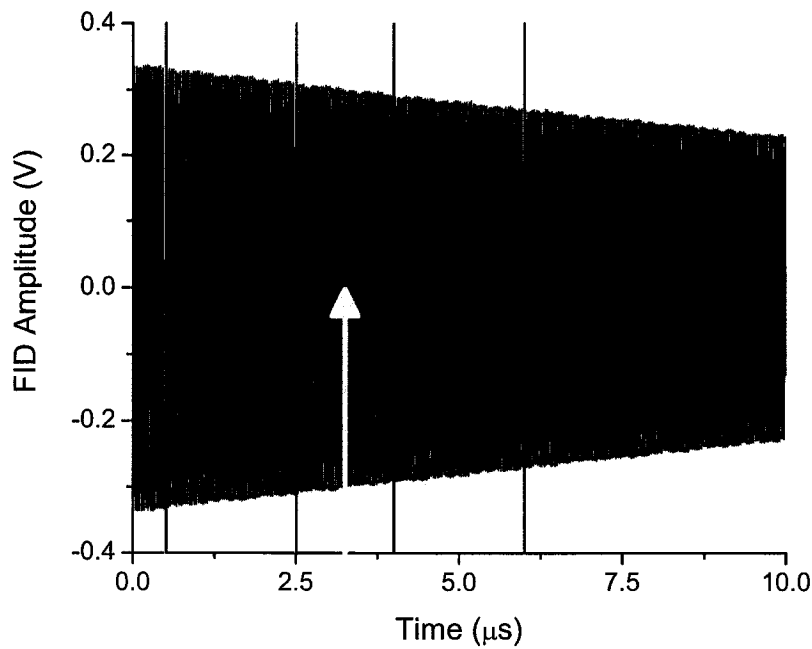


**Figure 5.2.** The above FID illustrates the two gate positions used for the dual gate coherence method. The first gate (between red lines) and second gate (between green lines) are windowed and Fourier transformed. The amplitude of the FT of gate 1 is subtracted from amplitude of the FT of the second gate. Due to the decay of the FID the amplitude the FT of the second gate is multiplied by a constant to obtain a signal near 0 mV. The timing of the laser pulse is illustrated using the arrow (yellow). When the laser is resonant there is only modulation of the FID to the second gate.

transitions are not perfect two level systems due to the M-dependence of the transition moment. This effect is illustrated in Figure 5.3, in which the signal resulting from the first  $\pi/2$  pulse is shown along with cancellation using a  $-\pi/2$  and  $\pi/2$  pulse. The  $-\pi/2$  pulse achieves a signal cancellation of 120:1 which is 14,400:1 cancellation in power. Figure 5.4 illustrates that there are no recurrences occurring to the FID at times up to 100  $\mu$ s.

The  $-\pi/2$  pulse effectively creates a FID 180 degrees out of phase with the first FID and the two destructively interfere. When the laser is resonant there is a 180 degree phase shift to the first FID which causes the two FIDs constructively interfere. The direction of the phase shift induced by the laser depends on which pure rotational level the laser is resonant with and is thereby a phase sensitive measurement. Similar to the GSD technique this Double Pulse-GSD (DP-GSD) method has bi-directional signals indicating which pure rotational level is resonant with the laser.

The DP-GSD mechanism can also be described using a Bloch vector model.<sup>24</sup> Figure 5.5 illustrates the Bloch model which shows the initial conditions and the effect of  $\pi/2$  pulse and a  $-\pi/2$  pulse. The Bloch vector points down initially because there is greater population in the lower rotational level. The  $\pi/2$  pulse removes the population difference and sets up coherence in the x-y plane. The application of a  $-\pi/2$  pulse rotates the Bloch vector down back to the initial conditions. Also shown in Figure 5.5 are the changes to the Bloch model when the laser is resonant with either the lower or upper rotational level.

As stated above DP-GSD is a phase sensitive measurement, and typically the

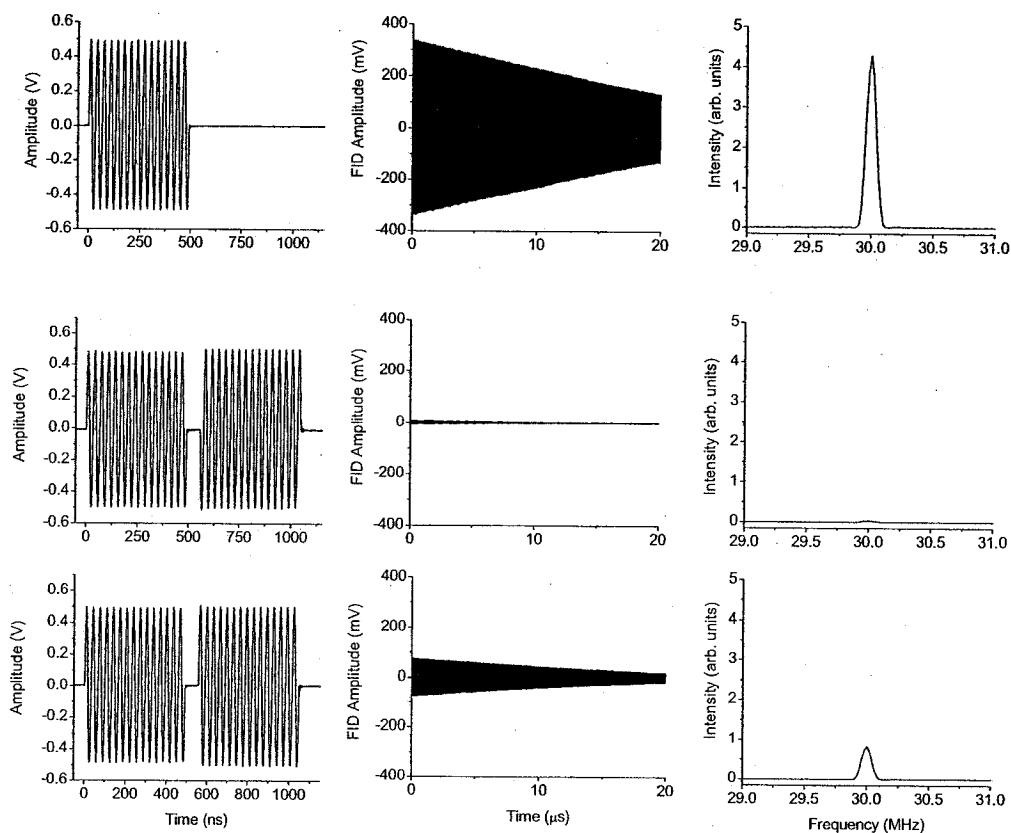


**Figure 5.3.** The above plots illustrate the output pulse(s) from the AFG (left column), the molecular rotational FID of phenylacetylene (middle column), and the Fourier transform (right column). The application of a single  $\pi/2$  pulse (top row),  $\pi/2 - -\pi/2$  pulse sequence (middle row), and  $\pi/2 - \pi/2$  pulse sequence (bottom row) are also illustrated.

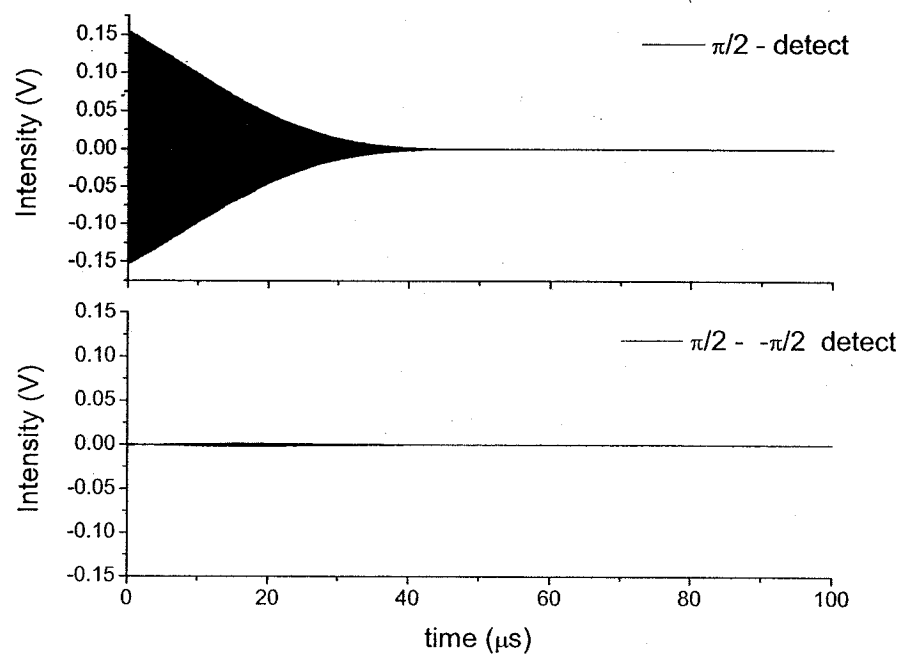


**Figure 5.4.** The above plots illustrate the rotational FID for normal single  $\pi/2$  pulse (top) and  $\pi/2$  -  $-\pi/2$  pulse sequence (bottom).

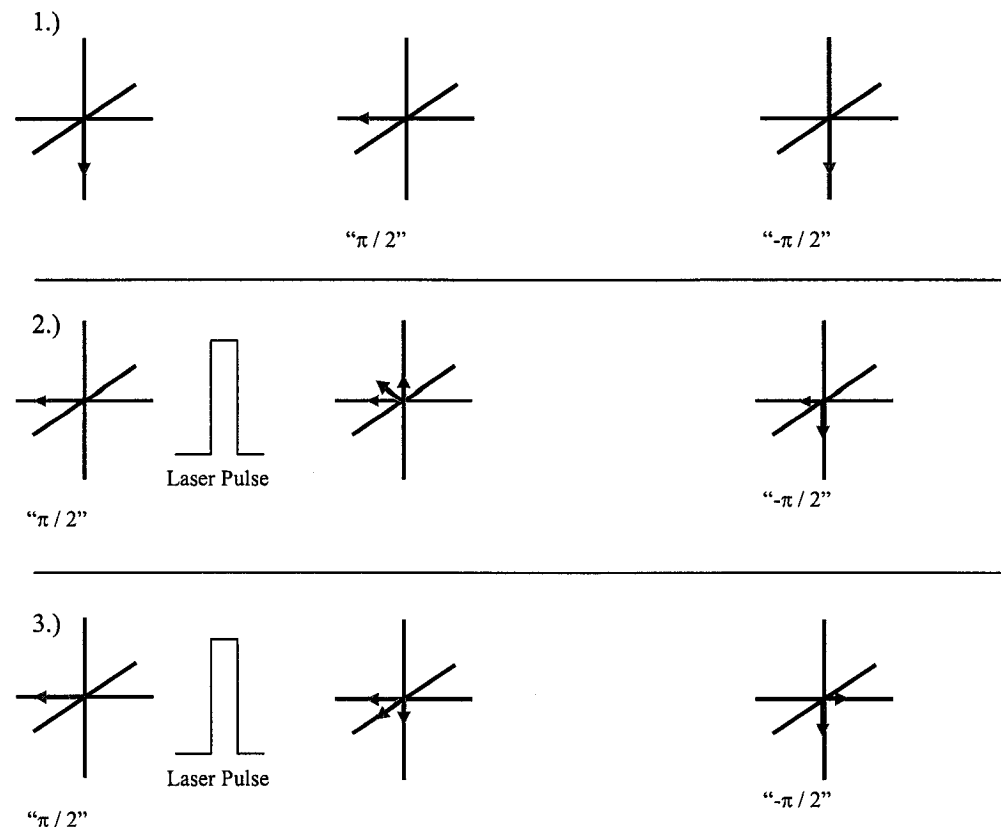


**Figure 5.5.** The above figures are used to illustrate the Bloch vector model at various points in the excitation scheme used in the DP-GSD technique. In panel one the Bloch vector (red) is shown for the initial conditions, then excitation using a  $\pi/2$  pulse brings the Bloch vector into the X-Y plane where the signal is detected, and a  $-\pi/2$  pulse brings the Bloch vector back out of the X-Y plane and no signal is detected. The second panel (2.) illustrates the effect resonant laser excitation on the Bloch vector after initial  $\pi/2$  excitation. The laser is resonant with the lower rotational level and therefore creates a positive population difference. The projection of the Bloch vector is shown for the X-Y plane and Z axis (green). After application of the  $-\pi/2$  pulse the projection onto the X-Y axis is rotated down and the laser induced population difference is rotated into the X-Y plane and detected. Therefore, only the laser induced effect is observed. Panel three illustrates this effect when the laser is resonant with the upper rotational level. The difference is in the sign of the laser induced population and gives rise to a signal 180 degrees out of phase from 2.).

magnitude Fourier transform (FT) is applied to the FID and the peak height of the monitored rotational transition is plotted versus the laser frequency. For DP-GSD the magnitude FT removes the phase information, and the laser induced signals are not bi-directional. To observe bi-directional signals it is necessary to use the phase information contained in the FID. This is achieved by storing the rotational FID for every step of the laser frequency. Because the molecular frequency is always at 30 MHz a modest sampling rate is required (250 – 500 Ms/s typical) to minimize the record length and ensures the spectrometer acquires data at the 10 Hz repetition rate of the laser. Figures 5.6 and 5.7 illustrate the phase change of the FID induced by the laser of the  $4_{04} - 3_{03}$  pure rotational transition of phenylacetylene<sup>19</sup> for electronic excitation of the  $0_0^0 + 492 \text{ cm}^{-1}$  band. In particular, Figure 5.7 illustrates the phase change across resonance as the laser scans.

During data acquisition the magnitude FT is applied to actively determine the location of the laser resonance. Once the spectrum is acquired an index is created to match each FID file with the appropriate laser frequency. The files are worked up offline and each FID is Fourier transformed using a real, imaginary, and magnitude FT and the peak height at 30 MHz is plotted versus laser frequency for all three FTs. Because the absolute phase of the FID varies from day-to-day it is necessary to adjust the phase angle to insure the phase is properly set. The technique allows for measuring the susceptibility of the laser transition because the real (dispersion) and imaginary (absorption) spectra are observed. Additionally, the phase of the FID can be plotted versus laser frequency. An

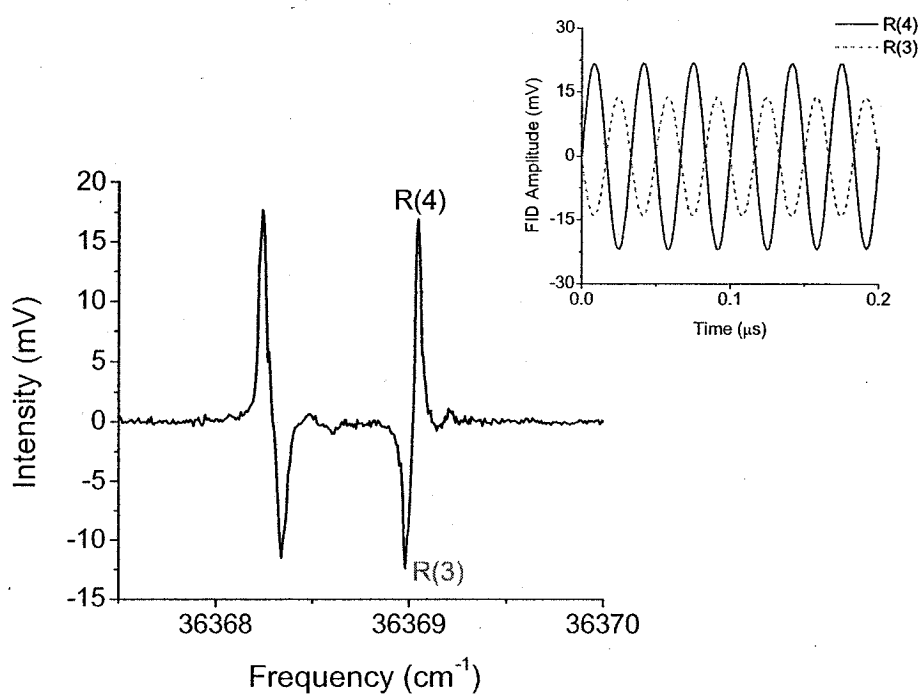


**Figure 5.6.** The DP-GSD spectrum of phenylacetylene for the electronic  $0_0^0 + 492 \text{ cm}^{-1}$  band is illustrated. The  $4_{04} - 3_{03}$  pure rotational transition at 10758.9550 MHz was monitored. The scan rate was  $10 \text{ cm}^{-1}/\text{hour}$  using 20 averages. Also illustrated (top inset) are the FIDs measured when the laser was resonant with the R(3) and R(4) transitions respectively.

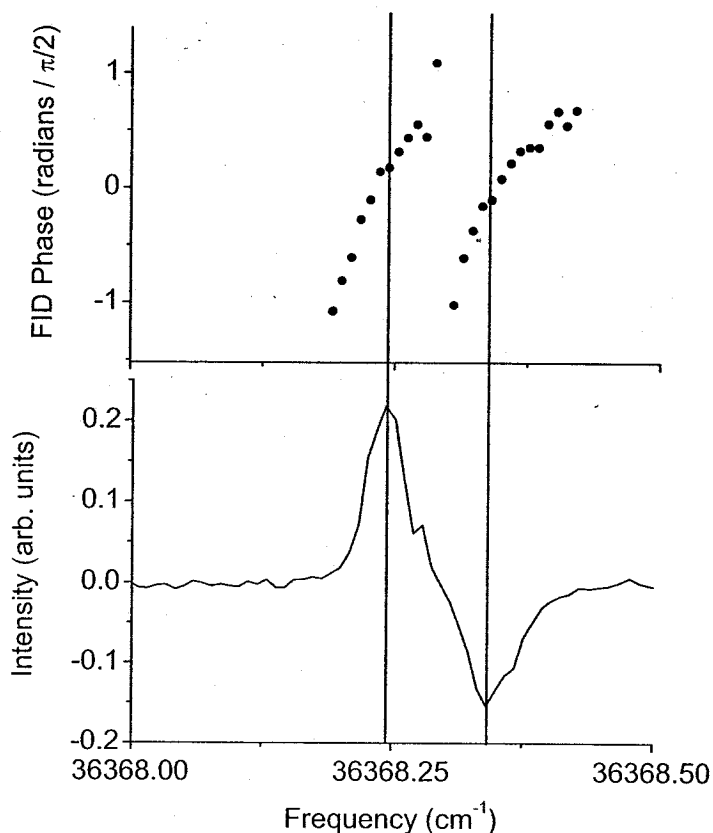


**Figure 5.7.** The above plots illustrate a zoom in on the P(4) and P(3) transitions of the rotationally resolved electronic spectrum of phenylacetylene shown in the previous figure. The top panel illustrates the phase of the FID as the laser scans through the resonances.

illustration of the magnitude, real, and imaginary spectra are shown in Figure 5.8 for propyne at the acetylenic C-H stretch fundamental.<sup>25</sup>

## Results

The sensitivity enhancement of the DP-GSD over the GSD technique is estimated to be a factor of ~10. A comparison of the DP-GSD and GSD methods for measuring the electronic spectrum of  $0_0^0 + 492 \text{ cm}^{-1}$  band of phenylacetylene is shown in Figure 5.9. A comparison of the dual gate coherence, GSD, and DP-GSD methods is illustrated for the electronic spectrum of the  $6a_0^1$  band of pyridine in Figure 5.10. The electronic spectrum of pyridine is broadened because of fast energy flow dynamics.<sup>18</sup>

### B. Electronic Spectrum of para-Methoxyphenethylamine

A significantly challenging system to test the sensitivity of the DP-GSD technique is para-methoxyphenethylamine (pMPEA). The recommendation for this molecule came from collaboration with the Pratt group in Pittsburgh. This molecule has 7 conformers which are shown in Figure 5.11 and is further complicated by nitrogen quadrupole coupling. This molecule also has a fairly high boiling point and requires heating of the sample (50°C) using a reservoir nozzle.<sup>5</sup> The high resolution electronic spectrum has previously been measured for pMPEA and serves as a starting point for this work.<sup>8</sup> The rotational spectrum of pMPEA was recorded using the methods described in Chapter 10. The rotational constants obtained from the high resolution UV experiment were used to assign all seven conformers observed in the pure rotational spectrum.

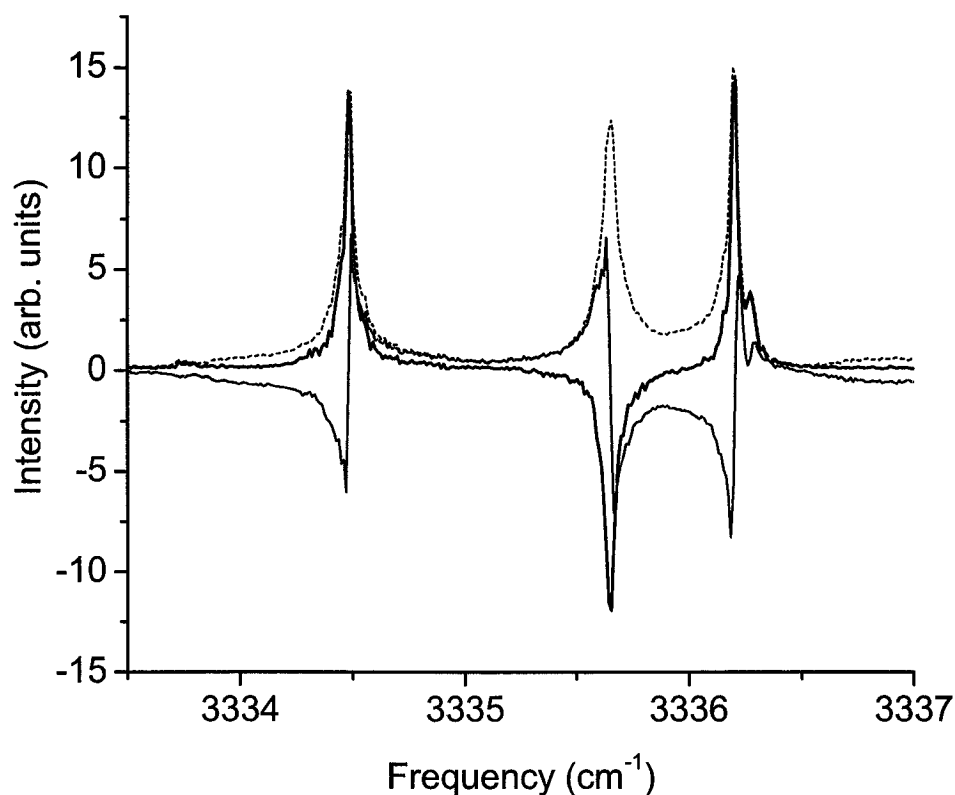


**Figure 5.8.** The above plot illustrates the magnitude (blue), real (dispersion red), and imaginary (absorption black) spectra for propyne at the acetylenic C-H stretch fundamental. The spectra were acquired monitoring the  $J=1 \leftarrow 0$  rotational transition at 17091.7434 MHz using a scan rate of  $10 \text{ cm}^{-1}/\text{hour}$  and 20 averages.

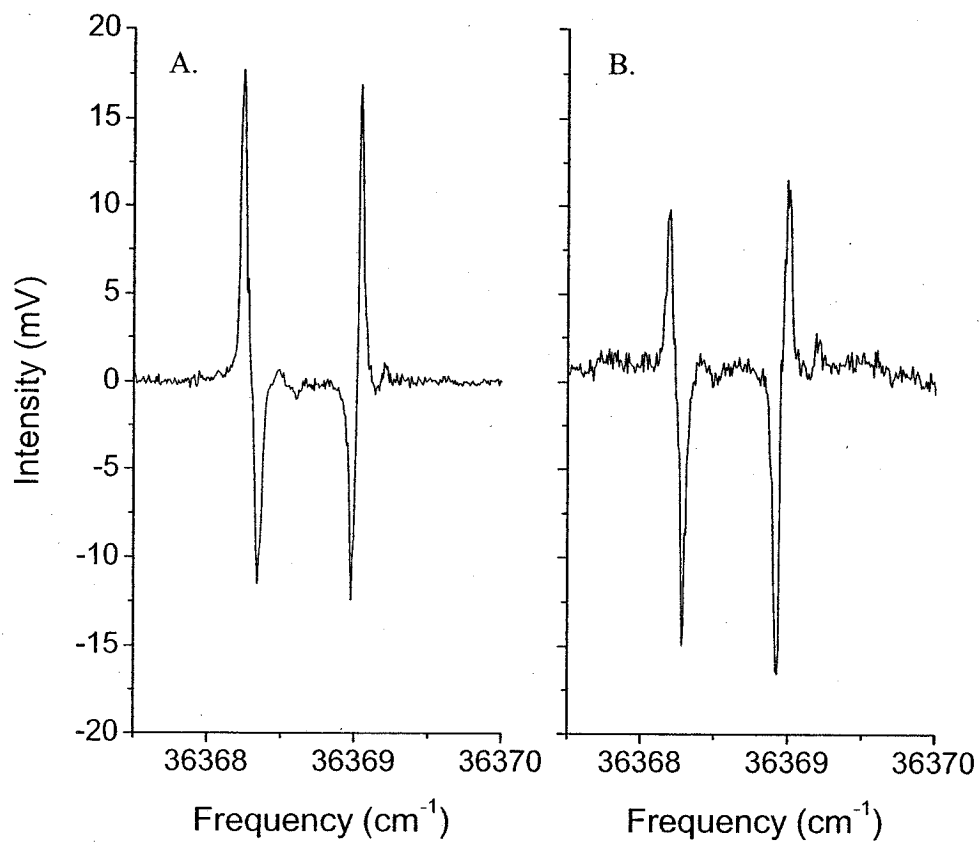


**Figure 5.9.** The DP-GSD spectrum (A.) and the GSD spectrum (B.) are illustrated for phenylacetylene for the electronic spectrum of the  $0_0^0 + 492 \text{ cm}^{-1}$  band. The spectra were acquired using a scan rate of  $10 \text{ cm}^{-1}/\text{hour}$  and 20 averages. The  $4_{04} - 3_{03}$  pure rotational transition at  $10758.9550 \text{ MHz}$  was monitored for both methods.

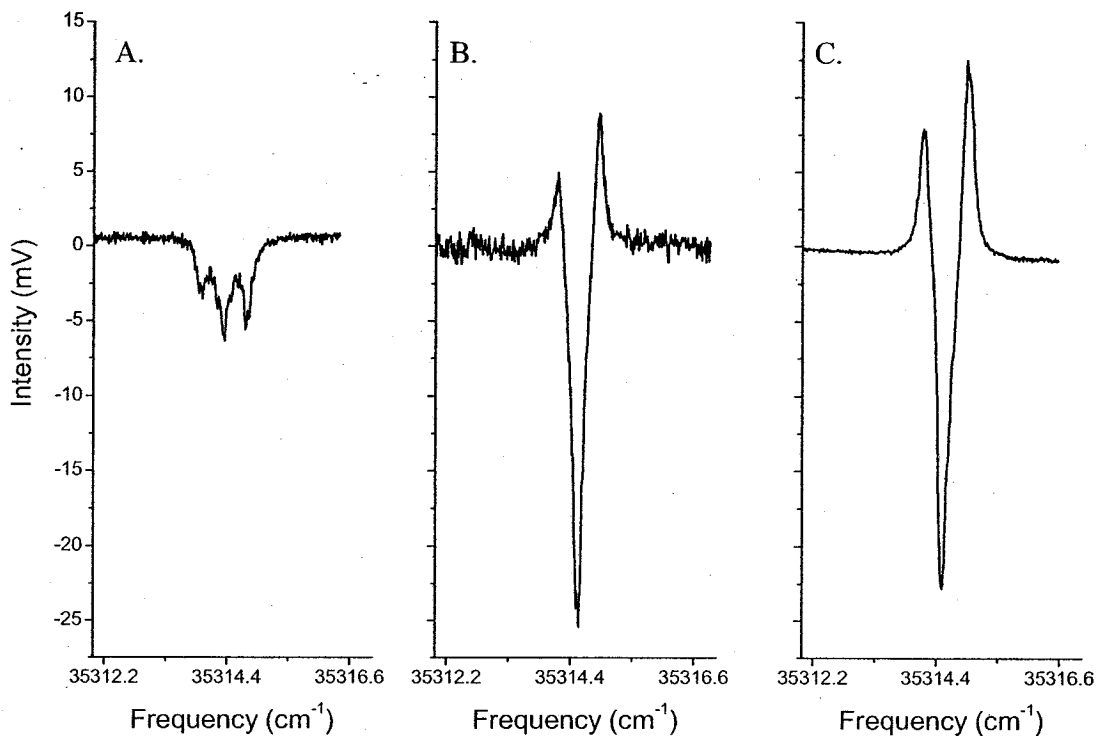


**Figure 5.10.** The electronic spectrum of pyridine is illustrated for the  $6a_0^1$  band using the internally referenced coherence (A.), GSD (B.), and DP-GSD (C.) methods. All three spectra were acquired using a scan rate of  $10 \text{ cm}^{-1}/\text{hour}$  and 20 averages. The  $2_{023}-1_{012}$  ( $J_{K_a K_c F}$ ) pure rotational transition of pyridine was monitored at 14092.9499 MHz.

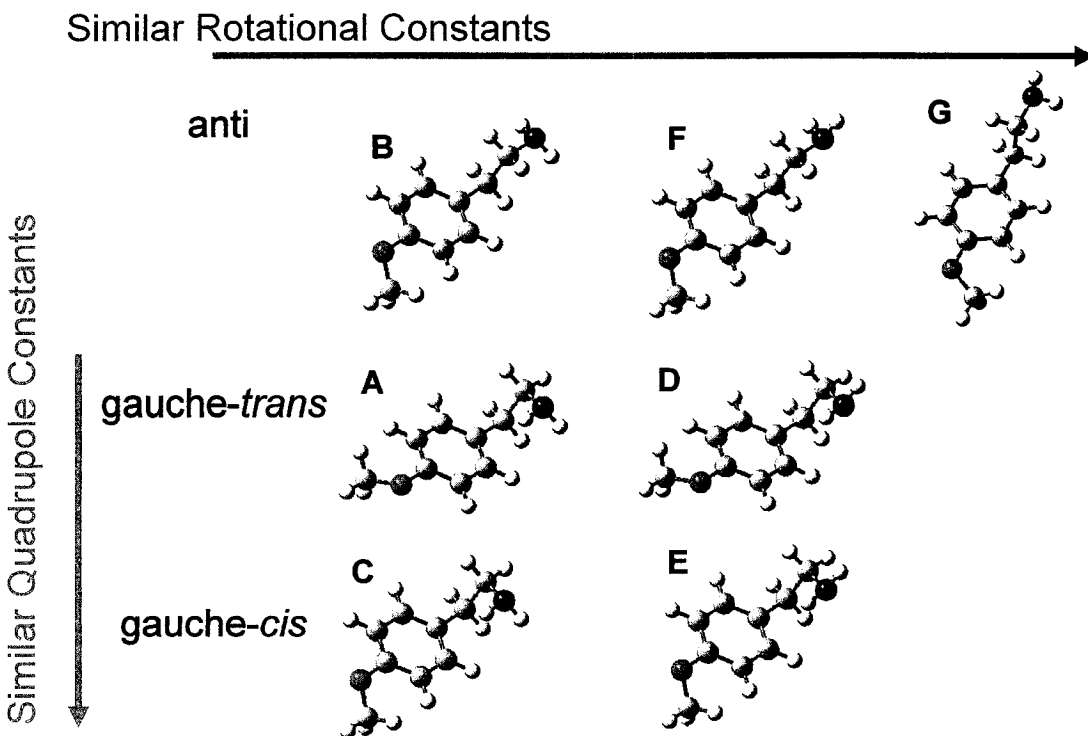


**Figure 5.11.** The above figure illustrates the seven lowest energy conformers of para-methoxyphenethylamine (pMPEA). The energy ordering from lowest to highest, E, D, C, A, B, F, and G.<sup>5</sup>

The S<sub>0</sub>-S<sub>1</sub> band origin electronic spectrum for each conformer of pMPEA is illustrated in Figures 5.12 and 5.13. For six of the seven conformers scan rates of 10 cm<sup>-1</sup>/hour were used with 20 averages per step. For the weakest conformer (F) a scan rate of 3.6 cm<sup>-1</sup>/hour was used with 100 averages per step. The results of experiments of pMPEA shown here support those previously determined by Yi et al.<sup>8</sup>

### Conclusions

The background-free DP-GSD method has been developed and offers roughly a factor of 10 improvement to the signal-to-noise of the IR-FTMW double resonance spectra. The new method has been extended to electronic spectroscopy, and further demonstrates the wide range of systems capable of being studied using laser-FTMW double resonance spectroscopy. The demonstration that all seven conformers of pMPEA could be measured using the DP-GSD technique with signal-to-noise comparable to other UV double resonance methods is a significant achievement.<sup>26-28</sup> The DP-GSD method should also have significant advantages for studying systems created using ablation or other novel sources because the shot-to-shot fluctuations have largely been eliminated.

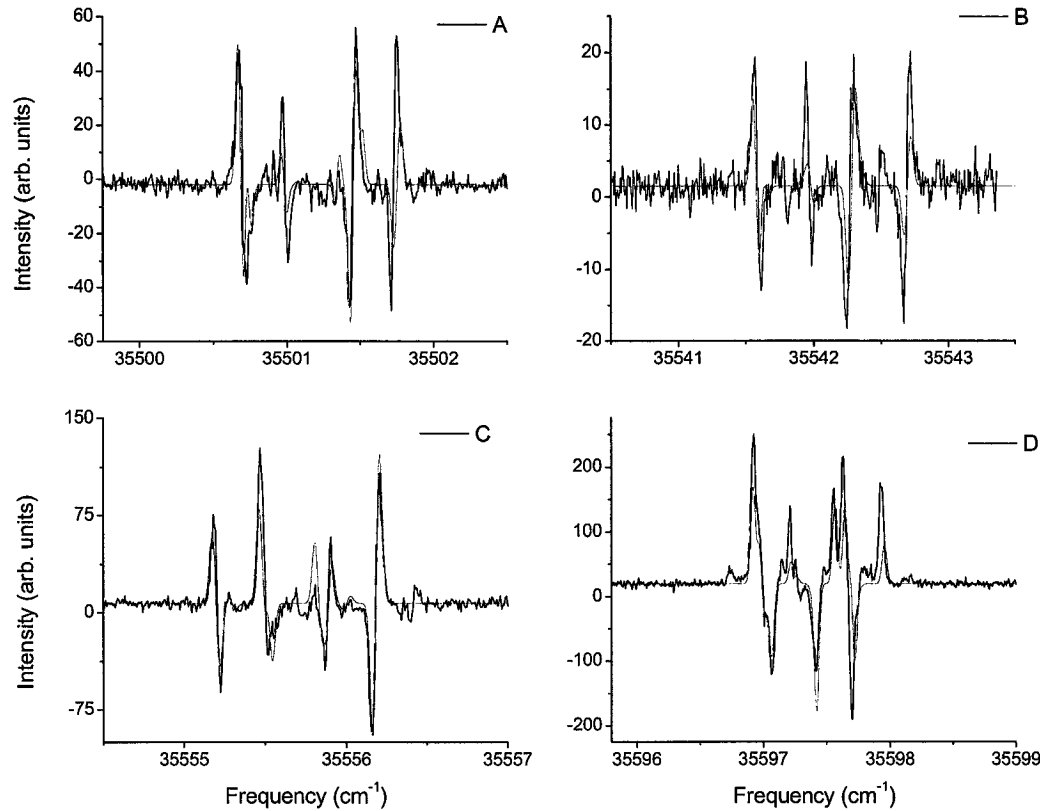


**Figure 5.12.** The electronic spectrum measured at the band origin of the  $S_0$ - $S_1$  transition is illustrated above for different conformers of pMPEA (A-D black). Also shown is the band contour (red) generated using the high resolution rotational constants from Yi et al. The different transitions monitored are  $11_{111}12 - 10_{110}11$  at 11342.1045 MHz conformer A,  $12_{112}13 - 11_{111}12$  at 10443.0978 MHz conformer B,  $10_{19}11 - 9_{18}10$  at 10652.8987 MHz conformer C, and  $10_{110}10 - 9_{09}9$  at 12041.0426 MHz conformer D. The quantum numbers are labeled using  $J'_{K_a'K_c'}F' - J''_{K_a''K_c''}F''$  notation. All four spectra shown were acquired using a scan rate of  $10 \text{ cm}^{-1}/\text{hour}$  and 20 averages.

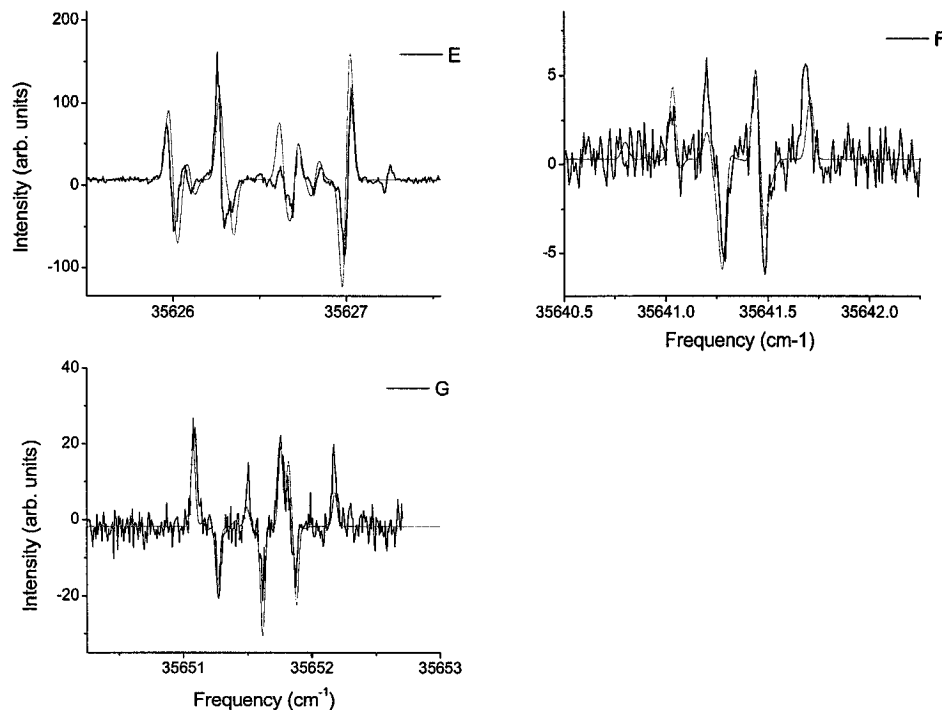


**Figure 5.13.** The electronic spectrum measured at the band origin of the S<sub>0</sub>-S<sub>1</sub> transition is illustrated above for different conformers of pMPEA (E-F black). Also shown is the band contour (red) generated using the high resolution rotational constants from Yi et al. The different transitions monitored are 10<sub>19</sub>11 – 9<sub>18</sub>10 at 10728.6091 MHz conformer E, 8<sub>17</sub>8 – 7<sub>0</sub>7 at 10854.6163 MHz conformer F, and 11<sub>11</sub>111 – 10<sub>0</sub>1010 at 12078.3415 MHz conformer G. The quantum numbers are labeled using J'K<sub>a</sub>'K<sub>c</sub>'F' - J''K<sub>a</sub>''K<sub>c</sub>''F'' notation. The spectra of conformers E and G were acquired using a scan rate of 10 cm<sup>-1</sup>/hour and 20 averages and the spectra of conformer F was acquired using a scan rate of 3.6 cm<sup>-1</sup> and 100 averages.

## Reference List

1. Lehmann, K. K.; Coy, S. L., *J.Chem.Phys.* **1984**, *81*, 3744-3745.
2. Coy, S. L.; Lehmann, K. K., *J.Chem.Phys.* **1986**, *84*, 5239-5249.
3. Lehmann, K. K.; Coy, S. L., *J.Chem.Soc.Faraday Trans.2* **1988**, *84*, 1389-1406.
4. Nakajima, M.; Sumiyoshi, Y.; Endo, Y., *Rev.Sci.Instrum.* **2002**, *73*, 165-171.
5. Arunan, E.; Dev.S.; Mandal, P. K., *Appl.Spectrosc.Rev.* **2004**, *39*, 131-181.
6. Dian, B. C.; Clarkson, J. R.; Zwier, T. S., *Science* **2004**, *303*, 1169-1173.
7. Chin, W.; Piuzzi, F.; Dimicoli, I.; Mons, M., *Phys.Chem.Chem.Phys.* **2006**, *8*, 1033-1048.
8. Yi, J. T.; Robertson, E. G.; Pratt, D. W., *Phys.Chem.Chem.Phys.* **2002**, *4*, 5244-4248.
9. Remmers, K.; Meerts, W. L.; Ozier, I., *J.Chem.Phys.* **2000**, *112*, 10890-10894.
10. Martinez III, S. J.; Alfano, J. C.; Levy, D. H., *J.Mol.Spectrosc.* **1993**, *158*, 82.
11. Unamuno, I.; Fernandez, J. A.; Longarte, A.; Castaño, F., *J.Phys.Chem.A* **2000**, *104*, 4364.
12. Robertson, E. G.; Simons, J. P.; Mons, M., *J.Phys.Chem.A* **2001**, *105*, 9990.
13. Fernandez, J. A.; Unamuno, I.; Castaño, F., *J.Phys.Chem.A* **2001**, *105*, 9993.
14. King, G. W.; So, S. P., *J.Mol.Spectrosc.* **1970**, *33*, 376-378.
15. King, G. W.; So, S. P., *J.Mol.Spectrosc.* **1971**, *37*, 543-570.
16. Powers, D. E.; Hopkins, J. B.; Smalley, R. E., *J.Chem.Phys.* **1981**, *59*, 5971.
17. Ribblett, J. W.; Borst, D. R.; Pratt, D. W., *J.Chem.Phys.* **1999**, *111*, 8454-8460.
18. Villa, E.; Amirav, A.; Lim, E. C., *J.Phys.Chem.* **1988**, *92*, 5393-5397.
19. Cox, A. P.; Ewart, I. C.; Stigliani, W. M., *J.Chem.Soc.Faraday Trans.* **1975**, *7*, 504.
20. Mata, F.; Quintana, M. I., *J.Mol.Spectrosc.* **1977**, *42*, 1-5.

21. Ye, E.; Bettens, R. P. A.; De Lucia, F. C.; Petkie, D. T.; Albert, S., *J.Mol.Spectrosc.* **2005**, 232, 61-65.
22. Balle, T. J.; Flygare, W. H., *Rev.Sci.Instrum.* **1981**, 52, 33-44.
23. Suenram, R. D.; Grabow, J. U.; Zupan, A.; Leonov, I., *Rev.Sci.Instrum.* **1999**, 70, 2127-2135.
24. Günther, H. *NMR spectroscopy : basic principles, concepts, and applications in chemistry*; Wiley: New York, 1995
25. Kerstel, E. R. Th.; Lehmann, K. K.; Pate, B. H.; Scoles, G., *J.Chem.Phys.* **1994**, 100, 2588-2595.
26. Berden, G.; Meerts, W. L.; Kreiner, W., *Chem.Phys.* **1993**, 174, 247-253.
27. Lipert, R. J.; Colson, S. D., *Chem.Phys.Lett.* **1989**, 161, 303.
28. Dian, B. C.; Longarte, A.; Winter, P. R.; Zwier, T. S., *J.Chem.Phys.* **2004**, 120, 133-147.

## Chapter 6

### Techniques for Dynamics Rotational Spectroscopy

#### Introduction

The application of Fourier transform microwave spectroscopy to the study of the rotational spectra of vibrationally excited states is described. Hitherto, rotational spectroscopy of excited vibrational states has been dominated by saturation spectroscopy techniques employing high-resolution cw lasers.<sup>1-3</sup> These techniques provide high sensitivity when it is possible to saturate the ro-vibrational transition pumped by the laser. High sensitivity is crucial for DRS because the transition strength between individual molecular eigenstates that make up the overall lineshape is diluted by spectral fragmentation.<sup>1;2;4</sup> However, saturation-based techniques face severe limitations for applications in DRS.

The key difficulty is that fast intramolecular dynamics cause fragmentation of the oscillator strength in the vibrational spectrum.<sup>5</sup> As the dynamics become faster, or the molecule becomes larger, the infrared transition strength to a single molecular eigenstate is reduced making it increasingly difficult to saturate the rovibrational transition. Because pulsed lasers offer higher peak power and broader tunability than cw lasers, an experimental technique built around FTMW spectroscopy has clear advantages for the development of DRS. Additionally, for small molecules, the application of infrared-FTMW double-resonance spectroscopy can be used to determine the rotational constants of the vibrational excited state to a higher precision than is typically possible from infrared spectroscopy.<sup>3</sup>

### A. IR-FTMW-cwMW Triple Resonance

The measurement strategy employed is similar to the approach that uses saturation spectroscopy.<sup>6</sup> In this IR-MW-MW triple-resonance approach, the single-eigenstate rotational spectrum is measured through the Autler-Townes splitting (or AC Stark effect).<sup>7</sup> To obtain the spectrum, the Autler-Townes splitting of the eigenstate must be probed. FTMW spectroscopy is used to probe the transition in the excited state. The basic measurement principles are illustrated for propyne excited to the fundamental of the acetylenic C-H stretch. These principles are extended to 3-fluoropropyne in which further analysis is described. The measurements reported for fluoropropyne show how the technique can be used to determine transition strengths, the  $\Delta J$  selection rules, and the relative energy ordering of the rotational levels of the transition. These capabilities are derived from the Autler-Townes effect which provides the mechanism for the technique. Both propyne and fluoropropyne are small polyatomic molecules that do not exhibit complex dynamics and therefore serve as a demonstration and also illustrate the information available by performing IR-FTMW-cwMW triple resonance spectroscopy.

### Experimental

The FTMW spectrometer used in the experiment is based on the design by NIST<sup>8</sup> which is described in chapter 2. Initially the spectrometer was constructed with a slower vacuum system and had the multipass optics placed 9 cm above the cavity centerline. The nozzle was placed directly above the multipass (12.5 cm above the cavity axis) for excitation in the region of high molecular density before the molecules begin to spread

out in the radial direction. To prevent rotation relaxation these experiments were performed at a 1 Hz repetition rate.

The MW pump radiation that creates the Autler-Townes splitting is generated using an active frequency doubler (DBS Microwave) that is connected directly to the gain horn inside the FTMW spectrometer. The frequency doubler provides 110 mW (+20.4 dBm) of power at the propyne  $2_0 - 1_0$  transition frequency in the vibrationally excited state (34102.72(2) MHz). This technique is referred to as IR-FTMW-cwMW spectroscopy because the second MW pump source is continuous-wave. The horn is setup in a 20 cm side arm of the chamber perpendicular to the cavity. The horn is mounted to be centered on the cavity axis and is placed as close as possible to the beam waist without causing distortion of the cavity mode. The horn is fixed to a 15.2 cm translation stage which is used for maximizing the resonance and minimizing cavity mode distortion and power pick-up. All light sources are polarized in the same direction for the experiment ( $\Delta M = 0$  selection rules for all transitions).

The important design issue for this experiment is the coupling of the laser to the FTMW spectrometer. Because vibrational excitation occurs above the cavity center line the pulse timing is arranged so that the laser firing can be moved in time relative to the FTMW pulse sequence (valve pulse, polarizing MW-pulse, and FID acquisition). This timing is used to optimize the number of molecules excited in the free jet expansion and also accounts for the ‘drift’ time into the FTMW cavity. The FTMW pulse sequence is initially optimized on a ground state signal leaving the laser firing time the final variable. The optimized timing sequence is depicted in Figure 6.1. After the valve pulse is fired

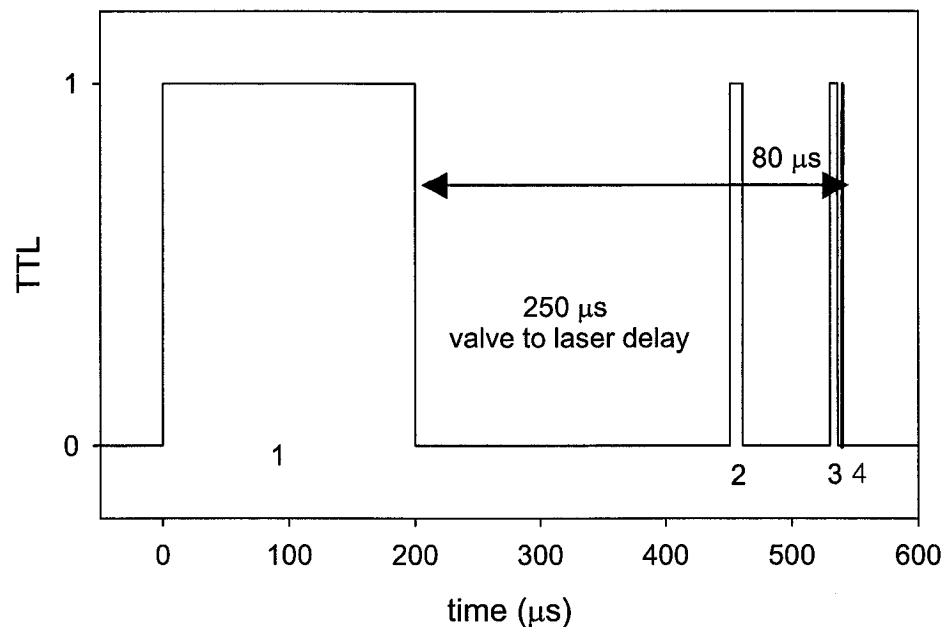


**Figure 6.1** The IR-FTMW Double Resonance timing sequence is displayed above. The valve pulse (1) has a 200  $\mu\text{s}$  duration. The laser pulse (2) is delayed 250  $\mu\text{s}$  from the falling edge of the valve pulse. The FTMW cavity pulse (3) duration is 6  $\mu\text{s}$  and is delayed from the laser pulse by 80  $\mu\text{s}$ . After the FTMW cavity pulse is fired a time of 4  $\mu\text{s}$  is elapsed until the data acquisition trigger pulse (4) is fired.

there is a narrow window of time in which the laser must fire to vibrationally excite the molecules. The timing accuracy of the laser pulse relative to the FTMW cavity pulse (i.e. delay of the cavity pulse from the laser pulse) must be within  $\sim \pm 3 \mu\text{s}$ . This timing is a critical step to getting this experiment to work and is largely dependent on nozzle position.

The IR-FTMW and IR-FTMW-cwMW spectra for fluoropropyne are obtained using the same general spectrometer setup and pulse timing as propyne. For the fluoropropyne experiment the 1 mm diameter pinhole nozzle was replaced with a 2.54 cm slit jet in order to provide greater overlap with the molecular beam. The 2.54 cm slit jet nozzle was made by adapting a modified General Valve Series 9 pulsed nozzle. This was done by bolting a pinhole nozzle (1 mm orifice) to a slit assembly 2.54 cm long and 0.01 mm wide. The slit jet design needed larger backing pressures (factor of 2-4) to obtain similar ground-state signals as compared to the pinhole nozzle.

The IR-FTMW-cwMW triple-resonance spectra of fluoropropyne are obtained by gating on the peak height of the IR-FTMW double-resonance signal in the frequency domain. The peak height is recorded as the cw MW frequency is scanned. A resonance is observed as a dip in the monitored excited state signal. These triple resonance signals are a result of the Autler-Townes splitting.<sup>7</sup> Similarly, FTMW-cwMW spectra are obtained without the laser excitation. The Autler-Townes technique and mechanism will be discussed for propyne.

## Results

### *Propyne*

The main purpose of the propyne experiment is to demonstrate an FTMW-based IR-MW-cwMW triple-resonance technique that can be applied to DRS measurements. In this context, the measurement goal is to obtain the rotational spectrum of the J=1 rotational level of propyne in the acetylenic C-H stretch excited state. The steps involved in the measurement are: 1) laser preparation of the J=0 rotational state through excitation of the P(1) rovibrational transition, 2) monitoring the J=1 rotational level in the excited state using FTMW spectroscopy, and 3) observing the rotational spectrum of J=1 through the Autler-Townes splitting when the applied MW pump radiation is resonant with a transition involving J=1.

The ability to monitor the rotational transition of a single vibrational eigenstate using FTMW spectroscopy is demonstrated in Figure 6.2, and the corresponding level diagram is illustrated in Figure 6.3. The pulsed infrared laser is used to prepare the vibrationally excited state  $0_0$  ( $J_K$ ) through P(1) for the acetylenic C-H stretch of propyne at  $3331.51\text{ cm}^{-1}$ . The excited state  $1_0 - 0_0$  rotational transition is observed at  $17051.41(1)\text{ MHz.}$

The rotational transition frequency in the excited state was initially estimated using the constants reported in a previous high-resolution infrared spectroscopy study of the acetylenic C-H stretch fundamental ( $17\ 051.84(26)\text{ MHz.}$ ).<sup>9</sup> The spectrum is obtained in a single molecular-beam pulse. Excellent sensitivity is achieved. Once the laser is allowed to stabilize on the P(1) transition (about 20 min), the excited state transition can be

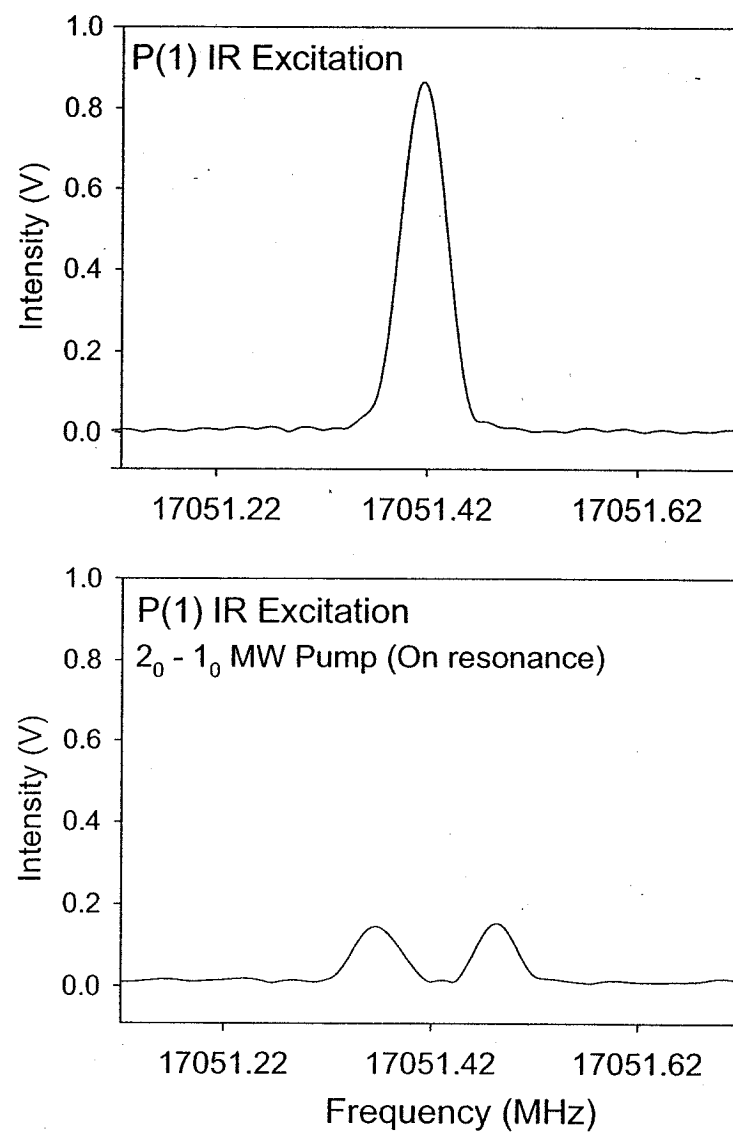


**Figure 6.2.** The  $1_0 - 0_0$  rotational transition in the acetylenic C–H stretch of propyne measured by FTMW spectroscopy is shown in the top panel. The Autler–Townes splitting of the  $1_0$  rotational level caused by microwave radiation resonant with the  $2_0 - 1_0$  excited state transition is shown in the bottom panel.

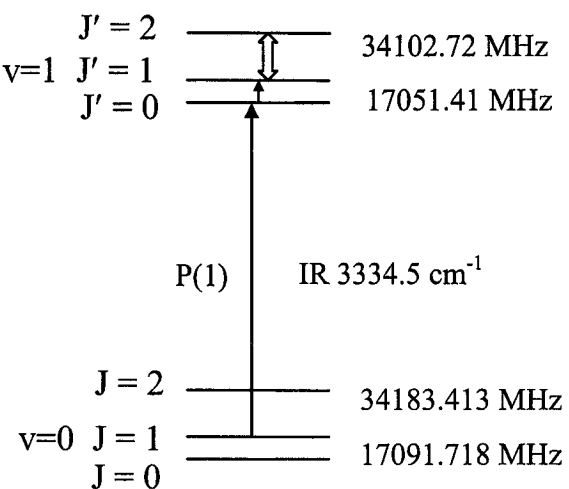


**Figure 6.3.** A level diagram for the propyne IR-FTMW-MW triple resonance measurement in Fig. 4.2 is shown. Laser excitation of the P(1) transition at  $3334.5 \text{ cm}^{-1}$  populates the  $J = 0$  state of the acetylenic C–H stretch excited state. The  $J=1 \leftarrow 0$  rotational level is probed by monitoring the  $1_0 \rightarrow 0_0$  rotational transition in the vibrational excited state at  $17051.41(1) \text{ MHz}$  using the FTMW spectrometer. The Autler–Townes splitting of the  $1_0$  level is produced by applying cw MW radiation resonant with the  $2_0 \rightarrow 1_0$  excited state rotational transition at  $34102.72(2) \text{ MHz}$ .

measured for times longer than 2 hours without adjusting the laser frequency. The excited state signal fluctuates by ~30% on a shot-to-shot basis and is dominated by pulse-to-pulse intensity fluctuations of the laser.

For applications in DRS, the rotational spectrum of a single eigenstate includes many eigenstate-to-eigenstate transitions (~100 transitions for each eigenstate are observed for chlorobutyne<sup>4</sup>). The dynamical information is contained in the overall lineshape of the spectrum. Therefore, it is essential to be able to measure accurate transition intensities, with transition frequency accuracy being less important. Given the relatively large amplitude fluctuation of the excited state signal, a method to measure intensities that is based on the *frequency splitting* of the J=1 rotational level caused by the Autler-Townes effect is preferred. When the microwave pump radiation is resonant with a transition involving J=1 (here the  $2_0 - 1_0$  rotational transition in the excited vibrational state), the level is split by the Rabi frequency of the transition.<sup>6;7;10</sup> This splitting is illustrated in the bottom panel of Figure 6.2. We achieve a 240 kHz splitting with 110 mW of MW power coupled into the active volume with the standard gain horn.

If population effects are ignored, the total intensity of the two Autler-Townes components should equal the original signal strength. In Fig. 6.2 it is shown that the total signal strength in the presence of the pump radiation is only 1/3 the field-free value. This effect is likely caused by population transfer among the three coupled levels during the measurement. In this case, the Rabi cycling time (4.2  $\mu$ s) is on the order of the duration of the FTMW polarization pulse (6  $\mu$ s). A quantitative treatment of the three-level system excited using cw and pulsed microwave radiation<sup>11</sup> inside a cavity<sup>12</sup> would be required

to fully analyze these spectra. However, the key feature of interest in this report is the fact that clear Autler-Townes splittings are observed using the current spectrometer design.

One of the strengths of the Autler-Townes method for DRS is that it can be used to determine whether the rotational transition reaches a quantum state higher or lower in energy. Although this determination is trivial for "normal" rotational spectroscopy, like propyne, it is not so clear in cases of DRS where the rotational spectrum is broader than the energy separation between rotational levels.<sup>4</sup> Using the Autler-Townes technique, the direction of the transition can be decided by pumping the rotational transition off-resonance. This idea has been used before in pure rotational spectroscopy in the technique often called "double-resonance modulation (DRM)" spectroscopy.<sup>3;13;14</sup> Although the effect can be described using time-dependent quantum mechanics, the easiest approach to understanding these effects comes from a time-independent dressed state formalism. The dressed state formalism is illustrated in Figure 6.4 for the transitions in the propyne experiment.<sup>10</sup>

If the MW pump frequency is higher than the  $2_0 - 1_0$  resonance frequency, then an unequal intensity splitting is observed in the spectrum. The weaker feature from the avoided crossing of the two dressed states will appear at lower frequency when the transition occurs to a quantum state at higher energy. This weaker component of the Autler-Townes doublet is called the "creeper" in DRM spectroscopy because away from the crossing it closely tracks the applied pump frequency.

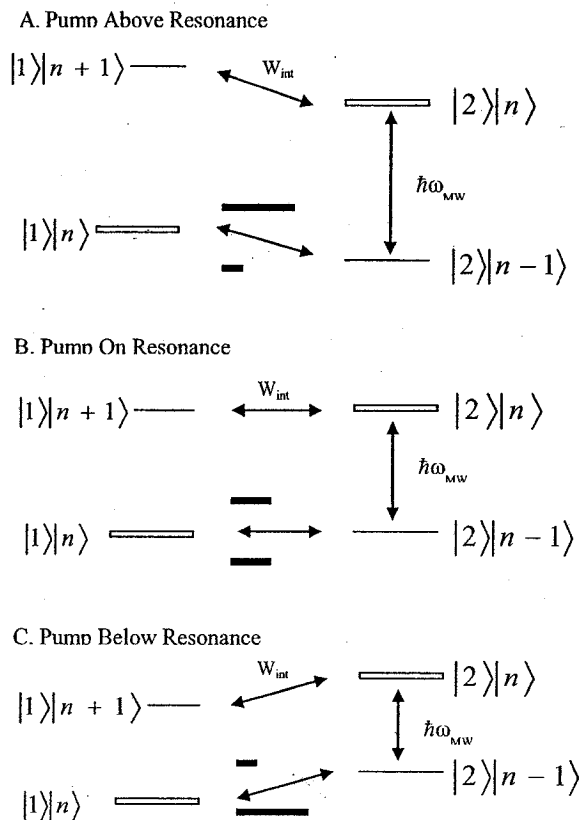


**Figure 6.4.** The Autler-Townes effect for off-resonant pumping of the propyne  $2_0-1_0$  rotational transition is illustrated using a dressed state approach. The dressed-state Hamiltonian is:  $H = (H_{\text{mol}} + H_{\text{light}}) + W_{\text{int}}$ . The basis states are taken to be direct products of the molecular and light eigenstates (harmonic oscillator). These are denoted  $|J\rangle|n\rangle$  in the figure ( $J$  is the total angular momentum quantum number). The sequence of dressed states for each molecular state (i.e.,  $|J\rangle|n-1\rangle, |J\rangle|n\rangle, |J\rangle|n+1\rangle, \dots$ ) are separated by the photon energy of the applied MW radiation.

In a rotating wave approximation, only the dressed states  $|J\rangle|n\rangle$  and  $|J+1\rangle|n-1\rangle$  are coupled through the light molecule interaction term:  $W_{\text{int}} = \frac{1}{2}(\mu \cdot E / \hbar)$ . This coupling just reflects the fact that there is an allowed  $J \rightarrow J+1$  rotational transition and that it occurs by removing a photon from the field ( $|n\rangle \rightarrow |n-1\rangle$  in the MW field quantum numbers). The spectrum observed by the  $J=0 - J=1$  probe transition can be obtained through diagonalizing the resulting near-resonant two-level system. For the probe transition, the  $|1\rangle|n\rangle$  dressed state provides the transition strength from the  $|0\rangle|n\rangle$  state since the probe transition does not affect the pump MW field ( $\Delta J=1, \Delta n=0$ ) selection rules for the probe transition.<sup>7</sup>

If the transition reaches a quantum state at lower energy, the creeper appears at higher frequency for pumping above resonance. The FTMW spectrum that monitors the J=1 level splitting through the  $1_0 - 0_0$  rotational transition is shown in Figure 6.5 as a function of the detuning of the pump radiation from resonance. The movement of the creeper through resonance confirms the obvious fact that the  $2_0$  rotational level lies above the  $1_0$  level in the excited state of propyne.

#### *Fluoropropyne*

The main goals of the fluoropropyne experiments are to demonstrate new techniques for obtaining the rotational spectrum of a vibrationally excited molecule. The basic FTMW-cwMW double-resonance technique is demonstrated through the measurement of the pure rotational spectrum of 3-fluoropropyne. The pure rotational spectra of 3-fluoropropyne and its  $^{13}\text{C}$  isotopomers have been previously measured using a conventional Stark spectrometer<sup>15</sup> making it possible to test the new double-resonance technique. The extension of the technique to vibrationally excited states is then demonstrated by measuring the same transitions in the first excited state of the acetylenic C-H stretch normal-mode.

#### *Pure Rotational Spectroscopy of 3-Fluoropropyne*

The pure rotational spectra for 3-fluoropropyne and its  $^{13}\text{C}$  isotopomers have been measured using FTMW spectroscopy and FTMW-cwMW double-resonance spectroscopy. Because 3-fluoropropyne is a small molecule, there are few rotational transitions in the frequency range of our FTMW spectrometer (8 – 18 GHz). Double-resonance spectroscopy provides a simple method to extend the frequency range for pure

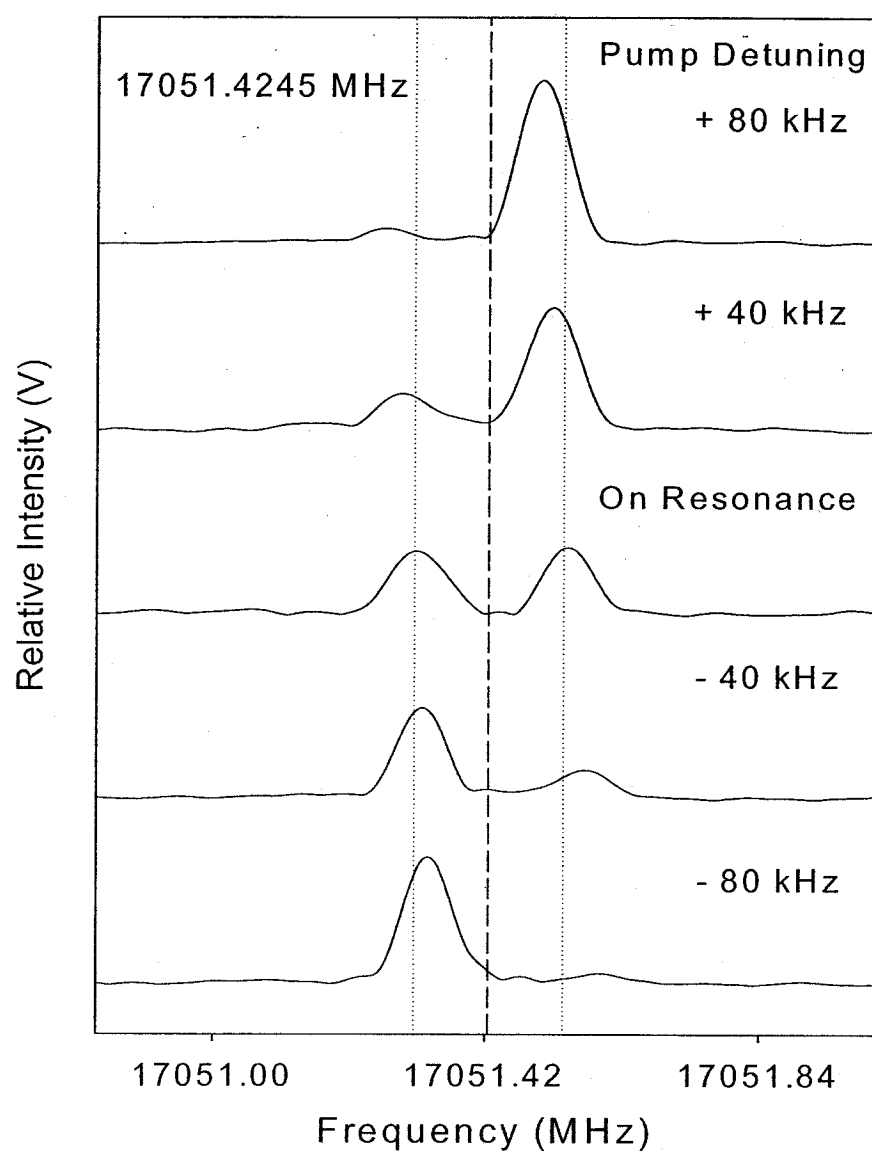


**Figure 6.5.** The variation of the Autler-Townes splitting of the  $1_0$  rotational level as a function of the MW pump radiation frequency is shown. The avoided crossing of the dressed states described in Figure 6.4 is observed in the FTMW probe spectrum.

rotational measurements. A list of measured rotational frequencies and the results of fitting to the Watson Hamiltonian in the  $I^r$  representation are given in Tables 6.1 and 6.2.

Two examples of double-resonance measurements are shown in Figures 6.6 and 6.7. In the measurements performed for this study, there have been no problems observed from the cw microwave source interfering with the FTMW signal. This lack of interference, which has been identified as a problem in other measurements,<sup>11;16</sup> is partly attributable to the fact that the frequencies used in the double-resonance measurements are above the high-frequency cut-off of the preamplifier used to amplify the FID emission signal. In this way, the detection components of the FTMW provide a good filter to the cw source.

A useful feature of the double-resonance measurements is that different lineshapes are obtained when the  $\Delta J = 1$  and  $\Delta J = 0$  rotational transitions are strongly pumped by the cw source (compare Figures 6.6 and 6.7). These differences are related to the underlying Autler-Townes effect mechanism of the double-resonance signal.<sup>7;17</sup> The spectrum in Fig. 6.6 is strongly power broadened. Narrower lineshapes that allow more precise determinations of the center frequency can be obtained by minimizing the power of the cw microwave source as shown by the power-dependence study of Figure 6.8. In practice, the power broadening effect can be used to determine rotational transition moment for the complex rotational spectra that result when IVR or isomerization occurs.<sup>18</sup> The power-dependent lineshape of a  $\Delta J=0$  transition (where the  $2_{11} - 2_{02}$  transition is pumped) is shown in Figure 6.9. In this case, the characteristic dip at the line

Table 6.1. Observed microwave transition frequencies (MHz)  
and fit residuals for fluoropropyne

Transition <sup>a</sup>	HCCCH <sub>2</sub> F	<sup>13</sup> CCH <sub>2</sub> F	HC <sup>13</sup> CCH <sub>2</sub> F	HCC <sup>13</sup> CH <sub>2</sub> F				
1 <sub>11</sub> -2 <sub>02</sub>	13448.66	-0.030	14030.96	-0.023	13526.03	-0.027	12598.11	-0.022
5 <sub>05</sub> -4 <sub>14</sub>	14703.18	-0.012	13181.52	-0.013	14460.41	-0.011	15481.00	-0.009
2 <sub>12</sub> -1 <sub>11</sub>	17159.70	-0.037	16622.15	-0.039	17064.00	-0.042	17074.68	-0.044
2 <sub>02</sub> -1 <sub>01</sub>	17580.29	-0.007	17018.48	-0.014	17480.61	-0.014	17505.94	-0.016
2 <sub>11</sub> -1 <sub>10</sub>	18010.13	0.039	17423.06	0.030	17906.32	0.039	17947.16	0.034
3 <sub>13</sub> -2 <sub>12</sub>	25736.72	-0.037	24930.72	-0.029	25593.24	-0.022	25609.00	0.001
3 <sub>03</sub> -2 <sub>02</sub>	26359.43	-0.020	25517.99	0.013	26210.12	-0.015	26247.02	-0.005
3 <sub>12</sub> -2 <sub>11</sub>	27012.29	0.029	26132.00	0.018	26856.62	0.026	26917.59	0.018
1 <sub>10</sub> -1 <sub>01</sub>	31454.18	0.016	31449.91	0.009	31427.81	0.020	30540.30	0.007
2 <sub>11</sub> -2 <sub>02</sub>	31884.02	0.061	31854.50	0.063	31853.51	0.053	30981.53	0.067
4 <sub>14</sub> -3 <sub>13</sub>	34310.43	0.032	33236.32	0.025	34119.19	0.025	34139.66	0.013
5 <sub>14</sub> -5 <sub>05</sub>	34553.27	-0.024	34361.98	-0.020	34496.30	-0.022	33726.60	-0.022
1 <sub>11</sub> -0 <sub>00</sub>	39821.30	-0.035	39560.64	-0.040	39749.11	-0.034	38859.41	-0.040

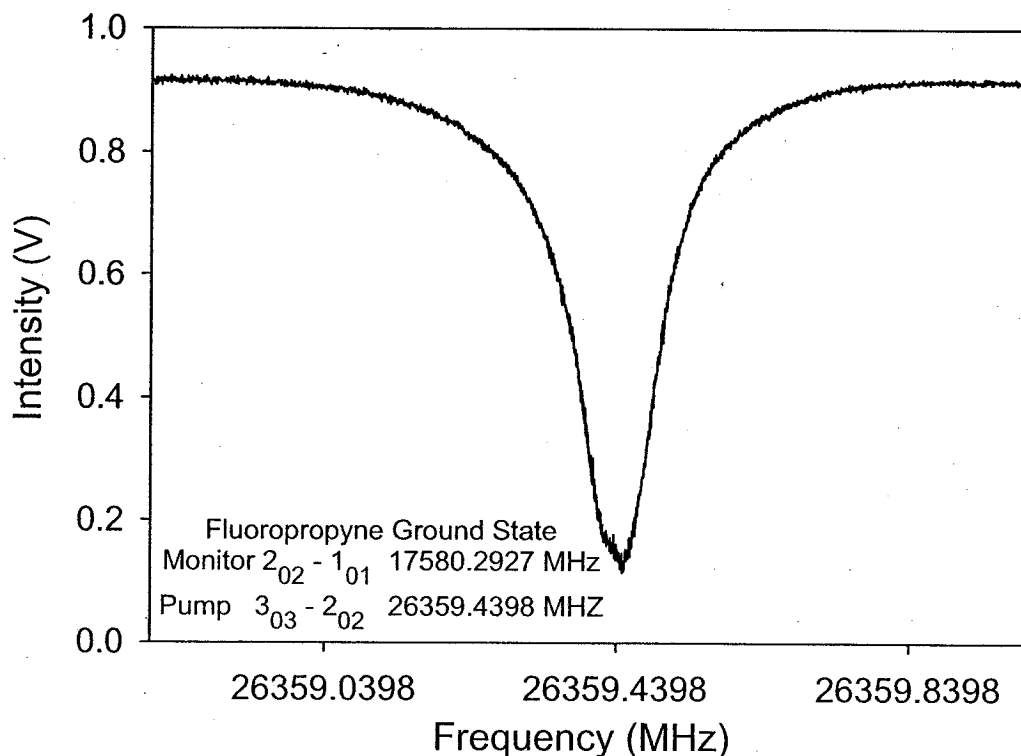
Transition <sup>a</sup>	v <sub>1</sub>	Excited state
1 <sub>11</sub> -2 <sub>02</sub>	13647.75	-0.578
5 <sub>05</sub> -4 <sub>14</sub>	14460.02	-0.212
2 <sub>12</sub> -1 <sub>11</sub>	17132.73	-0.975
2 <sub>02</sub> -1 <sub>01</sub>	17554.02	0.408
2 <sub>11</sub> -1 <sub>10</sub>	17979.72	-0.110
3 <sub>13</sub> -2 <sub>12</sub>	25696.78	-0.69
3 <sub>03</sub> -2 <sub>02</sub>	26319.50	0.198
3 <sub>12</sub> -2 <sub>11</sub>	26966.68	0.055
1 <sub>10</sub> -1 <sub>01</sub>	31625.37	0.367
2 <sub>11</sub> -2 <sub>02</sub>	32051.09	-0.130
4 <sub>14</sub> -3 <sub>13</sub>	34258.16	0.607
5 <sub>14</sub> -5 <sub>05</sub>	--	--
1 <sub>11</sub> -0 <sub>00</sub>	39981.10	0.130

Table 6.2. Spectroscopic constants for fluoropropyne normal species,  
 $^{13}\text{C}$  isotopomers, and the acetylenic C-H stretch fundamental

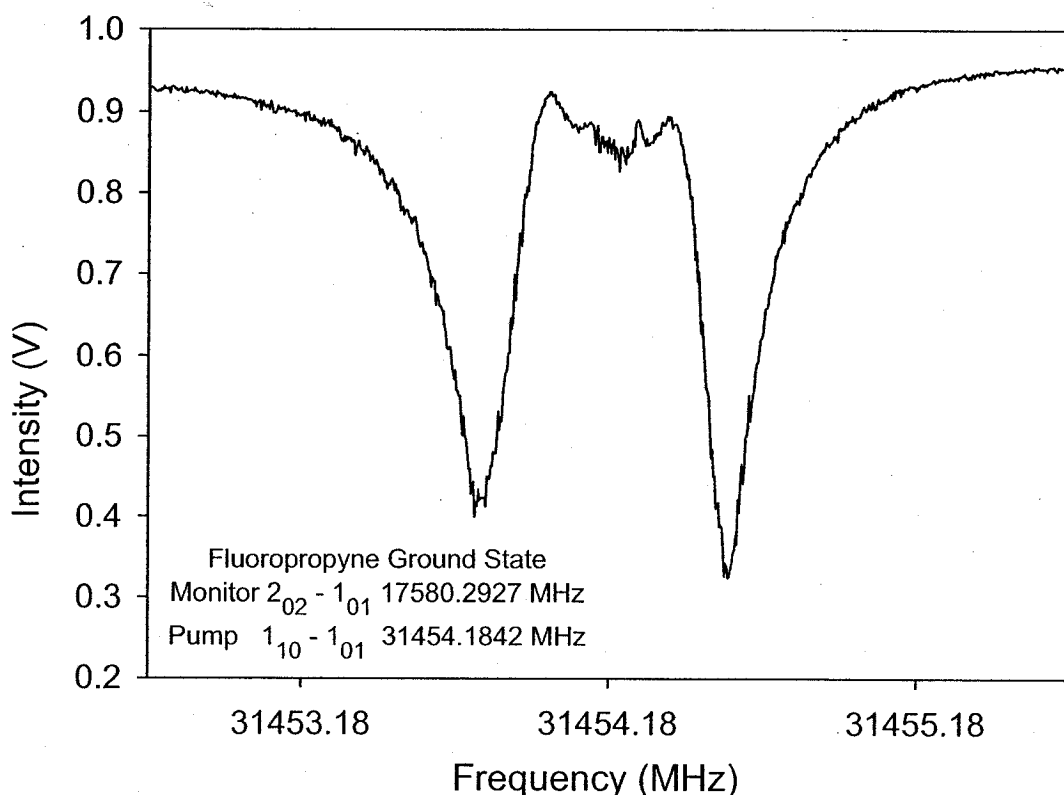
<b>Rotational Constants</b>	<b>HCCCH<sub>2</sub>F</b>	<b>H<sup>13</sup>CCCH<sub>2</sub>F</b>	<b>HC<sup>13</sup>CCH<sub>2</sub>F</b>
A /MHz	35637.615(24)	35505.157(22)	35588.337(22)
B /MHz	4608.7677(74)	4455.8141(68)	4581.8006(68)
C /MHz	4183.5903(49)	4055.3936(45)	4160.6811(45)
DJ /kHz	2.49(19)	2.37(17)	2.48(17)
DJK /kHz	-69.3(18)	-67.0(17)	-69.2(17)

	<b>HCC<sup>13</sup>CH<sub>2</sub>F</b>	<b>v<sub>1</sub> Excited state</b>
A /MHz	34699.748(22)	35803.55(41)
B /MHz	4595.7859(68)	4601.06(11)
C /MHz	4159.5847(44)	4177.99(13)
DJ /kHz	2.48(17)	7.2(30)
DJK /kHz	-64.5(17)	279.(53)



**Figure 6.6** The lineshape of the FTMW-cwMW double-resonance measurement for a  $\Delta J = 1$  rotational transition is shown. This measurement was obtained by monitoring the  $2_{02} - 1_{01}$  (17580.2927 MHz) pure rotational transition with the FTMW cavity while scanning the cw MW horn frequency through the  $3_{03} - 2_{02}$  (26359.4398 MHz) rotational transition. The horn frequency was scanned with a step size of 0.500 kHz and a power of 2.18 mW.



**Figure 6.7** The lineshape of a FTMW-cwMW double-resonance measurement for a  $\Delta J = 0$  rotational transition is illustrated. This measurement was obtained by monitoring the  $2_{02} - 1_{01}$  (17580.2927 MHz) pure rotational transition with the FTMW cavity while scanning the cwMW horn across the  $1_{10} - 1_{01}$  (31454.1842 MHz) rotational transition. The horn frequency was scanned with a step size of 4 kHz and a power of 79.40 mW.

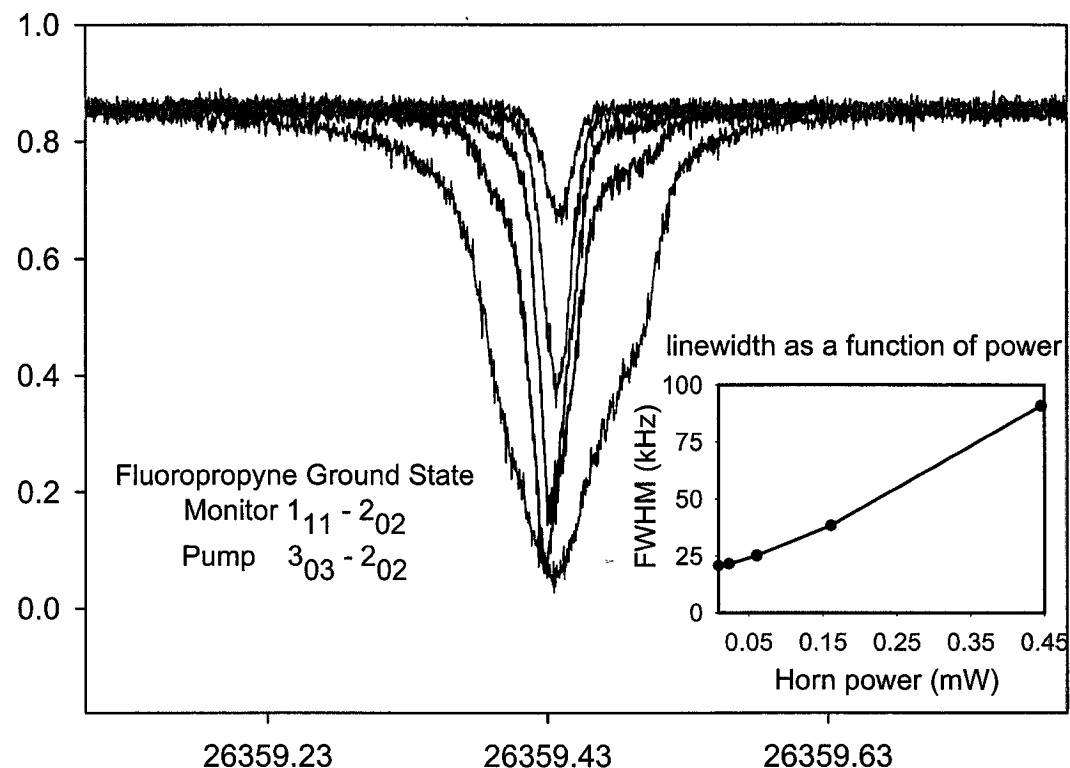


**Figure 6.8** The effect of cw MW power on the linewidth of an FTMW-cwMW double-resonance measurement is shown. These measurements were performed monitoring the  $1_{11} - 2_{02}$  (13448.66 MHz) rotational transition with the FTMW cavity while scanning the horn frequency across the  $3_{02} - 2_{02}$  (26359.4398 MHz) rotational transition. The scans shown in the figure (narrowest to broadest) were obtained by increasing the cwMW source power (0.01 to 0.45 mW).

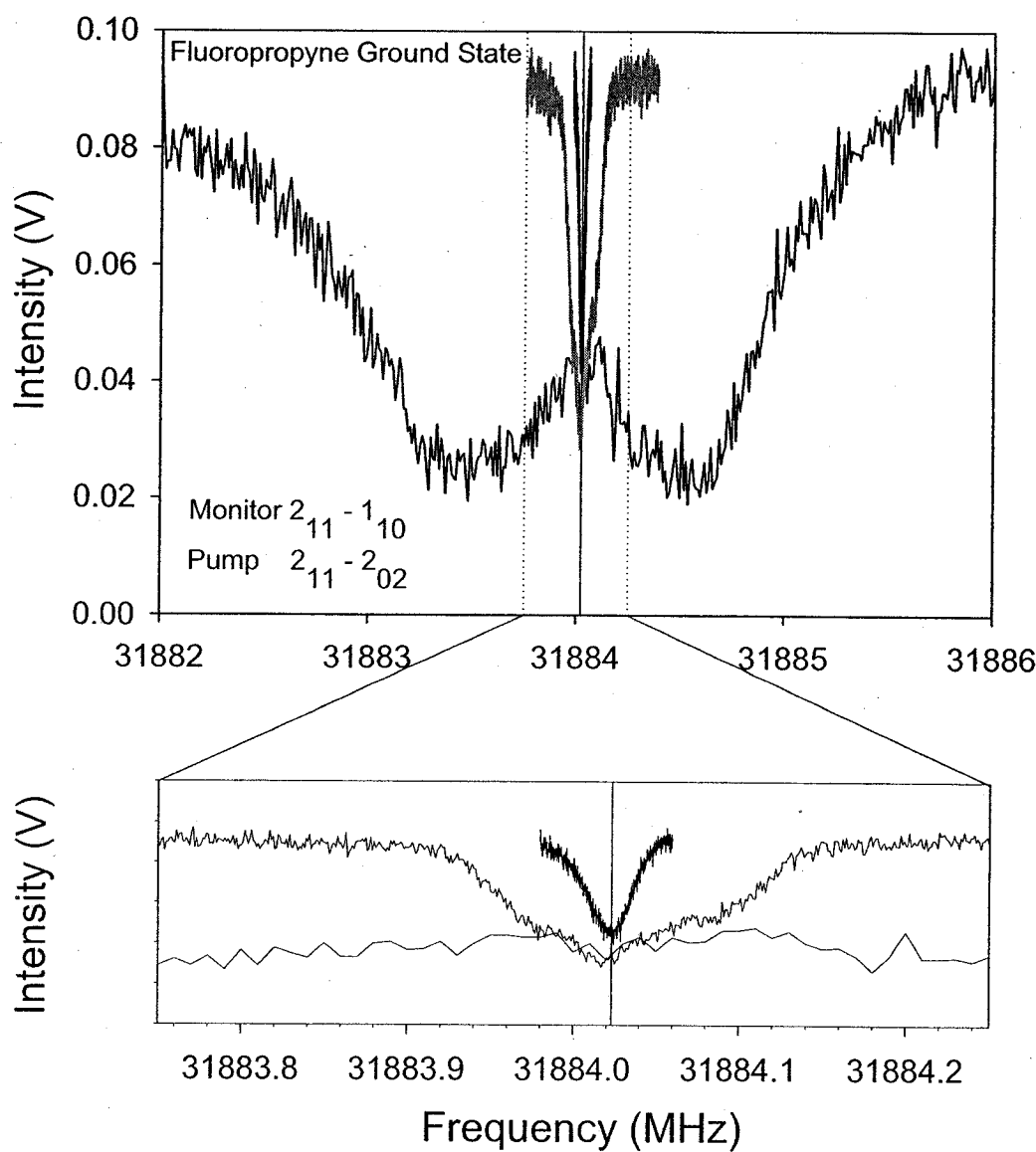


**Figure 4.9** The effect of cw MW power on the lineshape and linewidth of an FTMW-cwMW double-resonance measurement for  $\Delta J=0$  is shown. These measurements were performed monitoring the  $2_{11} - 1_{10}$  (18010.13 MHz) rotational transition with the FTMW cavity while scanning the horn frequency across the  $2_{11} - 2_{02}$  (31884.02 MHz) rotational transition. The scans shown in the figure (narrowest to broadest) were obtained by increasing the cwMW source power (0.06 to 79 mW).

center found in the strong-field measurement disappears at lower power giving a simpler, symmetric lineshape for the center frequency determination.

Precise rotational frequency determinations for the FTMW-cwMW measurements are made difficult by the complicated lineshapes that are observed and by the possibility of second-order Bloch-Siegert shifts<sup>19</sup> in the AC Stark effect. To assess the accuracy of the technique we have compared our measured frequencies to those previously reported for 3-fluoropropyne and its <sup>13</sup>C isotopomers using a Stark spectrometer. For the 31 common frequencies, the average frequency difference is 0.0095 MHz and the standard deviation is 0.050 MHz. These results indicate that the FTMW-cwMW technique provides accurate rotational frequencies with an estimated measurement uncertainty of about 50 kHz. Although this uncertainty is large compared to the best coaxial-design FTMW spectrometers,<sup>8,20</sup> it offers significant improvement over other techniques for dynamic rotational spectroscopy.<sup>2,1,6</sup>

#### *Rotational Spectroscopy in the First Excited State of the Acetylenic C-H Stretch*

The same set of rotational transitions is measured for the excited vibrational state of 3-fluoropropyne by first exciting the molecules using the single-longitudinal-mode infrared laser. An example of the FTMW signal recorded for vibrationally excited 3-fluoropropyne is shown in Figure 6.10. The measured rotational frequencies in the excited state and the results of a fit to the Watson asymmetric top Hamiltonian are presented in Tables 6.1 and 6.2. For the vibrationally excited state, the deviations between the measured and predicted rotational frequencies exceed the measurement uncertainty (50 kHz). We believe that these deviations are caused by weak perturbations

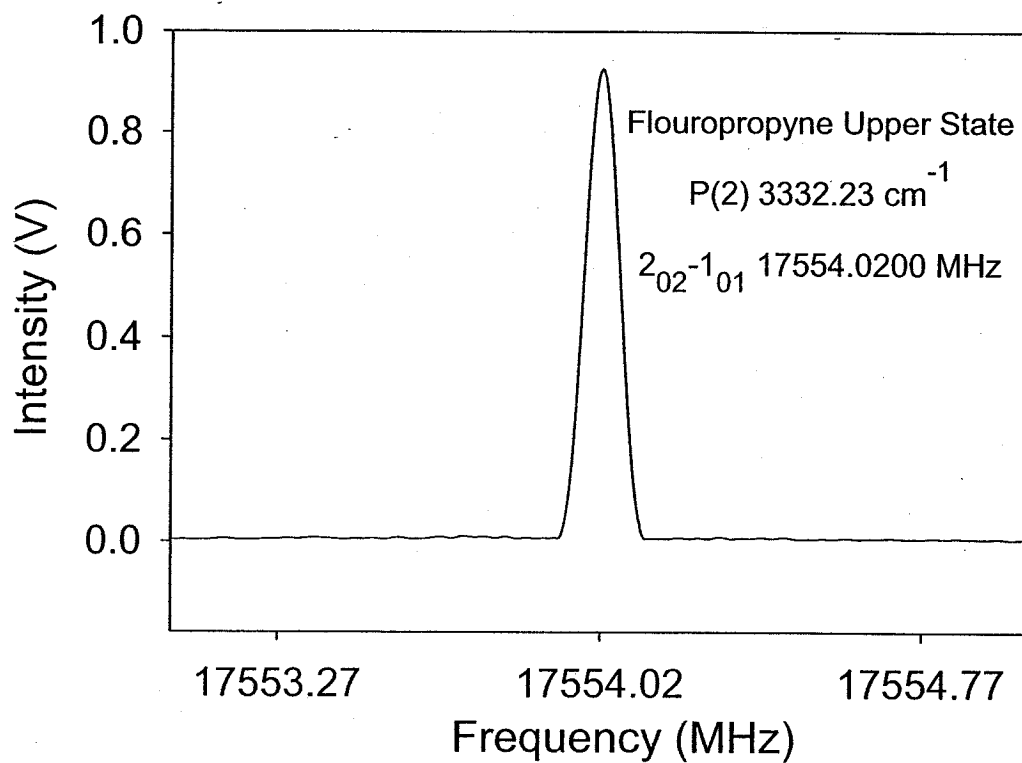


**Figure 4.10** The FTMW signal measured for the  $2_{02} - 1_{01}$  (17554.02 MHz) rotational transition of the first vibrationally excited state of the acetylenic C-H stretch is reported. This measurement was performed by pumping P(2) at  $3332.23(2)$   $\text{cm}^{-1}$  with 3 mJ/pulse of IR power.

to the acetylenic C-H spectrum. These are the same perturbations that eventually lead to extensive fragmentation of the vibrational spectrum in larger molecules where the density of possible perturbers is significantly higher.<sup>21-28</sup>

Examples of IR-FTMW-cwMW triple-resonance spectroscopy are shown in Figures 6.11 and 6.12 for both  $\Delta J = 1$  and  $\Delta J = 0$  rotational transitions. The signal-to-noise ratio for the excited states measurement is comparable to the measurement in the ground vibrational state (Figure 6.6 and Figure 6.7). In part, the low noise on the monitored FTMW signal is results from the strong saturation of the rovibrational transition. Under strongly saturated conditions, the population transferred to the excited state is less sensitive to shot-to-shot pulse energy fluctuations and frequency jitter of the laser. These figures also show a series of FTMW measurements that demonstrate the Autler-Townes mechanism of the MW-MW double-resonance signal.<sup>7</sup> The triple-resonance trace is obtained by monitoring the FTMW signal strength at the center frequency of the field-free rotational transition. The gate region is shown in the individual FTMW spectra by the black bar at the center frequency. As the cw microwave source is scanned through resonance, the Autler-Townes splitting of the transition is observed.<sup>6</sup>

The different lineshapes observed in Figure 6.11 and Figure 6.12 under strong field conditions for the cw MW pump source are produced by the  $|JKM_J\rangle$  dependence of the Stark matrix elements.<sup>29</sup> For the  $\Delta J = 1$  rotational transition being pumped by the cw field in Figure 6.11, all rotational states undergo an Autler-Townes splitting.<sup>7</sup> Under strong, resonant pump field conditions all rotational states are split outside the gate width

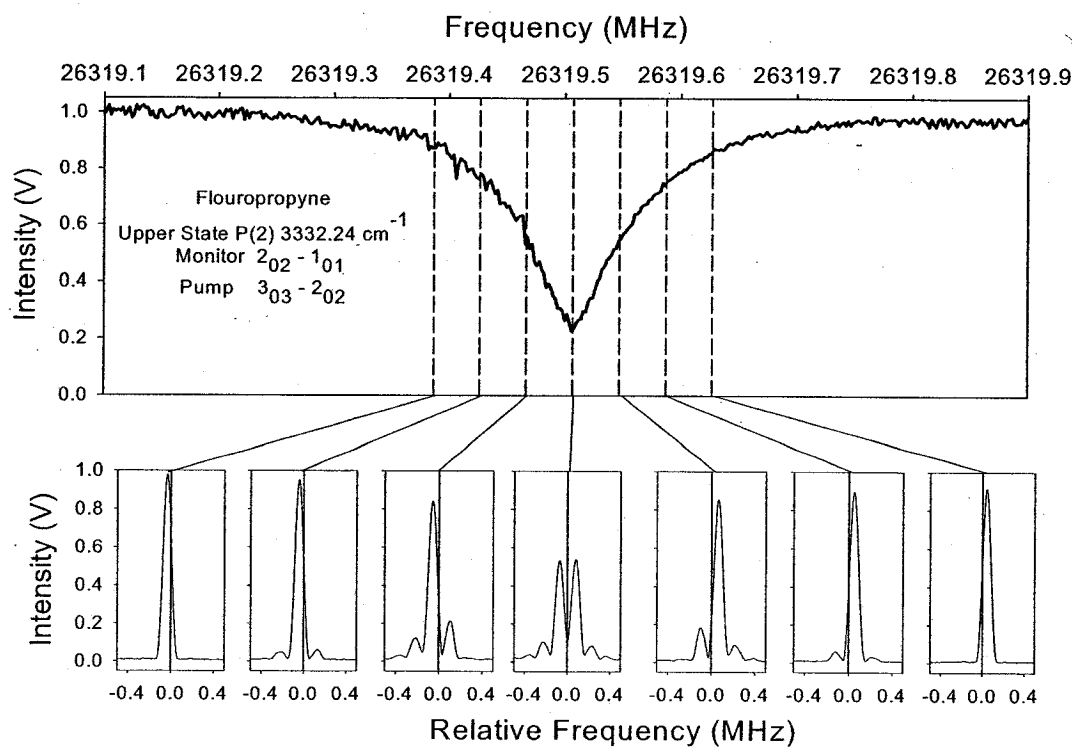


**Figure 6.11** An IR-FTMW-cwMW triple-resonance spectrum is shown for the  $\Delta J = 1$  case. The  $2_{02} - 1_{01}$  (17554.02 MHz) excited state rotational transition was pumped with  $P(2)$  at  $3332.23(2) \text{ cm}^{-1}$  of the acetylenic C-H stretch fundamental. The spectrum was obtained by monitoring the peak height  $2_{02} - 1_{01}$  excited state transition in the FTMW cavity while scanning the cwMW horn frequency across the  $3_{03} - 2_{02}$  (26319.50MHz) excited state transition. The power of the cwMW horn was 1.26 mW. The triple-resonance trace (top) was taken with horn power of 1.26 mW, a step size of 2 kHz, and the max height out of 5 acquisitions for every data point. The Autler-Townes effect is demonstrated for the each of the panels below at various offsets from resonance of  $\pm 120$  kHz,  $\pm 80$  kHz,  $\pm 40$  kHz, and on resonance. These panels illustrate the  $J=2$  level splitting through the  $1_{01} - 2_{02}$  rotational transition. The movement of the creeper through resonance indicates that the  $3_{03}$  level is at higher energy than the  $2_{02}$  level for excited state fluoropropyne.

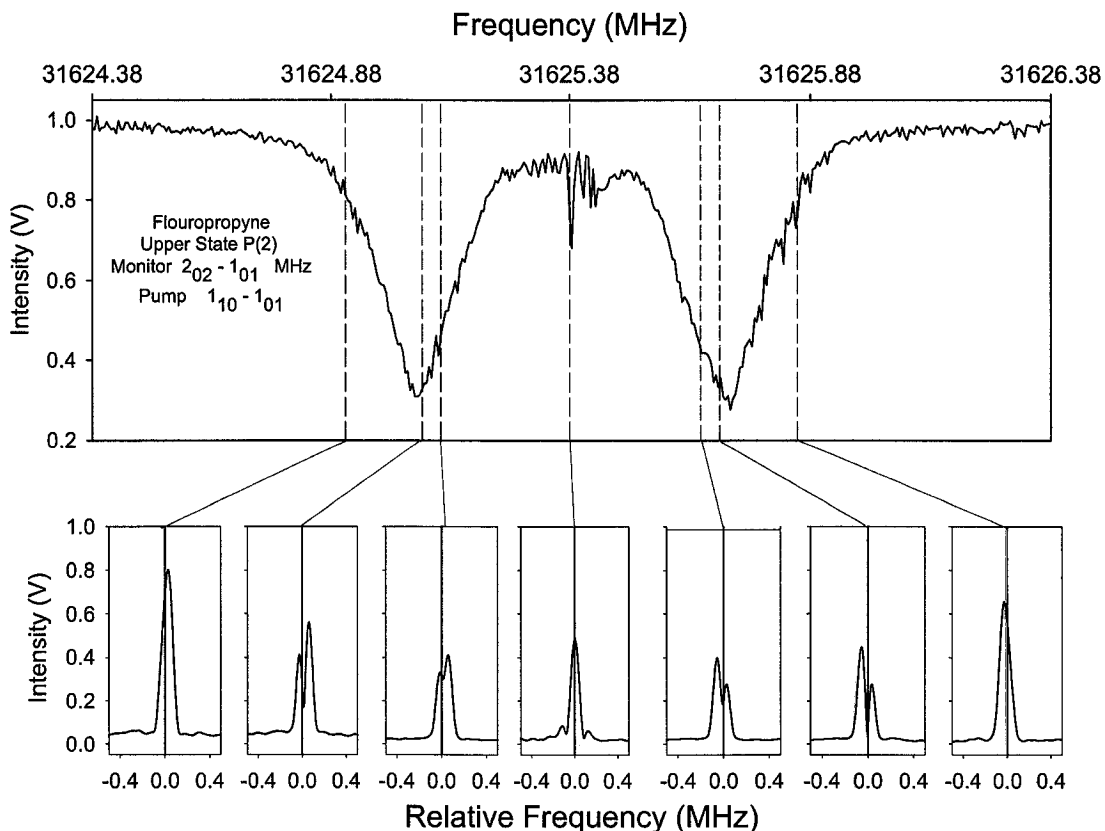


**Figure 6.12** An IR-FTMW-cwMW triple-resonance spectrum is shown for the  $\Delta J = 0$  case. The  $2_{02} - 1_{01}$  (17554.02 MHz) excited state rotational transition was pumped with P(2) at  $3332.23(2)$   $\text{cm}^{-1}$  of the acetylenic C-H stretch fundamental. The excited state was monitored with the FTMW cavity while scanning the cwMW horn across the  $1_{10} - 1_{01}$  (31625.38 MHz) rotational transition of the vibrationally excited state. The triple-resonance trace (top) was taken with a horn power of 79 mW, a step size of 5 kHz, and using the maximum of 5 measurements at each step. The Autler-Townes effect is demonstrated in each of the panels below at  $\pm 470$  kHz,  $\pm 315$  kHz,  $\pm 270$  kHz. These panels illustrate the  $J=1$  level splitting through the  $1_{01} - 2_{02}$  rotational transition.

and the double-resonance signal shows 100% depletion. However, for the  $\Delta J = 0$  rotational transition the  $M=0$  states are unaffected by the applied field so that even for resonant cw pumping intensity remains at the position of the field-free rotational frequency.<sup>30</sup>

A variation of the double-resonance technique used to obtain the signals in Figures 6.11 and 6.12 is illustrated in Figure 6.13. In this case we offset the gate position so that the FTMW signal strength 50 kHz below resonance is monitored. As the cw source approaches resonance, the initial response of the FTMW signal is a frequency shift caused by the Stark effect level repulsion. Therefore, this gate position produces first-derivative-like lineshapes that can be used to determine whether the transition being driven by the cw source reaches a rotational level that is higher or lower in energy. For more complex rotational spectra, like those of isomerizing molecules, a determination of the energy ordering of the initial and final state is not immediately obvious from the transition frequency.<sup>6</sup> The offset gating technique makes it possible to obtain this important information in the course of making the IR-FTMW-cwMW measurement.

### **Summary**

The results for propyne and fluoropropyne demonstrate that the FTMW-based IR-FTMW-cwMW triple-resonance technique preserves the important features of the previous methods for determining the transition intensity and direction. However, the FTMW component of the experiment offers unique advantages. The major advantage is the ability to use high-energy pulsed laser sources for DRS. Because pulsed lasers are available over essentially the full mid-infrared and visible region, this technique promises

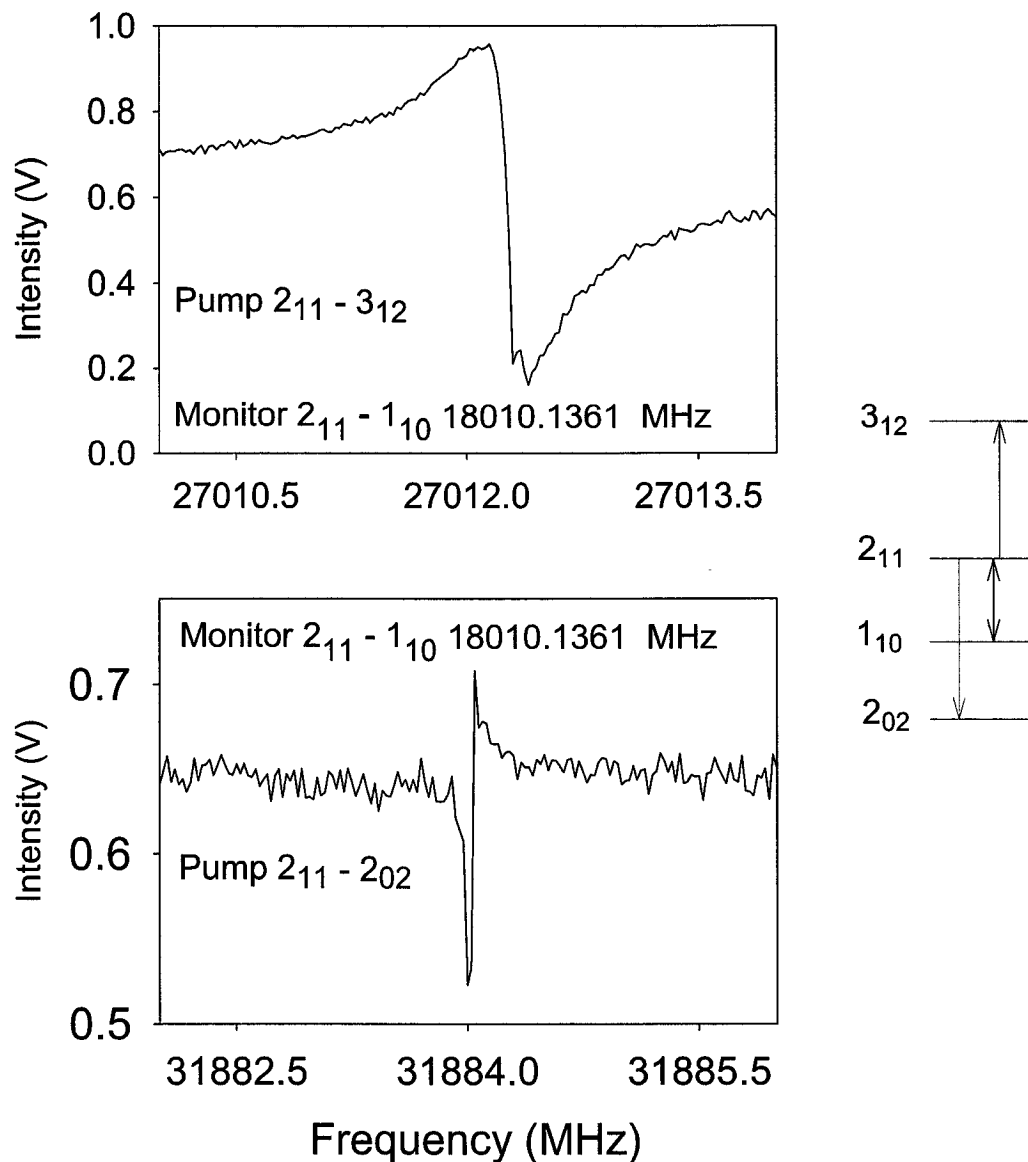


**Figure 6.13** A variation of the double-resonance technique used in Figs. 6 and 7 is shown. The  $2_{11}$  -  $1_{10}$  (18010.1361 MHz) ground vibrational state rotational transition was monitored with the FTMW (gate position offset 50 kHz below resonance) while the cwMW source was scanned over the  $2_{11}$  -  $3_{12}$  (27012.29 MHz) rotational transition (above) and the  $2_{11}$  -  $2_{02}$  (31884.02 MHz) rotational transition (below). These measurements were obtained by taking 25 kHz step-sizes with and a cwMW horn power of 0.27 mW.

to be a powerful and versatile method for high-resolution rotational spectroscopy of highly excited states. The high-resolution of the FTMW spectrometer improves the sensitivity for DRS. When the Autler-Townes method is employed, the detection sensitivity is determined by the minimum splitting that can be detected. This limit is given by the instrumental linewidth of the monitored rotational transition. In our IR-saturation method the linewidth is 300 kHz,<sup>1,6</sup> compared to the ~20 kHz linewidth that can be achieved using the FTMW spectrometer. For equivalent focusing of the MW pump radiation, the improved resolution of the FTMW spectrometer makes it possible to measure a transition with about 1/200 of the power required in the IR-saturation approach. Finally, the switch to a pulsed free jet expansion results in significantly lower sample consumption and makes it possible to use a wider variety of molecular beam sources to generate novel species.<sup>31-33</sup>

The fluoropropyne experiment, in particular, has demonstrated the ability to measure the rotational spectra of vibrationally excited states prepared by narrowband pulsed infrared laser excitation using the techniques of molecular-beam FTMW spectroscopy. Performing FTMW-cwMW double-resonance spectroscopy with a higher frequency cw source has effectively extended the frequency range of the FTMW spectrometer. The excited state measurements can be performed with signal-to-noise ratios that are comparable to the pure rotational measurements. The rotational spectrum of a relatively small asymmetric top molecule (3-fluoropropyne) in the first excited state of the acetylenic C-H stretch has been examined. The rotational spectrum of this excited state for fluoropropyne is believed to follow the pattern expected for a simple asymmetric

rotor (note: scanning was limited to searches around the predicted transition frequencies). However, the residuals to a fit for the excited state using the standard asymmetric top Hamiltonian are larger than observed for the pure rotational spectrum of the normal species and the three  $^{13}\text{C}$  isotopomers. These deviations are believed to be caused by non-resonant interactions with other combination and overtone vibrational states with about the same total vibrational energy. It is these weak perturbations that lead to the extensive fragmentation of the vibrational spectrum and excited state rotational spectrum of larger molecules. This occurs via intramolecular vibrational energy redistribution (IVR).<sup>5,34</sup>

The techniques described are especially well-suited for measuring the rotational spectra of highly excited molecules that undergo IVR and isomerization. In this case, the rotational spectrum of a single quantum state can consist of several spectroscopic transitions for each expected asymmetric top transition.<sup>4,6,18</sup> As this spectral fragmentation becomes more extensive, the individual quantum-state-resolved transitions become weaker. In addition, these transitions can cover a frequency range of several GHz, especially for isomerizing molecules, leading to an overlap of P-, Q-, and R-type transitions. The important features of the spectrometer design for tackling these types of rotational spectroscopy measurements are: 1) high-sensitivity of the FTMW-cwMW double-resonance part of the measurement, 2) the ability to gain information on the  $\Delta J$  selection rules from the double-resonance lineshape under strong field conditions (Figures 6.11 and 6.12), and 3) the ability to determine the “direction” of the transition using offset gating (Figure 6.13). For applications to more complex rotational

spectroscopy problems, the FTMW signal at both the field-free center frequency and the small frequency offset can be monitored simultaneously so that information about the transition strength (linewidth), transition type (center-frequency gate lineshape), and direction (offset gate lineshape) is obtained in a single FTMW-cwMW double-resonance scan.

### B. IR-FTMW-pulsed MW Triple Resonance

Now that triple resonance capabilities for propyne and fluoropropyne have been demonstrated, the next step is to test and/or adapt these spectroscopic techniques for larger molecules that exhibit fast IVR dynamics, but still do not exhibit complex dynamics such as isomerization. As described in chapter 1, when the molecule gets larger the state density increases providing a set a of bath states that may couple to the bright state providing various pathways for vibrational energy flow.<sup>34,35</sup> In terms of pure rotational spectroscopy as the molecule gets larger the moments of inertia increase so the rotational constants get smaller, thereby causing the rotational level spacing decrease to (B+C).<sup>36</sup> As a result there may now be several rotational levels within the range of the FTMW spectrometer (8-26 GHz). This provides problems for FTMW-cwMW double resonance and/or IR-FTMW-cwMW triple resonance spectroscopy because now the FTMW components do not serve as a filter against the cw MW source. Detecting the molecular emission signal is now complicated by the fact that power from the horn may couple into the cavity and saturate the amplifier causing interference.

As a solution to this problem we have developed techniques that do not rely on detecting the FID while there is light being coupled into the cavity region from the MW horn. These techniques are based on FTMW-pulsed-MW double resonance. MW-MW double resonance or double resonance modulation spectroscopy has long been a part of microwave spectroscopy.<sup>14</sup> Typically double resonance techniques are used to aid in the assignment of complicated spectra or to extend the tuning range of the spectrometer. These initial techniques were based on waveguide cells in which both sources were continuous-wave (cw).<sup>14</sup> Double resonance techniques have also been applied to transient phenomena in FTMW spectroscopy.<sup>37</sup> These techniques, also based on a waveguide cell, were developed with the first MW source pulsed and the second microwave source cw. This has lead the way to two-dimensional techniques in which both sources were pulsed.<sup>38;39</sup> More recently, these techniques have been adapted to the Balle-Flygare type spectrometer, in which double resonance was achieved using two crossed Fabry-Perot cavities.<sup>11;16;40;41</sup> Additionally, a triple resonance technique implementing a Balle-Flygare spectrometer and a waveguide cell has been used to obtain spectra of dipole forbidden double and triple quantum transitions.<sup>42</sup>

Two types of FTMW-pulsed-MW and/or IR-FTMW-pulsed-MW techniques have been developed and will be described. These techniques are based on the methods Endo developed for FTMW detected excited electronic states.<sup>43</sup> The different mechanisms for the two techniques results from the relative timing of the MW polarizing pulse to the MW horn pulse. The merits of both techniques will be analyzed with reference to dynamic rotational spectroscopy (DRS).<sup>4;44</sup> Additionally, the experimental steps

necessary to perform a complete DRS experiment will be presented for phenylacetylene, a large slightly asymmetric top molecule. These steps include obtaining 1.) a rotationally resolved IR spectrum, 2.) the vibrationally excited rotational spectrum, 3.) the rotational spectrum of a vibrationally excited single eigenstate. These steps will be used to demonstrate that all of the necessary spectroscopy can be preformed using the FTMW spectrometer and a pulsed laser.

### **Experimental**

This experiment utilized the spectrometer setup described in chapter 2 with the IR mirrors centered on the beam waist and an improved vacuum system. As described in chapter 2 a standard gain horn is placed under the cavity and points up into the active region. Through the use of two switches and an 8 watt amplifier high power MW pulses can be applied to the active region of the cavity. The timing for this pulse is controlled through a digital delay generator (DG535 Stanford Research).

Since phenylacetylene has a high boiling point ( $\sim 140^{\circ}\text{C}$ ) the reservoir nozzle was used with 250  $\mu\text{L}$  of sample. Clustering was a problem and was only minimized by using a backing pressure of  $\sim 2$  psi of the 80/20 Ne/He carrier gas. The clustering occurs largely down the centerline on the expansion which adversely affects the infrared depletion measurements because there are few monomers in the IR excitation region.

The infrared spectrum of phenylacetylene was obtained by using the ground state depletion (GSD) method described in chapter 4. This method monitors the amplitude of an assigned pure rotational transition as the IR frequency is scanned. The laser was

scanned over  $100 \text{ cm}^{-1}$  in order to obtain the many weak IVR perturbations. By determining the relative intensities of each perturbing band found in the long IR scan, the survival probability of the bright state can be calculated.

The excited state rotational spectrum was obtained by setting the laser to R(3) of the strongest IR band ( $3339.48 \text{ cm}^{-1}$ ), obtained from the IR spectrum, and scanning the FTMW cavity. The spectrum was scanned by stepping the cavity 250 kHz and averaging 10 consecutive acquisitions. The maximum height of the frequency domain signal was plotted at each 250 kHz step. This serves as a low resolution spectrum. For each 250 kHz scanning step a high resolution spectrum is also recorded in which every point of the 2 MHz frequency span is digitized with a 4 kHz/pt resolution. A separate program is used to compile the high resolution spectrum from the raw data. A laser shutter controlled by the acquisition program can be used to block the infrared beam so that at each frequency of the scan 10 averages are taken with the laser blocked and 10 averages are taken with the laser unblocked. The two spectra are plotted simultaneously with the "blocked" intensity inverted. This allows for immediate confirmation of excited state rotational transitions.

The IR-FTMW-pulsed MW triple resonance spectra can be obtained using two different methods which depends on their respective pulse timing as depicted in Figure 6.14. Also in Figure 6.14 the triple resonance excitation level diagram is shown. Figure 6.14 illustrates the relative timing of two pulse sequences in which the horn pulse fires relative to the laser and cavity pulse. Both MW pulse sequences occur after laser excitation. A  $1 \mu\text{s}$  delay is typical from laser Q-switch to the first MW pulse. If the MW

horn pulse interacts with the molecules before the polarizing pulse then the horn pulse causes population transfer. In the case shown, the laser excites the molecules to  $J=4$  in the vibrationally excited state and the population transfer pulse is used to move the population of a single eigenstate to  $J=5$ . The cavity is then scanned in the region of the  $J=5 \rightarrow J=6$  transitions. In this way the population transfer step acts as a single eigenstate filter. Good population transfer is ensured by monitoring an upper state rotational transition in the FTMW cavity while pumping the population transfer pulse at the same frequency and adjusting the parameters so as to null the signal. The signal is zeroed because there is near equal population in both excited state rotational levels, and the signal obtained from the FTMW spectrometer depends on the population difference between the rotational levels. This triple resonance technique will be referred to as the population transfer method.

Alternatively, if the horn pulse interacts with the molecular beam after the polarizing MW pulse then the horn pulse destroys the coherent molecular emission at resonance as illustrated in Figure 6.15. Triple resonance spectra are obtained by monitoring the peak height of the excited state rotational transition in the frequency domain as the horn frequency is scanned. A resonance is detected as an amplitude depletion in the frequency domain signal caused by changes in the time domain rotational FID. The data acquisition takes place 5  $\mu$ s after the horn pulse is fired to ensure no coupling into the detection amplifier. This technique will be referred to as the coherence method. In both methods the rotational spectrum of a vibrationally excited single eigenstate is obtained.

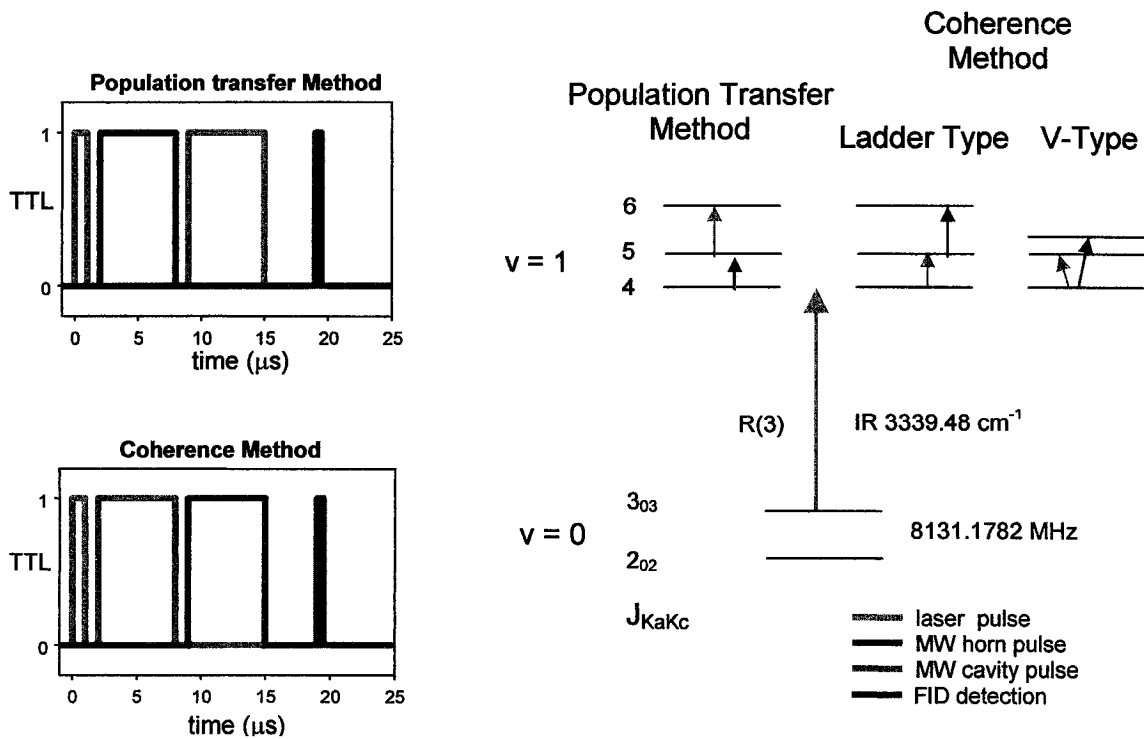


**Figure 6.14** The pulse timing for the two IR-FTMW-pulsed-MW triple resonance methods is illustrated on the left. The first step for both methods is laser preparation of the vibrationally excited state at  $J$ . The coherence method uses the FTMW cavity to monitor an excited state rotational transition. The horn pulse is used in this case to destroy the coherence of the rotational FID for a given resonant frequency and thereby measuring the rotational spectrum of a single eigenstate. The population transfer method uses the horn pulse to transfer population (to  $J+1$ ), and then measures the rotational spectrum of populated single eigenstate. The level diagram illustrates the difference between the population transfer method and the coherence method for the current experiment.

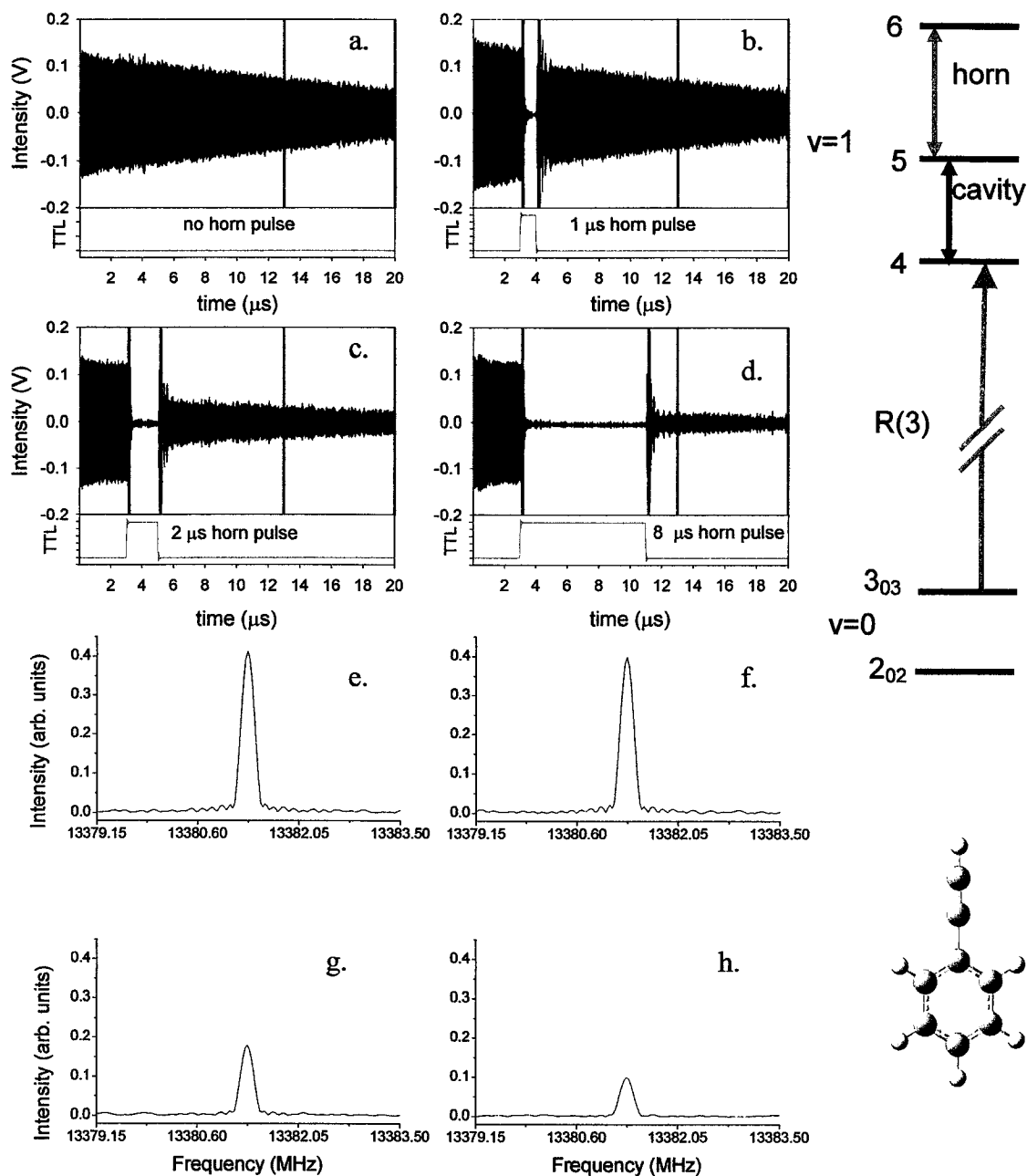


**Figure 6.15** Phenylacetylene is vibrationally excited at R(3)  $3339.51\text{ cm}^{-1}$  to populate  $J=4$  in  $v=1$  of the acetylenic C-H stretch fundamental. The cavity is used to monitor a single vibrationally excited state rotational transition in the region of  $J=4 \rightarrow 5$  at  $13381.32\text{ MHz}$  and the frequency of the second microwave source that is coupled to the horn is set to be resonant with  $J=5 \rightarrow 6$ , where the two transitions share a common eigenstate at  $J=5$ . The rotational FID (black) of the excited state transition and the duration of the horn pulse (red) are illustrated in the top panels (a.-d.). The vertical lines (green) represent the region of the FID that is gated and subsequently Fourier transformed. The lower panel illustrates the Fourier transform for each FID.(e.-h.)

## Results

The ground state MW transitions were initially obtained from previous assignment that used a Stark cell spectrometer.<sup>45</sup> In order to achieve higher precision constants and fit frequencies the ground state spectrum was scanned from 8 GHz to 20 GHz with 41 lines assigned and fit with a standard error of 2.46 kHz. The fit constants are shown in Table 6.3. The spectrum was obtained using the coaxially aligned nozzle with a backing pressure of ~5 psi. The cavity was scanned 250 kHz/step with 10 averages at each step.

The infrared spectrum of phenylacetylene for v=1 of the acetylenic C-H stretch is obtained using the ground state depletion method and is shown in Figure 6.16. The spectrum was obtained by monitoring the  $3_{03}-2_{02}$  pure rotational transition at 8131.1782 MHz. The laser was scanned at a rate of  $10.8 \text{ cm}^{-1}/\text{hr}$  with 20 averages at a 10 Hz repetition rate. The spectrum contains 9 vibrational bands in the region of the acetylenic C-H fundamental. The infrared spectrum of phenylacetylene demonstrates the highly fragmented oscillator bright state originating from strong IVR perturbations. As reported for cyclopropylacetylene in the previous chapter and seen in other molecules that have a vinyl acetylene structure, the  $\text{C}\equiv\text{C}$  stretch + 2 CH bend combination band is tuned into resonance through lowering of the out-of-plane acetylenic C-H bend frequency.<sup>46,47</sup> This interaction provides a “doorway” for subsequent IVR to other near-resonant vibrational modes.<sup>24,48,49</sup>

The excited state rotational spectrum was obtained by first maximizing the depletion signal of the  $3_{03}-2_{02}$  pure rotational transition using R(3) at  $3339.51 \text{ cm}^{-1}$ . Since the laser prepares J=4 in the vibrationally excited state the FTMW cavity was scanned

**Table 6.3** The spectroscopic constants for phenylacetylene

Parameter	C <sub>6</sub> H <sub>5</sub> CCH
A /MHz	5680.279(19)
B /MHz	1529.7403(3)
C /MHz	1204.9558(3)
ΔJ /kHz	0.037(2)
ΔJK /kHz	0.99(1)
ΔK /kHz	-0.028(4)
δJ /kHz	0.011(2)
fit std. dev./kHz	2.46
Number of lines in fit	41

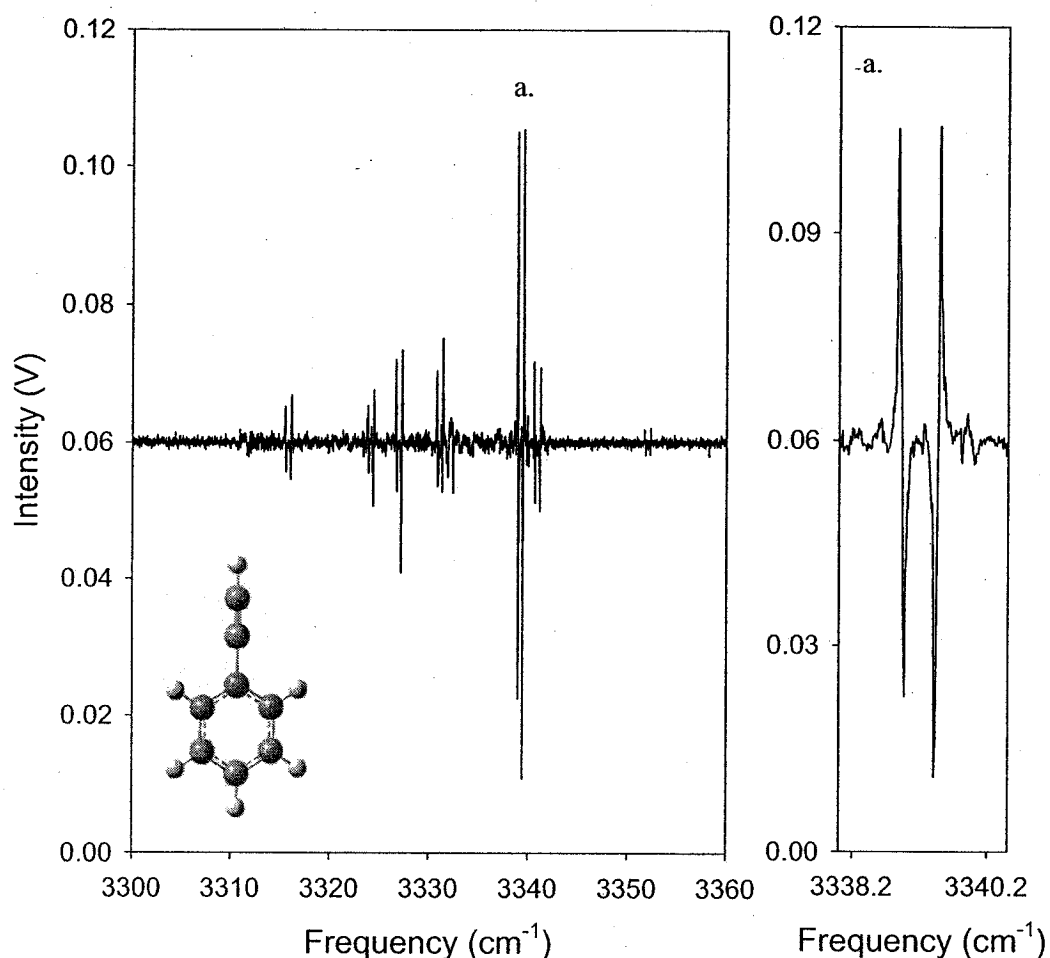


**Figure 6.16** The FTMW detected IR spectrum in the region of the acetylenic C-H stretch fundamental of phenylacetylene is shown. This spectrum was obtained by monitoring the  $3_{03}-2_{02}$  pure rotational transition at 8131.1782 MHz. The panel on the right (a.) illustrates is the main feature on an expanded scale.

500 MHz around the  $5_{05}-4_{04}$  pure rotational frequency in order to obtain  $5_{05}-4_{04}$  excited state rotational transitions. The upper state rotational spectrum from 13100 to 13600 MHz is illustrated in Figure 6.17. The top half of the plot contains both ground state and upper state transitions and the bottom half contains ground state transitions only. Although we have developed a program that records the rotational spectra with laser on and laser off, the bottom panel in Figure 6.4 was obtained with the coaxial aligned FTMW arrangement using the program developed at NIST.<sup>8</sup> This provides a clear-cut assessment of the upper state rotational frequencies. The dashed red line corresponds to the upper state transition (13386.78 MHz) that will be used to perform triple resonance.

The evidence of IVR is apparent in Figure 6.16, as there is now a spread of rotational transitions in contrast to propyne and fluoropropyne which exhibited only a single excited rotational state transition as would be predicted from the normal asymmetric top Hamiltonian.<sup>44</sup> Additionally, the strongest upper state lines are shifted up 70 MHz from the ground state  $5_{05}-4_{04}$ .<sup>44</sup> This results from a positive shift in the rotational constants (B+C) which in turn result from vibrational energy redistribution into bending modes that on average result in a smaller molecular geometry. Again this contrasts the results reported for propyne and fluoropropyne in which the excited state frequency shifts were negative because the energy remained localized in the acetylenic C-H stretch and on average gave rise to a larger molecule, reducing the effective rotational constants.

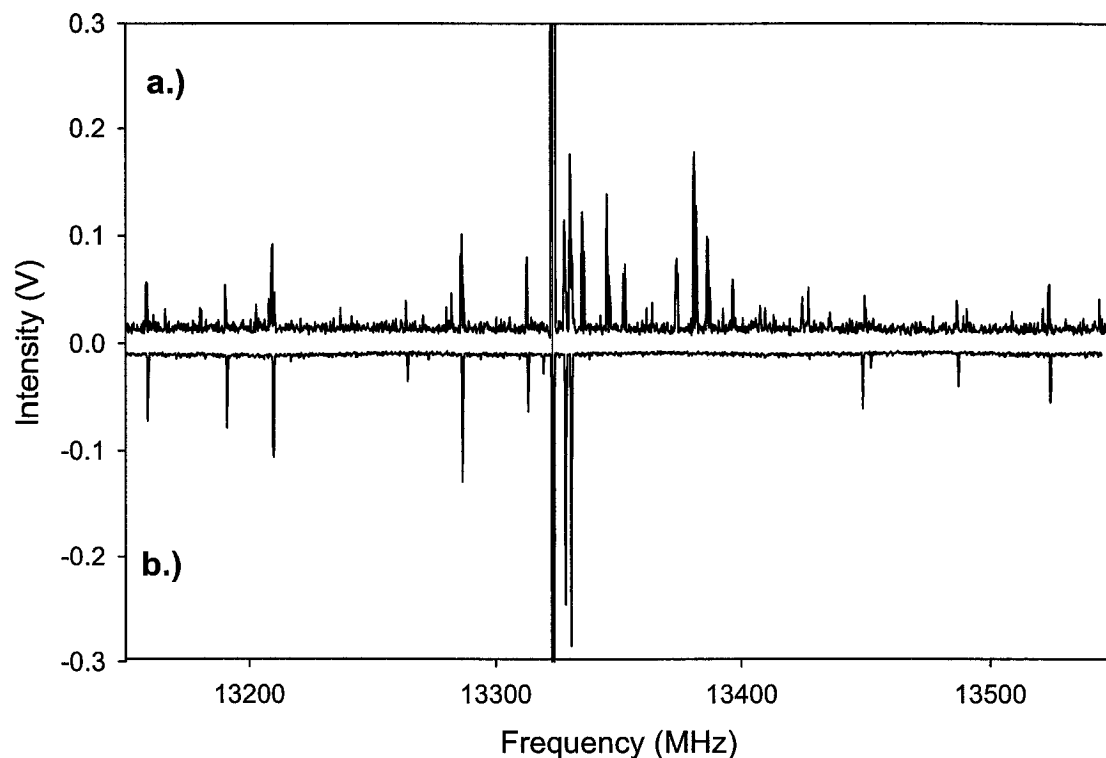


**Figure 6.17** The excited state rotational spectrum around the  $5_{05}$ - $4_{04}$  ground state transition (blue line) is illustrated. The laser was set to R(3) at  $3339.51\text{ cm}^{-1}$  to prepare  $J=4$  in the vibrationally excited state. The spectrum in panel a.) contains ground state and upper state transitions, the spectrum in panel b.) contains ground state transitions only. Many ground state transitions are due to  $^{13}\text{C}$  isotopomers in natural abundance.

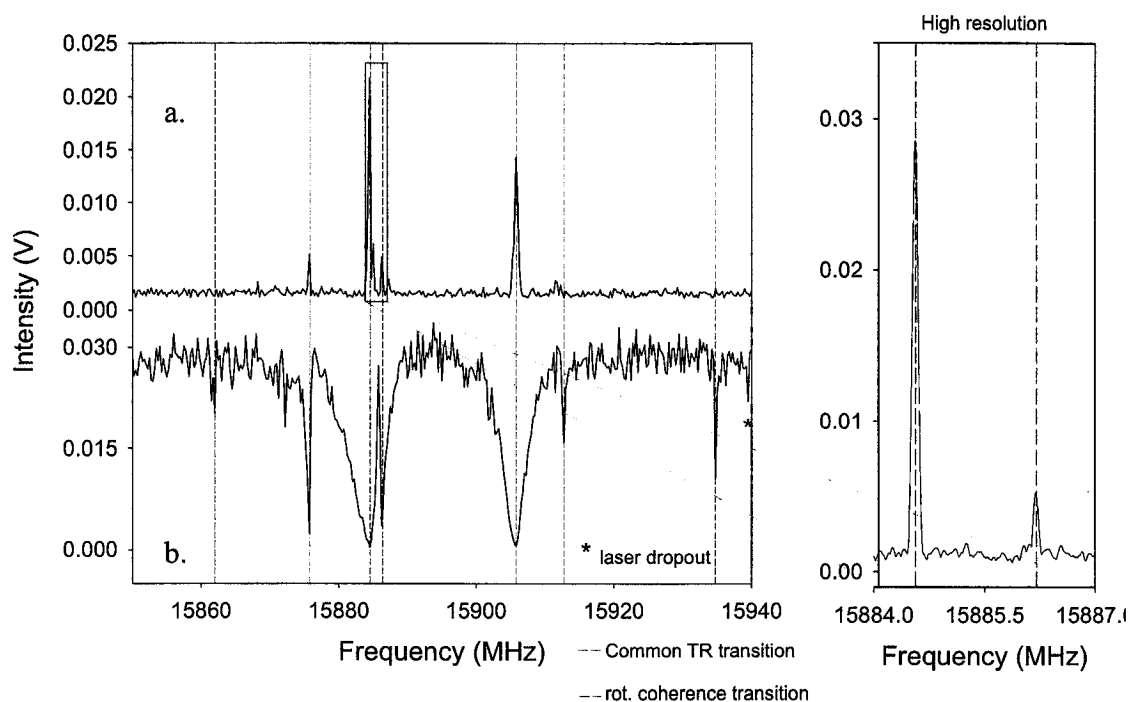


**Figure 6.18** The IR-FTMW-pulsed MW triple resonance spectra are illustrated above, a.) spectrum obtained from population transfer technique, b.) spectrum obtained from coherence technique. Note the high signal-to-noise- of the inset is taken from the 4 kHz/point high resolution data obtained using the population transfer method.

The spectra obtained using both the coherence method and the population transfer methods are illustrated in Figure 6.18. The level diagram in Figure 6.2 illustrates the pumping schemes for each method. In the top panel of Figure 6.5 the population transfer spectrum is shown. This spectrum was obtained by preparing  $J=4$  in the excited state using R(3) with the horn population transfer pulse set at 13386.78 MHz to prepare a single eigenstate in  $J=5$ . The cavity was then scanned from 15850 MHz to 15940 MHz to record the rotational spectrum of the single eigenstate around the  $6_{06}-5_{05}$  transition. In the bottom panel the rotational coherence spectrum is shown. This spectrum was obtained by preparing  $J=4$  using R(3) at  $3339.51 \text{ cm}^{-1}$  in the excited state and monitoring the peak height of the excited state  $5_{05}-4_{04}$  rotational transition at 13386.78 MHz as the horn frequency was scanned from 15850 MHz to 15940 MHz.

### Conclusion

As can be ascertained from the Figure 6.18, each technique has advantages and disadvantages. The rotational coherence scan is easy to perform because the triple resonance signal scales with power so all the available power can be used to maximize sensitivity. At the cost of the increased sensitivity large power broadening may wipe out nearby weak transitions (or cause 3 level maser effects).<sup>50</sup> The power broadening may be taken advantage of by the fact that, for a stable upper state transition, a triple resonance scan taking only 10 averages/step and a 500 kHz step size achieves a scan rate of 1800 MHz/hr. This 'fast' survey scan can then be used to find the strongest triple resonance lines. Since the rotational coherence method monitors the peak height of an

excited state rotational transition it acts as a monitor for the laser power and frequency drift, which can then be corrected as needed. At the same time however this method has low signal to noise (6:1) because of the laser fluctuations and as a result may contain many "false" peaks due to laser 'dropouts'. Because the strength of the transition is measured by the width this makes lineshape analysis less straightforward. To provide an accurate width many narrow peaks would have to be rescanned at a lower step size. For typical DRS measurements this may be hundreds of lines.

The population transfer method typically has a high signal to noise ratio (50:1 for the strongest line) and does not generally contain "false" peaks other than ground states and possible double resonance lines. The resolution of the population transfer method is much higher because there is no power broadening and as a result many closely spaced transitions can easily be resolved. This method also has the advantage that transition strength scales with peak amplitude making lineshape analysis straightforward. However, the population transfer method requires scans at a rate of 200 MHz/hr with 10 averages, which is nearly an order of magnitude slower than a typical coherence scan.

The population transfer method also suffers in that the laser frequency is not directly monitored and may have drifted during the scan, potentially leading to missed peaks or peaks arising from populating different eigenstates. The main difficulty of this technique is setting up the optimal population transfer and polarizing pulse conditions. Typically, a lower power population transfer pulse is required. The cavity is fixed to the same frequency as the horn, and pulses are configured so that the population transfer pulse power will deplete the monitored signal. Although this has been shown to work, greater

signal gains have been achieved after optimizing the population transfer and cavity pulse conditions on a known triple resonance transition.

The coherence method can be used to obtain maximum sensitivity, as illustrated in Figure 6.18, in which the coherence method pulls out three lines that do not appear in the population transfer spectrum. In this case the lines do not appear in the population transfer spectrum because they require an order of magnitude higher polarizing pulse power. Scanning with higher polarizing pulse power can be used to obtain the spectra of the weak transitions at the cost of losing the strong transitions. Missed lines in the population transfer spectrum result from non-optimal pulse power (for either MW pulse) or possibly laser frequency drift. Missed lines in the coherence spectra typically result from too large a step size or power broadening to the extent that nearby transitions are not observed. These trade-offs can be taken advantage of by using the coherence method as both a survey scan and/or to obtain very weak transitions. The triple resonance transitions from the survey scan can then be used to optimize the population transfer conditions. By closely monitoring the laser frequency the population transfer method can be used to obtain high resolution single eigenstate spectra with a lineshape profile that can be directly analyzed. The lineshape analysis of the single eigenstate spectrum is the crux of the dynamical rotational spectroscopy experiment.<sup>4</sup>

Alternatively, for double resonance scan spanning a large frequency range that contains many eigenstates the coherence method can be used to untangle the level connectivity of the measured eigenstates, i.e. to assign each transition to a particular eigenstate. This could be achieved by using the coherence method to measure v-type

triple resonance, in which the cavity is set to a known upper state transition and the horn is scanned in the same frequency region to determine which transitions have a common upper or lower level. This can be used to obtain a crude two-dimensional scan. It is crude because it only establishes a 'yes' or 'no' connectivity, there is no intensity information. Taking a double resonance scan spanning a large frequency range and then disentangling the spectrum in this manner may be a more efficient approach than measuring multiple single eigenstate rotational spectra.

## Reference List

1. Green, D.; Holmberg, R.; Lee, C. Y.; McWhorter, D. A.; Pate, B. H., *J.Chem.Phys.* **1998**, *109*, 4407-4414.
2. Takami, M.; Suzuki, M., *J.Chem.Phys.* **1980**, *72*, 4089-4098.
3. Shimoda, K. *Laser Spectroscopy of Atoms and Molecules*; Plenum: New York, 1974.
4. Keske, J.; McWhorter, D.; Pate, B. H., *Int.Rev.Phys.Chem.* **2000**, *19*, 363-407.
5. Nesbitt, D. J.; Field, R. W., *J.Phys.Chem.* **1996**, *100*, 12735-12756.
6. Keske, J. C.; B.H.Pate, *Chem.Phys.Lett.* **2001**, *342*, 51-57.
7. Autler, S. H.; Townes, C. H., *Phys.Rev.* **1955**, *100*, 703-722.
8. Suenram, R. D.; Grabow, J. U.; Zupan, A.; Leonov, I., *Rev.Sci.Instrum.* **1999**, *70*, 2127-2135.
9. Kerstel, E. R. Th.; Lehmann, K. K.; Pate, B. H.; Scoles, G., *J.Chem.Phys.* **1994**, *100*, 2588-2595.
10. Lee, C. Y.; Pate, B. H., *Chem.Phys.Lett.* **1998**, *284*, 369-376.
11. Wötzl, U.; Stahl, W.; Mäder, H., *Can.J.Phys.* **1997**, *75*, 821-830.
12. Zhou, P.; Swain, S., *Phys.Rev.A* **1997**, *57*, 3781-3787.
13. Wodarczyk, F. J.; Wilson, E. B., *J.Chem.Phys.* **1972**, *56*, 166-176.
14. Stiefvater, O. L., *Z.Naturforsch* **1975**, *30 a*, 1742-1755.
15. Wiedenmann, K. H.; Botskor, I.; Rudolph, H.-D., *J.Mol.Spectrosc.* **1985**, *113*, 186-195.
16. Martinache, L.; Jans-Bürli, S.; Vogelsanger, B.; Kresa, W.; Bauder, A., *Chem.Phys.Lett.* **1988**, *149*, 424-428.
17. Cox, A. P.; Flynn, G. W.; Wilson, E. B., Jr., *J.Chem.Phys.* **1965**, *42*, 3094-3105.
18. McWhorter, D. A.; Hudspeth, E.; Pate, B. H., *J.Chem.Phys.* **1999**, *110*, 2000-2009.
19. Bloch, F. and Siegert, A. *Phys.Rev.* **57**, 522. 1940.

20. Grabow, J. U.; Stahl, W.; Dreizler, H., *Rev.Sci.Instrum.* **1996**, *67*, 4072-4084.
21. de Souza, A. M.; Kaur, D.; Perry, D. S., *J.Chem.Phys.* **1988**, *88*, 4569-4578.
22. Go, J.; Bethardy, G. A.; Perry, D. S., *J.Chem.Phys.* **1990**, *94*, 6153-6156.
23. Bethardy, G. A.; Perry, D. S., *J.Chem.Phys.* **1993**, *98*, 6651-6664.
24. McIlroy, A.; Nesbitt, D. J., *J.Chem.Phys.* **1990**, *92*, 2229-2243.
25. Pate, B. H.; Lehmann, K. K.; Scoles, G., *J.Chem.Phys.* **1991**, *95*, 3891-3916.
26. McIlroy, A.; Nesbitt, D. J., *J.Chem.Phys.* **1994**, *101*, 3421-3435.
27. Brummel, C. L.; Mork, S. W.; Philips, L. A., *J.Chem.Phys.* **1991**, *95*, 7041-7053.
28. Miller, C. C.; Stone, S. C.; Philips, L. A., *J.Chem.Phys.* **1995**, *102*, 75-89.
29. McWhorter, D. A.; Cupp, S. B.; Lee, C. Y.; Pate, B. H., *J.Mol.Spectrosc.* **1999**, *193*, 150-158.
30. McWhorter, D. A.; Cupp, S. B.; Lee, C. Y.; Pate, B. H., *J.Mol.Spectrosc.* **1999**, *193*, 150-158.
31. Suenram, R. D.; Lovas, F. J.; Fraser, G. T.; Matsumura, K., *J.Chem.Phys.* **1990**, *92*, 4724-4733.
32. Suenram, R. D.; Fraser, G. T.; Lovas, F. J., *J.Mol.Spectrosc.* **1991**, *148*, 114-122.
33. Hirahara, Y.; Ohshima, Y.; Endo, Y., *J.Chem.Phys.* **1994**, *101*, 7342-7349.
34. Lehmann, K. K.; Scoles, G.; Pate, B. H., *Annu.Rev.Phys.Chem.* **1994**, *45*, 241-274.
35. Nesbitt, D. J.; Field, R. W., *J.Phys.Chem.* **1996**, *100*, 12735-12756.
36. Gordy, W.; Cook, R. L. *Microwave Molecular Spectra*; John Wiley & Sons: New York, 1984; p -929.
37. Dreizler, H.; Fliege, E.; Mäder, H.; Stahl, W., *Z.Naturforsch* **1982**, *37 a*, 1266-1271.
38. Stahl, W.; Fliege, E.; Dreizler, H., *Z.Naturforsch* **1984**, *39 a*, 858-864.
39. Stahl, W.; Gripp, J.; Heineking, N.; Dreizler, H., *Z.Naturforsch* **1987**, *42 a*, 392-394.

40. Jäger, W.; Krause, H.; Mäder, H.; Gillies, C. W., *J.Mol.Spectrosc.* **1990**, *143*, 50-60.
41. Jäger, W.; Haekel, J.; Andresen, U.; Mäder, H., *Mol.Phys.* **1989**, *68*, 1287-1309.
42. Vogelsanger, B., *Z.Naturforsch* **1990**, *45 a*, 707-710.
43. Nakajima, M.; Sumiyoshi, Y.; Endo, Y., *Rev.Sci.Instrum.* **2002**, *73*, 165-171.
44. Pate, B. H., *J.Chem.Phys.* **1998**, *109*, 4396-4406.
45. Cox, A. P.; Ewart, I. C.; Stigliani, W. M., *J.Chem.Soc.Faraday Trans.* **1975**, *7*, 504.
46. Evans, J. C.; Nyquist, R. A., *Spectrochim.Acta* **1963**, *19*, 1153-1163.
47. Nyquist, R. A.; Potts, W. J., *Spectrochim.Acta* **1960**, *16*, 419-427.
48. Cupp, S.; Lee, C. Y.; McWhorter, D.; Pate, B. H., *J.Chem.Phys.* **1998**, *109*, 4302-4315.
49. McIlroy, A.; Nesbitt, D. J.; Kerstel, E. R. Th.; Pate, B. H.; Lehmann, K. K.; Scoles, G., *J.Chem.Phys.* **1994**, *100*, 2596-2611.
50. Javan, A., *Physical Review* **1957**, *107*, 1579-1588.

## Chapter 7

### Cavity FTMW Spectroscopy: Motional Narrowing of Trifluoropropyne at 6550 cm<sup>-1</sup>

#### Introduction

Rotational spectroscopy has traditionally been employed for structure determination of gas-phase molecules and clusters.<sup>1-4</sup> The high frequency resolution of the technique, especially using the method of molecular-beam Fourier transform microwave (FTMW) spectroscopy introduced by Balle and Flygare<sup>5</sup>, leads to precise determinations of the moments-of-inertia and, subsequently, the molecular geometry.<sup>1</sup> Using either the vibrational dependence of the rotational constants<sup>6-9</sup> or the small frequency shifts in the rotational frequencies caused by off-resonant Coriolis interactions<sup>10,11</sup> it has been possible to determine the potential energy curves for large amplitude motion. Microwave spectroscopy is largely responsible for our quantitative understanding of the barriers to internal rotation<sup>1,12-14</sup> and the potential energy surfaces of weakly bound clusters.<sup>3,15-17</sup> A less developed area of rotational spectroscopy is its application to the intramolecular dynamics of highly excited molecules.<sup>18-24</sup> In this chapter, the basic principles of "dynamic rotational spectroscopy" for the simple case of a highly vibrationally excited symmetric top molecule are demonstrated.

The basic principles of dynamic rotational spectroscopy for molecules with a single conformational geometry have been described in the work of Makarov<sup>25</sup> and Pate.<sup>19</sup> The extension of these ideas to isomerizing molecules has also been presented.<sup>20</sup> Experimental demonstration of the effects of intramolecular vibrational energy redistribution (IVR)<sup>21</sup> and conformational isomerization on the rotational spectrum have

also been reported.<sup>22-24,26</sup> The key feature of the rotational motion of a highly excited molecule is that the moments-of-inertia are time-dependent quantities in the presence of intramolecular vibrational energy flow and isomerization. As a result, the rotational frequency is no longer precisely defined (as it is in pure rotational spectroscopy) and the rotational frequency covers a range of frequencies that reflects the nuclear excursions during IVR or isomerization.<sup>18,19,21</sup>

The overall lineshape of the dynamic rotational spectrum is strongly influenced by the IVR rate.<sup>18,19,24</sup> When IVR is slow compared to the rotational timescale, the lineshape directly reflects the distribution of rotational frequencies of the coupled normal-mode vibrational states. In principle, the range of frequencies expected in the spectrum can be predicted from the vibrational dependence of the rotational constants. As the population exchange rate between the interacting normal-mode vibrational states increases, the rotational spectrum displays the same type of motional narrowing phenomena found in nuclear magnetic resonance (NMR) spectroscopy.<sup>27-29</sup> For a molecule with a single energetically accessible isomer structure, the rotational spectrum will narrow as the IVR exchange rate increases. In the strongly narrowed case, the line shape is expected to have a Lorentzian line shape near the center frequency. This center frequency will be shifted relative to the pure rotational spectrum reflecting the changes in the average geometry caused by vibrational excitation.

The rotational spectrum of trifluoropropyne with 6550 cm<sup>-1</sup> of vibrational energy (above the vibrational zero point energy) is presented in this chapter. A new experimental technique is presented for dynamic rotational spectroscopy that couples

pulsed infrared laser excitation with the high sensitivity of Fourier transform microwave spectroscopy.<sup>30</sup> Trifluoropropyne provides a good test of the basic principles of dynamic rotational spectroscopy. Because it is a symmetric top, the pure rotational spectrum consists of a single rotational frequency. More important, the previous microwave study of Mills provides the vibration-rotation interaction constants ( $\alpha_v$ ) for the six lowest normal-mode vibrations.<sup>31,32</sup> As will be shown below, these modes dominate the vibrational energy distribution at 6550 cm<sup>-1</sup>. This additional characterization of the molecule's rotational spectroscopy makes it possible to estimate the range of rotational frequencies expected at the excitation energy and to demonstrate the IVR narrowing phenomenon. The highly vibrationally mixed quantum states of trifluoropropyne are prepared by laser excitation in the region of the acetylenic C-H stretch first overtone. The high-resolution molecular-beam infrared spectrum of this vibrational state has been reported previously<sup>33,34</sup> and shows that the extensive normal-mode vibrational mode-coupling necessary to create vibrationally mixed molecular eigenstates is present.<sup>35,36</sup> The IVR rate of the coherently prepared acetylenic C-H stretch overtone ranges from about 1000-170 ps (a rotational dependence of the IVR rate is inferred from the J-dependence of the linewidth).

## Experimental

The Fabry-Perot cavity setup<sup>37</sup> and the various MW and IR excitation sources are described in detail in chapter 2. The methods to obtain quantum-state-resolved infrared-pulsed microwave-Fourier transform microwave (IR-pulsedMW-FTMW) triple

resonance spectra were described in Chapter 6. Spectra of Trifluoropropyne (TFP) were recorded in a supersonic expansion using a mixture of 2% TFP in an 80%/20% He/Ne carrier gas sample. The mixture was then expanded into a vacuum using a pulsed valve (Series 9, General Valve, 10 Hz, 1 mm orifice). TFP was obtained from Aldrich Chemical Company (97% purity) and used without further purification.

Figure 7.1 shows the ground state depletion spectrum<sup>38,39</sup> of TFP in the v=2 region of the acetylenic C-H stretching mode. To record this spectrum, the 2<sub>0</sub>-1<sub>0</sub> ( $J_K$  nomenclature) amplitude of the ground state rotational transition was monitored with the FTMW spectrometer at 11511.81 MHz<sup>31</sup> while the infrared laser was scanned in frequency around the v=2 CH stretch of TFP (6557-6559 cm<sup>-1</sup>). The infrared laser was fired ~1  $\mu$ s before the polarizing FTMW microwave pulse. As described in detail in chapter 4 a change of the FID amplitude is detected whenever the IR laser is resonant with an infrared transition involving either the J=2 or J=1 ground state rotational levels. As can be seen in Figure 7.1, there is a directionality to the observed signal that arises from molecules being populated in either the J=1 or J=2 levels in the expansion ( $T_{rot} \sim 2K$ ). Population removed from the J=1 level through laser excitation induces a depletion of the FID signal and corresponds to a dip in the spectrum. Alternatively, population removed from J=2 by laser excitation increases the population difference between the J=1 and J=2 levels, producing a gain in the monitored signal strength. This figure demonstrates the selectivity of the laser to excite ground state population from either the J=1 or J=2 levels.

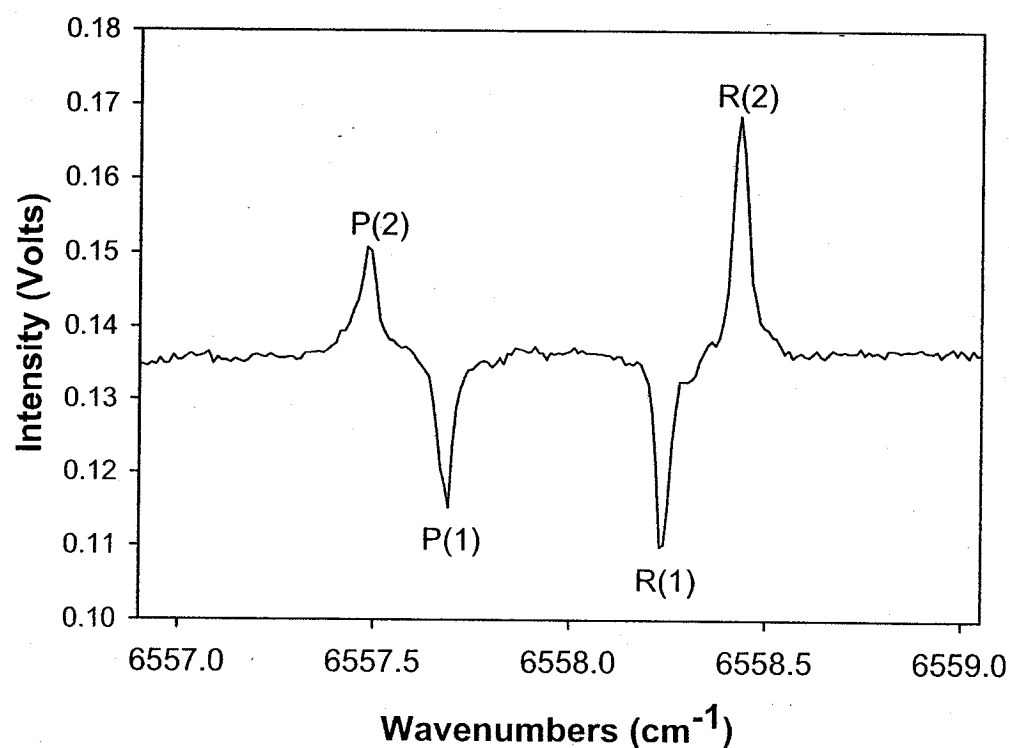


**Figure 7.1** The ground state depletion spectrum of trifluoropropyne. This spectrum was recorded by monitoring the free induction decay (FID) of the 2-1 rotational transition in the ground state (11511.81 MHz) and tuning the infrared laser over the  $v=2$  region of the  $2\nu_1$  acetylenic hydride stretching mode. The depletion signal arises from infrared transitions that occur out of the lower state ( $J=1$ ), while the gain signal arises from transition that occur out of the upper state ( $J=2$ ). P and R branch transitions are labeled in the figure.

## Results

### A. Infrared-Microwave Double-Resonance Spectroscopy

Infrared-microwave double-resonance spectra of TFP are obtained by tuning the laser to a single R-branch transition and measuring the rotational spectrum by scanning the cavity of the FTMW spectrometer. Other than the addition of the pulsed IR laser, this technique is equivalent to the measurement of the pure rotational spectrum by FTMW spectroscopy. The double-resonance spectra following laser preparation of  $J=1$  ( $R(0)$ ),  $J=2$  ( $R(1)$ ), and  $J=3$  ( $R(2)$ ) rotational levels are shown in Figure 7.2. These spectra show only the laser-induced rotational transitions (the pure rotational transitions are removed from the spectrum after data acquisition).

Three important rotational frequencies are indicated in these spectra by the vertical reference lines. The lowest rotational frequency indicates the frequency expected for the first overtone of the acetylenic C-H stretch in the absence of IVR (i.e. the unperturbed rotational frequency). This frequency is estimated from the rotational constant of the acetylenic C-H stretch fundamental. Previous high-resolution molecular-beam infrared spectroscopy has shown that several K-subbands of this vibrational state are unperturbed.<sup>34</sup> Using the IR-FTMW spectrometer the rotational constant in the C-H stretch fundamental ( $B=2873.66(1)$  MHz) from measurements of the  $K=0$  rotational transitions ( $J=2 \leftarrow 1$ : 11494.64(1) MHz,  $J=3 \leftarrow 2$ : 17241.94(1) MHz) have been determined. Our value from FTMW spectroscopy compares well with the rotational constant determined from the fit to the high-resolution infrared spectrum (2874.08(20) MHz).<sup>34</sup> The vibration-rotation constant for the acetylenic C-H stretch

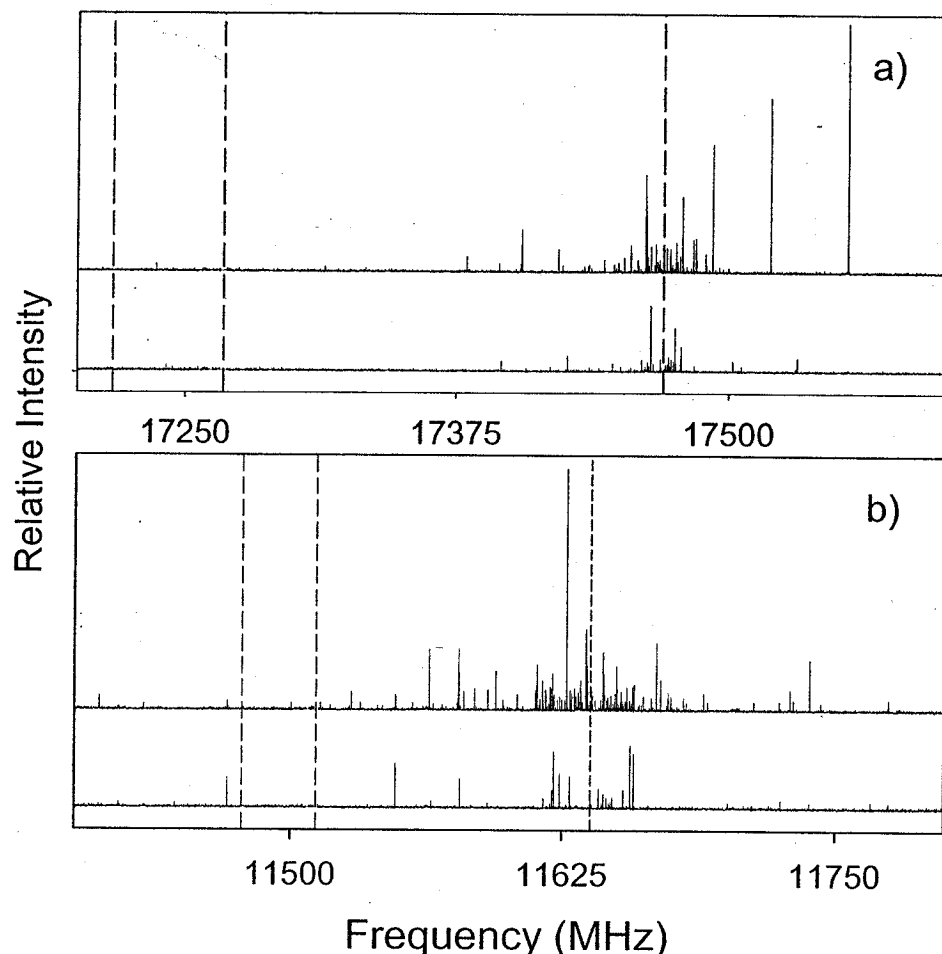


**Figure 7.2** The IR-MW double resonance spectra of trifluoropropyne following laser preparation of a)  $J=3$  (R(2), upper trace) and  $J=2$  (R(1), lower trace) and b)  $J=2$  (R(1), upper trace) and  $J=1$  (R(0), lower trace) rovibrational levels. The first set of dashed lines in a) and b) corresponds to the expected rotational transition if the excitation were localized in the acetylenic CH stretch ( $B_{\text{CH}} = 2869.39(1)$  MHz; estimated from  $v=1$ ). The second set of dashed lines corresponds to the position of the ground state rotational transition ( $B_{\text{GS}} = 2877.93$  MHz). The third set of dashed lines corresponds to the apparent average of the measured rotational transition distribution ( $\langle B \rangle = 2910 \pm 2$ ). Because the excitation step populates several single eigenstates at once, the double resonance spectra are a composite of several single eigenstate rotational spectra, giving rise to the large uncertainty in the average rotational constant.

( $\alpha_1 = 4.27(1)$  MHz) is obtained from the reported ground state rotational constant ( $B=2877.93$  MHz).<sup>31</sup> The reduction of the rotational constant upon excitation of the acetylenic C-H stretch is consistent with measurements from other small terminal acetylenes where no perturbations to the spectrum are evident.<sup>40</sup> This result is also consistent with the general expectations of rotational spectroscopy that excitation in stretching modes lowers the rotational frequency.<sup>2</sup> Using this value, the expected rotational constant for the acetylenic C-H stretch overtone is 2869.39(1) MHz. Because the centrifugal distortion constants of TFP are small,<sup>31</sup> we use the simple rigid rotor expression to calculate the rotational frequencies for the low-J rotational transitions ( $v_{ROT} = 2B(J''+1)$ ). The next lowest frequency shown in the double-resonance scans is the ground-state rotational frequency. The highest frequency reference line is determined by the clustering of rotational transitions for the highly mixed quantum states at  $6550\text{ cm}^{-1}$  prepared by laser excitation and indicates that the average rotational constant for the highly mixed quantum states is 2910(2) MHz.

The IR-FTMW double-resonance spectra show that the rotational spectrum of the molecular eigenstates near  $6550\text{ cm}^{-1}$  are shifted to higher frequency from the pure rotational spectrum. These excited state transitions also lie significantly higher than the expected frequency for an unperturbed acetylenic C-H stretch overtone. In fact, we do not observe any strong rotational transitions in this frequency region. This result implies that the vibrational quantum states of TFP are strongly mixed in this energy region so that no single zeroth-order normal-mode vibrational state makes a dominant contribution to the molecular eigenstate composition.<sup>41</sup> The other feature evident in these spectra is that

there is a spread of rotational frequencies observed for the excited vibrational eigenstates. However, it is difficult to determine the origin of this effect from the double-resonance spectra alone. This difficulty is caused by the fact that the IR excitation prepares several molecular eigenstates in this spectral region.<sup>34,42</sup> The distribution of rotational frequencies can come from a combination of the intrinsic spread of the rotational spectrum of a single molecular eigenstate and the variation in the average rotational constant for each eigenstate.<sup>19,24</sup> To remove this ambiguity we have performed the IR-pulsed-MW-FTMW triple-resonance measurements described in the next section.

### B. Infrared-pulsedMW-FTMW Triple-Resonance Spectroscopy

These measurements exploit the high-resolution of the FTMW spectrometer to obtain the rotational spectra of single molecular eigenstates at 6550 cm<sup>-1</sup>. Several eigenstates in the J=1 rotational level are prepared by IR excitation of R(0).<sup>34,42</sup> The J=2 ← 1 rotational spectra of all laser-prepared eigenstates are observed in the double-resonance spectrum shown in the lower trace of Figure 7.2b. In the triple-resonance measurement a short microwave pulse (5 μs) is used to transfer population from the IR prepared J=1 level to a single eigenstate at J=2. The frequency of the population transfer pulse is known precisely from the double-resonance measurement. The J=3 ← 2 rotational spectrum of this selectively prepared eigenstate at J=2 is then measured by scanning the FTMW spectrometer. From measurements on adjacent rotational frequencies in the double-resonance spectrum ( $\Delta v = 1.535$  MHz) we find that complete selectivity is achieved using this scheme. Because there is sufficient microwave power to saturate the

population transfer step, similar sensitivity is obtained for triple- and double-resonance measurements.

The  $J=3 \leftarrow 2$  rotational spectra of three single molecular eigenstates at the  $J=2$  level are shown in Figure 7.3. This measurement reinforces the behavior observed in Figure 7.2. All individual spectra have similar spectral properties. These properties can be characterized by calculating the spectrum center (first moment) and width (second moment).<sup>19</sup> These values are reported in Table 7.1 and illustrated in Figure 7.4.<sup>43</sup> As seen in Figure 7.4, the observed spectral centers and widths are uncorrelated with the total intensity of the spectrum suggesting that the spectral properties are well-determined.

The nature of the rotational spectroscopy of the highly vibrationally mixed quantum states of TFP at  $6550\text{ cm}^{-1}$  is illustrated in a different fashion in Figure 7.5. This figure places the spectra of Figure 7.3 on an energy scale. From "v-type" triple-resonance measurements<sup>44</sup> of the  $R(0)$  double-resonance spectrum it is possible to determine which  $J=2 \leftarrow 1$  rotational transitions share a common laser-prepared  $J=1$  eigenstate. This information makes it possible to "unfold" the spectra as shown in Figure 7.5. The rotational spectrum of each  $J=2$  eigenstate is built onto the same  $J=3$  molecular eigenstates.<sup>21</sup> This is indicated by the shared energy positions of different eigenstate rotational spectra. However, because each eigenstate has approximately the same average rotational frequency, the rotational spectrum continually shifts up this energy level pattern as the energy of the  $J=2$  eigenstate increases.

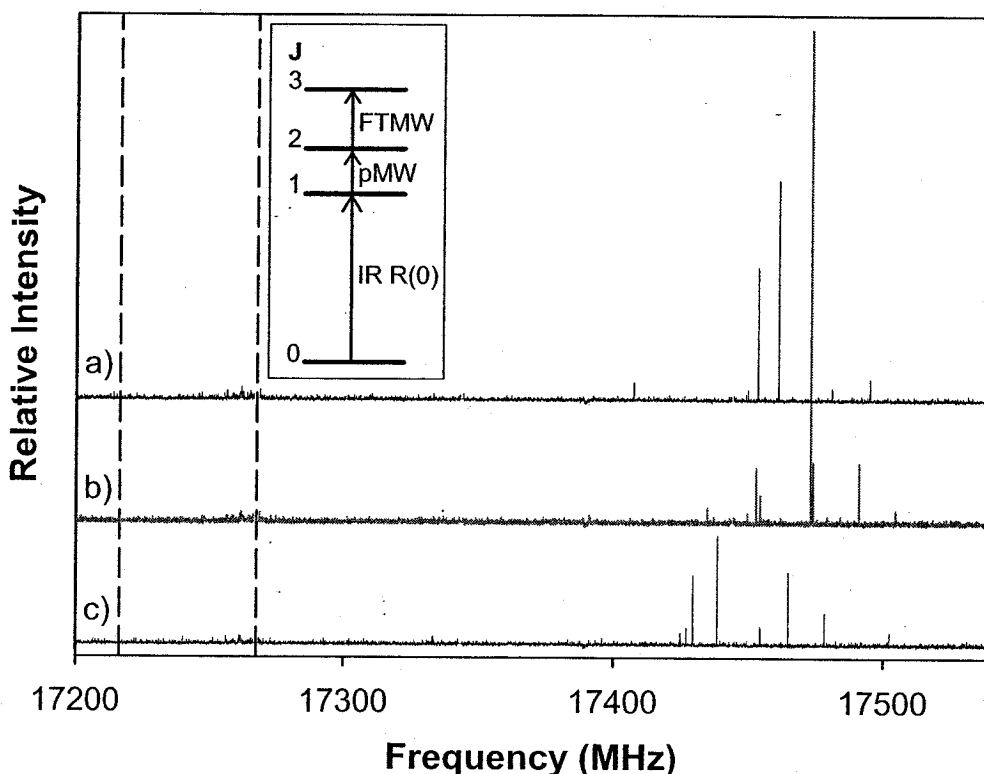


**Figure 7.3** Three single eigenstate rotational spectra of trifluoropropyne in the  $J=2$  rotational level, recorded using the IR-pMW-FTMW technique. These spectra were recorded by pumping the 2-1 rotational transitions arising from a single eigenstate in the  $J=1$  level at a) 11808.69 MHz, b) 11725.14 MHz and c) 11657.75. The lower and upper dashed lines correspond to the localized CH stretch (17216.34 MHz) and ground state (17267.58) rotational transitions, respectively. All of the single eigenstate rotational spectra are clumped in the same region of frequency space. These three spectra originate from the same eigenstate in  $J=1$ . The inset shows the triple resonance excitation scheme used to record the single eigenstate rotational spectra of trifluoropropyne.

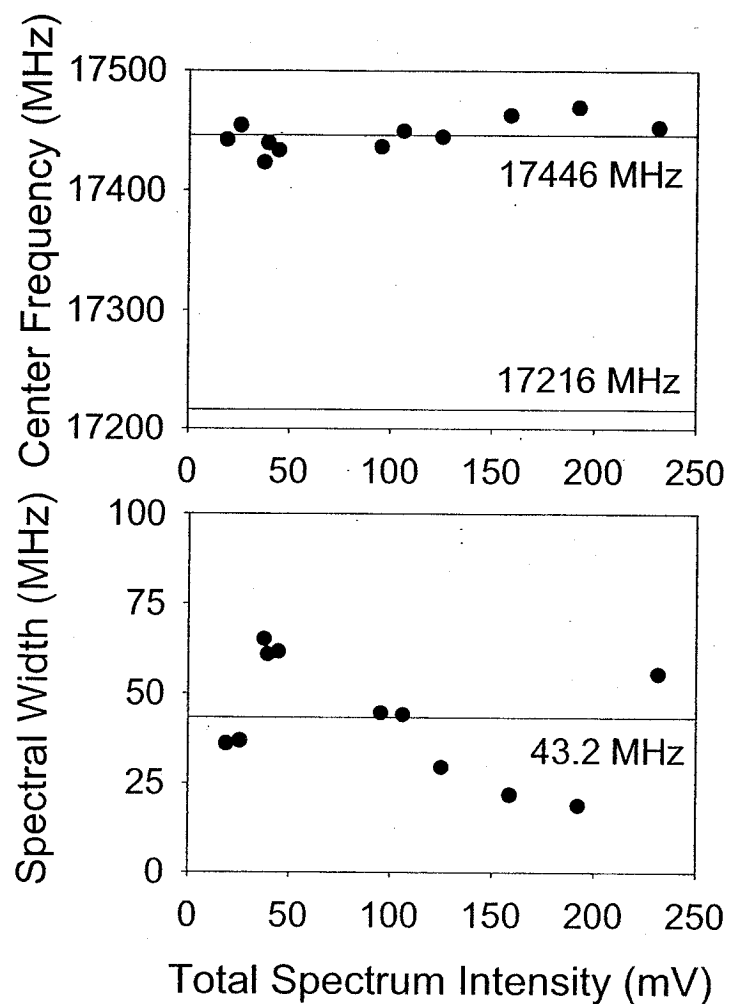


**Figure 7.4** Comparison of the average center frequency (upper trace) and distribution of the spectral width (lower trace) as a function of total spectrum intensity for the eleven measured triple resonance spectra. The center frequencies of the eleven spectra are tightly clumped about the average value of 17446 MHz, 230 MHz above the expected value at 17216 MHz.

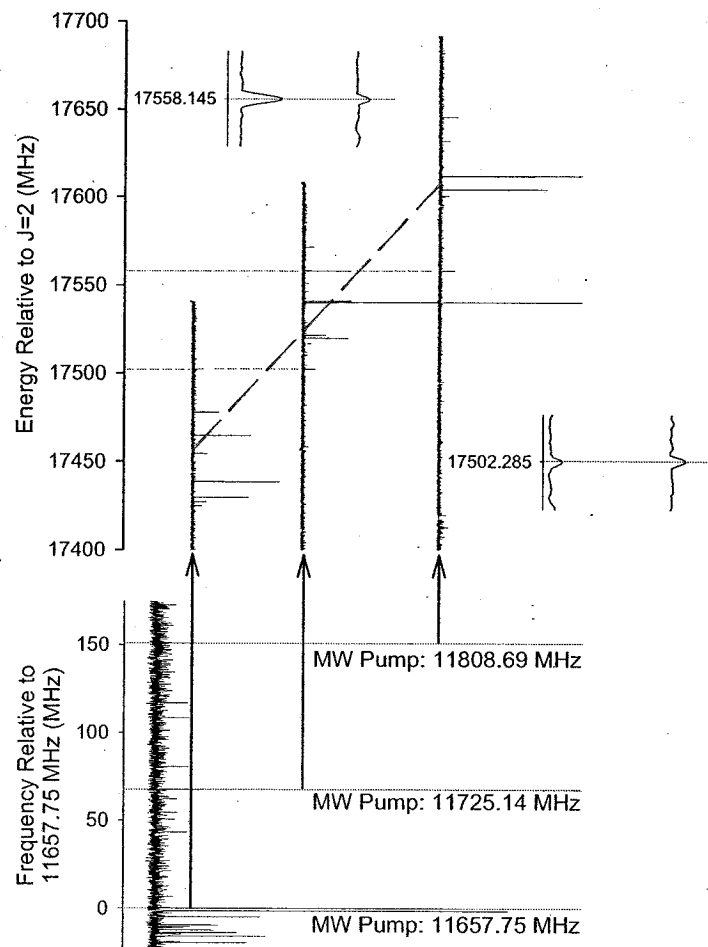


**Figure 7.5:** Energy level diagram depicting the IR-pMW-FTMW excitation scheme. The lower trace shows the double resonance spectrum obtained by scanning the 2-1 rotational spectrum after infrared excitation. The upper three traces show the resulting triple resonance spectra obtained by pumping single eigenstates at 11647.75 MHz, 11725.14 MHz and 11808.69 MHz. These three spectra are the same spectra shown in Figure 7.3, shifted in energy space. Once the energy difference between levels is known precisely and the spectra are shifted, transitions that terminate on the same upper state overlap from one spectrum to the next. The upper and lower insets are expanded by 1 MHz around common eigenstates in each of the spectra. From the lower inset, the spectra originating from the 11657.75 MHz and 11725.14 MHz intermediate levels share a common upper state at 17502.29 MHz, while the spectra originating from the 11725.14 MHz and 11808.69 MHz intermediate levels share a common upper state at 17558.14 MHz. While the spectra "slide" in energy space, the rotational transitions occur in the same region of frequency space. This is exhibited by the diagonal constant frequency tie-line connecting the three spectra and by comparison to Figure 7.3. The excitation scheme used to record the spectra is the same as that shown in Figure 7.3.

## Discussion

### A. Analysis of the Homogeneous Eigenstate Rotational Lineshape

In this section the eigenstate-resolved spectra are compared to the expected ensemble rotational properties of TFP at  $6550\text{ cm}^{-1}$  to demonstrate the IVR exchange narrowing effect<sup>19,25</sup> and to determine the time scale of energy flow in the low-frequency normal-modes. This rate determination is based on the width of the eigenstate spectra. To perform this analysis it is first necessary to remove the fluctuation of the spectral center frequencies that introduce an “inhomogeneous” contribution to the spectral width.<sup>19,23,24</sup> This is performed by shifting frequencies so that all spectra have a center frequency at the average value of the set (17446 MHz, see Figure 7.4). Also, the total intensity for each individual spectrum is normalized in this analysis.

The average lineshape for single eigenstate spectra at  $6550\text{ cm}^{-1}$  is determined by fitting the ensemble of the 11 individual normalized spectra. The cumulative intensity distribution provides a convenient method for carrying out this process for ensemble spectra with many discrete transitions.<sup>45</sup> A comparison of the experimental cumulative intensity distribution to Lorentzian line shapes with three different widths (full width at half maximum (FWHM) of 20, 40, and 60 MHz) over the measured frequency range (17200 – 17550 MHz) is shown in the left panel of Figure 7.6. From this comparison we estimate the spectral width of the Lorentzian line shape to be about 40 MHz. We have also performed this analysis using a Gaussian line shape for the eigenstate ensemble spectrum. A comparison of the best Lorentzian and Gaussian cumulative intensity distributions, both with 40 MHz FWHM, with the experimental distribution is shown in

the right panel of Figure 7.6. The Gaussian line shape cannot recover the intensity observed in the low frequency wing of the spectrum.

From this analysis, the average center frequency of the excited state rotational spectrum has been determined from the lineshape maximum to be 17456 MHz. The center frequency observed corresponds to an average rotational constant of 2909.33(33) MHz for the highly vibrationally mixed eigenstates at  $6550\text{ cm}^{-1}$ . Note that this value is 10 MHz higher than the average value of the first moments reported in Table 7.1. This difference is attributed to the asymmetric frequency range measured in the experiment. The measurement range is biased towards lower frequency because we were interested in detecting transitions that would remain near the expected acetylenic C-H stretch overtone frequency. Presumably, small peaks neglected in the high frequency wing of the spectrum would shift the average center frequency of the experimental spectrum to better match the cumulative intensity value.

### B. Comparison to the Predicted Ensemble Normal-Mode Rotational Frequency Distribution

The degree of vibrational excitation of TFP can be quantified by determining the effective microcanonical vibrational temperature at  $6550\text{ cm}^{-1}$ .<sup>46</sup> In this determination, all vibrational states in the energy range from  $6550 - 6600\text{ cm}^{-1}$  are calculated using a direct state count algorithm<sup>47</sup> and using the reported normal-mode frequencies of TFP given in Table 7.2. The frequency range used in the analysis extends to higher energy than the excitation energy to compensate for vibrational anharmonicity. There are about

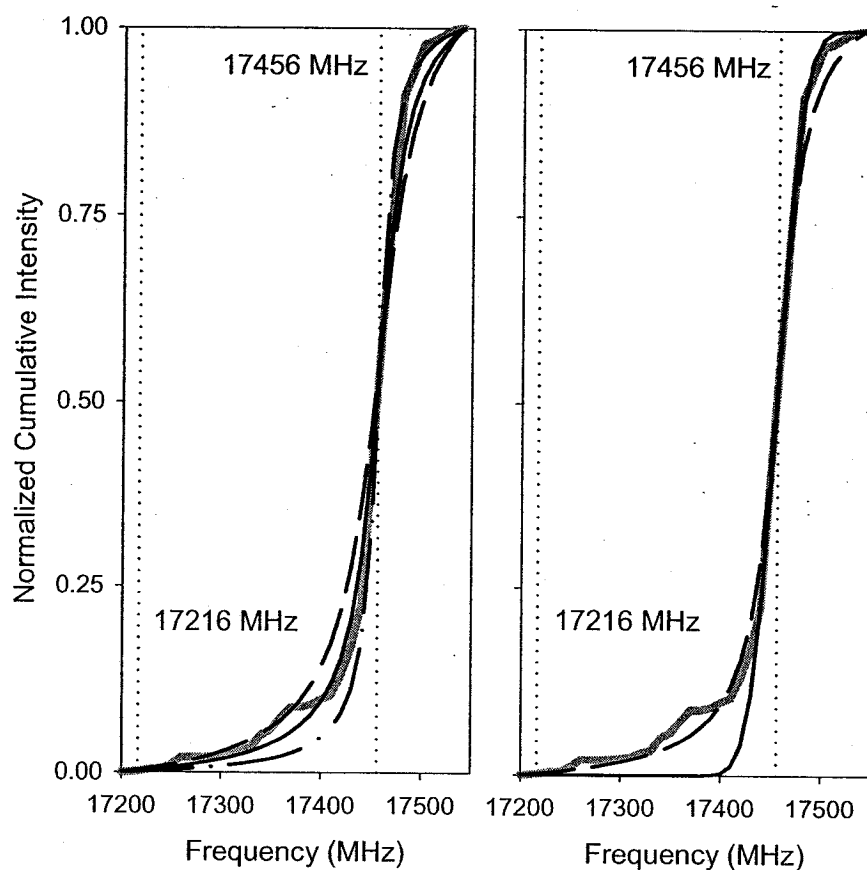


**Figure 7.6:** The left panel compares the experimentally measure cumulative intensity (solid gray line) of the eleven measured triple resonance spectra to Lorentzian lineshapes having full-width at half maximum of 20 (dot-dash line), 40 (solid line) and 60 (long dash line) MHz. The right panel compares the experimentally measured cumulative intensity (solid gray line) of the eleven measured triple resonance spectra to Lorentzian (long dash line) and Gaussian (solid line) distributions. The lower dotted vertical line in both traces corresponds to the pure acetylenic CH stretch rotational position at 17216 MHz.

Table 7.1. Spectroscopic Parameters of the Eleven Measured  
Single Eigenstate Rotational Spectra

Pump Frequency (MHz)	No. of Lines	Total Intensity (mV)	First Moment (MHz)	Second Moment (MHz)
11411.40	12	44.435	17433.181	61.709
11470.90	22	231.328	17452.434	55.520
11578.24	7	25.598	17454.288	36.804
11621.37	5	18.894	17442.116	35.965
11641.93	11	39.245	17439.493	60.919
11656.17	9	158.635	17462.641	21.790
11657.75	13	95.088	17436.393	44.559
11725.14	15	192.055	17469.202	18.824
11738.36	14	37.365	17423.196	65.226
11766.19	27	125.276	17444.718	29.429
11808.69	9	106.116	17449.403	44.129
Average			17446.097	43.170

Table 7.2. Normal Mode Frequencies and Rotational  $\alpha^B$  Constants for  $\text{CF}_3\text{CCH}$

Mode	Symmetry	Frequency ( $\text{cm}^{-1}$ ) <sup>a</sup>	$\alpha^B$ (MHz) <sup>b</sup>
$v_1$	$A_1$	3329.9	4.27
$v_2$	$A_1$	2165.4	-
$v_3$	$A_1$	1253.2	-
$v_4$	$A_1$	811.7	-0.549
$v_5$	$A_1$	536.0	-4.149
$v_6$	E	1179.0	-
$v_7$	E	686.0	2.710
$v_8$	E	612.0	-1.601
$v_9$	E	453.0	0.959
$v_{10}$	E	170.0	-5.480

<sup>a</sup> The normal mode frequencies for trifluoropropyne are from Ref. 31

<sup>b</sup> Values for  $\alpha^B$  are from Ref. 31, except for  $v_1$  which is determined in this study.

300,000 normal-mode vibrational states in this energy region. The vibrational mode population in this energy range is determined by making a histogram of the occupation number for the chosen mode over the list of normal-mode vibrational states obtained from the direct count. The histograms for the four lowest frequency normal-modes are shown in Figure 7.7. All four microcanonical population distributions are well approximated by a Boltzmann distribution with a temperature of 1200 K. If all energetically accessible zeroth-order normal-mode vibrational states are coupled by the IVR dynamics, the effective vibrational temperature of the molecule would be 1200 K.

The high microcanonical temperature of the TFP at 6550 cm<sup>-1</sup> leads to a distribution of rotational frequencies. The distribution of rotational constants in this energy region can be calculated using the experimental vibration-rotation interaction constants ( $\alpha_v$ ) listed in Table 7.2. The rotational constant of each normal-mode vibrational state found in the direct count list is estimated by the usual expression:<sup>1</sup>

$$B_v = B_e - \sum_{i=1}^{3N-6} \alpha_i \left( v_i + \frac{d_i}{2} \right) = B_0 - \sum_{i=1}^{3N-6} \alpha_i v_i \quad (7.1)$$

where  $v_i$  is the number of quanta in the  $i^{\text{th}}$  mode,  $d_i$  is the degeneracy of the  $i^{\text{th}}$  mode, and  $B_0$  is the rotational constant for the ground state.

The full normal-mode ensemble rotational constant distribution is shown in Figure 7.8. In this figure the distribution calculated using all seven known vibration-rotation interaction constants are compared with the distribution when only the lowest frequency normal-mode is included (the degenerate acetylene wag at 170 cm<sup>-1</sup>). The overall shape of the distribution is well-described using just the lowest frequency normal-

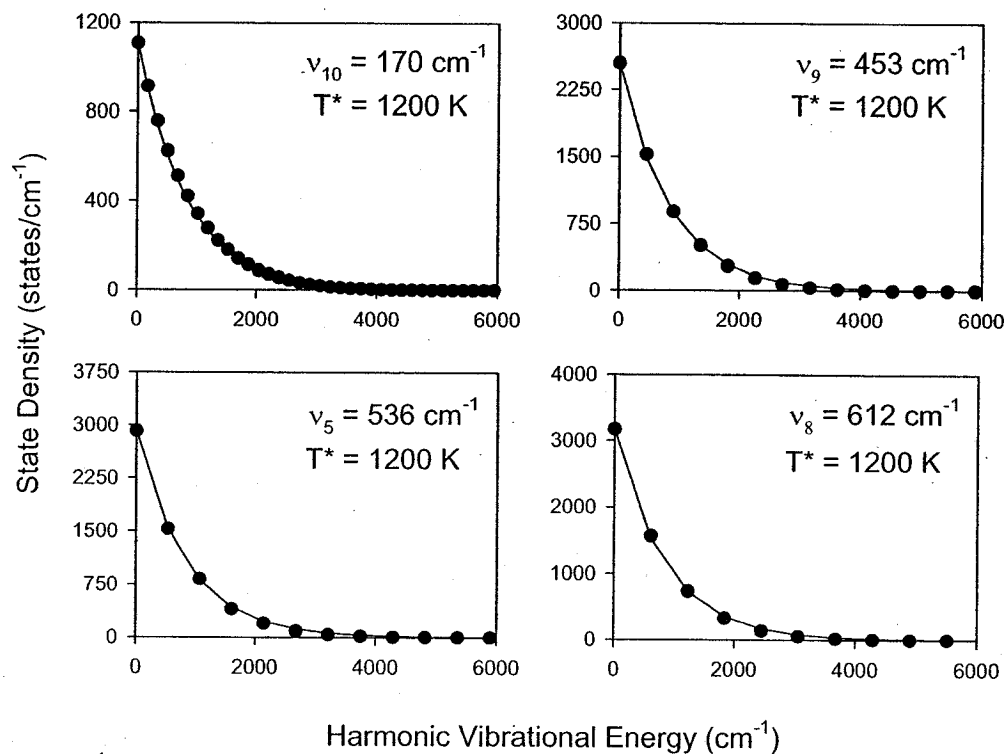


**Figure 7.7:** Population distribution for the four lowest energy vibrational modes of trifluoropropyne. Dots correspond to the number of states with  $n$  quanta in the indicated mode obtained from a direct count algorithm over the range of 6550-6600 cm<sup>-1</sup>. The solid lines correspond to a Boltzmann distribution at a microcanonical temperature of 1200 K.

mode. By the time the three lowest normal-modes are included, the bottom of Fig. 8, the full distribution is almost completely recovered. This result means that the dynamic rotational spectrum will be most sensitive to the IVR dynamics in the lowest frequency normal-modes. The three characteristic rotational constants of TFP (unperturbed  $v=2$  acetylenic C-H stretch (2869.39 MHz), ground vibrational state (2877.93 MHz), and highly excited states (2909.33 MHz)) are indicated by the vertical reference lines. The experimental rotational constant for highly excited TFP falls at the peak of the normal-mode ensemble distribution.

We have used the calculated normal-mode ensemble rotational constant distribution to estimate the extent of vibrational mixing in TFP at  $6550\text{ cm}^{-1}$ . The idea behind this analysis is illustrated in Figure 7.9. This figure shows how the normal-mode rotational constant distribution changes when there is a restriction on the total vibrational quanta for the vibrational state. When the distribution is calculated by including only those vibrational states with 5 or fewer total quanta, it is narrowly peaked around the ground state rotational constant. As the total quanta cutoff is increased, the center of the distribution moves towards the value of the full distribution and the width increases. These properties are shown quantitatively in Figure 7.10 where the average rotational constant, the distribution width (second moment), and the fraction of all vibrational states is calculated as a function of the total quanta cutoff value. In order to obtain the average rotational constant we find experimentally, the IVR dynamics needs to involve mixing of all vibrational states with 18 or fewer quanta. This limit corresponds to 73% of all energetically accessible states. These values are approximate because the linear

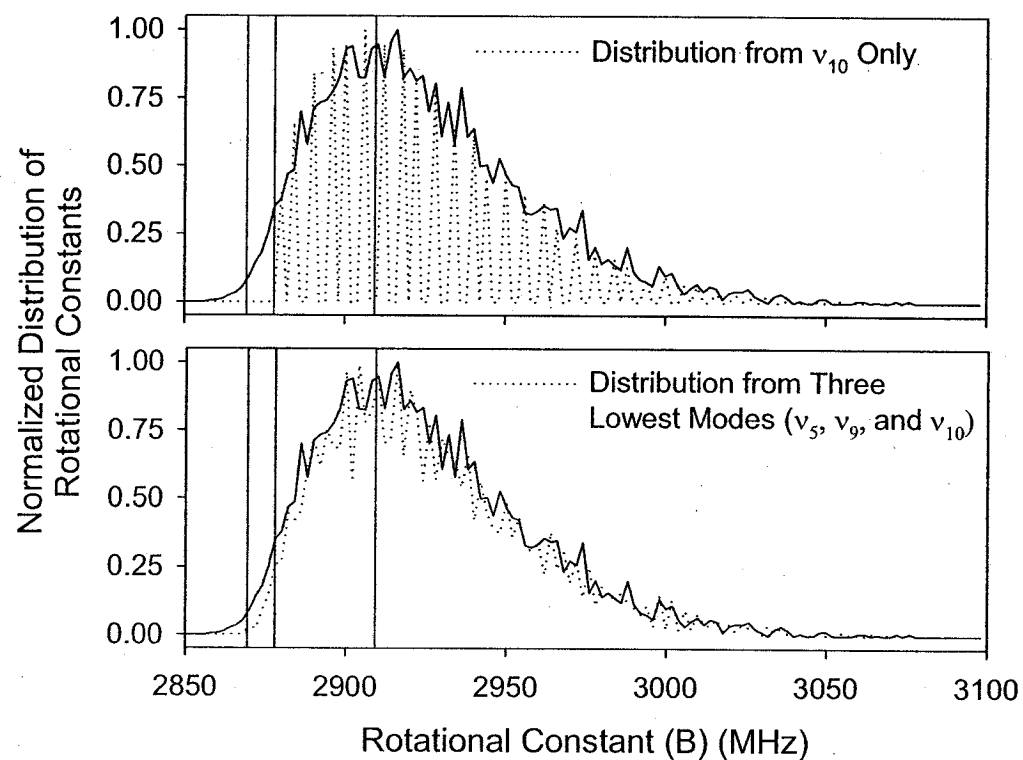


**Figure 7.8:** The upper panel compares the full normal-mode ensemble rotational constant distribution (solid line) to the distribution containing only the lowest frequency mode  $v_{10}$  (dotted line). The lower panel compares the full normal-mode ensemble rotational constant distribution (solid line) to the distribution containing only the three lowest frequency modes  $v_5$ ,  $v_9$  and  $v_{10}$ .

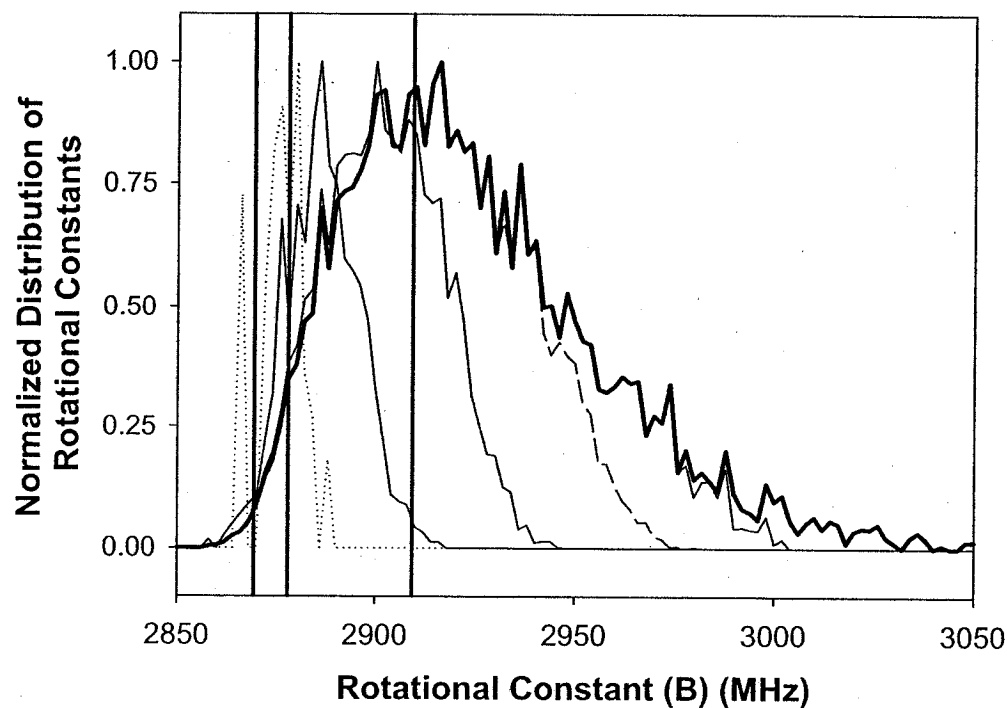


**Figure 7.9** Rotational constant distribution as a function of total quanta in a particular mode. The dotted line represents distributions that contain five or fewer quanta, the dashed line represents distributions that contain eighteen or fewer quanta, while the dark solid line represents the rotational constant distributions that contain all quanta. Intermediate cases are shown as thin solid lines. Reference lines mark the pure acetylenic CH rotational constant (lower line at the 2869 MHz) ground state rotational constant (middle line at 2878 MHz) and the measured average rotational constant from the single eigenstate rotational spectra (upper line at 2909 MHz). The distribution sharply peaked around the expected acetylenic CH stretch contain 5 or fewer total quanta. As the number of allowed quanta is increased, the mean distribution moves toward the observed average rotational constant.

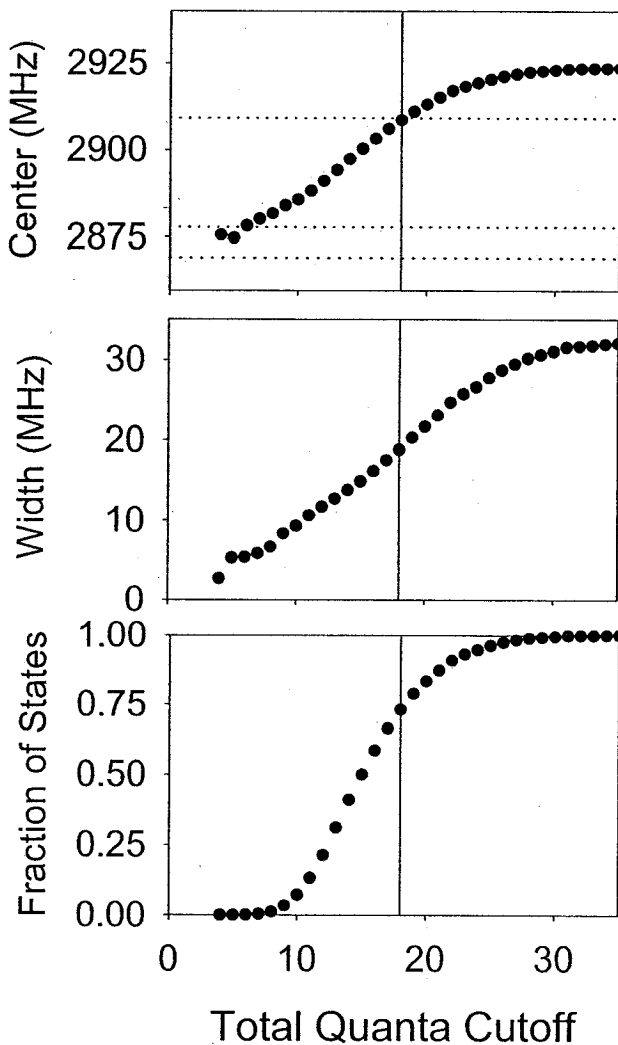


**Figure 7.10** Change in the calculated center frequency (top panel), spectral width (middle panel) and fraction of the total state density (bottom panel) as the total number of allowed quanta is increased. The horizontal lines in the top panel correspond to the ground state and measured center frequency distribution at 2878 MHz and 2909 MHz, respectively. The vertical bar corresponds to the cutoff value of 18 total quanta, which was determined by the intersection of the average center frequency with the measured frequency.

expression of Eq. (7.1) is likely to become inaccurate for the high levels of excitation in the low frequency modes that are found with a 1200 K effective vibrational temperature. Still, we believe this result is a good indication that essentially all normal-mode vibrational states of TFP at  $6550\text{ cm}^{-1}$  are coupled despite the large quanta interchange required in the intramolecular interaction matrix element.

If the rotational constant calculation of Eq. (7.1) is reasonably accurate, then the analysis of Figure 7.9 suggests that high total quanta vibrational states, which correspond to the rotational constants in the high tail of the distribution, are not participating in the dynamics. Inspection of the top panel of Fig. 10 shows that this part of the distribution is dominated by the normal-mode vibrational states with greater than 13 quanta of excitation in the lowest frequency normal-mode. Previous work on the IVR dynamics of polyatomic molecules has suggested that vibrational states with excitation localized in a low frequency normal-mode, the “extreme motion states”, are weakly coupled to other vibrational states.<sup>48-50</sup> (Although this type of localization in the more anharmonic hydride stretches may not achieve the same effect.<sup>51</sup>) If the extreme motion states are weakly interacting, then a cutoff like the one implied by Figure 7.10 is reasonable. These vibrational states are also sparse so that the product of the state density and the interaction matrix elements,  $\rho W$ , would rapidly decrease. Strong vibrational state mixing occurs for the “overlapping resonance condition” of Chirikov where  $\rho W \sim 1$ .<sup>52</sup> A decoupling of the extreme motion states might be a general feature of the IVR dynamics that could be detected by dynamic rotational spectroscopy.

### C. Estimate of the IVR Rate in the Low-Frequency Normal Modes

Finally, we use the comparison of the normal-mode ensemble rotational frequency distribution and the experimentally observed rotational lineshape to estimate the IVR exchange rate. Using the result from Figure 7.10, the rotational frequency distribution for the  $J=3 \leftarrow 2$  rotational transition is estimated using the distribution of rotational constants with 18 or fewer quanta. This cutoff value is chosen so that the experimental and normal-mode average rotational constants are the same. At this value, the width of the rotational constant distribution in the zeroth-order normal-mode vibrational states is 38 MHz (FWHM). Using this value, and the center frequency, we can define an approximate Gaussian distribution of  $J=3 \leftarrow 2$  rotational frequencies expected for highly excited TFP. This Gaussian approximation is shown with the calculated  $J=3 \leftarrow 2$  frequency distribution in Figure 7.11. The experimental eigenstate spectrum, obtained from the ensemble of 11 normalized single eigenstate rotational spectra, is also shown in this figure. The Lorentzian lineshape with FWHM of 40 MHz determined from the cumulative intensity analysis is superimposed on the experimental spectrum. This figure demonstrates the narrowing of the rotational spectrum caused by IVR exchange.

The previous theoretical description of IVR exchange narrowing used a model of a Gaussian distribution of normal-mode frequencies and appears to be appropriate for the present spectrum.<sup>19</sup> That work adapted the NMR motional narrowing formalism of Kubo<sup>27</sup> and Anderson<sup>28,29</sup> to the problem of rotational spectroscopy in the presence of IVR. It was shown that, like the case in NMR, the effect of rapid IVR is to narrow the width of the spectrum near the line center and to cause a lineshape change from Gaussian

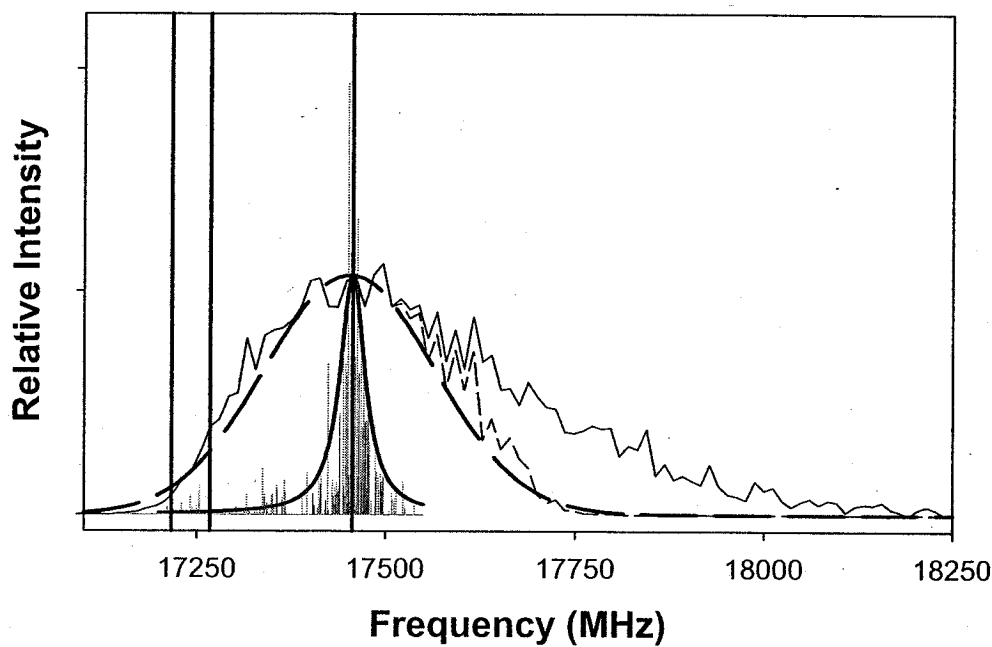


**Figure 7.11** Comparison of the full rotational constant distribution (solid line) to the rotational constant distribution containing 18 or fewer total quanta (dashed line) with a Gaussian fit (bold dashed line) to its distribution and the experimentally measured single eigenstate rotational spectra ensemble with a Lorentzian fit (bold solid line) to its distribution. The narrowing of the experimental Lorentzian distribution compared to that of the calculated Gaussian distribution illustrates the effect of IVR exchange narrowing.

to Lorentzian (near the center). These features are observed in Figure 7.11. When the widths of both the normal-mode and experimental frequency distributions are known, the IVR exchange rate can be estimated using the limiting form for a strongly narrowed spectrum<sup>19</sup>

$$\Delta\nu_{obs} = \Gamma_{rot} \frac{\Gamma_{rot}}{\Gamma_{IVR}} = 2(J''+1)\sigma(B) \frac{2(J''+1)\sigma(B)}{\Gamma_{IVR}} \quad (7.2)$$

where  $\Gamma_{rot}$  is the dephasing rate caused by the spread in zeroth-order rotational frequencies and  $\Gamma_{IVR}$  is the IVR rate.

For TFP, the normal-mode rotational width ( $\Gamma_{rot}$ ) is estimated to be 226 MHz (FWHM) and the observed width of the narrowed spectrum is 40 MHz (FWHM). Using Eq. (7.2) we estimate an IVR exchange rate of 1280 MHz, corresponding to an exchange time scale of 120 ps. As indicated by Figure 7.8, we believe that this time scale can be interpreted as the IVR exchange rate in the lowest frequency normal-mode. When compared to the high-resolution molecular-beam infrared spectrum, this rate is about 5-10 times faster than the rate at which energy is redistributed from the v=2 level of the acetylenic C-H stretch at the same rotational level.

A less direct method is also described for estimating the IVR rate from eigenstate-resolved rotational spectra.<sup>24</sup> This method is based on how the properties of the single-eigenstate rotational spectrum change as the extent of vibrational mixing increases. If there is no IVR (state mixing), then each normal-mode vibrational state would have an

unperturbed rotational spectrum with a single rotational transition. However, these rotational transitions would have the distribution of center frequencies shown in Figure 5. As the state mixing increases, the properties of the normal-mode ensemble pass into the spectra of single eigenstates. This behavior just reflects the fact that each molecular eigenstate could be represented as a linear combination of the interacting zeroth-order normal-mode vibrational states. In this way, the original ensemble properties are encoded into each "microcanonically averaged" quantum state.

In the limit of strong state mixing, each eigenstate spectrum has the same center frequency. However, it acquires a width (more accurately, a second moment) that matches the original normal-mode ensemble frequency distribution. Using random matrix modeling<sup>53</sup> we have shown that the standard deviation of the eigenstate rotational constants, which are obtained from the center frequencies of the rotational spectrum, is related to the normal-mode rotational constant distribution in the following way<sup>24</sup>

$$\sigma(\langle B \rangle_i) = \frac{\sigma(B)}{\sqrt{N_{\text{eff}}}} \quad (3)$$

Here,  $N_{\text{eff}}$  is a measure of the effective number of interacting normal-mode vibrational states. This quantity is frequently used to characterize vibrational spectra in an IVR regime.<sup>53,54</sup>

From the data in Table I, the standard deviation of the eigenstate rotational constants is 2.12 MHz. The standard deviation of the normal-mode rotational constant distribution with the 18 total quanta restriction is 18.83 MHz. This gives the value of the effective number of coupled states:  $N_{\text{eff}} = 80$ . This value places the spectrum in the

strongly mixed limit as expected based on the spectral properties we observe. We have also shown than there is a scaling relationship between  $N_{\text{eff}}$  and the measure of mixing,  $\rho W$ .<sup>19</sup> For  $N_{\text{eff}}=80$ , we estimate the value of this quantity as  $\rho W \sim 5$ . The density is known directly from the mean level spacing in the single eigenstate spectra and is about 5000 states/cm<sup>-1</sup> at J=3. This implies a root-mean-squared interaction matrix element (W) of about 0.001 cm<sup>-1</sup> in this energy region. This value agrees with the previous determination of the interaction matrix element using a Lawrence-Knight deconvolution<sup>55,56</sup> of the high-resolution molecular-beam infrared spectrum (0.0011 cm<sup>-1</sup>). With the value of  $\rho$  and W we estimate an IVR rate of 940 MHz (time scale of 165 ps). This rate is consistent with the rate derived from the IVR exchange narrowing line width analysis.

The relatively fast IVR rate in the low-frequency normal modes has one important implication for the rotational spectrum. In our previous description of the IVR exchange narrowing process we also considered the effects of the fluctuation of the dipole moment during IVR.<sup>19</sup> It was shown that the rotational spectrum of molecules undergoing IVR has two contributions. One part of the spectrum depends on the average dipole moment in the energy regime. This part of the spectrum was termed the "pure rotational" spectrum in the eigenstate basis. This part of the spectrum undergoes the IVR exchange narrowing process we have observed in TFP. The spectrum arising from the normal-mode vibrational dependence of the dipole moment behaves like a vibrational spectrum in the eigenstate basis. This part of the spectrum *broadens* as the IVR exchange rate increases. In the present analysis we find that the relative widths of these spectra are

about 40:1. Therefore, the transitions arising from the variation in the dipole moment should be spread over such a wide spectral range that the "pure rotational" contribution dominates the spectrum.

### Conclusions

A new experimental technique based on FTMW spectroscopy has been used to measure the rotational spectra of highly excited molecules. This spectrometer provides high-sensitivity and resolution. These features have made it possible to obtain eigenstate-resolved rotational spectra in the high state density region ( $5000 \text{ states/cm}^{-1}$  at  $J=3$ ) of the acetylenic CH stretch first overtone of TFP. The triple-resonance technique required to obtain eigenstate-resolved spectra is simple to implement. Because the infrared laser and microwave population transfer pulse are set to a constant frequency, the spectrum acquisition uses the same methods as pure rotational spectroscopy in FTMW spectrometers. The wide variety of pulsed laser sources that can be used with this system offer new opportunities for preparing highly excited molecules for dynamic rotational spectroscopy.

The rotational spectroscopy of TFP at  $6550 \text{ cm}^{-1}$  provides a simple illustration of the principles of dynamic rotational spectroscopy. The availability of the vibrational dependence of the rotational constants in most of the normal-modes has made it possible to illustrate the effect of IVR exchange narrowing. The information about the IVR dynamics obtained from dynamic rotational spectroscopy complements the results from high-resolution infrared spectroscopy of the acetylenic C-H stretch overtones. The

infrared measurements provide the time scale for energy leaving a coherently prepared high-frequency vibrational state. In contrast, the rotational measurement is sensitive to the dynamics of the low frequency modes in the "statistically relaxed" molecule. One advantage of rotational spectroscopy is that faster dynamics lead to narrowing of the rotational spectrum. Unlike the situation in vibrational spectroscopy, the transition intensities become stronger as the IVR rate increases. Even for very highly excited molecules, it should still be possible to obtain a "high-resolution" rotational spectrum. The narrowing of the spectrum by fast IVR within a single isomer is important to the application of dynamic rotational spectroscopy to isomerizing systems because it insures that the dominant cause of spectral broadening is the frequency modulation associated with changes in isomer geometry.<sup>24,41</sup>

## References

1. Gordy, W. and Cook, R. L., *Microwave Molecular Spectra*, 3rd. (John Wiley & Sons, New York, 1984).
2. Townes, C. H. and Schawlow, A. L., *Microwave Spectroscopy*, Dover Publications, New York, 1975).
3. A. C. Legon, *Annu.Rev.Phys.Chem.* **1983** *34*, 275.
4. C. C. Costain, *J.Chem.Phys.* **1985** *29*, 864.
5. T. J. Balle, W. H. Flygare, *Rev.Sci.Instrum.* **1981** *52*, 33.
6. R. Meyer, J. C. Lopez, J. L. Alonso, S. Melandri, P. G. Favero, and W. Caminati, *J.Chem.Phys.* **1999** *111*, 7871.
7. D. G. Melnik, S. Gopalakrishnan, T. A. Miller, and F. C. De Lucia, *J.Chem.Phys.* **2003** *118*, 3589.
8. F. J. Wodarczyk and E. B. Wilson, *J.Chem.Phys.* **1972** *56*, 166.
9. O. L. Stiefvater and E. B. Wilson, *J.Chem.Phys.* **1969** *50*, 5385.
10. D. R. Herschbach, *J.Chem.Phys.* **1957** *27*, 1420.
11. D. R. Herschbach, *J.Chem.Phys.* **1958** *31*, 91.
12. D. R. Herschbach and J. D. Swalen, *J.Chem.Phys.* **1957** *27*, 100.
13. D. R. Herschbach and J. D. Swalen, *J.Chem.Phys.* **1958** *29*, 761.
14. B. M. Landsberg and R. D. Suenram, *J.Mol.Spectrosc.* **1983** *98*, 210.
15. K. R. Leopold, G. T. Fraser, S. E. Novick, and W. Klemperer, *Chem.Rev.* **1994** *94*, 1807.
16. W. Klemperer, *Faraday Discuss.Chem.Soc.* **1977** *62*, 179.
17. G. T. Fraser, *Int.Rev.Phys.Chem.* **1991** *10*, 189.
18. A. A. Makarov, *Opt.Spectrosc.(USSR)* **1987** *62*, 697.
19. B. H. Pate, *J.Chem.Phys.* **1998** *109*, 4396.

20. B. H. Pate, *J.Chem.Phys.* **1999** *110*, 1990.
21. D. Green, R. Holmberg, C. Y. Lee, D. A. McWhorter, and B. H. Pate, *J.Chem.Phys.* **1998** *109*, 4407.
22. D. A. McWhorter and B. H. Pate, *J.Phys.Chem.A* **1998** *102*, 8795.
23. D. Green, S. Hammond, J. Keske, and B. H. Pate, *J.Chem.Phys.* **1999** *110*, 1979.
24. J. Keske, D. McWhorter, and B. H. Pate, *Int.Rev.Phys.Chem.* **2000** *19*, 363.
25. A. A. Makarov, *Opt.Spectrosc.(USSR)* **1987** *62*, 697.
26. E. Hudspeth, D. A. McWhorter, and B. H. Pate, *J.Chem.Phys.* **1997** *107*, 8189.
27. R. Kubo and, K. Tomita, *J.Phys.Soc.Japan* **1954** *9*, 888.
28. P. W. Anderson and P. R. Weiss, *Rev.Mod.Phys.* **1953** *25*, 269.
29. P. W. Anderson, *J.Phys.Soc.Japan* **1954** *9*, 316.
30. K. O. Douglass, J. C. Keske, F. S. Rees, K. Welch, Yoo.H.S., B. H. Pate, I. Leonov, and R. D. Suenram, *Chem.Phys.Lett.* **2003** *376*, 548.
31. I. M. Mills, *Molec. Phys.* **1969** *16*, 345.
32. Pate, B. H., *High-resolution infrared spectroscopy of acetylenic compounds: vibrational dynamics in the fundamental and first overtone of the acetylenic C-H stretch.*, PhD Dissertation, 1992.
33. K. K. Lehmann, B. H. Pate, and G. Scoles, *J.Chem.Soc.Faraday Trans.* **1990** *86*, 2071.
34. B. H. Pate, K. K. Lehmann, and G. Scoles, *J.Chem.Phys.* **1991** *95*, 3891.
35. K. K. Lehmann, G. Scoles, and B. H. Pate, *Annu.Rev.Phys.Chem.* **1994** *45*, 241.
36. D. J. Nesbitt and R. W. Field, *J.Phys.Chem.* **1996** *100*, 12735.
37. R. D. Suenram, J. U. Grabow, A. Zupan, and I. Leonov, *Rev.Sci.Instrum.* **1999** *70*, 2127.
38. K. O. Douglass, J. E. Johns, P. M. Nair, G. G. Brown, F. S. Rees, and B. H. Pate, *J. Mol. Spectrosc.* **2006** *239*, 29

- 39 M. Nakajima, Y. Sumiyoshi, and Y. Endo, *Rev.Sci.Instrum.* **2002** *73*, 165.
- 40 J. E. Gambogi, E. R. Th. Kerstel, K. K. Lehmann, and G. Scoles, *J.Chem.Phys.* **1994** *100*, 2612.
- 41 J. C. Keske and B. H. Pate, *Chem.Phys.Lett.* **2001** *342*, 51.
42. J. E. Gambogi, M. Becucci, C. J. Obrian, K. K. Lehmann, and G. Scoles, *Ber.Bunsenges.Phys.Chem.* **1995** *99*, 548.
43. K. O. Douglass, B. C. Dian, G. G. Brown, J. E. Johns, P. M. Nair, and B. H. Pate, *J.Chem.Phys.* **2004** *121*, 6845
44. M. Takamiand, M. Suzuki, *J.Chem.Phys.* **1980** *72*, 4089.
45. S. Mukamel, J. Sue, and A. Pandey, *Chem.Phys.Lett.* **2004** *105*, 134.
46. C. E. Klots, *J.Chem.Phys.* **1989** *90*, 4470.
47. S. E. Steinand B. S. Rabinovitch, *J.Chem.Phys.* **1973** *58*, 2438.
48. Y. S. Choiand C. B. Moore, *J.Chem.Phys.* **1991** *94*, 5414.
49. G. Hoseand, H. S. Taylor, *Chem.Phys.* **1984** *84*, 375.
50. J. Main, C. Jung, and H. S. Taylor, *J.Chem.Phys.* **2000** *107*, 6577.
51. M. J. Davis, G. A. Bethardy, and K. K. Lehmann, *J.Chem.Phys.* **1994** *101*, 2642.
52. B. V. Cherikov, *Phys.Rep.* **1979** *52*, 265.
53. D. S. Perry, *J.Chem.Phys.* **1993** *98*, 6665.
54. H. L. Kim, T. J. Kulp, and J. D. McDonald, *J.Chem.Phys.* **1987** *87*, 4376.
55. W. D. Lawrance and A. E. W. Knight, *J.Phys.Chem.* **1985** *89*, 917.
56. K. K. Lehmann, *J. Phys. Chem.* **1991** *95*, 7556.

## Chapter 8

### Cavity FTMW Spectroscopy: Conformational Isomerization Dynamics of Pent-1-en-4-yne

#### Introduction

Rotational spectroscopy is one of the most powerful tools in physical chemistry for the determination of gas-phase molecular structure.<sup>1-3</sup> The development of molecular beam spectrometers for rotational spectroscopy, most notably the Fourier transform microwave (FTMW) spectroscopy technique introduced by Balle and Flygare<sup>4</sup>, has greatly expanded the range of chemical systems that can be studied so that high-resolution rotational spectroscopy can be routinely applied to the conformers of large molecules<sup>5</sup>, weakly bound molecular complexes<sup>3;6</sup>, and radicals.<sup>7;8</sup> Rotational spectroscopy of low energy vibrational and torsional levels can also be used to determine accurate potential energy surfaces for large amplitude motion in “floppy” systems.<sup>9;10</sup> In this chapter rotational spectroscopy is applied to determine isomerization kinetics from the rotational spectrum of a highly vibrationally excited molecule.

Several experiments have demonstrated that the rotational spectrum can be used to probe dynamical effects such as intramolecular vibrational redistribution (IVR) and isomerization for gas-phase molecules that are excited to high-energy regions of the potential surface.<sup>11-14</sup> In this energy region molecular geometry is no longer static. As nuclei begin to move on the time scale of molecular rotation, the moments of inertia become time-dependant quantities. As a consequence, the rotational spectrum is no longer precisely defined by a single molecular geometry, as it is in pure rotational

spectroscopy, but covers a frequency range that is described by the extent of nuclear motion. The basic development for the theory of rotational spectroscopy in the presence of intramolecular vibrational redistribution (IVR) has been developed by Makarov<sup>15</sup> and Pate<sup>16</sup> and extended to isomerization reactions by Pate.<sup>17</sup>

The aim of this chapter is to measure the isomerization rate for the molecule pent-1-en-4-yne (hereafter referred to as pentenyne). Pentenyne consists of two conformational isomers (*cis* and *skew*) that undergo isomerization in the energy region of the acetylenic C-H stretch fundamental. The torsional potential is illustrated in Figure 8.1. The relaxed potential surface was calculated using G98W<sup>18</sup> at the B3LYP/6-31G\*\* level of theory. The torsional wavefunction probabilities are shown for the lowest torsional levels<sup>19</sup> of the more stable *cis* and less stable *skew* conformations. The ground state wavefunction probabilities are regular and localized around a particular molecular geometry. Also shown is a depiction of the torsional wavefunction probability at the excitation energy of the experiment ( $\sim 3330 \text{ cm}^{-1}$ ). At this energy, the intramolecular dynamics mix the near-resonant torsion-vibration states. The isomerization process causes the eigenstates of the vibrationally excited molecule to be mixed and contain character of *cis*, *skew*, and delocalized geometries. Dynamical information is obtained by measuring the rotational spectra of the mixed molecular eigenstates.

### Experiment

The Balle-Fygare type cavity FTMW spectrometer<sup>4</sup> and the pulsed infrared laser used in this experiment have been described in detail in chapter 2. The coherence method of IR-FTMW-pulsed-MW triple resonance described in chapter 6 for obtaining

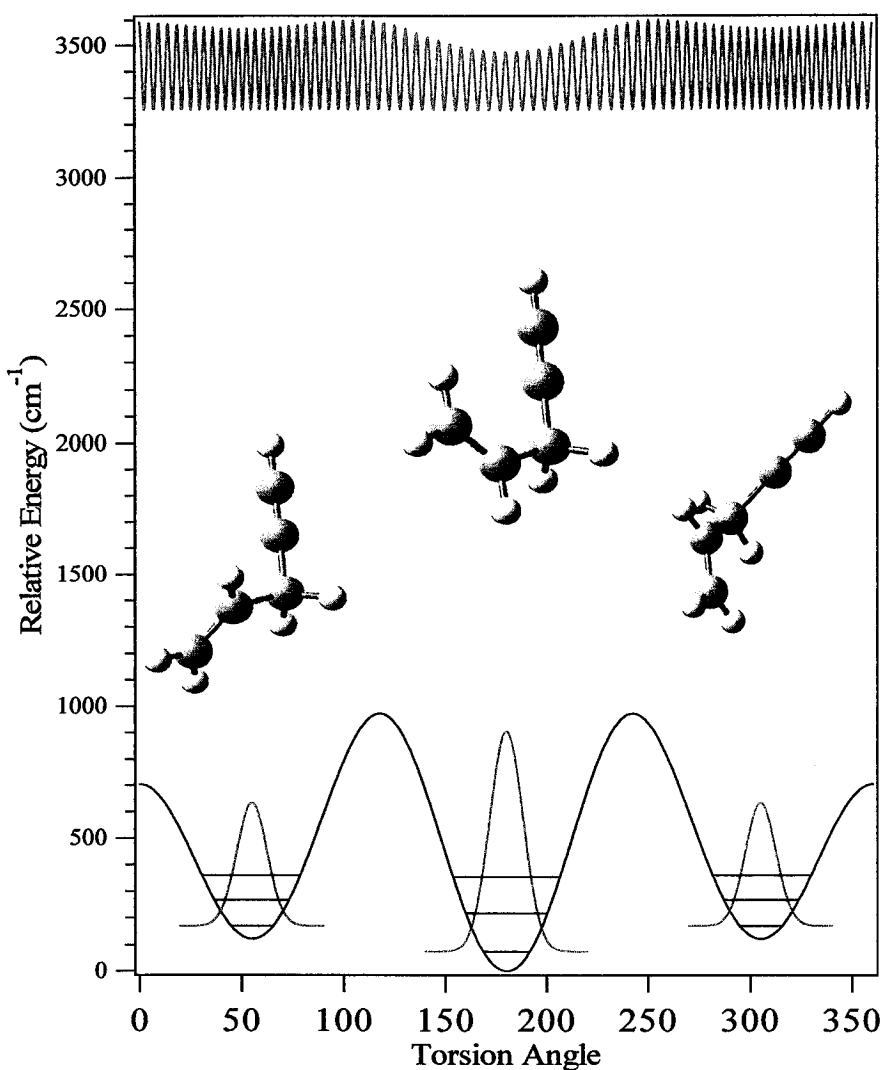


**Figure 8.1** Diagram showing the one-dimensional potential energy surface (PES) of pent-1-en-4-yne corresponding to torsional rotation about the isomerization coordinate calculated at the B3LYP/6-31G\*\* level of theory. Superimposed on the PES are the torsional levels (black lines) calculated by the methods outlined in Ref. 19. The molecular structures corresponding to the ground state conformations are shown above each well. The red lines correspond to the probability distributions of the wavefunction at the relevant energy levels. The ground state torsional probability exhibits localized character within each conformational well represented by the fact that the energy levels lie below the barrier to isomerization. The upper trace represents a typical probability distribution at  $\sim 3330\text{ cm}^{-1}$  (energy of IR excitation). This wavefunction is structurally mixed, as it lies above the barrier to isomerization, and has significant probability density over each conformational well.

rotational spectra of single eigenstates will be implemented. Triple resonance spectroscopy will be used to gain insight into the connectivity of the various eigenstates obtained in the IR-FTMW double resonance spectrum. The IR-FTMW double resonance spectrum measures the rotational spectrum of many eigenstates populated by the pulsed laser excitation.

The various rotational spectra of pentenyne were recorded in a supersonic expansion using a mixture of ~ 0.5 % pentenyne in an 80/20 He/Ne carrier gas sample. The mixture was then expanded into a vacuum using a pulsed valve (Series 9, General Valve, 10 Hz, 0.8 mm orifice). Pentenyne was obtained from GFS Chemical Company (98% purity) and used without further purification.

## Results

### A. Pure Rotational Spectrum

The first step before any dynamics experiments can be conducted is to measure and assign the pure rotational spectrum. The pure rotational spectrum obtained using the cavity FTMW spectrometer is illustrated in Figure 8.2. Also illustrated are the simulated spectra of the *cis* and *skew* conformers using SPCAT.<sup>20</sup> The pure rotational spectrum of the *cis* and *skew* pentenyne conformers were fit using jb95 spectral fitting program using 19 and 24 lines with a fit uncertainty of 5.387 and 4.764 kHz respectively. Table 8.1 and 8.2 contains the rotational constants obtained from the fit and *ab initio* calculations.

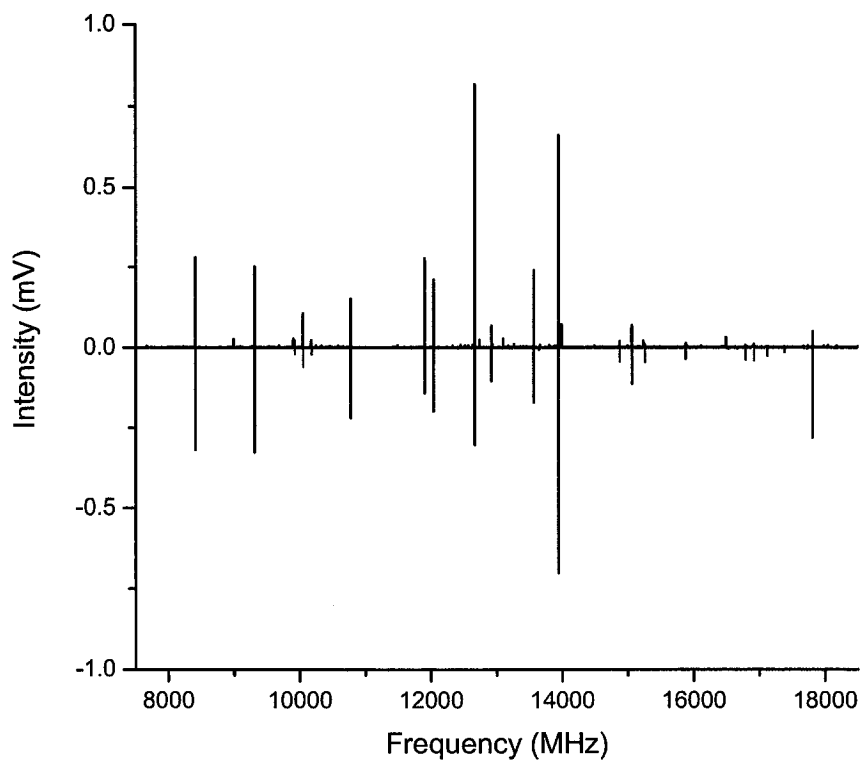


**Figure 8.2.** The ground state rotational spectrum is shown for pent-1-en-4-yne (black). Also shown are the simulated spectra for the *cis* (blue) and *skew* (red) conformers using fit constants and the SPCAT spectral simulation program.

**Table 8.1:** Ground State Spectroscopic Constants for *Cis* and *Skew* Pent-1-en-4-yne

	<i>cis</i>	<i>skew</i>
<b>Rotational Constants</b>		
A / MHz	11178.41187	19235.37629
B / MHz	3600.727536	2576.171111
C / MHz	2767.672278	2446.668675
$\Delta J$ / MHz	2.48E-03	1.74E-03
$\Delta JK$ / MHz	-1.52E-02	-7.78E-02
$\delta K$ / MHz	5.47E-02	
$\delta J$ / MHz	8.36E-04	1.88E-04
N	19	24
std. dev. / kHz	5.387	4.764

**Table 8.2:** Ab Initio Molecular Parameters<sup>a</sup>

		<i>cis</i>	<i>skew</i>
A	/ MHz	11341	19141
B	/ MHz	3487	2546
C	/ MHz	2711	2424
$\mu_A$	/ Debye	0.36	-0.462
$\mu_B$	/ Debye	0.53	-0.329
$\mu_C$	/ Debye	0.00	-0.09
$E_{rel}$	/ cm <sup>-1</sup>	0.00	133
Barrier	/ cm <sup>-1</sup>	968	835

<sup>a</sup>Calculated at the B3LYP/6-31+G\* Level of Theory<sup>b</sup>Rotated to the Principle AxesCis-->Skew and Skew-->Cis Barrier Height Reported  
in Each Column

### B. Infrared Spectrum

The high resolution IR spectrum of the *cis* conformer of pentenyne was previously recorded in the Pate lab using the electric resonance optothermal spectrometer (EROS) and a high resolution cw laser (6 MHz; 0.0002 cm<sup>-1</sup> linewidth).<sup>21</sup> The advantage to having the high resolution spectrum is that it contains the frequency and intensity of single molecular eigenstates. The high resolution spectrum resolves each of the molecular eigenstates that will be excited by the pulsed laser. Additionally, the high resolution spectrum provides a precise level diagram of the molecular eigenstates which is illustrated in Figure 8.3. Lastly, the frequencies and intensities of the single molecular eigenstates can be used to perform a survival probability calculation to determine the IVR lifetime. The IVR lifetime of the *cis* (1.2 ns) conformer of pentenyne has previously been determined using the high resolution optothermal technique for the acetylenic C-H stretch fundamental.<sup>21;22</sup>

The infrared spectrum of pentenyne was also recorded using the ground state depletion (GSD) technique described in chapter 4. Figure 8.4 illustrates the GSD spectrum of both the *cis* and *skew* conformers monitoring the 2<sub>02</sub>-1<sub>01</sub> pure rotational transitions (12671.7460 MHz and 10044.8720 MHz). Also illustrated in Figure 8.4 is the band contour generated using the ground state rotational constants. The IR spectra of both the *cis* and *skew* conformers are A-B hybrids. The band origin of the *cis* and *skew* conformers has been determined (3332.39 cm<sup>-1</sup> and 3333.04 cm<sup>-1</sup>) by modeling the spectrum with the band contour.

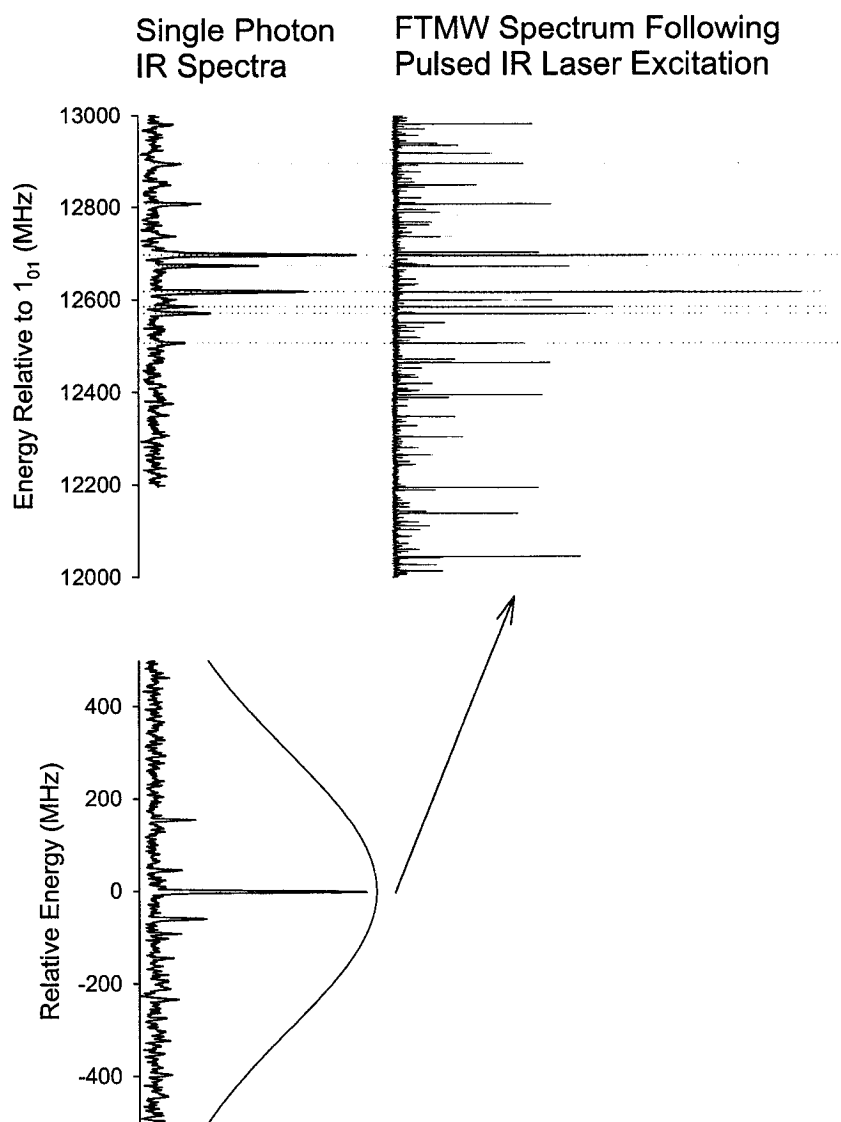


**Figure 8.3** The IR spectrum obtained using the high resolution technique is illustrated on the left for  $J = 1$  and  $J = 2$  for the *cis* conformer of pentenyne. This is a representation of the pulsed-IR-FTMW level diagram. The bandwidth of the pulsed laser excitation is illustrated schematically at  $J = 1$  and excites several molecular eigenstates. The rotational spectrum between the molecular eigenstates is recorded by the FTMW spectrometer. The rotational spectrum obtained using pulsed-IR-FTMW technique is illustrated (left) and contains the molecular eigenstates observed in the high resolution IR measurement.

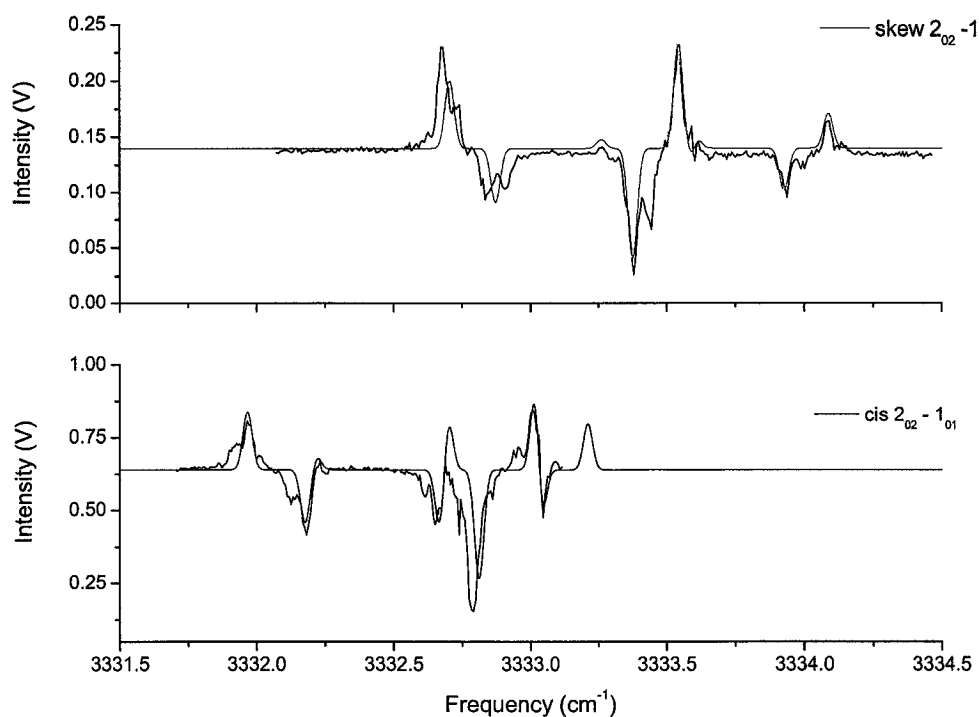


**Figure 8.4.** The above panels illustrate the rotationally resolved IR spectra of the *skew* (top) and *cis* (bottom) conformers obtained using the ground state depletion technique. The band contour for the *skew* (red) and the *cis* (blue) conformers generated using the ground state rotational constants are overlaid with their respective spectra.

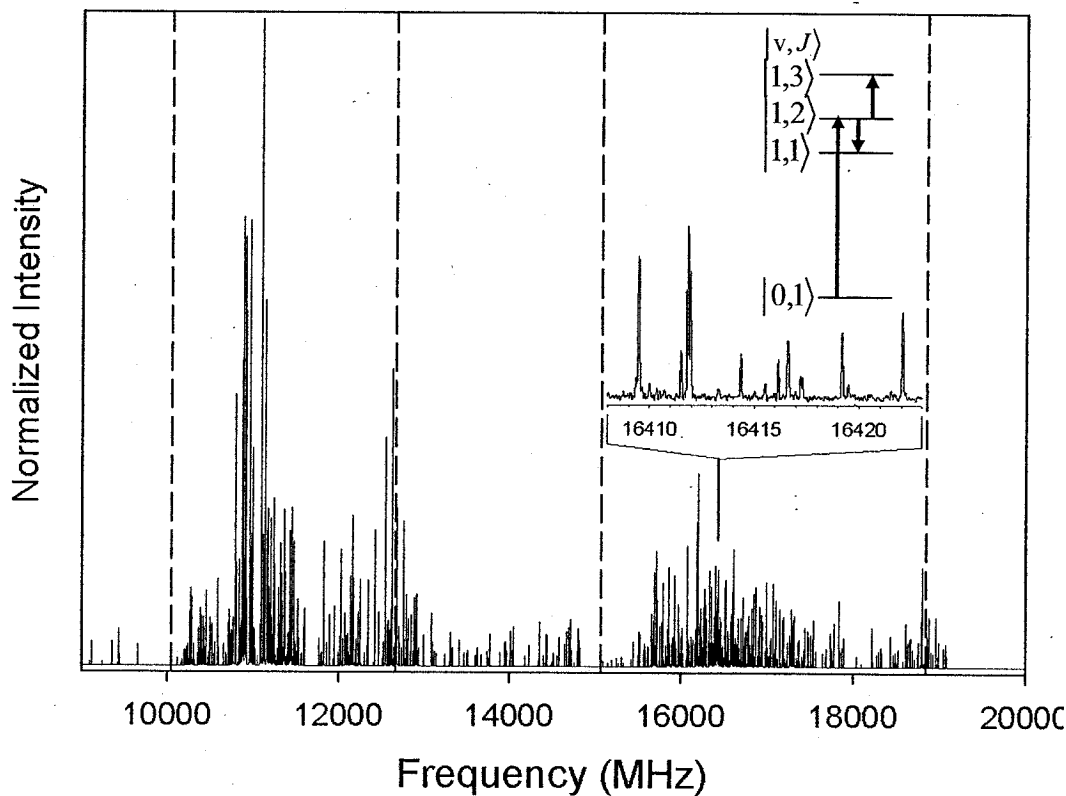
### C. Dynamic Rotational Spectroscopy

The high-resolution infrared spectrum of the *cis* conformer of pentenyne contains seven molecular eigenstates at  $J = 2$ . This spectrum was previously recorded using the high resolution optothermal technique. The isomerization dynamics of pentenyne can be determined by measuring the rotational spectra of these seven molecular eigenstates. Measuring all seven will serve to construct an ensemble picture of the isomerization dynamics.

#### Double Resonance

The rotational spectrum in the vibrationally excited state is illustrated in Figure 8.5. The spectrum in Figure 8.5 contains the rotational spectra of all the molecular eigenstates excited under the bandwidth of the laser. This double resonance spectrum was recorded by pumping the R(1) transition of the *cis* conformer at  $3332.78\text{ cm}^{-1}$  with the pulsed infrared laser, while scanning the frequency of FTMW cavity spectrometer from 9 - 20 GHz in order to measure the  $\Delta J=1 \leftarrow 2$  and  $\Delta J=3 \leftarrow 2$  transitions of the *cis* and *skew* conformers.

Although the *cis* conformer of pentenyne is the dominant conformer in the supersonic expansion, there is sufficient population in the *skew* conformer to perform IR-FTMW double resonance to measure the rotational spectrum in the vibrationally excited state that originated from the *skew* conformer. The ratio of the *cis:skew* population is approximately 5:1 based on FTMW ground state intensities and ab initio dipole moments.



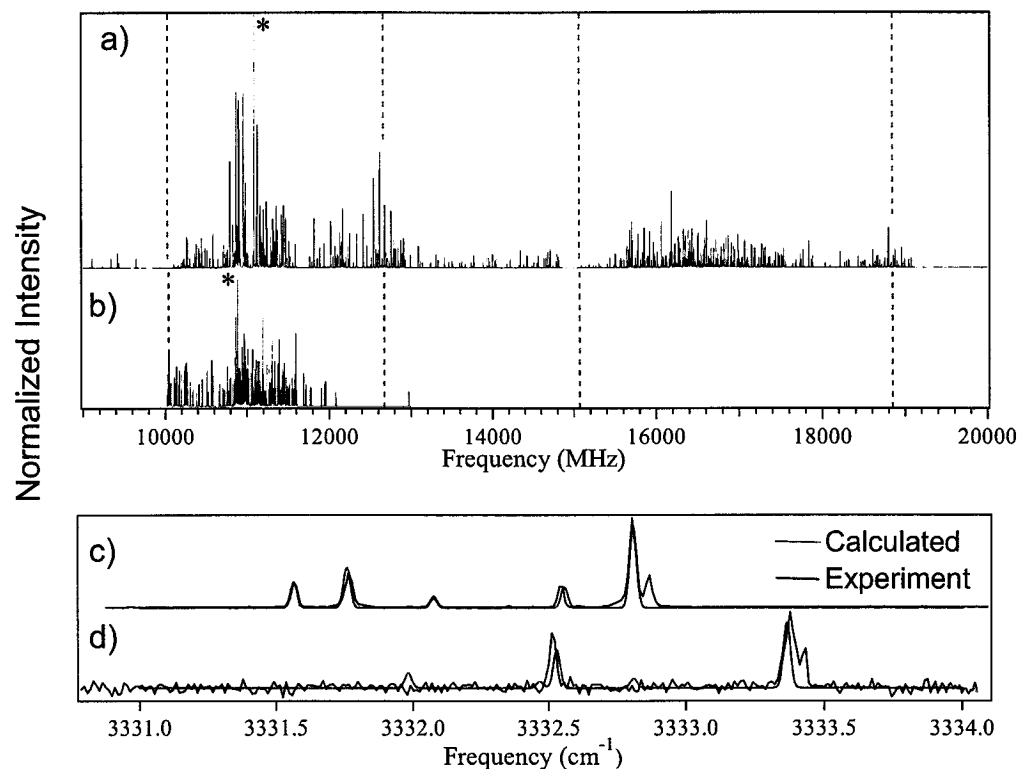
**Figure 8.5.** The above panels shows the rotational spectrum (stick) following laser excitation at R(1) 3332.78  $\text{cm}^{-1}$  of the *cis* conformer. The inset is the actual data recorded by the FTMW spectrometer 250 kHz step size and 20 averages per step. Also shown is a energy level diagram illustrating that infrared excitation at R(1) is used to populate the  $J=2$  rotational level in the vibrationally excited state. The rotational spectrum of this level is subsequently recorded. The dashed lines correspond to the ground state rotational transitions for the *cis* (12671.7460 and 18847.6410 MHz) and *skew* (10044.8720 and 15065.3230 MHz) conformers

Figure 8.6 compares the IR-FTMW double resonance spectra for population that is initially localized in the *cis* or *skew* conformational wells. The IR-FTMW double resonance spectrum of the *skew* conformer was obtained by pumping the R(1) transition of the *skew* conformer at  $3333.35\text{ cm}^{-1}$ , and scanning the frequency of the FTMW spectrometer over the  $\Delta J=1 \leftarrow 2$  region of both conformers. Due to signal-to-noise constraints the  $\Delta J=3 \leftarrow 2$  region of the *skew* conformer was not scanned. The IR-FTMW double resonance spectra of the two conformers are very similar. The important point is that the same dynamics are observed independent of where the population originates.

To confirm that the two spectra originated from their respective conformers, the frequency of a particular rotational transition in the excited state was monitored with the FTMW cavity while the infrared laser was scanned from  $3331\text{-}3334\text{ cm}^{-1}$ . In Figure 8.6 a  $\Delta J=2 \leftarrow 1$  transition is monitored with the FTMW cavity for both of the initially localized *cis* and *skew* species. Peaks occur in the spectrum when the laser populates a common level in the monitored excited state rotational transition. Figure 8.6 also shows an overlay of the experimental data with the calculated band contour. The band contour was calculated using the ground state rotational constants. The spacing of the peaks and the shift in the band origin of the *cis* and *skew* spectra prove that the two double resonance spectra arise from different conformational species.

### Triple Resonance

As stated previously, to obtain the dynamical information the rotational spectrum of a single eigenstate should be obtained. Because the rotational spectra of all the eigenstates are measured in the IR-FTMW double resonance spectrum and the



**Figure 8.6.** The IR-FTMW double-resonance spectra of pentenyne at  $\sim 3330 \text{ cm}^{-1}$  are shown. These spectra were recorded by fixing the infrared laser R(1) transition, promoting population to the infrared excited state and subsequently scanning the microwave source. Spectrum a) was recorded by exciting population initially localized in the *cis* conformer ( $3332.78 \text{ cm}^{-1}$ ), while spectrum b) was recorded by exciting population initially localized in the *skew* conformer ( $3333.35 \text{ cm}^{-1}$ ). The red dashed lines show the position of the ground state rotational transition of the  $\Delta J=1\leftarrow 2$  and  $\Delta J=2\rightarrow 3$  transition for the *cis* (12617 MHz, 18848 MHz respectively) and *skew* (10044 MHz, 15065 MHz) conformers. The spectrum in b) was multiplied by a factor of five. The traces in c) (*cis*) and d) (*skew*) correspond to excited state infrared spectra and are obtained by monitoring the excited state peaks in a) and b) marked with an asterisk (the most intense peak in each spectrum). These spectra were recorded by fixing the microwave source to a particular excited state transition and scanning the infrared laser from  $3330.5$ - $3334.25 \text{ cm}^{-1}$ . The black traces correspond to the experimentally recorded spectra, while the red traces correspond to the calculated spectra using the *cis* (c) and *skew* (d) rotational constants.

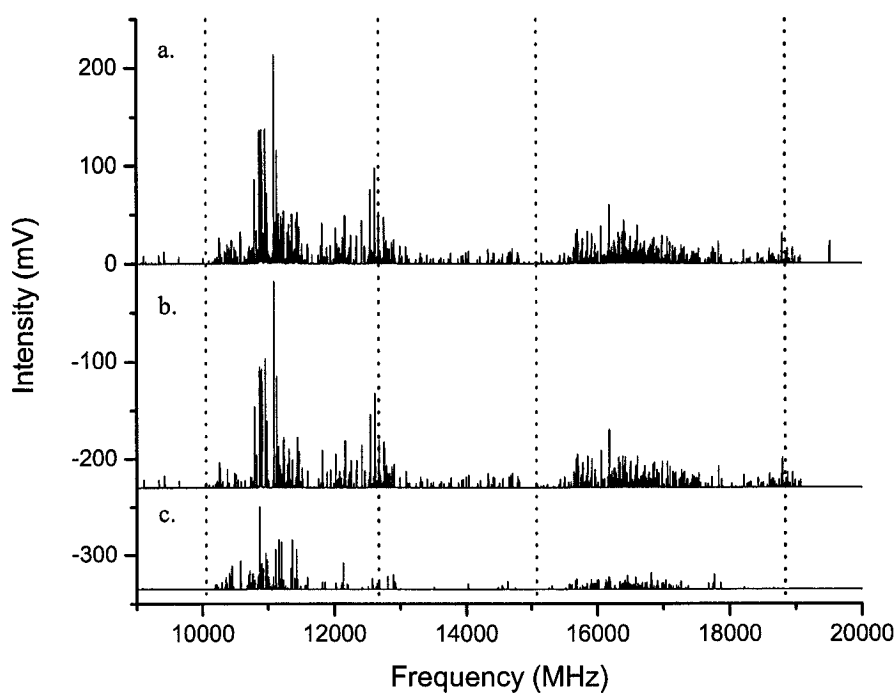
frequencies of the molecular eigenstates are known from the high resolution IR measurement all that is needed is to "assign" the transitions observed in the double resonance spectrum to one of the seven molecular eigenstates. To achieve this goal, IR-FTMW-pulsed-MW triple resonance is used. For this case the coherence method described in chapter 6 will be implemented.

For the coherence method of triple resonance spectroscopy a transition is monitored in the FTMW spectrometer and a MW pulse from a MW horn (with independent frequency source) destroys the coherence of the FID on resonance. For this experiment no scanning of any sources is necessary because all of the frequencies are known. The cavity is used to monitor the amplitude of one of the seven molecular eigenstates and the horn steps through all of the frequencies that contained transitions in the double resonance spectrum (with signal-to-noise > 3:1). If the frequency of the horn modulates the cavity frequency the two transitions share either an upper or lower level. This serves as the basis of the assignment and was performed for all seven eigenstates.

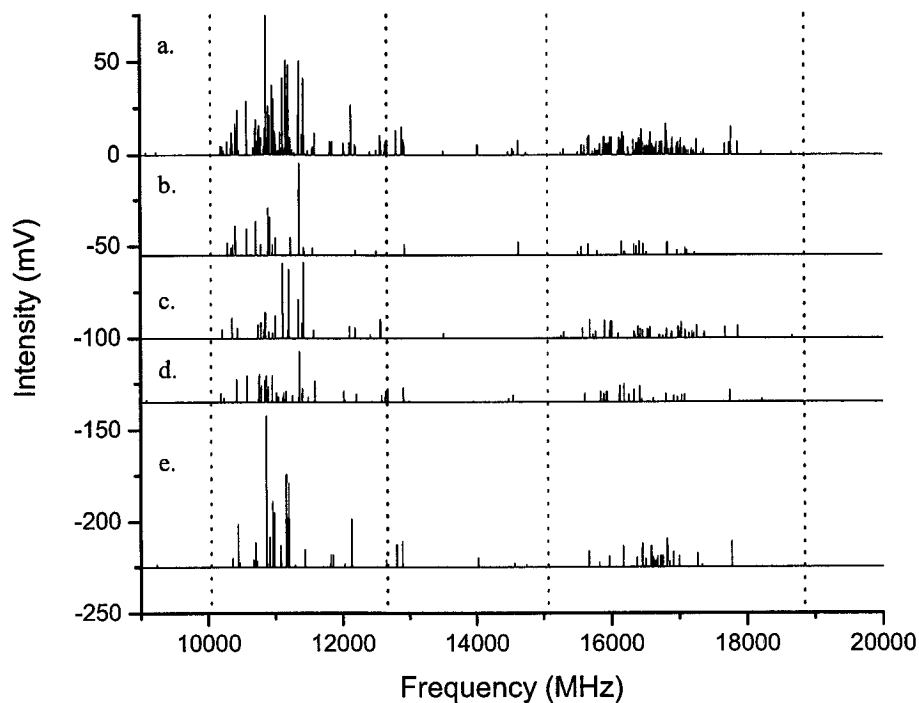
While it is impossible to know exactly whether the states share a lower or an upper level with this method, the assumption has been made that all peaks occurring below 14500 MHz arise from a  $\Delta J=1 \leftarrow 2$  transition, while those peaks above 14500 MHz arise from a  $\Delta J=3 \leftarrow 2$  transition. This assumption is presumed adequate due to the fact that peaks occurring outside this cut-off occur in the wings of a Lorentzian lineshape profile having negligible intensity outside the primary J region, therefore falling below the instrumental signal-to-noise level. A total of 322 lines were assigned to the  $\Delta J=1 \leftarrow 2$  transition and 369 were lines assigned to the  $\Delta J=3 \leftarrow 2$  transition.

Figure 8.7 compares a composite of the rotational spectra of the three strongest molecular eigenstates, and a composite of the rotational spectra of the four weakest molecular eigenstates. The more intense molecular eigenstates contain a large fraction of bright state character and therefore the rotational spectrum contains rotational transitions that resemble the bright state. These are the strong transitions localized around the *cis*  $2_{02} - 1_{01}$  pure rotational transition (12671.7460 MHz) and are referred to as infrared scars. These scars are not as prevalent in the rotational spectra of the weaker molecular eigenstates because these eigenstates have significantly less bright state character.

In Figure 8.8 a comparison is shown of the rotational spectra of the four lowest intensity infrared molecular eigenstates (12507 MHz, 12571 MHz, 12585 MHz, 12807 MHz) to the combined rotational spectrum of these four molecular eigenstates. The shape of the overall spectrum is preserved in the single quantum state spectra. It is also clear from Figure 8.8 that the peak intensity of the  $\Delta J=1 \leftarrow 2$  is greater than the peak intensity of the  $\Delta J=3 \leftarrow 2$ . There are two main reasons that account for this effect. The first of which is that the frequency difference between the *cis* and *skew* ground state rotational transitions increases with increasing  $J$ . The consequence is that the transitions observed in the rotational spectrum of the vibrationally excited state of the higher  $J$  are spread over a larger frequency range. The other factor is that the ro-vibrational state density is proportional to  $2J+1$ . As a result the state density at  $J=3$  is roughly 2.3 times that at  $J=1$ . Because the total intensity of the spectrum of at a given  $J$  is a conserved quantity the increased state density at  $J=3$  spreads the intensity over twice as many lines thereby decreasing the intensity of the individual transitions.



**Figure 8.7.** Illustrated above is a composite of the seven single eigenstate rotational spectra originating from the *cis* conformer (a.). These spectra were recorded by fixing the infrared laser on the R(1) transition ( $3332.78\text{ cm}^{-1}$ ), promoting population to the vibrationally excited state then using triple resonance to assign an IR-FTMW double resonance transition to a particular molecular eigenstate. The FTMW cavity is used to monitor (probe) one of seven molecular eigenstates, then a second MW source is coupled in using a MW horn with a frequency of an observed transition in the IR-FTMW double resonance spectrum. For this method the coherence of the monitored transition is destroyed if the pump transition shares a common level with the probe transition. A composite is shown of the three spectra corresponding to the strong molecular eigenstates (b. 12617 MHz, 12673 MHz, and 12696 MHz) and the four weak molecular eigenstates (c. 12571 MHz, 12807 MHz, 12585 MHz, and 12507 MHz). The pure rotational transitions of the *skew* (red) and *cis* (blue) conformers are designated by the dashed lines. The noticeable difference between a. and b. is the intensity in the region localized around the *cis* conformer.



**Figure 8.8.** Illustrated above is a composite of the four weak single eigenstate rotational spectra originating from the *cis* conformer (a.). These spectra were recorded by fixing the infrared laser on the R(1) transition ( $3332.78\text{ cm}^{-1}$ ), promoting population to the vibrationally excited state then using triple resonance to assign an IR-FTMW double resonance transition to a particular molecular eigenstate. The FTMW cavity is used to monitor (probe) one of four molecular eigenstates, then a second MW source is coupled in using a MW horn with a frequency of an observed transition in the IR-FTMW double resonance spectrum. For this method the coherence of the monitored transition is destroyed if the pump transition shares a common level with the probe transition. The single eigenstate rotational spectra of the four weak molecular eigenstates are illustrated in the four individual traces (b. 12571 MHz, c. 12807 MHz, d. 12585 MHz, and e. 12507 MHz). The pure rotational transitions of the *skew* (red) and *cis* (blue) conformers are designated by the dashed lines.

## Discussion

### A. Lineshape analysis

Dynamical information about the isomerization rate can be determined from the overall lineshape profile of the rotational spectrum of the single molecular eigenstates. To determine the overall lineshape it is convenient to use cumulative intensity of the spectrum.<sup>23</sup> Figure 8.9 shows the cumulative intensity plots for excitation of the *cis* conformer in which the spectrum is broken into two regions.

The first region spans 9000-14500 MHz corresponding to the  $\Delta J=1 \leftarrow 2$  region of the spectrum, and the second region shows the cumulative intensity plot from 14500-20000 MHz corresponding to the  $\Delta J=3 \leftarrow 2$  region of the spectrum. The broken blue lines in each panel of Figure 8.9 correspond to the four individual quantum state spectra that do not exhibit scarring from the IR-excitation (12507 MHz, 12571 MHz, 12585 MHz, 12807 MHz), while the solid red line is the ensemble average of all four molecular eigenstate spectra. The three strongest molecular eigenstates have been omitted from the lineshape analysis because the IR-scarring skews the intensity at high frequency for both  $J$  (although it is less pronounced for the  $\Delta J=3 \leftarrow 2$  spectrum).

A key feature in comparing the single quantum state cumulative intensity with the ensemble cumulative intensity is that the overall linshape is preserved. Figure 8.9 exhibits individual quantum state fluctuations about the ensemble average lineshape, but the overall dynamical information remains embedded onto single quantum states. Figure 8.9 also shows that the fluctuations in the individual quantum states are small, demonstrating the highly mixed character of the single quantum states.

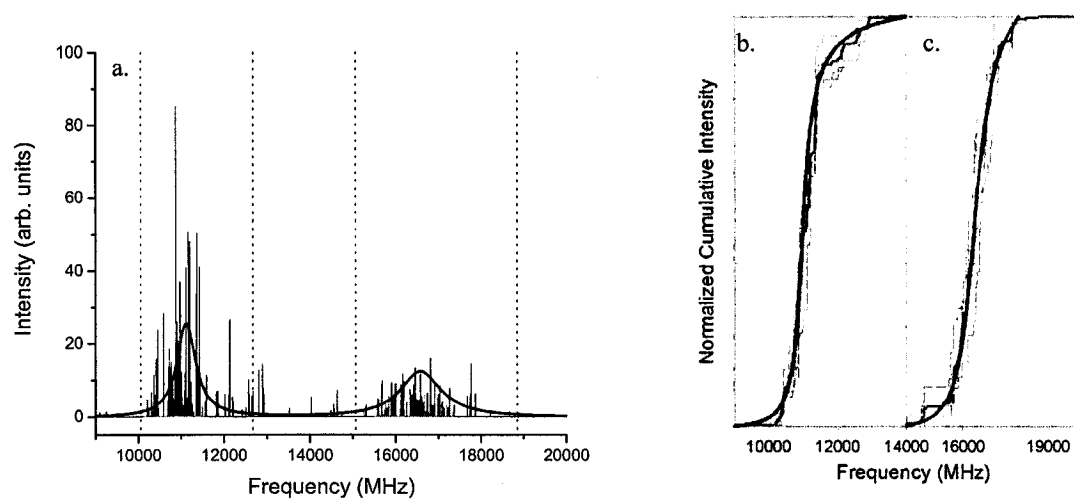


**Figure 8.9.** Illustrated in panel a. is a composite of the four weak single eigenstate rotational spectra originating from the *cis* conformer (red) with the analytic lineshape derived from the Bloch model (black). The traces in b) ( $\Delta J=2 \rightarrow 1$ , 10000-14000 MHz) and c) ( $\Delta J=3 \leftarrow 2$ , 14000-18000 MHz) correspond to cumulative intensity analysis of the single eigenstate spectra of a). The dashed blue lines represent the single eigenstate spectra, the solid red line represents the cumulative intensity of the four composite eigenstate spectra, and the black line represents the analytic lineshape derived from a three-state Bloch model.

The isomerization rate is determined from an analysis of the overall rotational lineshape using a three-state Bloch model modified for chemical exchange.<sup>24</sup> The three state model has been described in detail previously.<sup>25</sup> The interaction matrix elements are defined using a Fermi Golden Rule expression as:

$$\Gamma_{\text{isomerization}} = 2\pi \langle W^2 \rangle \rho \quad (8.1)$$

where  $W$  is the rms matrix coupling element, and  $\rho$  is the density of states. From this expression a model Hamiltonian can be constructed which produces the analytic lineshape of the rotational spectrum. The breadth of this spectrum can be directly compared to experiment to determine the isomerization rate. The center frequency (in the coalescence limit) is determined by the quantity  $\rho$  in equation (8.1). This value is determined by the ratio of the *cis* and *skew* conformer state densities at 3330 cm<sup>-1</sup>. Because the state densities were calculated using the 1-D torsional energy levels and scaled harmonic frequencies, this value was shifted by 150 MHz to give better agreement with experiment.

The cumulative intensity of the Bloch model (black trace) is overlaid with the experimental cumulative intensities at  $\Delta J=1 \leftarrow 2$  and  $\Delta J=3 \leftarrow 2$  in Figure 8.9. The Bloch model results shown in Figure 8.9 correspond to a microcanonical isomerization lifetime  $\tau(E,J) = 25$  psec, and also demonstrates that a single isomerization lifetime fits both  $J$ .

Best fits of the analytic lineshape to the experimental spectrum were determined by a chi squared analysis. The results of this analysis are shown in Figure 8.10 as a two dimensional surface. Ideally we would like to independently determine the *cis*→*skew* and *skew*→*cis* isomerization rates. It is clear from Figure 8.10 that the forward and reverse rates of reaction cannot be determined from this lineshape analysis. Therefore, the rates reported here are the sums of the forward and reverse rates. The chi squared analysis was used to determine the  $\Delta J = 2 \rightarrow 1$  rate as  $k(E,J) = 25 \pm 10$  psec and the  $\Delta J = 3 \leftarrow 2$  rate as  $k(E,J) = 35 \pm 10$  psec.

### B. Rate analysis

The microcanonical rate constant for isomerization of pentenyne has been measured and this allows for a direct comparison to the rate predicted by RRKM theory. The unimolecular rate constant predicted by RRKM theory has the form:

$$k(E,J) = \frac{\sigma W(E,J)}{h\rho(E,J)} \quad (2)$$

where  $\rho(E,J)$  is the density of *cis* states at  $3330 \text{ cm}^{-1}$ ,  $W(E,J)$  is the number of states between the reaction energy ( $3330 \text{ cm}^{-1}$ ) and the top of the *cis*-*skew* isomerization barrier ( $969 \text{ cm}^{-1}$ ), and  $\sigma$  is the reaction symmetry number (two for this isomerization reaction).<sup>26</sup> Based on previous studies of large polyatomic molecules, it is expected that all  $K_a$  states will participate in the dynamics. This assumption can be made because all  $K_a$  are active in all energy regions above the barrier and therefore the  $J$  dependence of the unimolecular rate constant can be neglected.

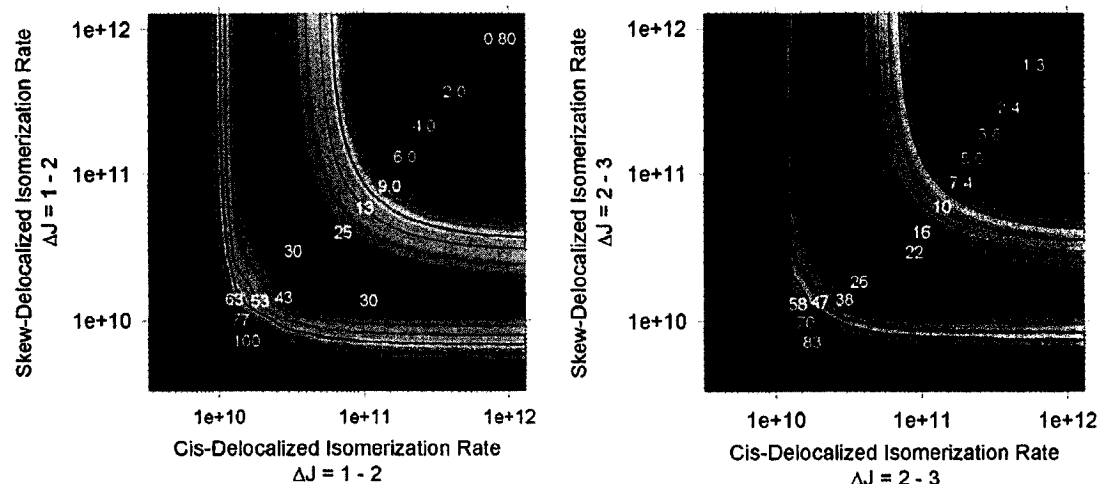


**Figure 8.10.** The above plots illustrate the Chi squared error analysis of the rate determined using the Bloch model for the  $\Delta J = 1-2$  (left) and the  $\Delta J = 2-3$  (right) region of the rotational spectrum.

The direct count algorithm<sup>27</sup> used to calculate the density of states has previously shown to agree well with experimentally determined state density and is therefore believed to provide an accurate measure of the state density at the reaction energy of 3330 cm<sup>-1</sup>.<sup>22</sup> From a direct count the number of states above the isomerization barrier is 57 states. Using this value and those reported in Table 8.3, the RRKM value for the unimolecular rate constant for the isomerization of pentenyne is  $\sim 1 \times 10^{12}$ /sec. As stated previously, the measured isomerization lifetime reported above for pentenyne (25 psec.) is a measure of the forward and reverse lifetimes. In order to make a direct comparison to the rate obtained by RRKM and the experimentally determined rate the RRKM value is scaled by a factor of two which leads to an isomerization lifetime  $\tau_{\text{RRKM}} = 0.5$  psec.

There is a factor of 40 difference between the experimentally measured lifetime (25 psec) and that predicted by RRKM (0.5 psec). Isomerization reactions form a special class of unimolecular reactions where no bond cleavage occurs. Disparities from the RRKM may result from the basic assumptions of RRKM which are that IVR is fast relative to the reaction rate and that once the molecule traverses the reaction barrier to form the products, it cannot cross back over the barrier to form reactants. Work by Leitner and Wolynes have demonstrated that RRKM predictions are inadequate for low barrier reactions and in particular for isomerization *trans* to *cis* isomerization of stilbene.<sup>28,29</sup>

### Conclusions

In this Chapter the three basic steps required for a complete dynamics measurement were presented for pentenyne. These steps are 1.) measure and assign pure rotational

**Table 8.3.** Calculated State Densities for Structures of Pent-1-en-4-yne

	Transition Frequency (MHz)	State Density <sup>a</sup> (cm <sup>-1</sup> )	Transition Moment (Debye)
<i>cis</i>	12671	197	0.33
delocalized	11641	120	0.50
<i>skew</i>	10054	470	0.46

<sup>a</sup>Anharmonic state density

spectrum, 2.) obtain rotationally resolved conformer specific infrared spectra, and 3.) measure the rotational spectrum in the vibrationally excited state. Lineshape analysis developed from NMR spectroscopy was applied to the rotational spectra of three weakest molecular eigenstates to determine the conformational isomerization rate (25 ps). The rotational spectra of the single molecular eigenstates are in the motionally narrowed regime. Coalescence is observed when the isomerization rate is roughly 2.2 times the frequency separation which would correspond to an isomerization rate of ~170 ps. As the rate of isomerization increases the spectra motionally narrowed. Measuring dynamics from the rotational spectrum has the advantage that as the dynamics get faster the spectrum becomes narrower.

### Reference List

1. Kraitchman, J., *J.Chem.Phys.* **1952**, 17-24.
2. Gordy, W.; Cook, R. L. *Microwave Molecular Spectra*; John Wiley & Sons: New York, 1984; p -929.
3. Legon, A. C., *Annu.Rev.Phys.Chem.* **1983**, 34, 275-300.
4. Balle, T. J.; Flygare, W. H., *Rev.Sci.Instrum.* **1981**, 52, 33-44.
5. Fraser, G. T.; Suenram, R. D.; Lugez, C. L., *J.Phys.Chem.A* **2001**, 105, 9859-9864.
6. Xu, Y.; Wijngaarden, J. v.; Jäger, W., *Int.Rev.Phys.Chem.* **2005**, 24, 301-338.
7. Ohshima, Y.; Endo, Y., *J.Mol.Spectrosc.* **1992**, 153, 627-634.
8. Arunan, E.; Dev.S.; Mandal, P. K., *Appl.Spectrosc.Rev.* **2004**, 39, 131-181.
9. Wodarczyk, F. J.; Wilson, E. B., *J.Chem.Phys.* **1972**, 56, 166-176.
10. Hershbach, D. R.; Swalen, J. D., *J.Chem.Phys.* **1958**, 29, 761-776.
11. Keske, J. C.; McWhorter, D. A.; Pate, B. H., *Int.Rev.Phys.Chem.* **2000**, 19, 363-407.
12. Keske, J. C.; Rees, F. S.; Pate, B. H., *Phys.Rev.Lett.* **2000**.
13. Green, D.; Holmberg, R.; Lee, C. Y.; McWhorter, D. A., *J.Chem.Phys.* **1998**, 109, 4407-4414.
14. Douglass, K. O.; Dian, B. C.; Brown, G. G.; Johns, J. E.; Nair, P. M.; Pate, B. H., *J.Chem.Phys.* **2004**, 121, 6845-6854.
15. Makarov, A. A., *Opt.Spektrosk., USSR* **1987**, 62, 697-699.
16. Pate, B. H., *J.Chem.Phys.* **1998**, 109, 4396-4406.
17. Pate, B. H., *J.Chem.Phys.* **1999**, 110, 1990-1999.
18. Frisch, M. J., Trucks, G. W., Sclegel, H. B., Scuseria, G. E., Robb, M. A., Cheeseman, J. R., Zakrzewski, V. G., Montgomery, J. A. Jr., Stratmann, R. E., Burant, J. C., Dapprich, S., Millam, J. M., Daniels, A. D., Kudin, K. N., Strain, M. C., Farkas, O., Tomasi, J., Barone, V., Cossi, M., Cammi, R., Mennucci, B., Pomelli, C., Adamo, C., Clifford, S., Ochterski, J., Petersson, G. A., Ayala, P. Y., Cui, Q., Morokuma, K., Malick, D. K., Rabuck, A. D., Raghavachari, K.,

- Foresman, J. B., Cioslowski, J., Ortiz, J. V., Baboul, A. G., Stefanov, B. B., Liu, G., Liashenko, A., Piskoz, P., Komaromi, I., Gomperts, R., Martin, R. L., Fox, D. J., Keith, T., Al-Laham, M. A., Peng, C. Y., Nanayakkara, A., Challacombe, M., Gill, P. M. W., Johnson, B., Chen, W., Wong, M. W., Andres, J. L., Gonzalez, C., Head-Gordon, M., Replogle, E. S., and Pople, J. A. Gaussian 98, Revision A.7. Gaussian, Inc., Pittsburgh PA . 1998.
19. Lewis, J. D.; Malloy, T. B., Jr.; Chao, T. H.; Laane, J., *J.Mol.Struct.* **1972**, *12*, 427-449.
  20. Pickett, H. M., *J.Mol.Spectrosc.* **1991**, *148*, 371-377.
  21. Rees, F. S. *Vibrational Dynamics of the Acetylenic C-H Stretch Fundamental for C<sub>5</sub>H<sub>6</sub> Isomers: New Spectroscopic Techniques for IVR Research.* 2005. PhD. Thesis.
  22. Engelhart, C.; Keske, J. C.; Rees, F. S.; Self-Medlin, Y. B.; Yoo, H. S.; Pate, B. H., *J.Phys.Chem.A* **2001**, *105*, 6800-6807.
  23. Mukamel, S.; Sue, J.; Pandey, A., *Chemical Physics Letters* **1984**, *105*, 134-139.
  24. Slichter, C. P. *Principles of Magnetic Resonance*; Springer: New York, 1996.
  25. Keske, J. C. Dynamic Rotational Spectroscopy. 2002. University of Virginia.
  26. Baer, T.; Hase, W. L. *Unimolecular Reaction Dynamics: Theory and Experiments*; Oxford University Press: New York, 1996; p -438.
  27. Kemper, M. J. H.; Van Dijk, J. M. F.; Buck, H. M., *Chem.Phys.Lett.* **1978**, *53*, 121-124.
  28. Leitner, D. M.; Wolynes, P. G., *Chem.Phys.Lett.* **1997**, *280*, 411-418.
  29. Leitner, D. M.; Levine, B.; Quenneville, J.; Martinez, T. J.; Wolynes, P. G., *J.Phys.Chem.A* **2003**, *107*, 10706-10716.

## Chapter 9

### Principles of Chirped-Pulse Fourier Transform Microwave Spectroscopy

#### Introduction

Rotational spectroscopy dates back to nearly the WWII era with the development of the microwave Stark spectrometer by Wilson, McAfee, and Hughes.<sup>1,2</sup> This technique provided a general tool to physical chemists studying molecular structure. Measurements employing this waveguide spectrometer design examined several important topics in molecular structure including the existence of stable conformations separated by low energy barriers<sup>3,4</sup> and the tunneling dynamics of methyl group internal rotation.<sup>5</sup> However, the need for sufficient vapor pressure in the waveguide cell limited the size range of molecules that could be interrogated by pure rotational spectroscopy.

In 1979 Fourier transform methods to perform rotational spectroscopy employing a high Q cavity had been developed into the now well known Balle-Flygare cavity Fourier transform microwave (FTMW) spectrometer.<sup>6-8</sup> In the years to follow several improvements have been made such as improved resolution, automated scanning, and improved sensitivity due to improved microwave electronics.<sup>9-12</sup> This spectrometer used advances in time-domain microwave spectroscopy to provide sensitive detection of the rotational free induction decay (FID) following polarization by a short microwave pulse.

By performing spectroscopy in the time domain it became possible to achieve high frequency resolution without power broadening or the line shape distortion found in Stark modulation spectrometers. A second advantage of this technique was that by using pulsed time domain techniques it became possible to use pulsed molecular beam sources,

which greatly expanded the range of molecular systems amenable to study by rotational spectroscopy such as large molecules<sup>13-15</sup>, weakly bound clusters<sup>16-19</sup>, and radical and ion species.<sup>20-24</sup> This basic Balle-Flygare cavity spectrometer design, with important modifications to improve sensitivity and frequency resolution<sup>10,25</sup>, currently dominates the field of pure rotational spectroscopy.

The high Q Fabry-Perot FTMW spectrometer by definition is a narrowband spectrometer. The use of a cavity with high quality factor, Q ( $\sim 10^4$ ) limits the measurable frequency bandwidth to less than 1 MHz in most spectrometer designs. The cavity element has two major advantages which are passive amplification of the microwave polarizing pulse and the free induction decay signal. Often these spectrometers are called "broadband" to indicate that they operate over a wide frequency range, typically about 10 GHz. However, the process of acquiring a spectrum over the full operating range of the spectrometer is laborious. The spectrum scanning process requires a series of steps where the cavity is tuned precisely to resonance, a narrow frequency range is measured ( $\sim 500$  kHz), and the cavity is moved to its next position. This process is automated so that a spectrum over a frequency range of several GHz can be obtained without user intervention, but the basic spectrometer design leads to long spectrum acquisition times.

For example, the cavity FTMW spectrometer described in chapter 2, takes about 14 hours to acquire a spectrum over an 11 GHz range. The time-consuming spectral acquisition process poses difficulties for using FTMW spectroscopy in analytical chemistry applications, optimizing source conditions for previously unknown species,

and performing rotational spectroscopy in excited vibrational or electronic states prepared by laser excitation. Measuring rotational spectra in the vibrationally excited state is a major focus of this research and difficulties arise when the laser frequency drifts as the cavity is scanning. This makes scanning over large frequency regions exceptionally labor intensive and scan rates for measuring rotational spectra in the vibrationally excited state were often limited to 200 MHz/hr.

In this Chapter a new approach is described for molecular-beam FTMW spectroscopy based on chirped pulse excitation. The new ‘true’ broadband Chirped-Pulse FTMW (CP-FTMW) spectroscopy technique and the design challenges of broadband frequency generation, sample polarization, and digitization of the broadband signal will be described in detail. The new CP-FTMW spectrometer exploits recent advances in arbitrary waveform generators and digital oscilloscopes to perform time-domain rotational spectroscopy over an 11 GHz bandwidth for every pulse of the valve.

## **Experimental**

The chirped-pulse Fourier transform microwave (CP-FTMW) spectrometer can be separated into three general components: 1.) chirped microwave pulse generation, 2.) broadband excitation and free induction decay (FID) collection, and 3.) FID detection and digitization. Figure 9.1 shows a schematic of the three components of the spectrometer and also illustrates the triggering scheme. The following sections will be dedicated to explaining the importance of low phase noise and stable triggering, the details of the three components, and the application of different apodization filters.

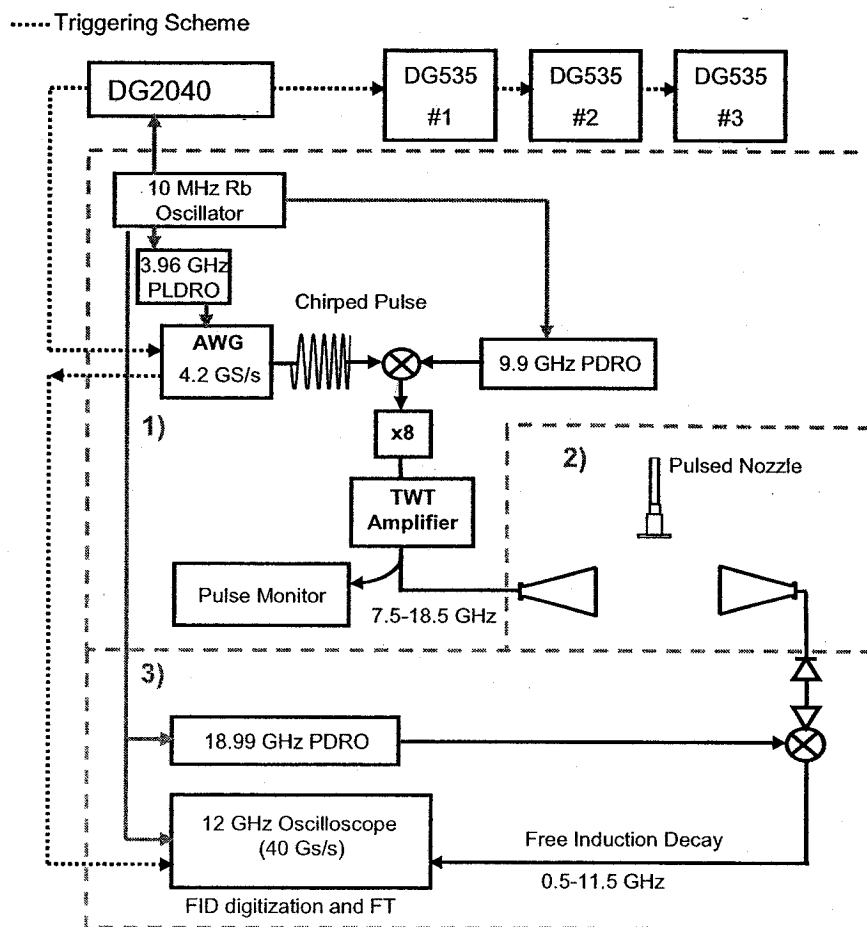


**Figure 9.1** A schematic of the 11 GHz chirped-pulse Fourier transform microwave (CP-FTMW) spectrometer. The spectrometer consists of three main components: 1) chirped-pulse microwave generation, 2) free space molecular beam chamber, and 3) free induction decay detection. Also illustrated is the triggering scheme (black dotted line) which uses the DG2040 as the master trigger source for the experiment.

### A. Phase Noise and Triggering

The best signal-to-noise ratio is achieved by averaging in the time domain before Fourier transforming to the frequency domain.<sup>26,27</sup> The primary experimental requirement to achieve stable averaging of the time domain FID is that the phase noise of the system must be kept as low as possible (small fraction of highest frequency) and the trigger for the oscilloscope must have very low jitter ( $\sim 5$  ps). The phase noise of an oscillator is the rapid, short-term, random fluctuations in the phase of the wave caused by time-domain instabilities. To achieve this all components used in the microwave pulse production, FID detection, and digitization must be phase-locked to the 10 MHz clock. This insures that all light waves start with the same relative phase in each measurement event.

A Rb-disciplined crystal oscillator operating at 10 MHz (Stanford Research Systems FS725) provides the absolute frequency clock for the experiment. The fractional frequency accuracy of the 10 MHz reference is  $\pm 5 \times 10^{-10}$  and ultimately determines the accuracy of the microwave frequency measurements. An important feature of this reference source is the low phase noise (<-130 dBc/Hz at 10 Hz spectral density of phase fluctuations). The phase noise of a system is difficult to measure but can be performed using a spectrum analyzer in the frequency domain and is determined by difference between the noise power at a particular offset from the carrier frequency and the power at the carrier frequency.<sup>28,29</sup> This is the spectral density of the phase fluctuations. Low phase noise on the clock is especially important because the theoretical limit for phase

noise scaling is  $20 \log N$ , where N is the multiplication factor. All frequency sources are harmonics of the 10 MHz and the chirped pulse circuit is an x8 multiplication stage.

Low phase noise on the arbitrary waveform generator (AWG) is achieved by using a 3.96 GHz PLDRO (Microwave Dynamics PLO-2000-03.96), phase locked to the 10 MHz rubidium oscillator, as an external clock for the AWG. The external clock feature reduces the phase jitter on the AWG by a factor of ~10 compared with the internal AWG clock (estimated from spec). This clock also reduces the jitter of the TTL pulse from the AWG which triggers the oscilloscope. In practice, 10,000 sequential FIDs can be averaged in the time domain while retaining 90% of the single measurement signal amplitude. A demonstration of the phase control using the AWG is shown in Figure 9.2.

The master triggering source for the experiment is a two channel 1 Gs/s Data Pattern Generator (Tektronix DG2040) which sets the repetition rate of the experiment to 10 Hz. The triggering scheme is shown schematically in Figure 9.1. The fast sampling rate of the DG2040 ensures low jitter on the TTL pulses. Channel 0 is used to trigger the AWG and channel 1 triggers the digital delay generators (DG535 Stanford Research) that control the laser (DG535 #1), valve (DG535 #2), and TWTA control and MW switch (DG535 #3) in the FID detection circuit (Figure 5). The AWG also has two independent digital data channels to create TTL level pulses. Channel 1 provides a trigger pulse to the digital oscilloscope to initiate data collection and channel 2 provides a TTL pulse to control the microwave switch in the chirped pulse generation circuit shown in Figure 9.3. The components to the chirped pulse generation circuit are shown in Table 9.1.

The DG2040 has a very important feature; a 10 ps delay control knob. This delay

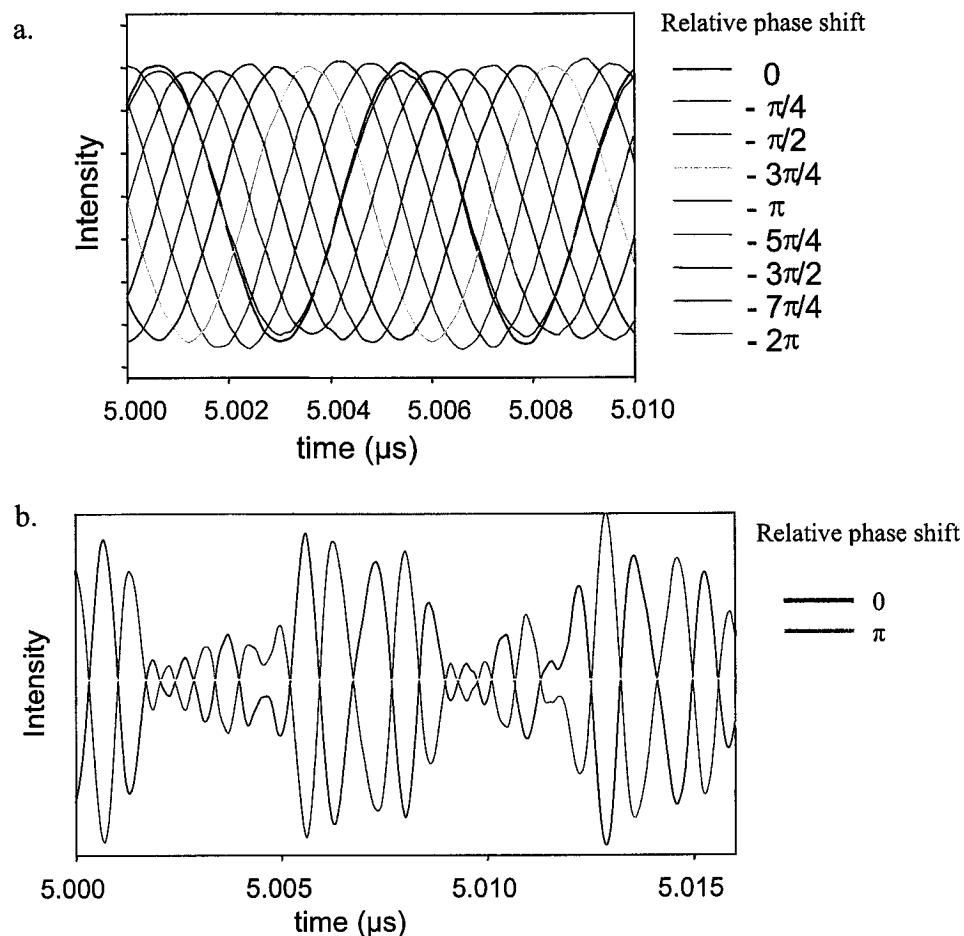


**Figure 9.2** The above panels illustrate the phase control using the arbitrary waveform generator (AWG). A small section of the broadband rotational FID is shown for the propyne  $1_0 - 0_0$  transition at 17091.7434 MHz at  $\pi/4$  relative phase shifts (a.). The FID only contains a single frequency because there is only a single transition in the operating frequency of the CP-FTMW spectrometer. Also illustrated is a small section of the FID of cyclopropanecarboxaldehyde (CPCA) with 0 and  $\pi$  phase shift (b.). This demonstrates phase agility even for species with many rotational transitions measured using the CP-FTMW spectrometer. All the relative phase shifts in the two plots are performed using the AWG.

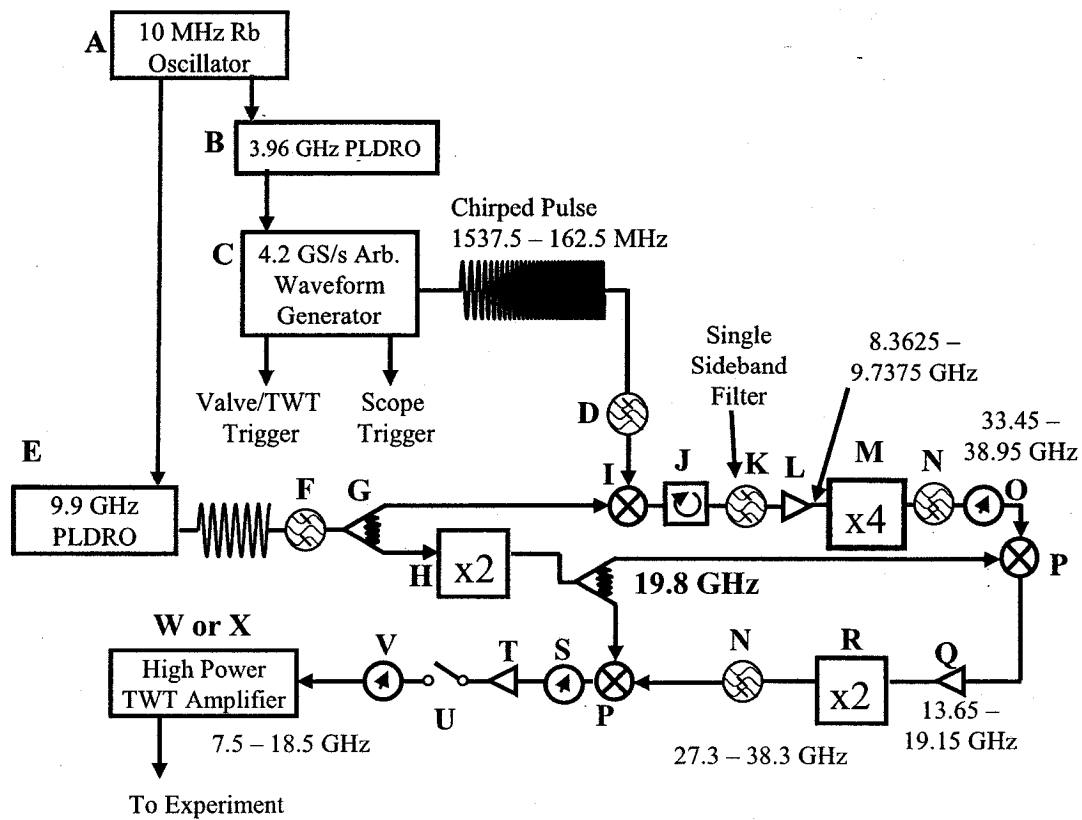


**Figure 9.3** The microwave circuit used to up convert and frequency multiply the digital frequency sweep (chirped pulse) output of the arbitrary waveform generator (AWG) is shown in full detail. The 10 MHz output of a Rubidium oscillator is used to phase lock the two frequency sources in the circuit (3.96 GHz and 9.9 GHz PLDROs). A detailed component list is also shown in Table 9.1. The details of the circuit are discussed in the text.

**Table 9.1 Component List for Pulse Generation Circuit**

<b>Component</b>	<b>Manufacturer</b>	<b>Description</b>	<b>Part No.</b>
A	Stanford Research Systems	10 MHz Rubidium Frequency Standard	FS725
B	Microwave Dynamics	3.96 GHz phase locked oscillator	PLO-2000-03.96
C	Tektronix	4.2 GS/s Arbitrary Waveform Generator	AWG710B
D	Mini Circuits	1.7 GHz low pass filter	VLF-1700
E	Miteq	9.9 GHz phase locked oscillator	PLDRO-010-09900-15P
F	Lorch	9.9 GHz bandpass filter	3CF7-99001200-S
G	Narda	6 - 18 GHz power divider	4326-2
H	Phase One	9 - 13.25 GHz active frequency doubler	SX26-223
I	Miteq	4 - 12 GHz double balanced mixer	DM0412LW2
J	Ditom	6 - 18 GHz circulator	DMCB018
K	Lorch	8.990 GHz 13 pole bandpass filter	13EZ5-8990/1515-S
L	Phase One	6- 12 GHz amplifier	SG12-2515
M	Phase One	6.5 - 10 GHz active frequency quadrupler	SX40-420
N	Microwave Circuits	26.6 - 40 GHz high pass filter	H26G4061
O	ATM	26 -40 GHz continuously variable attenuator	28-620A-30-6-6
P	Miteq	triple balanced mixer 4 - 40 GHz	TB0440LW1
Q	Miteq	12 - 26 GHz low noise amplifier	JS4-12002600-25-5P
R	DBS Microwave	13 -20 GHz active frequency doubler	DBS-2640X218
S	ATM	8 - 18 GHz continuously variable attenuator (0 - 30 dBm)	AV066H-30
T	Miteq	8 - 18 GHz low noise amplifier	AMF-5F-0800-1800-14-10P
U	ATM	SPST microwave switch	S1517D
V	Agilent	DC - 26 GHz programmable step attenuator (0 - 81 dBm)	HP11713A
W	Amplifier Research	8 - 18 GHz traveling wave tube amplifier 2 kW	1000TP8G18
X	Amplifier Research	8 - 18 GHz traveling wave tube amplifier 200 W	200T8618A

adjustment is used to ensure that the AWG is not triggered on an unstable region of the clock but on the zero crossing. If the AWG is triggered unstably averaging in the time domain becomes difficult. Stable triggering of the AWG is achieved by observing the output of a 400 MHz PLDRO directly on the oscilloscope when the oscilloscope is triggered by the AWG. The delay on the DG2040 is adjusted to trigger the AWG unstably which is observed by the appearance of 'jumping' in the phase of the 400 MHz signal, typically a full clock cycle of the 3.96 GHz. The delay is then set exactly a half clock cycle away from the 3.96 GHz. This routine ensures stable triggering with the lowest possible jitter and is typically set once a day.

### B. Chirped Microwave Pulse Generation

To perform broadband Chirped Pulse-FTMW (CP-FTMW) spectroscopy a microwave source is required that can produce a phase-locked linear frequency sweep over an 11 GHz frequency range in times ranging from 100 ns to 1  $\mu$ s (sweep rates of  $10^{11} - 10^{10}$  MHz/s). The short sweep durations are required so that the sample is polarized on a time scale faster than the pure dephasing time,  $T_2$ , (typically  $\sim 8\mu$ s) of the rotational FID. Traditional microwave synthesized sweepers cannot produce these fast sweep rates and are typically limited to sweep rates of about  $10^6$  MHz/s, and therefore newer methods based on arbitrary waveform generators have been developed.

With the requirements of rapid linear sweep and broadband excitation a chirped microwave pulse based on a 4.2 Gs/s arbitrary waveform generator (AWG) is described and the block diagram is illustrated in Figure 9.3. The arbitrary waveform generator is limited to producing frequencies from DC to 1.98 GHz (Nyquist) when using the

3.96 GHz PLDRO as the clock source. The microwave circuit shown in Figure 9.3 is used to accomplish two tasks: expand the sweep bandwidth by a factor of 8 and up convert the frequencies into the 7.5 – 18.5 GHz frequency range. As explained below bandwidth expansion is performed using active frequency multipliers and frequency up or down conversion is accomplished using single frequency sources and a broadband mixer. The combination of linear sweep and active frequency multipliers is special because a sweep is the only type of pulse where the frequency and the bandwidth get multiplied (i.e. this does not work for transform limited pulses) and therefore this combination provides a simple mechanism to increase the bandwidth of the polarization pulse.

The first step to generating the 11 GHz chirped pulse is the digital synthesis of a chirped pulse from 1537.5 – 162.5 MHz with pulse durations from 10 ns to 1  $\mu$ s. As previously indicated the AWG (C) has a bandwidth limit, the high frequency side is limited from the entire AWG bandwidth (1.98 GHz) because of internal mixing with the clock source of the AWG and harmonics. To remove these spurious frequencies the output of the AWG is filtered with a 1.7 GHz lowpass filter (D). The low frequency limit (162.5 MHz) is chosen such that the chirped pulse can be isolated from the carrier frequency by use of a filter as discussed in the frequency up conversion step.

The next step in the microwave pulse generation scheme is to up convert the filtered output of the AWG into the microwave frequency range. This is accomplished using a broadband microwave mixer (I) and a single frequency PLDRO source (E) at 9.9 GHz (i.e. 990<sup>th</sup> harmonic of the 10 MHz reference). This PLDRO source has a dual

lock loop design and requires only a direct input of the 10 MHz reference frequency. The output of the mixer contains two linear sweep sidebands above (11437.5 – 10062.5 MHz) and below (8362.5 – 9737.5 MHz) the 9.9 GHz carrier frequency. To extend the bandwidth of the pulse using microwave frequency multipliers it is necessary to isolate a single sideband otherwise the active frequency multipliers undo the mixing and fold the sidebands back into the carrier frequency. A 13 pole microwave bandpass filter (3 dB points at 9.748 and 8.232 GHz and 40 dB attenuation at 9.9 GHz, K) is used to extract the lower sideband frequency sweep and to reject any residual microwave power at the 9.9 GHz carrier frequency.

After frequency up conversion and filtering the bandwidth of the chirped pulse is increased a factor of 4 using an active frequency quadrupler (M) to 33450 – 38950 MHz. The output of the frequency quadrupler passes through a continuously variable attenuator (O) and is filtered in a high pass filter (N) with 25 GHz cut off frequency to remove the residual power leakage of the sweep that appear on the output channel. The attenuator is used to precisely set the input power for the next step; input into the broadband mixer. The frequency multiplied sweep is subsequently down converted by 19.8 GHz in a broadband mixer (P). The local oscillator for this mixer is provided by the frequency doubled (H) output of the 9.9 GHz PLDRO source. The mixer output is amplified in a broadband microwave amplifier (Q, 32 dB gain) and sent to an active frequency doubler (R) to increase the sweep bandwidth by a factor of 8 overall (after two multiplier stages). The output of the active doubler is directed to a second high pass filter (N) to remove the power leakage of this device. The bandwidth multiplied sweep is down converted a

second time into the 7.5 – 18.5 GHz range using a broadband mixer (P) and the doubled output of the 9.9 GHz PLDRO at 19.8 GHz as the local oscillator.

The final stage of the circuit diagram in Figure 9.3 consists of a continuously variable attenuator (S), low-noise pre-amplifier (T), programmable attenuator (U), and finally a single-pole-single-throw (SPST) microwave switch (V). The continuously variable attenuator is used to precisely set the power input to the low noise amplifier to achieve maximum signal-to-noise of the chirped pulse after pre-amplification. The low noise amplifier is used to bring the output of the x8 circuit to a power level that is sufficient to drive the Traveling Wave Tube amplifier (TWTA, W) into saturation (~5 dBm). The programmable attenuator is used to control the power input to the TWTA to optimize sample excitation conditions. The SPST switch is used to time slice the chirped pulse out of the background noise generated by the active frequency multipliers before entering the high power TWTA.

As just indicated after the chirped pulse is generated the next step is amplification to high peak power for molecular sample polarization. The power requirements for CP-FTMW spectroscopy will be discussed in the section F. Sample Polarization. Several microwave power amplifiers have been tested in these experiments including a 5 W solid state amplifier (Microwave Power L0818-37, 8 – 18 GHz) and pulsed traveling wave tube amplifiers (TWTA) with peak powers of either 300 W or 2 kW (W or X). All of these amplifiers have demonstrated sufficient shot-to-shot phase stability to permit time domain averaging of the FID and have sufficiently low noise power to allow for coherent sample polarization.

To analyze the properties of the chirped pulse the output from the sample port (-30 dBm) on the TWTA is down converted with the 18.99 GHz PLDRO and a broadband mixer which is then digitized and Fourier transformed on the fast oscilloscope with a 40 GS/s sampling rate. The full linear frequency sweep microwave pulse (7.5 – 18.5 GHz) generated from the circuit diagram in Figure 9.3 and amplified using the 2 kW TWTA is displayed in Figure 9.4 in both time (top) and frequency domain (middle). The frequency bandwidth of the pulse is clearly illustrated in the middle panel where the Fourier transform of the time domain chirped pulse is shown.

Further characterization of the chirped microwave pulse is achieved using a time-frequency analysis of the pulse (a spectrogram) using a moving gate Fourier transform method. This analysis begins by breaking the 1  $\mu$ s pulse into a series of 10 ns time slices. The time slices are windowed with a Kaiser-Bessel function (window functions will be discussed in Section E) and Fourier transformed to the Frequency domain. The Fourier transform of each time slice is represented as a function of time in a contour plot in the bottom panel of Figure 9.4. This analysis method shows the linear frequency sweep of the microwave pulse and the signal purity at each instantaneous frequency. The spurious signals in the pulses created using this technique are at least 20 dBm lower in power than the instantaneous sweep frequency across the full 11 GHz range of the pulse.

Several critical design aspects of the chirped pulse circuit need to be discussed before moving forward. There are three mixers in the chirped pulse generation circuit and the input powers to each of these mixers are carefully set to minimize harmonics and spurious frequencies on the output for each mixer using the oscilloscope to analyze the

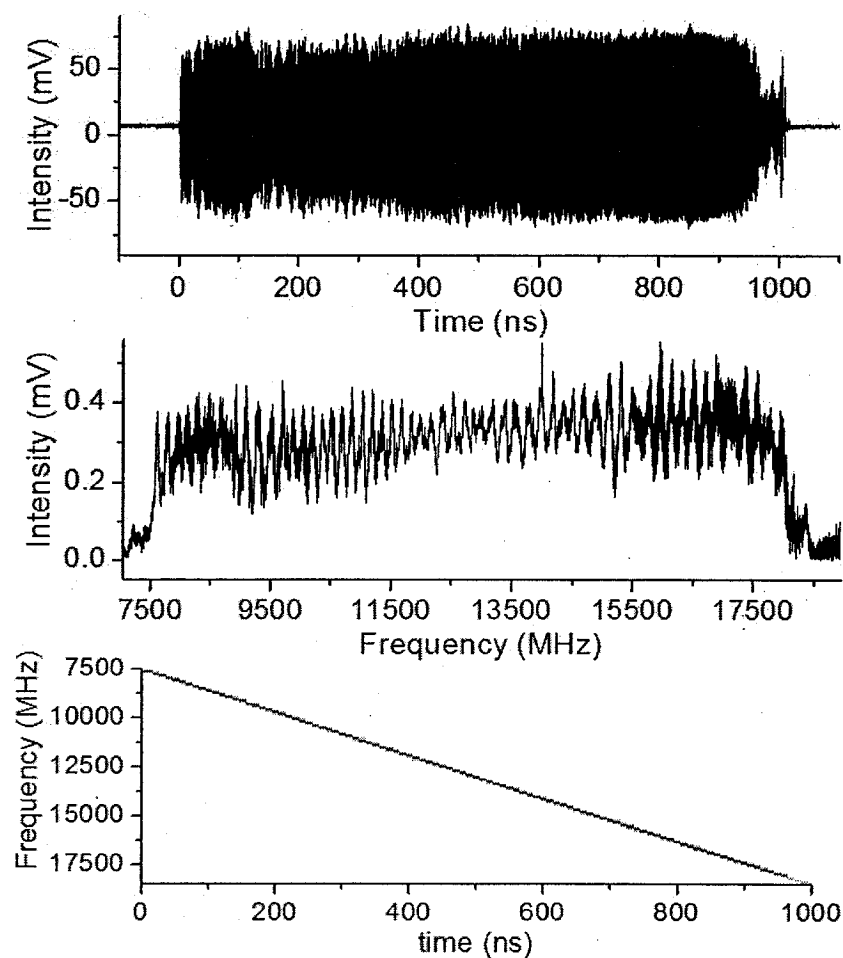


**Figure 9.4** The above panels illustrate time domain (top), frequency domain (middle), and a time-frequency analysis (bottom) of the  $1 \mu\text{s}$  11 GHz chirped pulse after amplification by the 2 kW TWTA after 100 time domain signal averages. This measurement was performed on the pulse the sample port (-50 dB down) of the TWTA. The 7.5 – 18.5 GHz pulse was down converted by mixing with an 18.99 GHz PLDRO, and digitized at 40 GS/s by the oscilloscope. The time-frequency analysis (bottom) is depicted as contour plot. This analysis method shows the linear frequency sweep of the microwave pulse and the signal purity at each instantaneous frequency. The spurious signals in the pulses were measured to be at least 20 dB lower in power than the instantaneous sweep frequency across the full 11 GHz range of the pulse.

pulse. In general before all filters an isolator is used to prevent reflected power from getting back into the previous component which would otherwise create spurious frequencies. Another important design aspect of the microwave circuit is that only a single external microwave frequency source (9.9 GHz PLDRO) is used, which minimizes the phase noise. The circuit is also designed to minimize harmonics and spurious frequencies at several points by the use of various filtering stages and by the choice of components.

It is important to note that directly multiplying up the bandwidth and frequency of the AWG output would most likely have disastrous consequences on the pulse signal purity for many reasons. The lower frequency or RF frequency multipliers typically have poor harmonic isolation and these harmonics are now in the frequency range of interest making them difficult or impossible to filter out. Additionally, to cover a similar frequency range and bandwidth multiplication on the order of 10 would be necessary which would further degrade the signal purity and phase stability.

### C. Free Space Molecular Beam Chamber

The next design challenge is broadband sample polarization and collection of the rotational FID because the high Q cavity can no longer be implemented. As indicated in the free space molecular beam chamber design illustrated in Figure 9.5, sample polarization and detection over the full bandwidth of the linear sweep pulse is achieved using two microwave antennas. These antennas operate over two octave bands (8 – 12 and 12 – 18 GHz) allowing measurement of the full 7.5 – 18.5 GHz generated in the chirped pulse circuit.

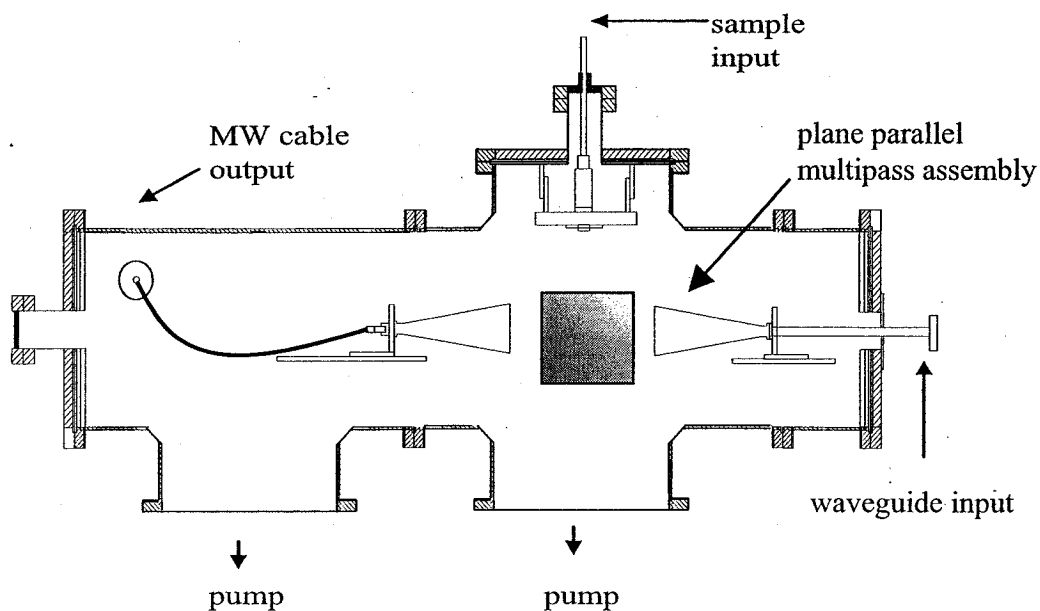


**Figure 9.5.** The side view of the free space molecular beam chamber is illustrated above. A pulsed valve (General Valve Series 9) produces the pulsed molecular beam perpendicular to the microwave pulse propagation. The amplified chirped microwave pulse is coupled into the vacuum chamber using double ridge waveguide and a Kapton window. The pulse is broadcast by a double ridge standard gain horn antenna into the sample interaction region. A second horn is placed opposite the broadcast horn (~20 cm apart) in order to receive the broadband rotational free induction decay (FID) of the polarized sample. The MW power collected by the receiving horn is coupled out of the chamber by microwave cables through a hermetically sealed SMA coupler. Both the valve height (relative to the MW horns) and the valve tension (adjusted by turning the valve relative to the faceplate) are adjustable from outside the spectrometer.

The high-power microwave polarizing pulse is coupled into the chamber using a double-ridge waveguide bulkhead feed-through that is sealed against the conflat flange of the chamber. A Kapton window (ATM 750-230-2-2) with o-ring seal is mounted in between the double-ridge bulkhead feed-through and the horn antenna and is used to transmit the microwave radiation while maintaining vacuum. The polarizing pulse is broadcast into the chamber using a double-ridge rectangular standard gain horn (20 dBi gain, -3 dB beam width of 32° at 7.5 GHz, Amplifier Research AT4530). A second, identical horn antenna is used to collect the rotational FID signal. The receiver horn antenna is mounted on a translation stage and can be manually adjusted to maximize the molecular signal.

The broadcast and receiver horns are aligned with the same polarization orientation and are separated by about 20 cm. At this distance, the receiver collects about 10% of the broadcast power over most of the bandwidth of the spectrometer (7.5 – 16 GHz) with lower collection efficiency at higher frequencies (16 – 18.5 GHz). Since the peak power transmitted to the receiver from the strong polarizing pulse is less than 200 W, (for 2 kW TWTA) it can be safely handled using microwave cables and SMA connectors.

The free space molecular beam chamber (Figure 9.5) consists of a standard 13.25" conflat flange six-way cross and tee. Two 10" diffusion pumps (Varian VHS-10), backed by a mechanical pump – Roots blower combination (Edwards E2M40 and EH250) are used to achieve high throughput with typical chamber pressures of  $\sim 10^{-7}$  torr. The diffusion pump below the microwave interaction region has a water cooled baffle to

prevent oil build up on the multipass mirrors used in laser-CP-FTMW double resonance experiments. The pulsed valve (General Valve Series 9) is mounted to the top flange of the six-way cross and its height relative to the microwave interaction region can be manually adjusted. All interior surfaces of the molecular beam chamber are covered by microwave foam absorber that is secured to metal foil backing (Emerson and Cuming HR-25/ML). The microwave absorber is needed to prevent long-lived resonances in the molecular beam chamber that produce spurious frequencies in the collected microwave signal.

#### **D. Free Induction Decay Detection**

The detection components for the spectrometer are shown schematically in Figure 9.6. A description of the components used in the FID detection circuit are shown in Table 9.2 Because the full spectral bandwidth (11 GHz) is measured in each data acquisition event, this part of the spectrometer design is relatively simple. The first two components in the detection assembly, a high-power PIN diode (D) and a SPST switch (E) are required to protect the low noise amplifier and other circuit elements from the high-power microwave polarizing pulse. The PIN diode is rated for a 1 kW peak power with pulse duration of 1  $\mu$ s. The specification for the recovery time is < 40 ns. The leakage peak power from the diode is still too high (~1 Watt) for the low noise amplifier used to amplify the rotational FID, so the microwave switch is placed after the diode. This switch is controlled by the complement pulse that activates the TWTA pulse output (DG535 #3) and therefore blocks the TWTA power when the pulse is fired.

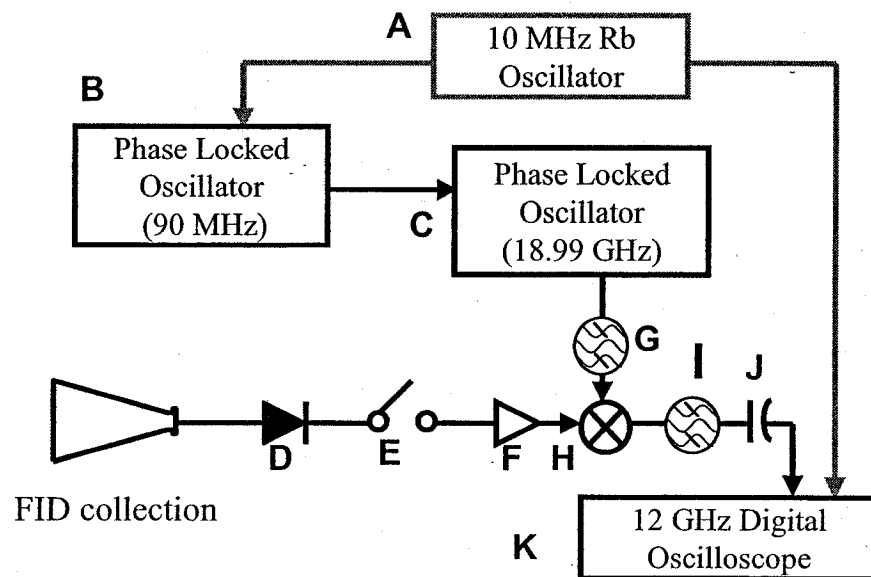


**Figure 9.6** The broadband detection circuit is displayed above. The broadband molecular free induction decay (FID) first passes through a pin diode limiter and a single pole single throw (SPST) switch, which are necessary to protect the receiver amplifier from the high peak power MW polarization pulse. After the switch, the FID is amplified by a broadband low noise MW amplifier. The amplified FID is then down converted by the filtered output of an 18.99 GHz PLDRO. The 90 MHz PLDRO input for the 18.99 GHz PLDRO is locked to the same 10 MHz Rubidium oscillator as the pulse generation frequency components. The down converted signal (0.49 – 11.49 GHz) is sent through a low pass filter (12.2 GHz) and a DC block (250 MHz), and then digitized by a 40 GS/s (12 GHz hardware bandwidth) digital oscilloscope. A component list is also shown.

**Table 9.2 Component List for Detection Circuit**

<b>Component</b>	<b>Manufacturer</b>	<b>Description</b>	<b>Part No.</b>
<b>A</b>	Stanford Research Systems	10 MHz Rubidium Frequency Standard	FS725
<b>B</b>	Miteq	90 MHz phase locked oscillator	PLD-10-90-15P
<b>C</b>	Microwave Dynamics	18.99 GHz phase locked oscillator	PLO-2000-18.99
<b>D</b>	Advanced Control Components	8 - 18 GHz power limiter diode	ACLM-4539-C36-1K
<b>E</b>	ATM	SPST microwave switch	S1517D
<b>F</b>	Miteq	8 -18 GHz low noise amplifier	AMF-5F-0800-1800-14-10P
<b>G</b>	Lorch	18.99 GHz bandpass filter	3CF7-18990/200-S
<b>H</b>	Miteq	triple balanced microwave mixer	TB0440LW1
<b>I</b>	K&L	12.2 GHz low pass filter	11L250-12200/T20000-0/0
<b>J</b>	Midwest	DC - 250 MHz DC Block	3510
<b>K</b>	Tektronix	Digital Storage Oscilloscope 40GS/s, 12 GHz bandwidth	TDS6124C

The rotational FID signal is amplified by a high gain (38 dBm), low noise (noise figure 1.4) solid-state broadband microwave amplifier (F). The amplified FID signal is down converted to the 500 MHz – 11500 MHz frequency range using an ultra broadband triple balance mixer (H). The down converted FID signal passes through a low pass filter (I) that removes the local oscillator signal that leaks through the mixer. A DC block (J) follows the low pass filter to remove the low frequency (1/f) noise prior to digitization.

To minimize phase noise the local oscillator frequency used to down convert the FID is selected to be an integer multiple of the 10 MHz reference frequency. This local oscillator is a single frequency PLDRO source at 18.990 GHz (C). This PLDRO produces a phase-locked harmonic of an input 90 MHz reference signal. The 90 MHz signal for the PLDRO is supplied by a second PLDRO (B) that uses the 10 MHz signal from the Rb-disciplined crystal oscillator as its phase reference.

The 500 – 11500 MHz FID signal is digitized directly using a digital oscilloscope (Tektronix TDS6124C, K) at 40 GS/s sampling rate. Down conversion is necessary because the hardware bandwidth limit of the oscilloscope is 12 GHz. A windowing function is then applied to the FID before Fourier transforming. The use of various window functions as they apply to broadband rotational spectroscopy will be discussed in section E. Apodization. The digitizer clock is phase locked to the 10 MHz reference from the Rb-disciplined master reference (A).

The repetition rate of the experiment is limited by the data collection of the oscilloscope and depends on the record length (sample rate \* gate duration). Although the sample rate must be fixed in order to accurately digitize the broadband signal the gate

duration can be manipulated to affect the size of the record length with an obvious consequence to the linewidth of the spectrum. For high spectral resolution typically used to obtain and assign pure rotational spectra a 20  $\mu$ s gate (800,000 points) reduces the experiment repetition rate to about 3.5 Hz. For a 4  $\mu$ s gate (160,000 data points) the spectrometer can acquire data at approximately 7 Hz. A 1.2  $\mu$ s gate duration the scope runs at the full 10 Hz repetition rate, which will become important for laser-CP-FTMW double resonance studies discussed in Chapter 10.

#### **E. Apodization**

A problem common to FTIR and FT-NMR and other Fourier transform techniques is the lineshape of the spectrum that results from Fourier transforming a truncated time domain signal (or interferogram). Methods have been developed based on apodization of the FID by which a weighting or window function is applied to the FID prior to Fourier transform. The observed spectrum is the convolution of the Fourier transform of the window function and 'true' spectrum. In the absence of applying a window function there is still an effective rectangular window applied to the FID. The observed spectrum is then a convolution of the  $\sin x / x$  (sinc) function and a Gaussian (typically) function and contains the characteristic sidelobes of the sinc  $x$  function. The aim of the window function is to suppress the sidelobes or frequency leakage. Many window functions have been developed for FTIR and FT-NMR and the relative advantages of several window functions as they apply to resolution, sidelobe suppression, and signal-to-noise will be presented.

Sidelobe suppression is especially important for instances where there is a weak rotational transition close in frequency to a strong transition, which is typical in broadband rotational spectroscopy. Without proper apodization the strong transition distorts or possibly prevents the weak transition from being observed. There are many examples where this problem would arise in rotational spectroscopy such as the rotational transitions of  $^{13}\text{C}$  isotopes in natural abundance, minor conformers, or a-type transitions near b-type transitions depending on the respective dipole moments, etc.

In general there are trade-offs between using different types of window functions. Six different window functions are presented in Figures 9.7 and 9.8 which illustrates the windowed FID and the Fourier transform as applied to cyclopropanecarboxaldehyde (CPCA) in the region of the *cis* conformer  $1_{11} - 0_{00}$  transition at 15267.2048 MHz.<sup>30</sup> These figures are used to demonstrate the relative advantages of each type of window function. The six windows are rectangular (no window), Hamming, Kaiser-Bessel, TekExp, exponential damped at the  $T_2$  time, and a Lorentz-Gauss.<sup>31-33</sup> The functional form of the windows are listed in Table 9.1 of appendix 9.A. The first four shown in Figure 9.7 window functions demonstrate the effect of minimizing the sidelobes at the cost of increasing the linewidth at FWHM and are standard windows on the oscilloscope. The last two windows shown in Figure 9.8 are typically used in NMR spectroscopy. The damped exponential at  $T_2$  maximizes the signal-to-noise at the expense of line broadening. The noise is effectively scaled down at long times where the noise dominates the FID. The Lorentz-Gauss window is a resolution enhancement window

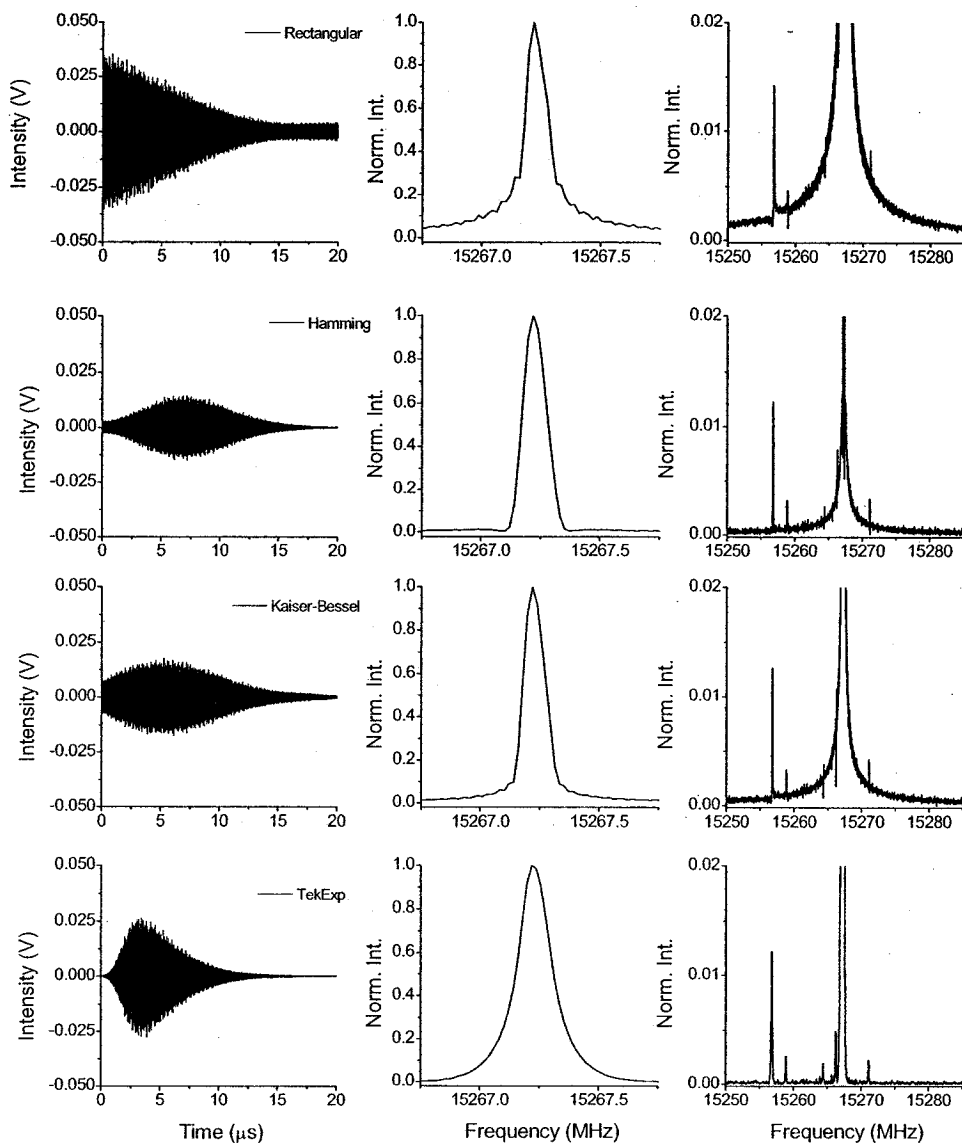


**Figure 9.7** The effect of a weighting function applied to the rotational FID (left) and the resulting Fourier transform (right) is illustrated in the above panels for cyclopropanecarboxaldehyde (CPCA) in the region of the normal species *cis* conformer  $1_{11}-0_{00}$  at 15267.2048 MHz. Just to the left of normal species is a  $^{13}\text{C}$  isotopomer  $5_{15}-4_{22}$  at 15271.1451 MHz. The windows used are rectangular, Hamming, Kaiser-Bessel, TekExp. The windows are in order of increasing sidelobe suppression as clearly illustrated in the zoomed scale of the right panel.

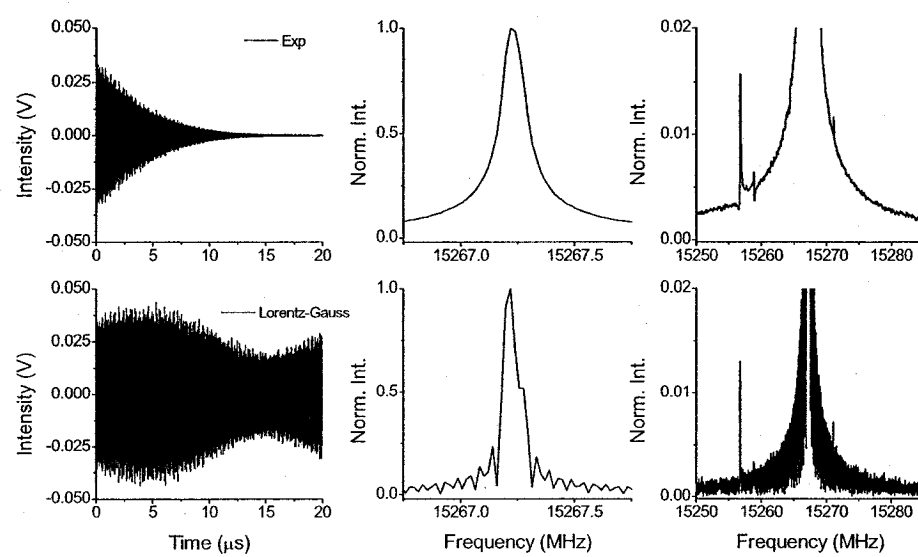


**Figure 9.8** This figure is a continuation of Figure 9.7, the windows used are typically used in NMR spectroscopy. The windows are a exponential decay with the lifetime set to the experimental  $T_2$  dephasing time ( $\sim 8 \mu\text{s}$ ) and a Lorentz-Gauss. The two windows are complementary; the exponential decay window maximizes the signal-to-noise at the expense of linewidth, while the Lorentz-Gauss minimizes linewidth at the expense of signal-to-noise.

and is used to minimize the linewidth at FWHM at the expense of signal-to-noise, however it also contains a peculiar lineshape and artifacts at the baseline. Figures 9.7 and 9.8 clearly demonstrates that sidelobe suppression by application of window function significantly reduces the spectrometer line width at baseline making it easier to detect weak transitions in the proximity of strong ones. The Kaiser-Bessel window function (69 dBm of sidelobe suppression and a 97% increase in the FWHM linewidth) is typically used when acquiring broadband rotational spectra.

## F. Sample Polarization

The mechanism of chirped pulse excitation as it compares with excitation using a transform limited pulse will be discussed along with the power requirements of broadband excitation.

### i. Linear Sweep Excitation

The description of the macroscopic polarization using a fast frequency sweep has been presented previously by McGurk, Schmalz, and Flygare to describe experiments where the molecular resonance was swept through a fixed microwave frequency using the Stark effect.<sup>34</sup> In this work, McGurk *et al.* point out that fast passage excitation is an efficient way to excite the molecular sample. In a later work, Wolf has demonstrated fast passage excitation by chirped millimeter pulses for rotational spectroscopy.<sup>35</sup> In this experiment, a chirped pulse covering 280 MHz (72840 – 73120 MHz), created using a backward wave oscillator (BWO), was used to sweep over the  $J = 6 - 5$  molecular transition of two OCS isotopomers. More recently, Khodos, Ryndyk, and Vaks have

proposed using frequency sweeps to apply the fast passage effect to microwave molecular spectroscopy.<sup>36</sup> However, until now there has been no microwave source that could generate chirped microwave pulses covering the 7.5 – 18.5 GHz region of the spectrum. With the development of a suitable microwave source based on arbitrary waveform generators described above, we can now pursue a true broadband spectrometer based on fast passage excitation.

In their study of fast passage excitation using the molecular Stark shift, McGurk, *et al.* provide an analysis of the polarization of the molecular sample by a linear frequency shift. The measurement of Wolf<sup>35</sup> supported the basic results of their work. The measurements presented in this chapter using the chirped-pulse FTMW spectrometer further confirm these results. The electric field for a chirped pulse that produces a linear frequency sweep is

$$E(t) = E_0 e^{i(\omega_0 t + \frac{\alpha}{2} t^2)} \quad (9.1)$$

where the instantaneous frequency is

$$\omega = \frac{d}{dt} (\omega_0 t + \frac{\alpha}{2} t^2) = \omega_0 + \alpha t \quad (9.2)$$

The linear sweep rate is given by  $\alpha$  in the two previous expressions. The sweep range for the pulse is linearly related to the pulse duration ( $t_{\text{pulse}}$ )

$$\Delta\omega = \alpha \cdot t_{pulse} \quad (9.3)$$

Unlike simple transform limited pulses with a single carrier frequency, the chirped pulse separates the bandwidth from the pulse duration. This makes it possible to separately control the frequency range of the excitation and the amount of energy delivered to the sample.

For microwave spectroscopy, the linear frequency sweep pulse has been shown by McGurk *et al.* to be particularly efficient at polarizing the molecular sample. Using a Bloch equation analysis they showed (Eq. 23 of Ref. 31) that the macroscopic polarization of the sample for a linear sweep pulse of fixed duration (in the weak excitation limit) is

$$P \propto \frac{\hbar\kappa^2\varepsilon}{4} \Delta N_0 \left( \frac{\pi}{\alpha} \right)^{\frac{1}{2}} \quad (9.4)$$

$\varepsilon$  is the magnitude of the electric field, and  $\Delta N_0$  is the equilibrium value of the population difference.  $\kappa$  is related to the transition dipole moment matrix element by the equation

$$\kappa = \left( \frac{2}{\hbar} \right) \left| \langle a | \mu | b \rangle \right| \quad (9.5)$$

where  $\mu$  is the dipole moment operator and  $a$  and  $b$  represent the lower and upper levels, respectively. All the parameters of equation (23) from McGurk<sup>34</sup> are reproduced in

Appendix 9.A Table 2. In Eq. (9.4), the polarization scales as  $\alpha^{-1/2}$ . In practice, the pulse duration for FTMW measurements is fixed by the requirement that the sample is polarized faster than the pure dephasing rate,  $T_2$ . With an upper limit to the pulse lengths in experiments, the  $\alpha^{-1/2}$  scaling means that observed signals only decrease with the inverse square root of the pulse bandwidth. This gives more favorable signal scaling compared to using a transform limited pulse with a single carrier frequency where the polarization scales linearly with the excitation bandwidth.<sup>29</sup> The difference in this scaling comes from the fact that for transform limited pulses, increasing the bandwidth is achieved by decreasing the pulse duration and, therefore, the total energy delivered to the sample. Using the linear sweep chirped pulse the maximum amount of pulse energy, limited by  $T_2$ , can be delivered to the sample for any excitation bandwidth.

The results of McGurk *et al.* have been tested by measuring the  $1_0 - 0_0$  pure rotational transition of 1-propyne (17091.743 MHz) for variable sweep rates. In this test, the sweep rate was adjusted by changing the frequency range of the pulse while maintaining a constant pulse duration. The signals are compared to measurements using a transform limited Gaussian pulse with variable pulse duration. This shaped microwave pulse is generated using the arbitrary waveform generator to create the Gaussian profile and mixing this with the output of a microwave synthesizer tuned to resonance.

The results of these measurements are shown in Figure 9.9. This figure verifies the  $\alpha^{-1/2}$  signal scaling predicted by Eq. (9.4) and also illustrates the favorable signal scaling of the chirped pulse for large bandwidth measurements compared to transform

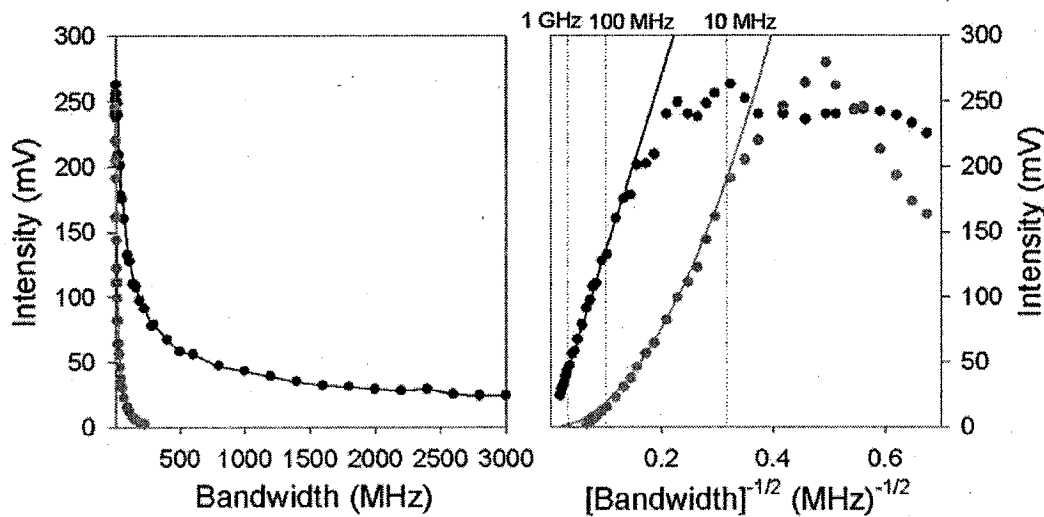


**Figure 9.9.** The molecular signal intensity of 1-propyne ( $1_0 - 0_0$  transition, 17091.743) is plotted versus pulse bandwidth using a transform limited Gaussian shaped polarizing pulse (gray) and a linear frequency sweep chirped polarizing pulse (black) of the same peak power. For the chirped pulse, the sweep rate is adjusted in the waveform by changing the frequency range while maintaining the same pulse duration. For the Gaussian pulse, the bandwidth is adjusted by changing the pulse duration. This shaped microwave pulse is generated using the arbitrary waveform generator to create the Gaussian profile and mixing this with the output of a microwave synthesizer tuned to resonance. When the signal intensity is plotted versus the bandwidth of the pulse (left), we observe a faster fall-off in signal intensity of the Gaussian pulse. In the graph on the right, the same data is plotted versus the inverse of the square root of the bandwidth. In this case, the  $\alpha^{1/2}$  signal scaling predicted by Eq. (4) is demonstrated, while the Gaussian pulse excitation scheme results in an  $\alpha$  scaling. Note that the peak signal intensities for both excitation methods are the same.

limited pulse shapes. We have also tested the sweep rate dependence of Eq. (9.4) by fixing the bandwidth of the chirped pulse and varying the time duration to adjust the sweep rate. These measurements (not shown) also display the  $\alpha^{-1/2}$  signal dependence. Note that the maximum signal for the propyne transition is the same for optimal excitation using either the chirped or transform limited pulse.

The inverse-square-root scaling for linear sweep excitation means that the optimal way to perform the experiment is to sweep as much bandwidth as possible. For example, when comparing the signals for a 4 GHz bandwidth scan and a 1 GHz scan, the signal will drop by a factor of 2 in the 4 GHz measurement. To achieve the same signal-to-noise ratio in the two measurements will require 4 times as many signal averages for the 4 GHz experiment ( $S/N \sim N^{1/2}$ ). However, it has covered 4 times the spectral range of the 1 GHz spectrum. When the full spectrum needs to be acquired, the time required to reach a target signal-to-noise ratio is independent of the bandwidth.

## ii. Power Requirements for Broadband FTMW Spectroscopy

For CP-FTMW spectroscopy, the power requirements depend on the pulse properties (bandwidth and duration) and the molecular properties (the magnitude of the dipole moment). In comparison to the Balle-Flygare cavity FTMW spectrometer, more peak power is required by the CP-FTMW spectrometer in order to optimally polarize the sample for two reasons. First, the CP-FTMW lacks the passive amplification which the Fabry-Perot cavity provides. The peak power requirement scales as the cavity  $Q$ . The miniature cavity FTMW spectrometer in our laboratory has a cavity  $Q$  on the order of 10,000. Therefore, to optimally excite the same transition, the CP-FTMW spectrometer

( $Q = 1$ ) requires a factor of 10,000 more power. Second, while the cavity FTMW spectrometer covers approximately 1 MHz of bandwidth with each microwave pulse, the CP-FTMW spectrometer covers 11 GHz. This results in another factor of 11,000 power requirement.

The cavity FTMW spectrometer in our laboratory typically requires on the order of 10  $\mu$ W of peak power to optimally excite molecules with a 1 D dipole moment. Therefore, the CP-FTMW spectrometer should require on the order of 1 kW to optimally excite the same transition using an 11 GHz sweep of the same pulse duration. In practice, the 2 kW TWTA can optimally excite molecules with dipole moments of about 0.7 D for a 1  $\mu$ s pulse that covers 11 GHz of spectral bandwidth.

The above peak power estimates assume the same pulse duration for both spectrometers. Pulse durations on the order of 1  $\mu$ s are typically used in both the cavity FTMW spectrometer and the CP-FTMW spectrometer. This pulse duration is possible for the CP-FTMW spectrometer since we are using a chirped pulse to polarize the sample. However, if one were to polarize 11 GHz of bandwidth with a transform limited pulse, the pulse duration would have to be on the order of 40 ps (Gaussian pulse). In this case, the broadband spectrometer would require an additional factor of 25,000 peak power in order to optimally polarize the sample. Applying this to the example above, a molecule with a dipole moment of 1 D would require peak polarization power of 25 MW for a transform limited pulse covering 11 GHz of spectral bandwidth. Needless to say, amplification to a peak power of this magnitude is not commercially available.

### Summary

The principles of a broadband chirped-pulse Fourier transform microwave (CP-FTMW) spectrometer capable of measuring an 11 GHz (7.5 – 18.5 GHz) frequency range in each FID has been presented. The aspects of generating an 11 GHz chirped pulse, broadband polarization and detection of the sample have been presented. The advantages for chirped pulse excitation namely, decoupling bandwidth from pulse duration and also that multiplication of a chirped pulse multiplies both the frequency and the bandwidth have been discussed. The following Chapters 10 and 11 will demonstrate broadband rotational spectroscopy for the measurement of pure rotational spectra with comparisons to the narrowband cavity FTMW spectrometer and for the measurement of rotational spectra in the vibrationally excited state.

## Reference List

1. McAfee Jr., K. B.; Hughes, R. H.; Wilson Jr., E. B., *Rev.Sci.Instrum.* **1949**, *20*, 821.
2. Hughes, R. H.; Wilson Jr., E. B., *Phys.Rev.* **1947**, *71*, 562.
3. Jones, G. I. L.; Owen, N. L., *J.Mol.Struct.* **1973**, *18*, 1-32.
4. Scroggins, D. G.; Riveros, J. M.; Wilson Jr., E. B., *J.Chem.Phys.* **1974**, *60*, 1376.
5. Owen, N. L., *J.Mol.Spectrosc.* **1970**, *6*, 37.
6. Balle, T. J.; Campbell, E. J.; Keenan, M. R.; Flygare, W. H., *J.Chem.Phys.* **1979**, *71*, 2323.
7. Balle, T. J.; Campbell, E. J.; Keenan, M. R.; Flygare, W. H., *J.Chem.Phys.* **1980**, *72*, 922-932.
8. Balle, T. J.; Flygare, W. H., *Rev.Sci.Instrum.* **1981**, *52*, 33-44.
9. Grabow, J. U.; Stahl, W., *Z.Naturforsch* **1990**, *45a*, 1043-1044.
10. Grabow, J. U.; Stahl, W.; Dreizler, H., *Rev.Sci.Instrum.* **1996**, *67*, 4072-4084.
11. Suenram, R. D.; Grabow, J. U.; Zupan, A.; Leonov, I., *Rev.Sci.Instrum.* **1999**, *70*, 2127-2135.
12. Arunan, E.; Dev.S.; Mandal, P. K., *Appl.Spectrosc.Rev.* **2004**, *39*, 131-181.
13. Fraser, G. T.; Suenram, R. D.; Lugez, C. L., *J.Phys.Chem.A* **2001**, *105*, 9859-9864.
14. Fraser, G. T., *J.Chem.Phys.* **2000**, *112*, 6209-6217.
15. Suenram, R. D.; Plusquellic, D. F.; Lovas, F. J.; Hight Walker, A. R.; Liu, Q.; Xu, L. H.; Jensen, J. O.; Samuels, A. C., *J.Mol.Spectrosc.* **2003**, *223*, 9-19.
16. Legon, A. C., *Annu.Rev.Phys.Chem.* **1983**, *34*, 275-300.
17. Bauder, A., *J.Mol.Spectrosc.* **1997**, *408/409*, 33-37.
18. Wijngaarden, J. v.; Jäger, W., *J.Am.Chem.Soc.* **2003**, *125*, 14631-14641.
19. Xu, Y.; Wijngaarden, J. v.; Jäger, W., *Int.Rev.Phys.Chem.* **2005**, *24*, 301-338.

20. Hirahara, Y.; Ohshima, Y.; Endo, Y., *J.Chem.Phys.* **1994**, *101*, 7342-7349.
21. Ohshima, Y.; Endo, Y., *J.Mol.Spectrosc.* **1992**, *153*, 627-634.
22. Seki, K.; Sumiyoshi, Y.; Endo, Y., *J.Chem.Phys.* **2002**, *117*, 9750.
23. Ohshima, Y.; Endo, Y., *Chem.Phys.Lett.* **1996**, *256*, 653.
24. Legon, A. C.; Stephenson, D., *J.Chem.Soc.Faraday Trans.* **1992**, *88*, 761.
25. Gerhards, M.; Unterberg, C.; Gerlach, A.; Jansen, A., *Phys.Chem.Chem.Phys.* **2004**, *6*, 2682-2690.
26. Hudspeth, E.; McWhorter, D. A.; Pate, B. H., *J.Chem.Phys.* **1997**, *107*, 8189-8192.
27. Lee, C. Y.; Pate, B. H., *J.Chem.Phys.* **1997**, *107*, 10430-10439.
28. Brannon, B. Understand the effects of clock jitter and phase noise on sampled systems. EDN . 12-7-2004.
29. Clock (CLK) Jitter and Phase Noise Conversion. Maxim Integrated Products Application Note 3359 . 9-23-2004.
30. Volltrauer, H. N.; Schwendeman, R. H., *J.Chem.Phys.* **1971**, *54*, 260-267.
31. Elliott, D. F. *Handbook of Digital Signal Processing Engineering Applications*; Academic Press Inc.: San Diego, 1987.
32. Pickerd, J. J. Impulse-Respone testing lets a single test do the work of thousands. EDN Access . 1995.
33. Günther, H. *NMR spectroscopy : basic principles, concepts, and applications in chemistry*; Wiley: New York, 1995
34. McGurk, J. C.; Schmalz, T. G.; Flygare, W. H., *J.Chem.Phys.* **1974**, *60*, 4181-4186.
35. Wolf, F., *J.Phys.D: Appl.Phys.* **1994**, *27*, 1774.
36. Khodos, V. V.; Ryndyk, D. A.; Vaks, V. L., *J.Appl.Phys.* **2004**, *25*, 203.

### Appendix 9.A

Table 9.1 Definition of Window Functions

Window Function	Functional Form
Hamming	$W(t) = 0.54 * \cos\left(\frac{2\pi t}{N}\right)$
Kaiser-Bessel	$W(t) = \frac{J_0\left[\beta \cdot \sqrt{1 - \left(1 - \frac{2 \cdot t}{N}\right)^2}\right]}{J_0(\beta)}$
TekExp	$W(t) = a_0 \left[ \left( \frac{1}{1 + 2 \frac{\frac{n}{a_3} - c_1 - c_2}{a_3}} \right) \cdot \left( 1 - \frac{1}{1 + 2 \frac{\frac{n}{a_4} - c_3 - c_4}{a_4}} \right) \right]^x$ $a_0 = \left[ \left( \frac{1}{1 + 2 \frac{\frac{N-a_1+a_2}{2}}{a_3}} \right) \cdot \left( 1 - \frac{1}{1 + 2 \frac{\frac{(N-a_1)-a_2}{2}}{a_4}} \right) \right]^{-x}$ $c_1 = -\frac{a_1}{a_3} \quad c_2 = \frac{2}{a_3} \quad c_4 = -\frac{2}{a_4}$ $a_1 = \frac{N-1}{5} \quad a_2 = \frac{N-1}{3} \quad a_3 = 0.03125 \cdot N \quad a_4 = \frac{N}{2}$ <p>x is empirically determined (4 typical)</p>
Exp	$W(t) = \exp\left(\frac{-T_2}{t}\right)$
Lorentz-Gauss	$W(t) = \exp\left(\frac{t}{a}\right) \cdot \exp\left(-\frac{t^2}{b^2}\right)$ <p>a and b are empirically determined</p>

Table 9.2

Eq. 23 from McGurk et al.<sup>31</sup>

$P(\Delta\omega_f) = \frac{\hbar\kappa^2\varepsilon}{4} \Delta N \left( \frac{\pi}{\alpha} \right)^{\frac{1}{2}} \left\{ \sin \left( \frac{(\Delta\omega_f)^2}{2a} \right) \left[ \pm C \left( \left  \frac{\Delta\omega_i}{(\pi\alpha)^{\frac{1}{2}}} \right  \right) \pm C \left( \left  \frac{\Delta\omega_f}{(\pi\alpha)^{\frac{1}{2}}} \right  \right) \right] - \cos \left( \frac{(\Delta\omega_f)^2}{2a} \right) \left[ \pm S \left( \left  \frac{\Delta\omega_i}{(\pi\alpha)^{\frac{1}{2}}} \right  \right) \pm S \left( \left  \frac{\Delta\omega_f}{(\pi\alpha)^{\frac{1}{2}}} \right  \right) \right] \right\}$
----------------------------------------------------------------------------------------------------------------------------------------------------------------------------------------------------------------------------------------------------------------------------------------------------------------------------------------------------------------------------------------------------------------------------------------------------------------------------------------------------------------------------------------------------------------------------------------------------------------------------

## Chapter 10

### Broadband Rotational Spectroscopy: Applications to Pure Rotational Spectroscopy

#### Introduction

In this chapter the performance of the broadband Chirped-Pulse FTMW (CP-FTMW) spectrometer will be presented for the measurement of pure rotational spectra. The performance aspects will be broken into two categories; basic experimental performance and comparisons to the narrowband cavity FTMW spectrometer. The basic experimental performance consists of the following: 1) Frequency accuracy and measurement precision and 2) relative intensity accuracy and dynamic range. The comparisons to the cavity spectrometer will be discussed in terms of sensitivity for optimally polarized samples, and also measurement speed. Also discussed will be the advantages that arise from recording the full 11 GHz bandwidth of the spectrometer for every data acquisition event.

#### A. Experimental Performance

The standard molecule used for calibration of an FTMW spectrometer is carbonyl sulfide (OCS). This is because OCS has a single rotational transition at ( $J=0 \rightarrow 1$  at 11 GHz) which typically gives rise to an exceptionally strong microwave signal. Using OCS has the advantage that there are many possible isotopomer configurations from the oxygen, carbon, or sulfur nucleus. This leads to transitions from many species whose relative intensities should be exactly known based on the relative abundance of the particular isotope. However, there is a small amount of error due to small changes in the

dipole moment. The OCS standard provides a way to calibrate absolute sensitivity, relative intensity accuracy, frequency accuracy, and measurement precision.

In the previous chapter a method for measuring the rotational spectrum from 7.5 – 18.5 GHz using a chirped-pulse FTMW (CP-FTMW) spectrometer was described. For obtaining high signal-to-noise pure rotational spectra 10,000 time-domain averages of the broadband free induction decay (FID) are acquired using the CP-FTMW spectrometer. Although the digital oscilloscope only has an 8-bit digitizer averaging effectively increases this bit resolution (>11 bit spec). This is one advantage to averaging over the entire spectrometer bandwidth.

The rotational spectrum of OCS (0.1% in a mixture of 70% neon and 30% helium) measured using the CP-FTMW spectrometer is illustrated in Figure 10.1. The normal species 1 - 0 OCS transition (12162.9778 MHz) has a signal-to-noise of ~95000:1 peak-peak, indicating 10,000 averages leads to an effective 17 bit vertical resolution. The noise is ~275 nV peak-peak and the signal is 26.5 mV. The sensitivity limit for the CP-FTMW spectrometer after 10,000 signal averages is determined by observing the different isotopomers of OCS. The lowest natural abundance isotopomer observed is  $^{18}\text{O}^{13}\text{CS}$  which is 0.0021% natural abundance (down a factor of 46,870 from the normal species) with a signal-to-noise of about 2:1 peak-peak.

Frequency accuracy and measurement precision benchmarks are obtained by measuring the frequencies of 11 isotopomers of OCS (in natural abundance) using the CP-FTMW spectrometer with comparison to the mini-FTMW spectrometer at NIST.<sup>1</sup> On

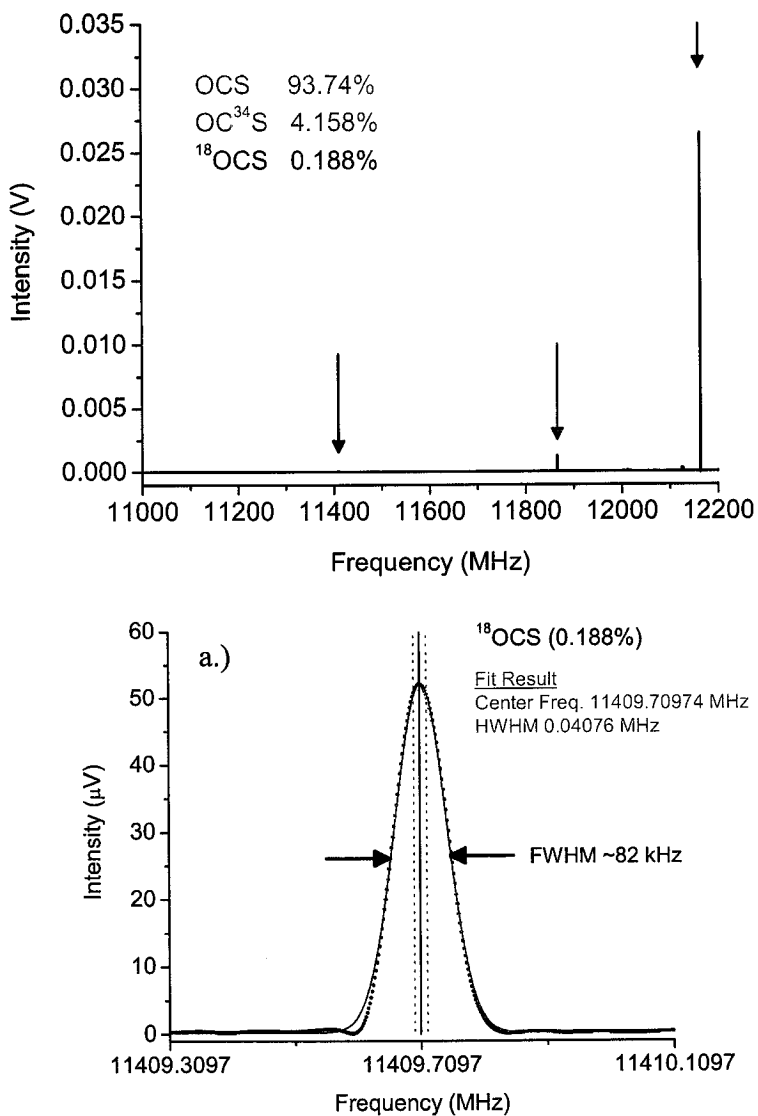


**Figure 10.1** The top panel illustrates the rotational spectrum of the 1 – 0 rotational transition of three isotopomers of carbonyl sulfide (OCS) in natural abundance measured by the CP-FTMW spectrometer with 10,000 time-domain averages. The colored arrows correspond to the normal species (green),  $\text{OC}^{34}\text{S}$  isotopomer (red), and  $^{18}\text{OCS}$  isotopomer. The signal-to-noise ratio achieved by the CP-FTMW is observed by the transition of the  $^{18}\text{OCS}$  species (~170:1), shown on an expanded scale of the lower panel (a.). The blue line in the lower panel is a reference line corresponding to the molecular frequency measured by the NIST cavity FTMW

Table 10.1 Comparison Frequencies and intensities for 11 isotopomers of OCS.

Isotope	F'<--F"	BB Freq. (MHz)	NIST Freq. (MHz)	BB-NIST (kHz)	experimental		literature
					natural abundance	natural abundance	% error
OCS		12162.9778	12162.9790	-1.2	93.74	93.74	---
OC <sup>34</sup> S		11865.6638	11865.6628	1.0	4.35373	4.158	4.70
O <sup>13</sup> CS		12123.8458	12123.8420	3.8	0.96362	1.053	-8.48
OC <sup>33</sup> S			12009.824*		0.6804	0.7399	-8.04
	3/2<--3/2	12004.0038	12004.0029	0.9	0.22607	0.24	-5.80
	5/2<--3/2	12011.2858	12011.2849	0.9	0.32848	0.37	-11.22
	1/2<--3/2	12017.1058	12017.1050	0.8	0.12583	0.13	-3.20
<sup>18</sup> OCS		11409.7097	11409.7097	0.0	0.1808	0.188	-3.82
O <sup>13</sup> C <sup>34</sup> S		11823.4638	11823.4625	1.3	0.03867	0.04672	-17.22
<sup>17</sup> OCS			11767.3346*		0.0311	0.03495	-11.01
	5/2<--5/2	11767.1338	11767.1315	2.3	0.00991	0.012	-17.39
	7/2<--5/2	11767.4058	11767.4015	4.3	0.01342	0.015	-10.53
	3/2<--5/2	11767.5398	11767.5330	6.8	0.00777	0.008	-2.92
OC <sup>36</sup> S		11599.3858	11599.3816	4.2	0.01533	0.0167	-8.21
<sup>18</sup> OC <sup>34</sup> S		11119.9337	11119.9346	-0.9	0.00966	0.00834	15.83
O <sup>13</sup> C <sup>33</sup> S			11969.1284*		0.00714	0.00831	-14.07
	3/2<--3/2	11963.3078	11963.3002	7.6	0.00246	0.00274	-10.09
	5/2<--3/2	11970.6078	11970.5845	23.3	0.00318	0.00416	-23.58
	1/2<--3/2	11976.4160	11976.4055	10.5	0.0015	0.00141	6.11
<sup>18</sup> O <sup>13</sup> CS		11382.1237	11382.1280	-4.3	0.00200	0.00211	-5.17
				absolute average deviation	2.67 kHz		
						absolute average %	9.87
						error	

the left in Table 10.1 lists the measured frequencies from both the CP-FTMW and the NIST spectrometers, and also indicates the measurement deviation between the two methods. These comparisons indicate that line positions can be determined to within ~3 kHz which is typical for FTMW spectrometers.

The 11 observed isotopomers of OCS are also used to test the accuracy of the relative intensities. The intensity measurements from the rotational spectrum obtained using the CP-FTMW spectrometer of 11 isotopomers of OCS were used to experimentally determine the natural abundance of each isotopomer. On the right in Table 10.1 the experimental relative abundances scaled to the normal species are illustrated, for the 1 - 0 transition of all observed OCS isotopomers. The experimental relative abundance measurements are compared to the literature values with an average percent error less than 10%. This illustrates accurate measurement of relative intensities over a dynamic range of 95,000:1.

OCS was used to show the relative intensity accuracy of the CP-FTMW spectrometer, however this was limited to ~1 GHz of bandwidth. The relative intensity accuracy over the full bandwidth will be demonstrated using the rotational spectrum of suprane. In this case relative intensity differences are due to variations of the transition strength due to different dipole components along the principle axis.

In Figure 10.2, the rotational spectrum of suprane ( $C_3H_2F_6O$  10,000 signal averages) obtained using the CP-FTMW spectrometer is plotted versus a spectrum simulation using predicted frequencies and intensities from Pickett's SPCAT program.<sup>2</sup> The prediction is generated by using known rotational constants

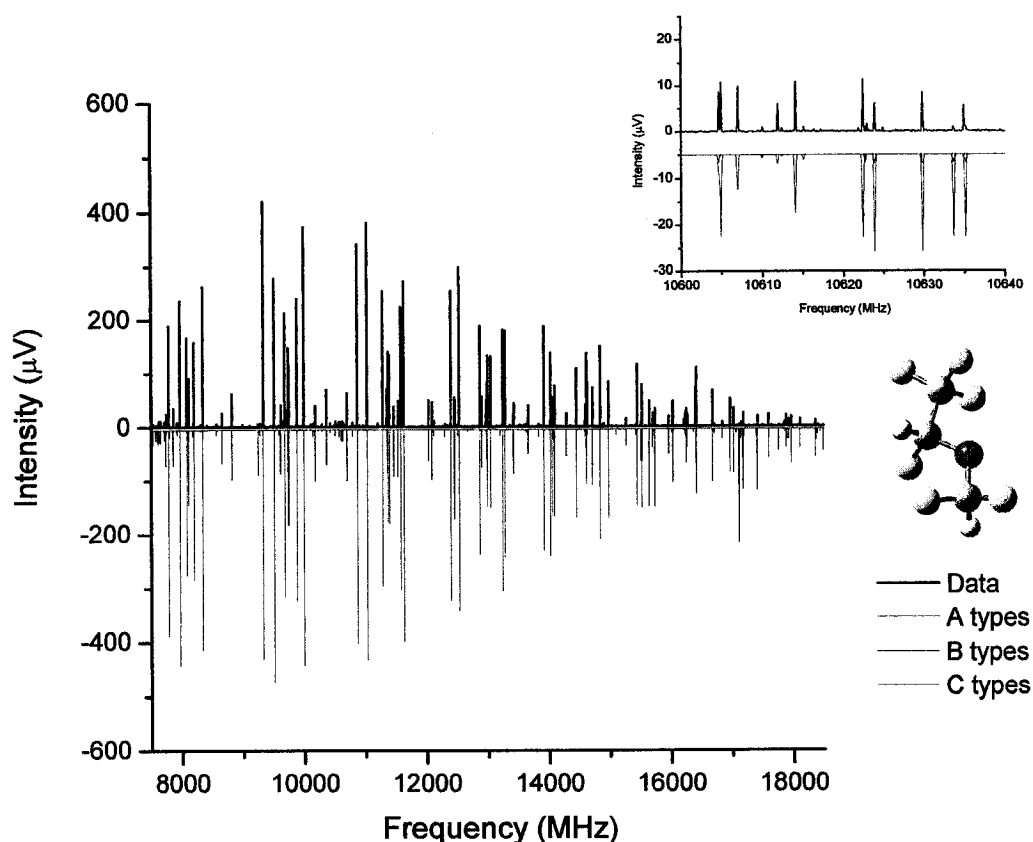


**Figure 10.2** The rotational spectrum of suprane (desfluorane) measured by the CP-FTMW spectrometer is compared to simulated a-type (red), b-type (blue), and c-type (green) spectra using known rotational constants ( $A = 2330.14 \text{ MHz}$ ,  $B = 865.37 \text{ MHz}$ ,  $C = 753.18 \text{ MHz}$ ) and dipole moments ( $\mu_A = 1.48 \text{ D}$ ,  $\mu_B = 0.761 \text{ D}$ ,  $\mu_C = 0.243 \text{ D}$ ). The inset displays a narrow spectral region on an expanded scale to illustrate the intensity agreement of the b and c-type transitions. Above 16 GHz, the intensities measured by the CP-FTMW begin to fall off due to poor coupling efficiency of the horn antenna.

( $A = 2330.14$  MHz,  $B = 865.37$  MHz,  $C = 753.18$  MHz) and dipole moment components ( $\mu_A = 1.48$  D,  $\mu_B = 0.761$  D,  $\mu_C = 0.243$  D) to generate the a-type, b-type, and c-type rotational spectra.<sup>3</sup> Note that below 16 GHz, the intensities of the rotational spectrum match the predicted intensities well. Above 16 GHz the CP-FTMW measured intensities fall off due to poor coupling efficiency of the horn antenna.

To test the relative intensity accuracy of the CP-FTMW spectrometer the rotational spectrum of suprane is simulated using SPCAT with the intensities of each of the dipole components set to 1 Debye. The simulated spectra (a-,b-,and c-types) and the rotational spectrum of suprane are overlaid in jb95 and the respective a, b, or c type simulation is scaled to best approximate the observed intensities. The scale factors obtained by using a simulation at 0.9 K are 41.4 : 9.3 : 1 and are proportional to the dipole moment squared. The scale factors proportional to the dipole moment are 6.4 : 3.04 : 1 and agree very well with the measured relative dipole moments obtained from Stark spectroscopy (6.1 : 3.1 : 1).

A major advantage of the CP-FTMW spectrometer is that the amount of time required to measure 11 GHz can now be varied in order to achieve a desired signal-to-noise ratio, whereas in the cavity machine acquisition time and signal-to-noise can not be traded. This aspect of the spectrometer is highlighted in Figure 10.3, where the rotational spectrum of suprane is shown after a single valve pulse (using a single microwave polarizing pulse and collecting a single FID), 100 signal averages, and 10,000 signal averages. In this case, 100 signal averages which is less than 30 seconds of acquisition time, provides a spectrum with sufficient signal-to-noise ratio (~750:1 S:RMS

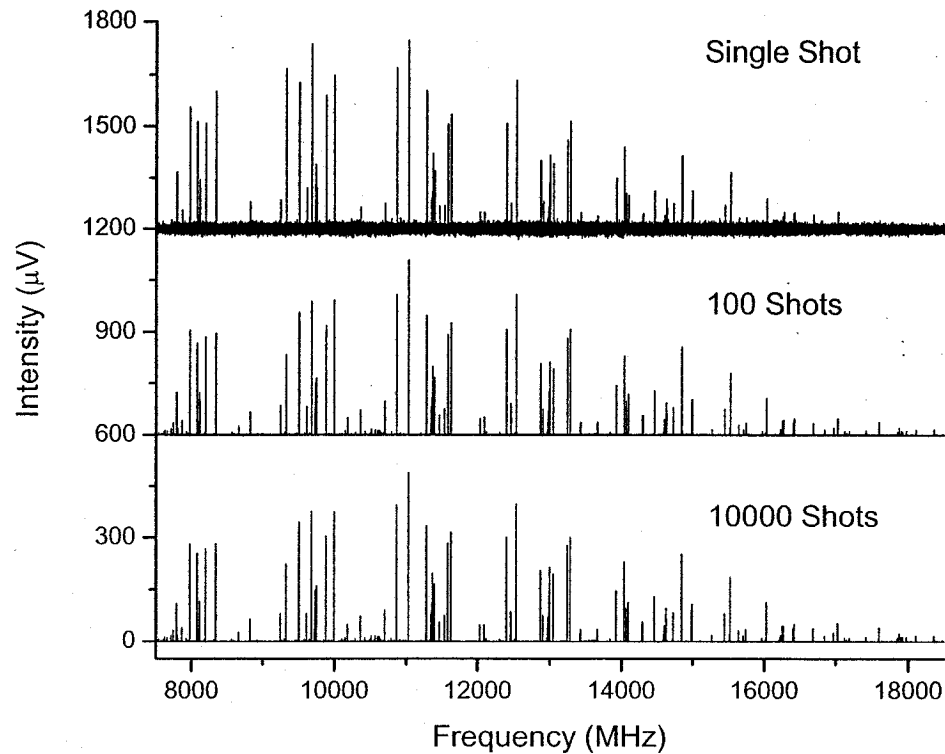


**Figure 10.3** The above panel illustrates the rotational spectrum of suprane measured using the CP-FTMW spectrometer after a single acquisition, 100 signal averages, and 10,000 signal averages. The intense a-type rotational transitions ( $\mu_A = 1.48 \text{ D}$ ) are easily observed after a single acquisition (using a single valve pulse and a single microwave polarizing pulse). This requires less than 1 second of data acquisition time. After 10,000 signal averages (~48 minutes data acquisition time), weaker c-type transitions ( $\mu_C = 0.24 \text{ D}$ ) as well as transitions from less abundant isotopomers are observed. This feature of the CP-FTMW spectrometer allows the user to "choose the sensitivity" for the experiment. The measurement time becomes a function of the sensitivity required.

noise on the most intense transitions in the spectrum) for many applications. The accurate intensity and rapid acquisition makes the CP-FTMW spectrometer ideally suited for use as a detection device, such as in laser CP-FTMW double-resonance spectroscopy.

### B. Comparison to Balle-Flygare cavity FTMW spectrometer

The CP-FTMW spectrometer is compared to the mini-Balle-Flygare cavity FTMW spectrometer<sup>1</sup> because its smaller microwave beam waist is compatible with laser excitation experiments, the main application of CP-FTMW spectroscopy in the Pate laboratory. The CP-FTMW spectrometer matches the sensitivity of the cavity FTMW spectrometer after 10,000 signal averages or approximately 48 minutes of data acquisition time. The same 7.5 - 18.5 GHz spectrum requires approximately 14 hours of data acquisition time on the cavity FTMW spectrometer using 10 averages and a 500 kHz step size.

A comparison of the rotational spectrum of cyclopropanecarboxaldehyde (CPCA)<sup>4</sup> as measured by the CP-FTMW spectrometer (using 10,000 signal averages) and the Balle-Flygare cavity FTMW spectrometer (using 10 signal averages per step, 500 kHz steps) is shown in Figure 10.4. The cavity FTMW spectrum intensity has been scaled so that the noise levels of the two spectra are approximately equal. Sensitivity comparisons can be made using the low abundance isotopomers of CPCA as illustrated in Figure 10.4, in particular the <sup>18</sup>O isotopomer appears in both spectra with approximately the same signal-to-noise ratio. The vertical dynamic range of the two spectra is compared in Figure 10.5 for CPCA. The cavity signal-to-noise ratio is limited by the 8 bit digitizer and low number of signal averages while the broadband machine (also 8 bit)

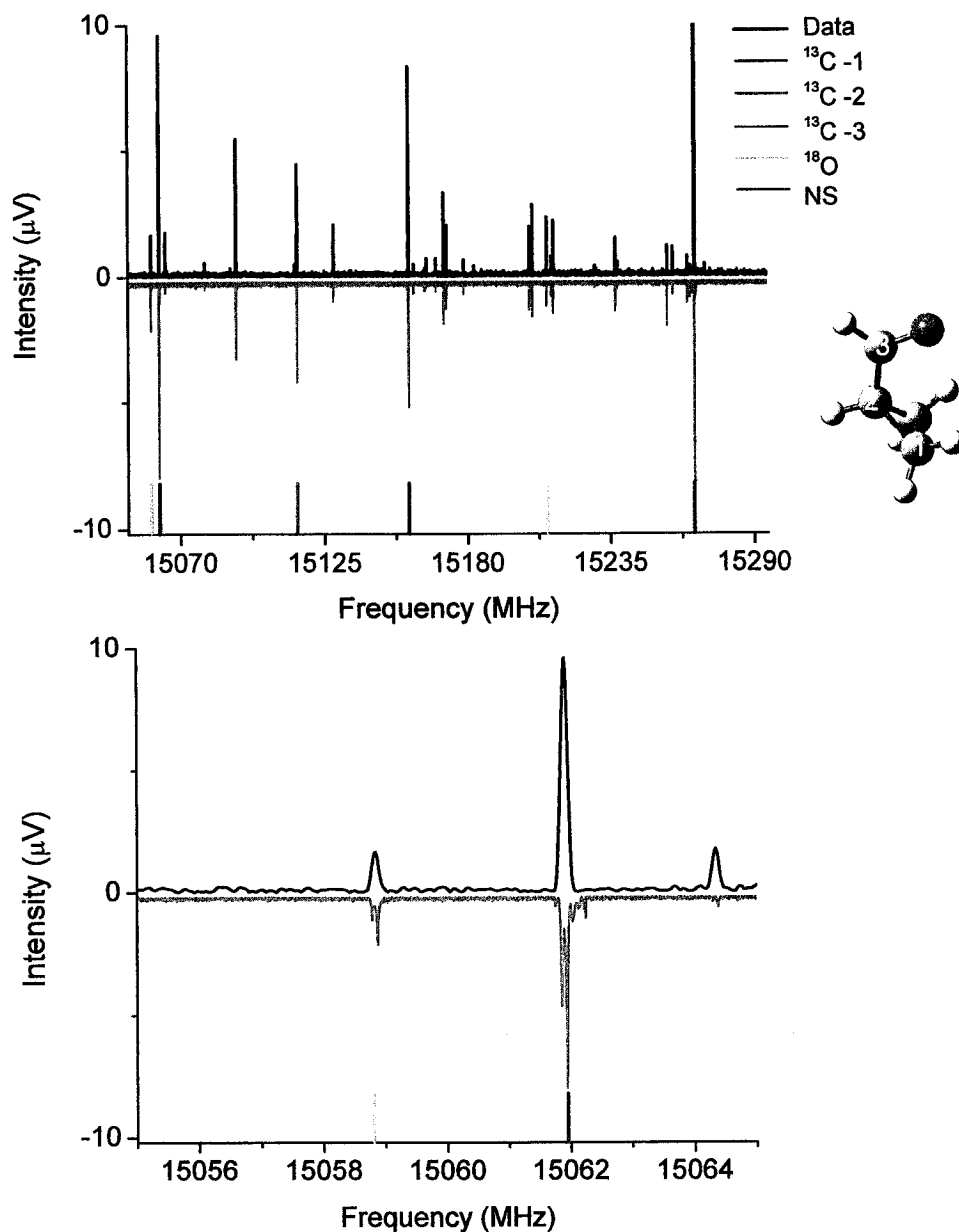


**Figure 10.4** Shown above is a section of the rotational spectrum of cyclopropanecarboxaldehyde (CPCA) in the region of the *cis* conformer measured using the CP-FTMW spectrometer (black) and the cavity FTMW spectrometer (red). Rotational transitions for all three unique  $^{13}\text{C}$  isotopomers, the  $^{18}\text{O}$  isotopomer, and the normal species are labeled. The lower panel illustrates sensitivity comparison of the two techniques zoomed in on the region of the  $^{18}\text{O}$  and  $^{13}\text{C}$  isotopomers. The CP-FTMW spectrum was recorded after 10,000 signal averages (~48 minutes of data acquisition), while the cavity

uses a high number of averages (10,000 typical) over the entire bandwidth which effectively increases the bit resolution, allowing for greater dynamic range and more accurate relative intensities.

Another advantage to the broadband technique is that nearly all samples are polarized in the weak pulse limit, i.e. not overpowered. This is not true in the cavity method, which results in missing lines if the power is not set correctly. A demonstration of the cavity missing lines is illustrated in Figure 5.6 for suprane. The spectrum acquired using the cavity machine in (Figure 5.6) was obtained by optimizing the polarizing power on the larger dipole component (a-type transition) with 10 averages per step and a 100 kHz step size). The missed lines from the cavity scan were only observed after centering the cavity mode on the frequency obtained from the CP-FTMW spectrum and optimizing the polarizing power for each of the missed lines.

### Conclusions

The aim of this Chapter was to present the application of CP-FTMW spectroscopy for the measurement of pure rotational spectra with comparisons to the most sensitive technique available for rotational spectroscopy. The sensitivity of the CP-FTMW spectrometer exceeds that of the miniature cavity FTMW spectrometer after 10,000 time-domain signal averages. This requires ~48 minutes of acquisition time, a factor of 18 faster than the cavity FTMW spectrometer over the same frequency range. For many applications, the CP-FTMW spectrometer can measure a suitable rotational spectrum in less time as illustrated by suprane in Figure 10.3. Also the CP-FTMW spectrometer was

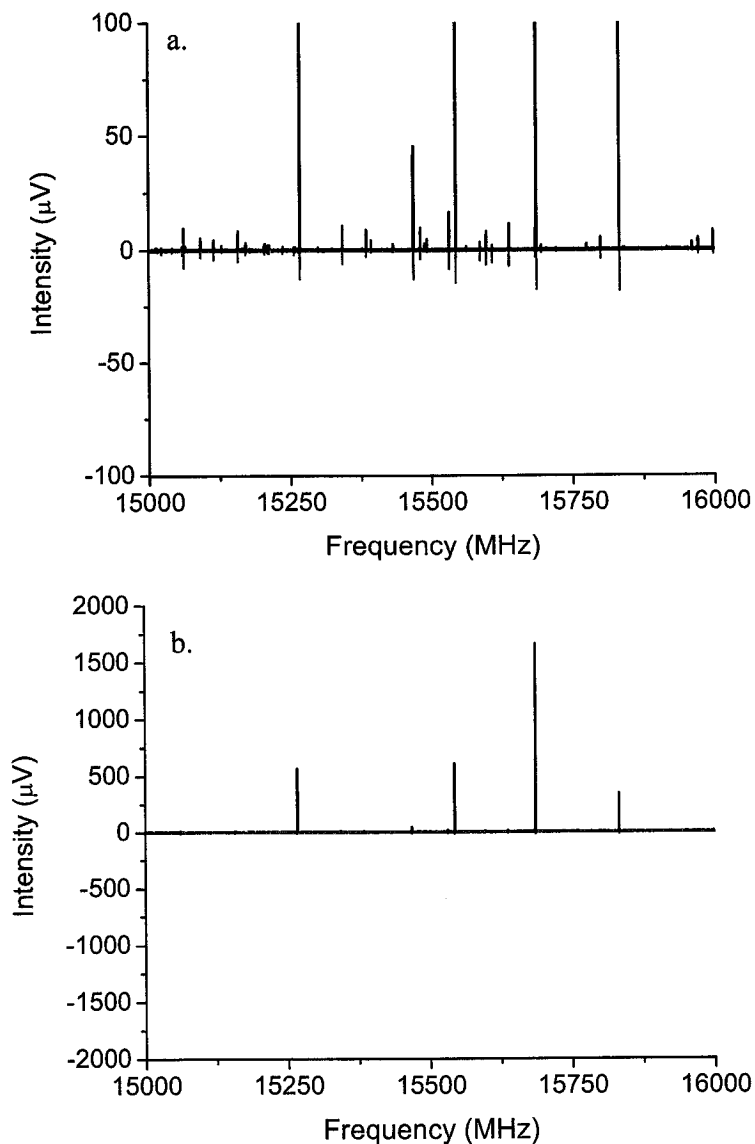


**Figure 10.5** The above plots illustrate a 1 GHz section of the rotational spectrum of CPCPA measured using the CP-FTMW spectrometer (black) and the cavity FTMW spectrometer (red). Panel a. is used to demonstrate the enhanced dynamics range of the CP-FTMW spectrometer, the spectrum obtained using the cavity spectrometer is barely observed while the spectrum form the CP-FTMW spectrometer is still off scale. In the lower panel (b.) the spectrum obtained from the CP-FTMW spectrometer is on scale while spectrum obtained using the cavity FTMW spectrometer cannot be observed.

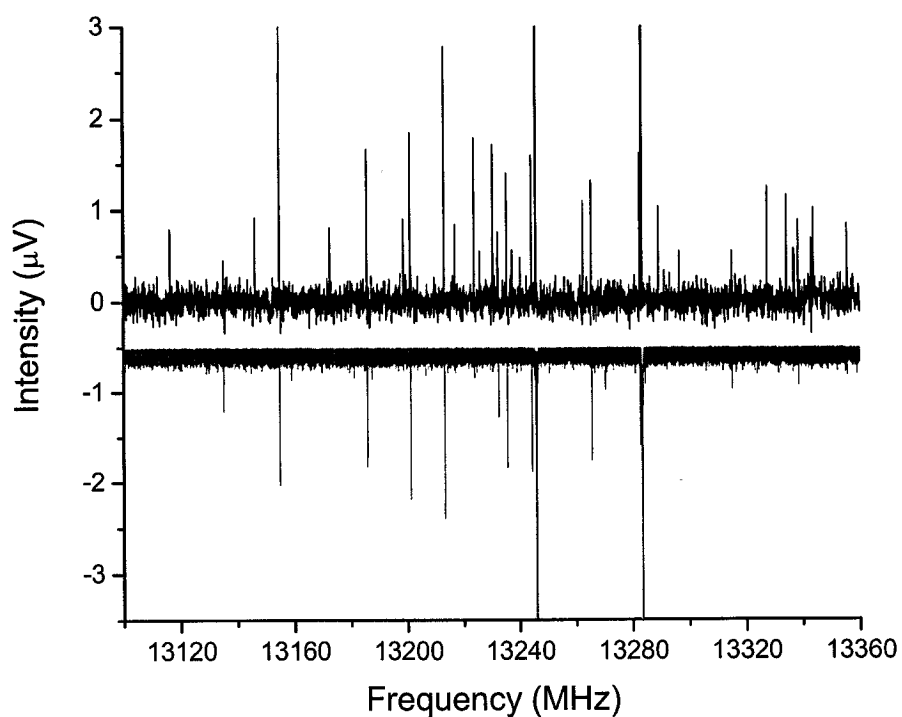


**Figure 10.6** The above plot shows a small section of the rotational spectrum of suprane measured using the CP-FTMW (black) after 10,000 signal averages (valve on – valve off) and the cavity FTMW spectrometer (red) using 10 averages per step and 100 kHz step size. The spectrum acquired using the CP-FTMW spectrometer contains several lines not observed in the scan acquired using the cavity spectrometer. These lines are either missed due stepping over the molecular frequency or because of non-optimal power settings.

demonstrated to have the ability to accurately measure molecular frequencies (within ~3 kHz) and intensities.

The ability to measure a broad spectral range in a short measurement time is important for many applications of rotational spectroscopy. In the Pate laboratory, the high sensitivity, fast acquisition time, and accurate relative-intensity over a large dynamic range make CP-FTMW spectroscopy ideal for studying the dynamics of laser-excited molecules. The focus of the following chapter will be on using CP-FTMW spectroscopy as a detector for IR-CP-FTMW double resonance spectroscopy and to record the rotational spectrum in the vibrationally excited state.

### Reference List

1. Suenram, R. D.; Grabow, J. U.; Zupan, A.; Leonov, I., *Rev.Sci.Instrum.* **1999**, *70*, 2127-2135.
2. Pickett, H. M., *J.Mol.Spectrosc.* **1991**, *148*, 371-377.
3. Suenram, R. D. and Lovas, F. J. Suprane. 2006.
4. Volltrauer, H. N.; Schwendeman, R. H., *J.Chem.Phys.* **1971**, *54*, 260-267.

## Chapter 11

### Broadband Rotational Spectroscopy: Applications for Dynamics Rotational Spectroscopy

#### Introduction

A major focus of the Pate group is to study the dynamics that result from intramolecular vibrational energy redistribution (IVR).<sup>1</sup> The dynamical information is contained in both the high-resolution infrared spectra<sup>2</sup> and the rotational spectrum of a vibrationally excited molecule.<sup>3</sup> The IR spectrum provides a measure of the time scale of energy flow out of the bright state into the bath states creating a set of molecular eigenstates. The rotational spectra of mixed molecular eigenstates provide information on the time scale of energy flow between the bath states. This is referred to as Dynamic Rotational Spectroscopy (DRS).<sup>4-6</sup>

For molecules with a single energetically accessible conformer the rotational spectrum in the excited vibrational state may exhibit the effects of motional narrowing.<sup>7</sup> The effects of motional narrowing have been presented in chapter 7 for trifluoropropyne (TFP) where it was determined that the time scale of energy flow between the three lowest energy modes was 120 ps. When there are two conformers with similar relative energies it may be possible that conformational isomerization occurs and the rotational spectrum of the highly excited molecule exhibits coalescence phenomena. In this case it is possible to measure the isomerization rate of the molecule. An example of this has been presented in chapter 8 for pent-1-en-4-yne where the isomerization rate was

determined to be 25 ps. In both cases the time scale of the dynamics is measured from lineshape analysis similar to that developed for NMR spectrometers.<sup>8,9</sup>

The previous two chapters demonstrated the principles and applications for pure rotational spectroscopy of broadband Chirped-Pulse Fourier Transform Microwave (CP-FTMW) spectroscopy. The aim of this chapter is to extend the applications of CP-FTMW spectroscopy to Dynamic Rotational Spectroscopy (DRS). The characterization of CP-FTMW spectroscopy for measuring dynamics will be two fold. First, benchmark measurements using IR-CP-FTMW double resonance spectroscopy to measure the rotational spectrum in the vibrationally excited state of TFP and pentenyne will be presented with comparisons to spectra acquired using IR-cavity-FTMW double resonance spectroscopy. Second, a full dynamics experiment will be presented for cyclopropanecarboxaldehyde (CPCA). CPCA has two conformers, *cis* and *trans*, which may undergo conformational isomerization upon laser excitation.

As discussed in Chapter 6, there are three main steps to performing a dynamics experiment which consist of measuring the following; 1. the pure rotational spectrum, 2. the rotationally-resolved conformer-specific IR spectra, and 3. the rotational spectrum in the vibrationally excited state. These three measurements will be demonstrated for CPCA in a way not previously possible using the cavity based FTMW spectrometer. New possibilities arise from experiments based on CP-FTMW spectroscopy because the spectra are acquired so rapidly.

## Experimental

The spectrometers used to perform IR-FTMW double resonance spectroscopy have been described in detail in chapters 2 and 9 for the cavity and the CP-FTMW spectrometer respectively. For experiments on TFP and CPCPA the 300 Watt Traveling Wave Tube amplifier (TWTA) was implemented due to the larger dipole moments of these species. For pentenyne the 2 kW TWTA was used. TFP, CPCPA, and pentenyne were purchased from Aldrich and used without further purification with sample concentrations of 2%, 1% and 0.5% in 80/20 Ne/He respectively.

## Results

### A. IR-CP-FTMW and IR-cavity-FTMW Double Resonance Comparison

The rotationally resolved IR spectrum and assignment of pure rotational spectra has previously been determined for both TFP and pentenyne. The emphasis here is the comparison of the two techniques for recording rotational spectra in the vibrationally excited state. The rotational spectrum of TFP measured at the acetylenic C-H stretch overtone is illustrated in Figure 11.1 using both the CP-FTMW and cavity FTMW spectrometers. The vibrational excitation at  $R(1)$   $6558.25\text{ cm}^{-1}$  was used to transfer population to  $J=2$  in the excited state and the  $J=2 \rightarrow 1$  transitions were recorded for both techniques. For these comparisons the noise of the CP-FTMW measurement is scaled to the noise of the cavity FTMW measurement.

The molecule pentenyne has two stable geometries, *cis* and *skew*, with a barrier to isomerization of  $\sim 1000\text{ cm}^{-1}$ . As demonstrated in chapter 8 upon vibrational excitation at the acetylene C-H stretch fundamental the rotational spectrum exhibits coalescence

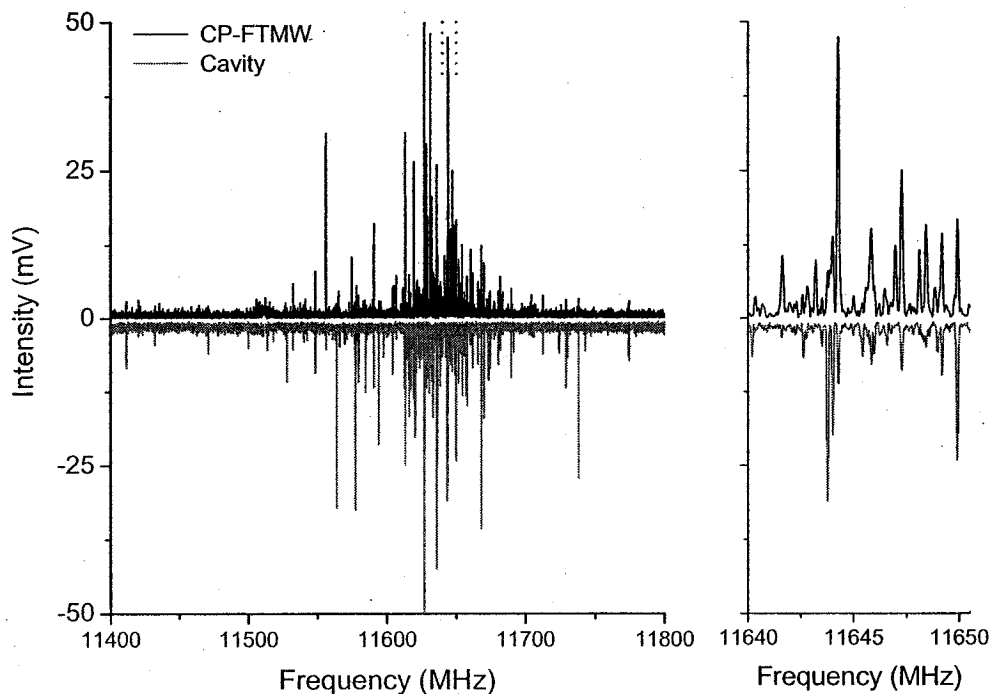


**Figure 11.1.** The above plots compare IR-FTMW double resonance spectra for trifluoropropyne obtained using the CP-FTMW (black) and cavity-FTMW (grey) spectrometers. The panel on the right illustrates a small section of the full double resonance spectrum (dotted red lines) shown on the left. Both spectra were acquired with the laser frequency fixed to R(1) at  $6558.28\text{ cm}^{-1}$  of the acetylenic C-H stretch overtone in the region of the J=2-1 pure rotational transition (11494.64 MHz). The CP-FTMW spectrum was acquired using 10,000 averages and the spectrum obtained using the cavity-FTMW spectrometer was acquired using 10 averages per step and a 250 KHz step size.

phenomena resulting from conformational isomerization on the time scale of molecular rotation. Figure 11.2 illustrates the IR-FTMW double resonance spectrum with vibrational excitation at  $R(1) 3331.33 \text{ cm}^{-1}$  of the *cis* conformer to measure in the region of  $J=2 \rightarrow 3$  rotational transition of both the *cis* and *skew* conformers in the vibrationally excited state for both the CP-FTMW and cavity FTMW technique. Note that the noise of the CP-FTMW spectra was scaled to match that of the cavity spectra.

The spectra of both molecules as measured using the CP-FTMW spectrometer accurately reproduce the spectra obtained using the cavity FTMW spectrometer with similar signal-to-noise ratio. The main difference of the CP-FTMW technique is that on average a higher number of lines are observed and the intensities are also different. In the previous chapter it was demonstrated that the cavity misses lines for pure rotational spectra and also that the intensity information is quite accurate from the CP-FTMW technique. Therefore, we have reason to believe that in a fraction of the time the CP-FTMW spectrometer outperforms the cavity FTMW spectrometer for measuring rotational spectra in the vibrationally excited state. The CP-FTMW spectrometer also has the advantage that for every laser shot a full spectrum is recorded thereby limiting problems of laser drift.

### B. Dynamic Rotational Spectroscopy of CPCAs

The performance of CP-FTMW spectroscopy for measuring pure rotational and rotational spectra in the vibrationally excited state has been demonstrated. The aim in this section is to apply the new CP-FTMW technique to a new system to perform dynamic rotational spectroscopy. The molecule to be investigated is

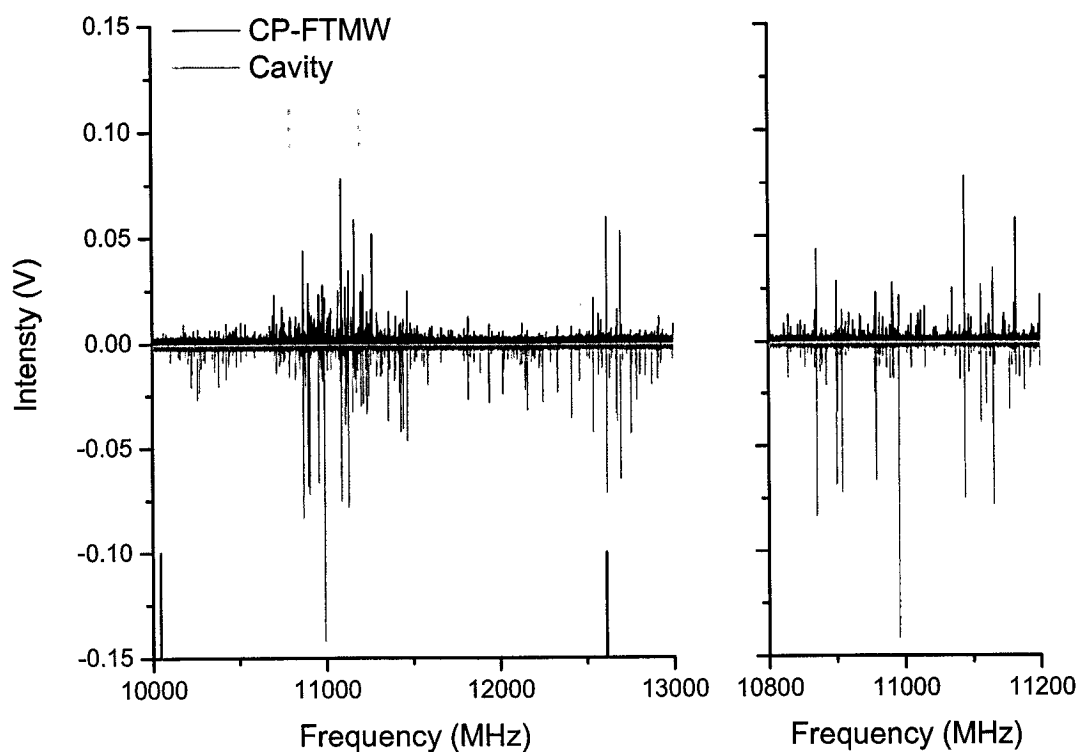


**Figure 11.2.** The above plots compare IR-FTMW double resonance spectra for pent-1-en-4-yne obtained using the CP-FTMW (black) and cavity-FTMW (grey) spectrometers. The panel on the right illustrates a small section of the full double resonance spectrum (dotted grey lines) shown on the left. Both spectra were acquired with the laser frequency fixed to R(1) at  $3332.78\text{ cm}^{-1}$  of the acetylenic C-H stretch fundamental of the *cis* conformer. The red and blue lines indicate the frequency of the  $2_{02}-1_{01}$  pure rotational transitions for the *cis* and *skew* conformers (10044.8725 MHz and 12671.7459 MHz). The CP-FTMW spectrum was acquired using 10,000 averages and the spectrum obtained using the cavity-FTMW spectrometer was acquired using 10 averages per step and a 250 KHz step size.

cyclopropanecarboxaldehyde (CPCA) which has two stable conformations *cis* and *trans*. The 1-dimensional potential energy surface for this torsional motion is illustrated in Figure 11.3. This potential energy curve was calculated by *ab initio* methods<sup>10</sup> (B3LYP/6-31+G\*\*) and predicts that the minimum energy of the two conformers differ by 46 cm<sup>-1</sup> (zero-point corrected), with *trans* being the most stable, and that the barrier to conformational isomerization is approximately 2200 cm<sup>-1</sup>. These computation results are in good agreement with previous microwave<sup>11</sup> and infrared studies<sup>12</sup> of CPCA which have determined a small difference in the conformational energies (10-30 cm<sup>-1</sup>) and that the barrier to isomerization, determined by extrapolation of the low frequency torsional vibrational structure, is on the order of 2000 cm<sup>-1</sup> (~1600 cm<sup>-1</sup> by microwave spectroscopy<sup>11</sup> and ~1500 cm<sup>-1</sup> using far-infrared measurements<sup>12</sup>).

The first step to studying the new system is measuring the pure rotational spectrum. This system has previously been studied using microwave spectroscopy by Volltrauer et al.<sup>11</sup> in which the rotational constants and dipole moments for both conformers were previously determined. The pure rotational spectrum of CPCA measured using CP-FTMW spectroscopy shown in Figure 11.4 was acquired using a single molecular beam pulse. The strongest lines in the spectrum result from the a-type 2<sub>02</sub> – 1<sub>01</sub> transitions of both the *cis* (15687 MHz) and the *trans* (12470 MHz) conformers. The signal-to-noise ratio on these transitions is about 100:1. Signal-to-noise ratios on the order of ~1000:1 can be obtained on the strongest transitions in a matter of seconds with the current repetition rate of the spectrometer, further demonstrating the advantage of the broadband spectrometer.

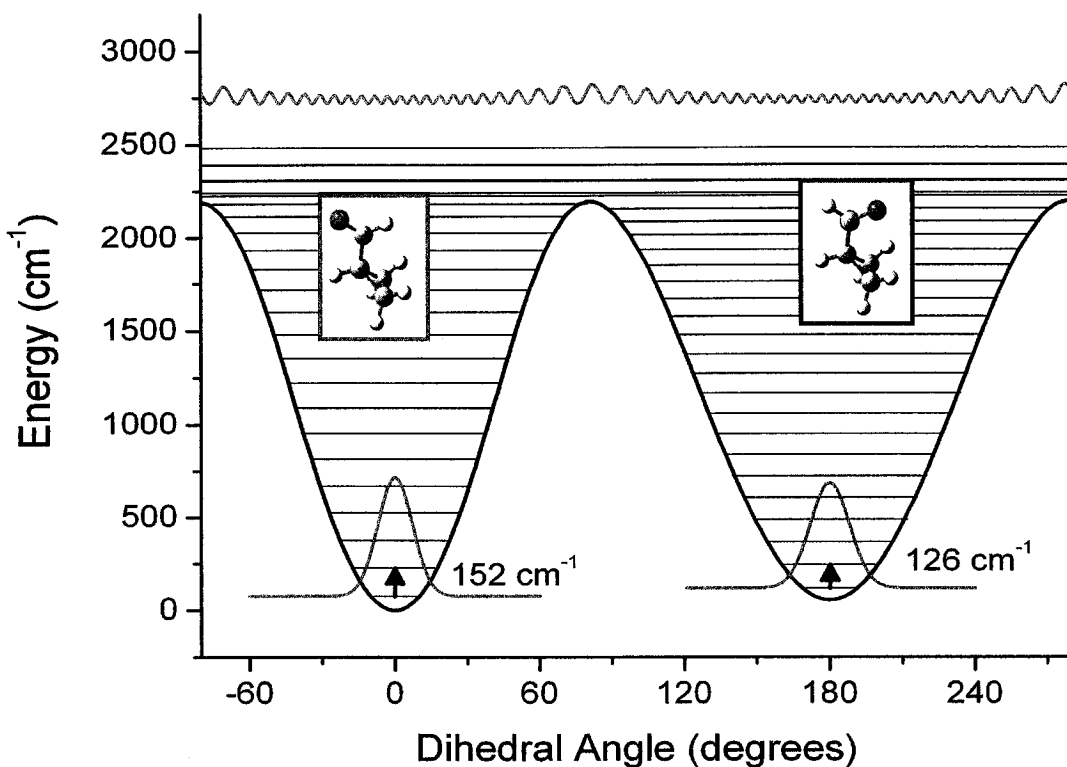


**Figure 11.3.** The above plot illustrates the potential energy surface of CPCA calculated at the B3LYP/6-31+G\*\* level of theory. Superimposed on the surface are the torsional energy levels calculated by diagonalizing the 1-D Hamiltonian for the torsional potential in a free rotor basis set. Molecular structures of the *cis* and *trans* conformers are shown as insets above their respective minima. The wavefunctions (red) of the *cis* and *trans* conformer are shown for  $v = 0$  and at higher energy above the barrier to isomerization.

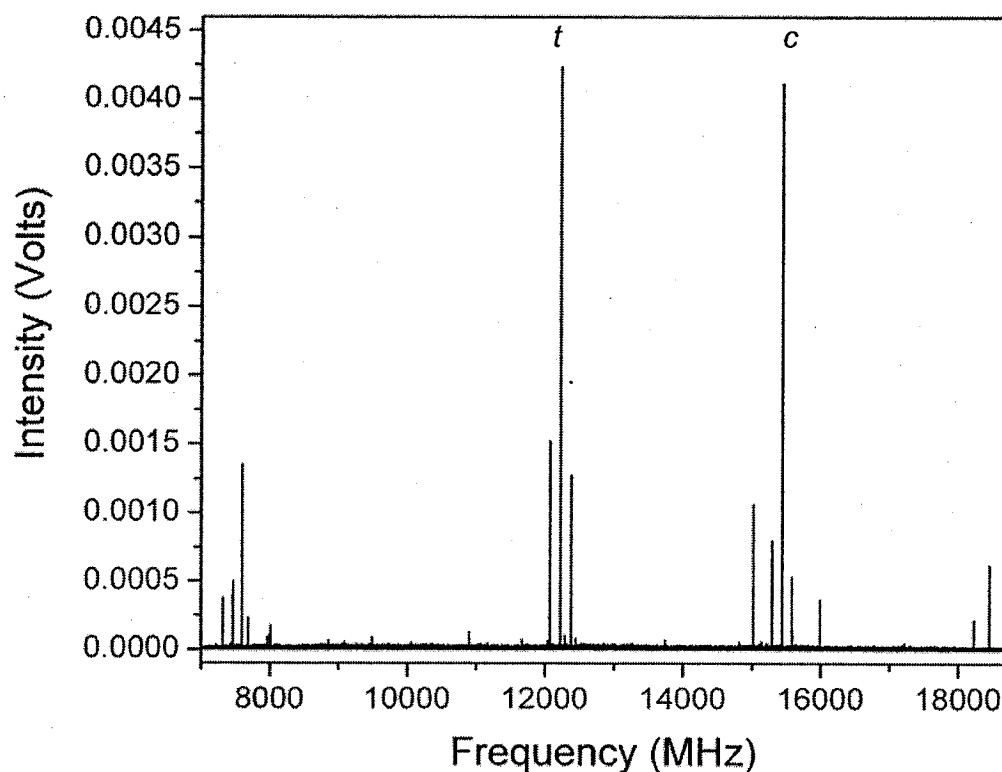


**Figure 11.4.** The plot above illustrates the rotational spectrum of CPCA obtained using the CP-FTMW spectrometer after a single valve pulse. The region of interest is near the *trans* (*t*) and *cis* (*c*)  $2_{02}-1_{01}$  pure rotational transitions (12470.6601 MHZ and 15686.0567 MHz).

The second and third steps, measuring the rotationally resolved conformer specific IR spectrum and measuring the rotational spectrum in the vibrationally excited state, can now be performed in a single measurement step using IR-CP-FTMW double resonance spectroscopy. This is because the sensitivity is so high and spectra can be acquired so quickly that now the full 11 GHz rotational spectrum can be measured with each step of the laser frequency. As a result the important dynamical questions can be answered "on the fly" as the laser scans such as; What are the mode dependent IVR rates of each of the conformers? Is the molecule isomerizing? If so, how fast is the molecule isomerizing?

As described in chapters 4 and 5, IR spectra obtained using the ground state depletion (GSD) method would require scanning the laser over the same region twice, monitoring each conformer once. Archiving the rotational spectrum from 7.5 – 18.5 GHz for each step of the laser provides a multiplex advantage whereby the GSD spectra of both conformers are acquired simultaneously and now only a single scan is required. Recording the spectra for each laser step is achieved by acquiring the rotational spectra at the 10 Hz repetition rate of the laser, and this is accomplished by reducing the record length of FID to 160,000 points which corresponds to a 4.0  $\mu$ s gate duration.

The rotationally resolved conformer specific IR spectrum from 2650 – 3125  $\text{cm}^{-1}$  is illustrated in Figure 11.5. The 2650 – 2900  $\text{cm}^{-1}$  frequency region of the infrared spectrum is predicted to include a single normal mode vibrational transition: the aldehyde C-H stretch. However, several absorption features appear for each conformer. These extra features indicate the presence of intramolecular vibrational energy redistribution (IVR). This strong perturbation is most likely a result of a stretch – bend interaction of

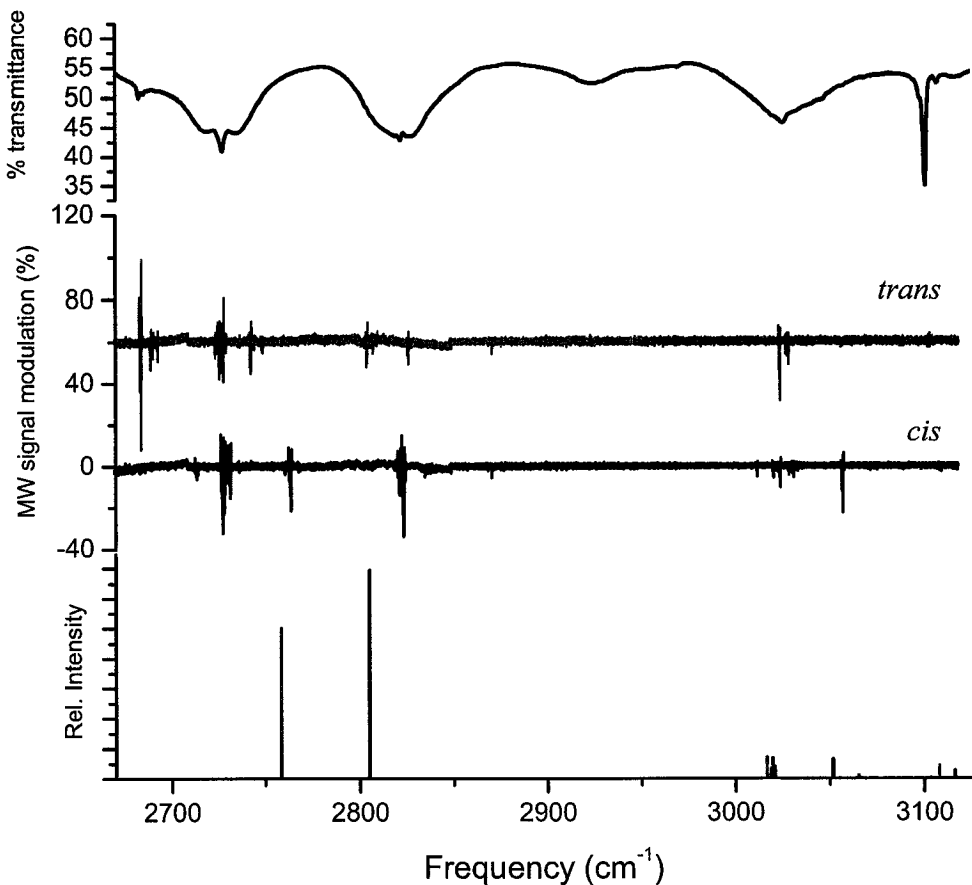


**Figure 11.5.** The above panels show the infrared spectrum of CPCA. The 55° C gas-phase FT-IR spectrum of CPCA is shown in the upper panel for comparison. The two lower traces are the IR-CP-FTMW double resonance spectra using the ground state depletion method. The bottom panel illustrates the intensities and scaled frequencies predicted by ab initio (B3LYP/6-31+G\*\*). The spectra and predictions for the *trans* conformer are shown in blue and *cis* in red.

the aldehyde C-H stretch with the aldehyde C-H bend overtone. These stretch bend interactions have been previously demonstrated to play an important role in IVR.<sup>13,14</sup> In this case the aldehyde C-H bend overtone provides a “doorway” for IVR into other near resonant vibrational modes. In addition to the strong vibrational coupling that produces the few discrete vibrational bands in the 2670 - 2850 cm<sup>-1</sup> region, there also exists a weaker vibrational interaction due to near-resonant vibrational states that causes further local fragmentation of the infrared oscillator strength.

This hierarchical spectral structure corresponds to IVR that occurs on two time scales: a fast initial energy redistribution to a single quantum state in about 100 fs (reflected by the overall frequency spread of the distinct bands) and a slower time scale for more complete energy redistribution into the full vibrational bath (reflected by the narrower frequency spread within the distinct vibrational bands). A plot of the survival probability for the aldehyde C-H stretch is illustrated in Figure 11.6 for both *cis* and *trans* conformers. Although the vibrational spectrum shows that IVR is exceptionally fast, this does not guarantee that isomerization occurs.

The conformer specific IR spectra illustrated in Figure 11.5 also provide information about the location of absorption frequencies where traditionally the laser would be fixed and the rotational spectrum in the vibrationally excited state would be recorded. With the CP-FTMW technique the rotational spectrum is recorded as the laser scans. By observing the rotational spectrum in the vibrationally excited state it can be immediately determined whether or not the molecule is undergoing conformational isomerization based on the coalescence model illustrated in Figure 11.7. If the molecule

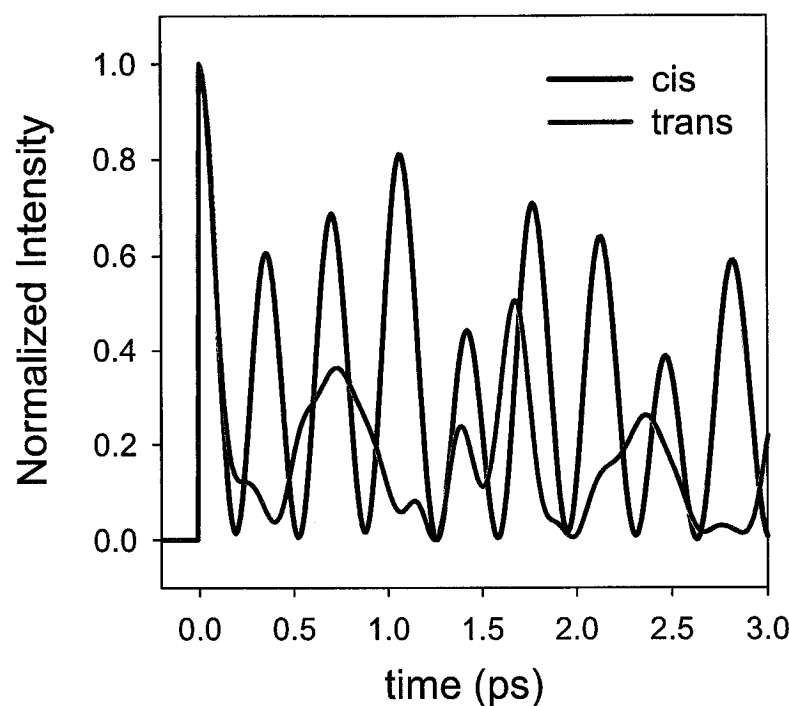


**Figure 11.6.** The survival probability for the *cis* and *trans* conformers of CPCPA calculated using the frequencies and intensities from the GSD spectrum in Figure 11.5 is shown for the aldehyde C-H stretch.

is isomerizing lineshape analysis developed by Pate<sup>5</sup> can be applied to the excited state rotational spectrum and an isomerization rate can be determined.

The IR-CP-FTMW double resonance contour plot shown in Figure 11.8 illustrates the rotational spectra in the vibrationally excited state as a function of laser frequency. The pure rotational transitions have been removed. The conformer specific IR spectra are illustrated in the top panel and indicate selective excitation of the *cis* conformer. Laser induced rotational transitions appear in the region of both *cis* and *trans* conformers, when only the *cis* conformer is vibrationally excited, this is evidence for conformational isomerization. The maximum projection illustrated on the left in Figure 11.8 contains essentially all of the laser induced rotational transitions over 2819 – 2825 cm<sup>-1</sup> frequency region collapsed into one dimension and analyzed to obtain dynamical information.

The determination of the isomerization rate of CPCPA in the energy region around 2823 cm<sup>-1</sup> by line shape analysis is illustrated in Figure 11.9. The rate analysis is based on the overall intensity pattern of the spectrum. Because the intensities of each individual rotational transition must fluctuate around the smooth line shape profile, the cumulative spectral intensity is analyzed to focus on the line shape contour (Figure 11.9). The cumulative intensity for the contour of a coalescence line shape characterized by a reaction rate of  $k(E) = 9.5 \pm 1.2 \times 10^9 \text{ s}^{-1}$  ( $2\sigma$  error bars) is found to best represent the data, corresponding to a lifetime of 109 ps. The reaction rate determined by line shape analysis is an upper limit (spectral broadening from IVR processes that retain the conformational structure can also contribute to the line shape). The quality of the lineshape fit is shown in Figure 11.10 by the chi-squared surface generated by varying

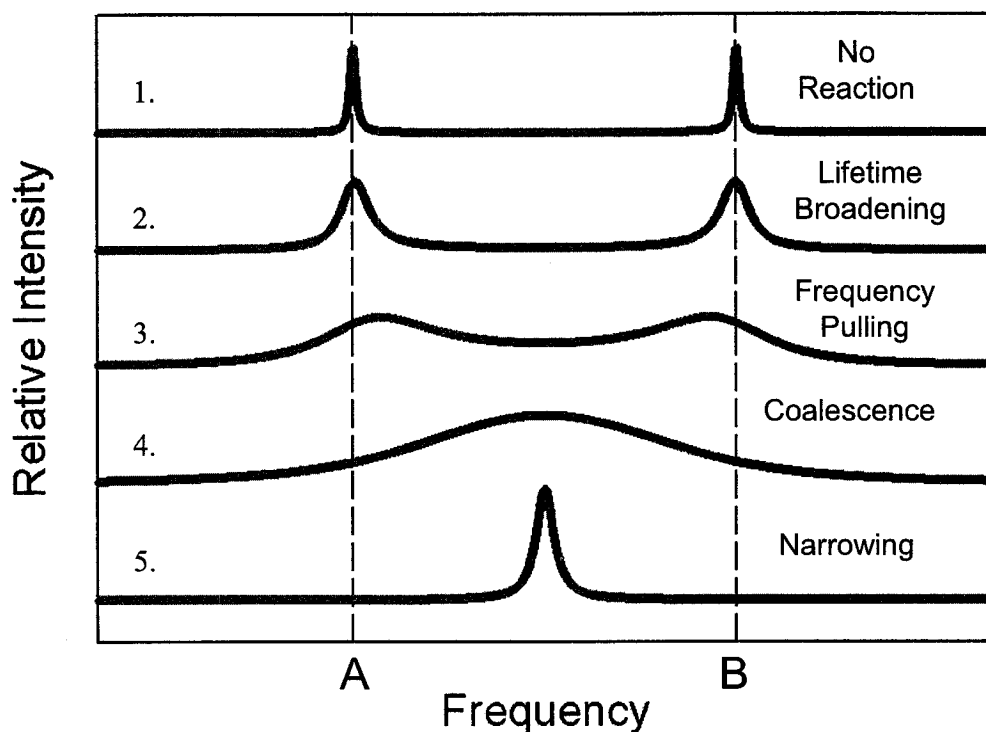


**Figure 11.7.** The above five traces illustrate the effect of isomerization on the over lineshape profile of the excited state rotational spectrum for two conformers A and B. No reaction (1.) is observed when a single conformer is excited and there are no transitions in the region of the other conformer, i.e. no product is formed. As isomerization occurs a distribution of transitions is observed in the region around both conformers (2.) and as the isomerization rate increases the transitions are pulled towards the center (3.). Coalescence into a single lineshape (4.) occurs at  $\sim 2.2 \times$ frequency spacing between the conformers as the molecule isomerizes at a rate near molecular rotation. Finally, as the isomerization rate increases further narrowing of the spectrum is observed (5.).

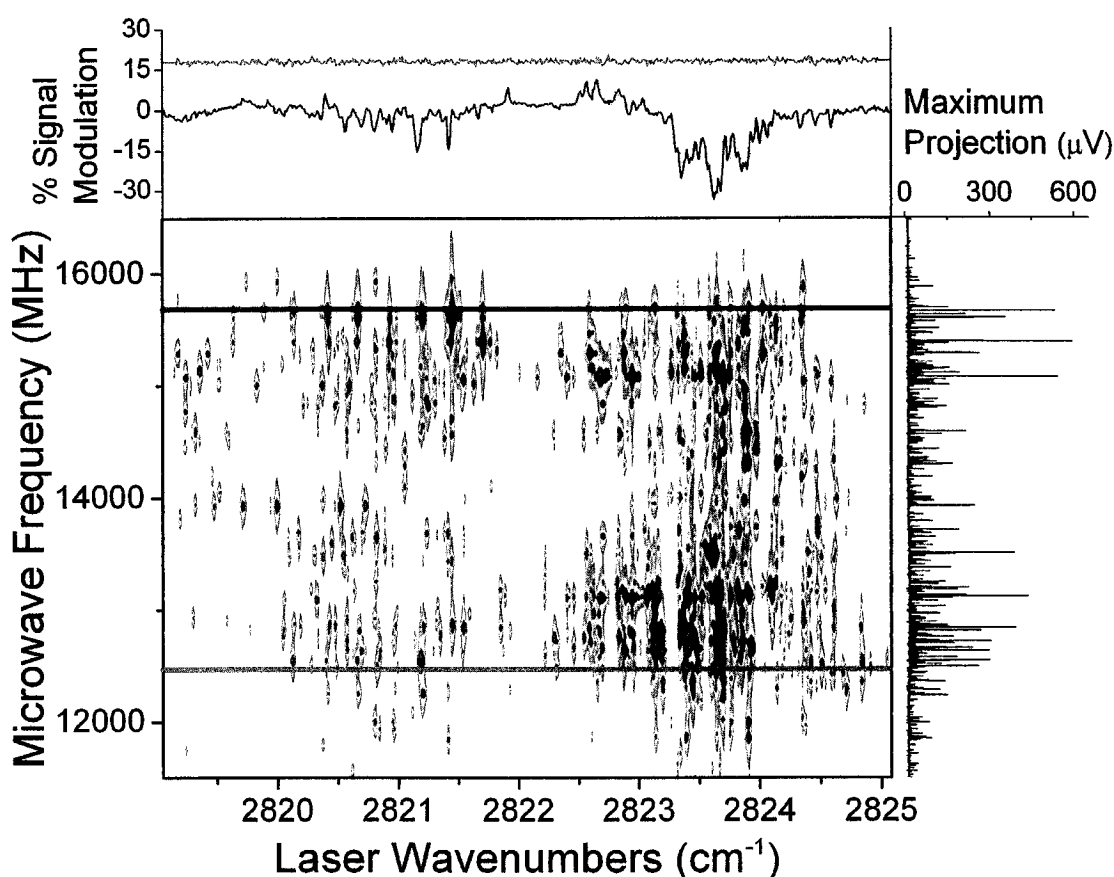


**Figure 11.8.** The rotational spectrum of CPCA in the vibrationally excited state shown is above as a contour plot for the region near 2823 cm<sup>-1</sup> for excitation out of the *cis* conformer. The bottom axis corresponds to the laser position in wavenumbers while the left axis corresponds to microwave frequency in MHz. The red and blue lines mark the ground state positions of the *trans* and *cis* 2<sub>02</sub>-1<sub>01</sub> transitions, respectively. The upper panel shows the IR-CP-FTMW double resonance spectrum for the *cis* and *trans* along the 1-D slices of the ground state microwave transitions, ie the ground state depletion spectra. The right panel shows the maximum peak height along the microwave axis at all laser positions, collapsing the x-axis to a single 1-D microwave spectrum.

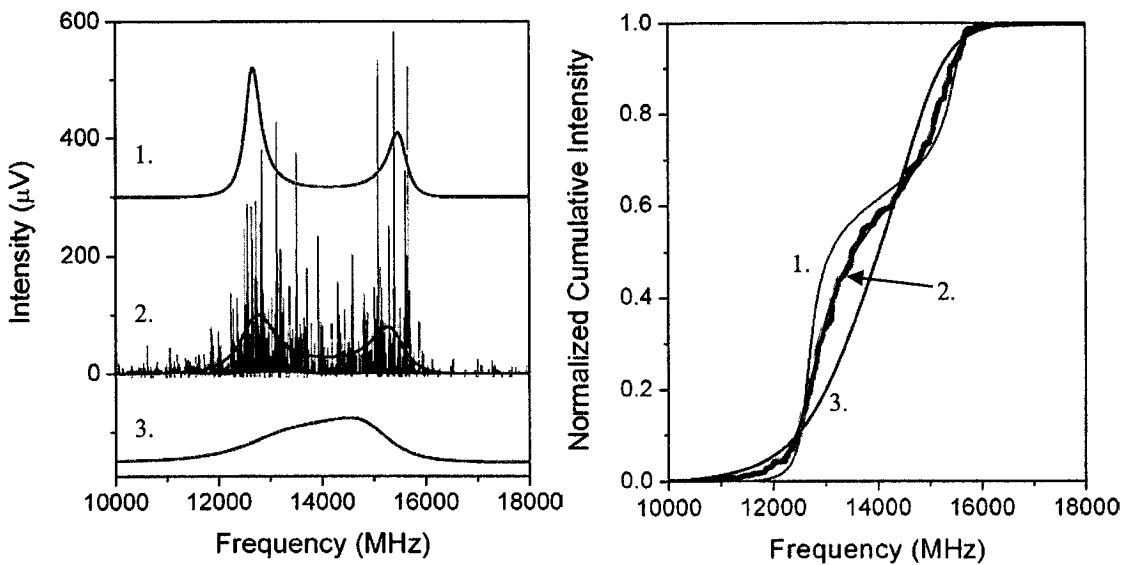


**Figure 11.9.** The plot on the left illustrates the best fit analytical lineshape (2. red) overlaid with the experimental spectrum (black). Upper and lower traces are the analytical lineshapes for rates a factor of three slower (1.) and faster (3.), respectively. The panel on the right illustrates the normalized cumulative intensity plot used to determine the reaction information for the isomerization of CPCPA at  $2824\text{ cm}^{-1}$ . The experimental data is shown in green, while the best fit analytical lineshape is shown in black (2.). The additional curves show the change in the analytical lineshape when the rate is decreased (1.) and increased (3.) by factors of three from the best fit rate.

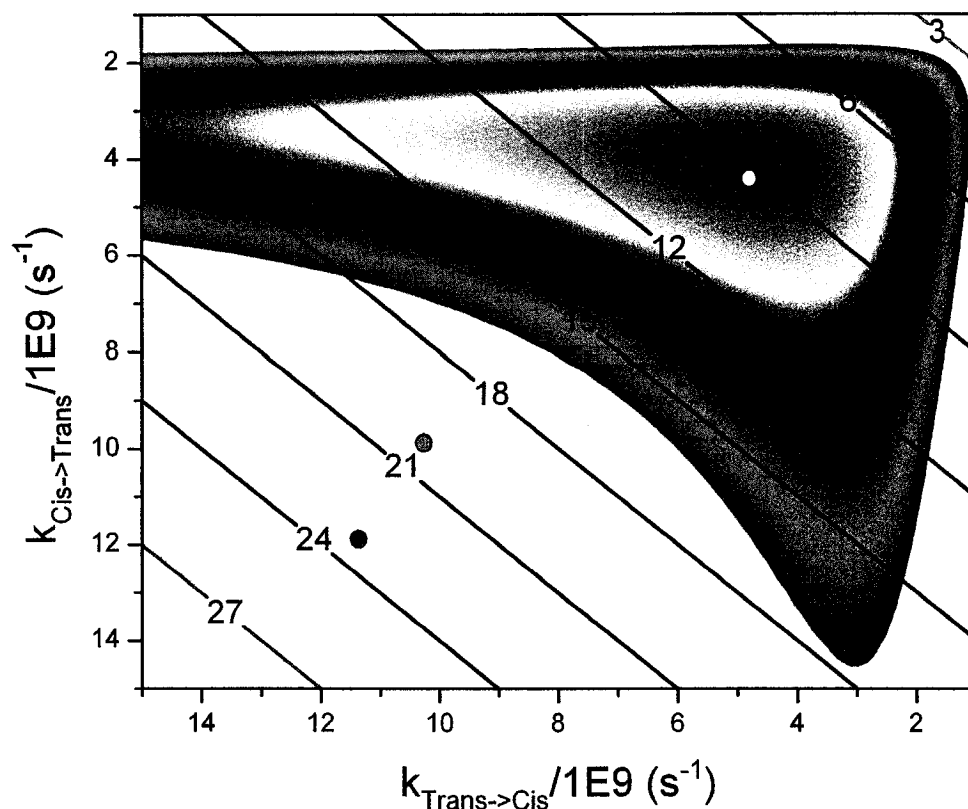


**Figure 11.10.** The above plot illustrates the Chi squared surface generated for determination of the best fit of the analytical lineshape to experiment. Horizontal lines correspond to constant-rate tie-lines. Different rate information is illustrated using colored circles. The best Fit ( $k(E)_{\text{isom}} = 9.5 \pm 1.2 \times 10^9 \text{ s}^{-1}$ ) (white circle);; The RRKM rate using scaled harmonic frequencies and 1-D torsional energy levels ( $k(E)_{\text{isom}} = 20 \times 10^9 \text{ s}^{-1}$ ) (red circle). The RRKM rate using anharmonic frequencies and 1-D torsional energy levels ( $k(E)_{\text{isom}} = 23 \times 10^9 \text{ s}^{-1}$ ) (blue circle).

the forward and reverse rates while holding all other fit parameters fixed.

Because the measurement occurs for isolated molecules in the collision free region of the molecular beam, this analysis provides the microcanonical rate ( $k(E)$ ) for the conformational isomerization reaction. The experimental result can be compared to a statistical rate theory prediction using Rice-Ramsperger-Kassel-Marcus (RRKM) theory:

$$k(E) = \frac{\sigma * W(E)}{h * \rho(E)} \quad (1)$$

where  $\sigma$  is the symmetry number of the reaction coordinate,  $W(E)$  is the number of energy levels of the transition state,  $h$  is Planck's constant, and  $\rho$  is the density of states of the reactant.<sup>15</sup> These quantities are evaluated using the scaled normal-mode frequencies obtained in the *ab initio* calculation and use the theoretical prediction of the reaction barrier ( $2200\text{ cm}^{-1}$ ). The measured rate constant for the reversible conformation isomerization of CPCPA is the sum of the forward and reverse reaction rates ( $k_{\text{TOT}}$ ). The RRKM theory calculation using the scaled harmonic frequencies and the calculated 1-D torsional energy levels predicts a reaction rate that is 2.2 times faster than the experimental determination:  $k_{\text{TOT}} = 2.0 \times 10^{10}\text{ s}^{-1}$ . This rate becomes even faster if the experimentally determined barrier estimate of  $1550\text{ cm}^{-1}$  is used:  $k_{\text{TOT}} = 3.7 \times 10^{11}\text{ s}^{-1}$ .

Other vibrational features illustrated in Figure 11.5 that can be uniquely assigned to either the *cis* or *trans* conformer have also been studied. The lower energy *cis* absorption at  $2764\text{ cm}^{-1}$  illustrated in Figure 11.11 has an isomerization rate [ $k(E) = 8.3 \times 10^9\text{ s}^{-1}$ ] which is similar to the  $2824\text{ cm}^{-1}$  *cis* absorption of Figure 11.8. In both excitation regions ( $2764\text{ cm}^{-1}$  and  $2824\text{ cm}^{-1}$ ) the product distributions are similar.

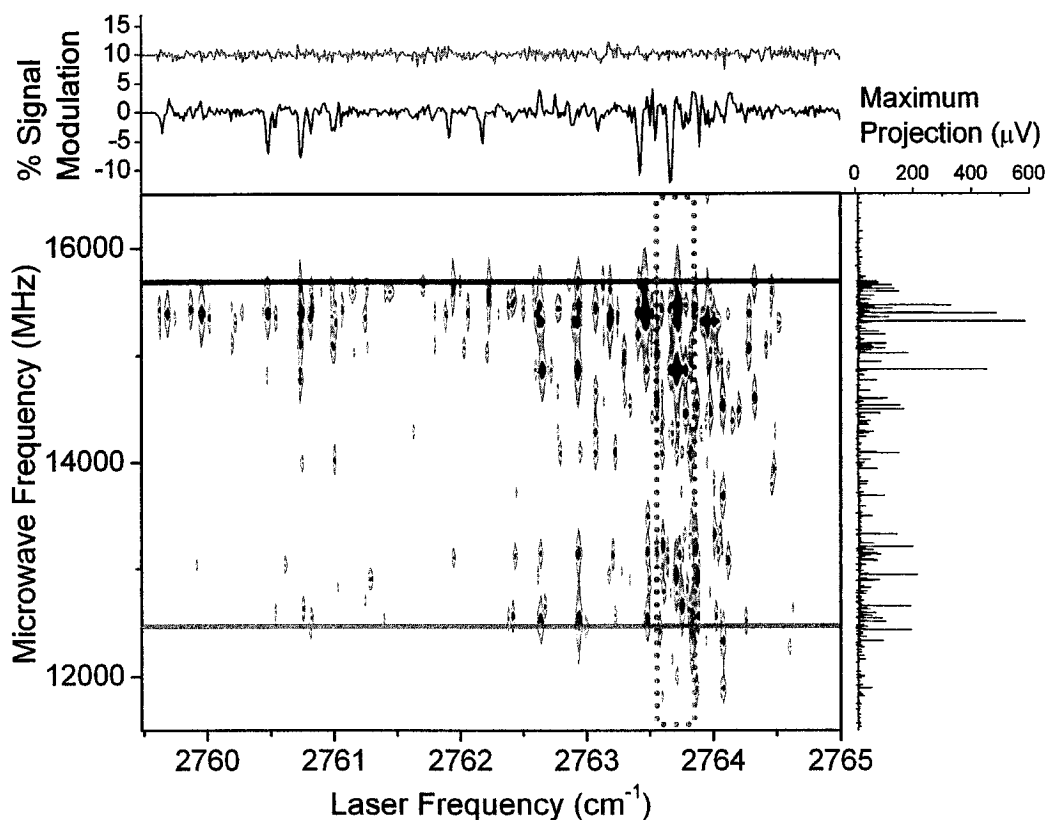


**Figure 11.11** The rotational spectrum of CPCA in the vibrationally excited state shown is above as a contour plot for the region near  $2764\text{ cm}^{-1}$  for excitation out of the *cis* conformer. The bottom axis corresponds to the laser position in wavenumbers while the left axis corresponds to microwave frequency in MHz. The red and blue lines mark the ground state positions of the *trans* and *cis*  $2_{02}-1_{01}$  transitions, respectively. The upper panel shows the IR-CP-FTMW double resonance spectrum for the *cis* and *trans* along the 1-D slices of the ground state microwave transitions, ie the ground state depletion spectra. The right panel shows the maximum peak height along the microwave axis at all laser positions, collapsing the x-axis to a single 1-D microwave spectrum.

The *cis* absorption feature at 3057 cm<sup>-1</sup> also exhibits evidence of isomerization, as indicated in the IR-CP-FTMW double resonance contour plot of Figure 11.12. To increase the sensitivity for measuring the rotational spectrum in the vibrationally excited state 10,000 signal averages were performed with the laser frequency fixed to R(1) at 3057.08cm<sup>-1</sup> and is illustrated in Figure 11.13. There is evidence for isomerization, however a complete rate analysis was not possible due to low number of excited state rotational transitions.

For excitation originating from the *trans* conformer the absorption feature at 2804 cm<sup>-1</sup> shows evidence for isomerization. For this case rate information can be extracted from the region around 2804 cm<sup>-1</sup> as depicted in Figure 11.14 yielding a rate of  $k(E) = 8.4 \times 10^9 \text{ s}^{-1}$ . The product distribution is heavily weighted towards the *trans* conformer. For the other regions, there is little evidence for any isomerization in the excited state rotational spectra at the lowest frequency *trans* absorption at 2684 cm<sup>-1</sup> illustrated in Figure 11.15, the higher frequency absorption at 3102 cm<sup>-1</sup> illustrated in the IR-CP-FTMW contour plot in Figure 11.16, or the fixed frequency 10000 average spectra illustrated in Figure 11.17.

### Conclusions

These results show conformation specific isomerization reaction dynamics and suggest that the overall isomerization rate is independent of excitation energy over this narrow energy range; however the product distribution depends strongly on the excitation energy of the molecule. These results show that an increase in product yield is not correlated with an increase in excitation energy. This is demonstrated in Figure 11.14.

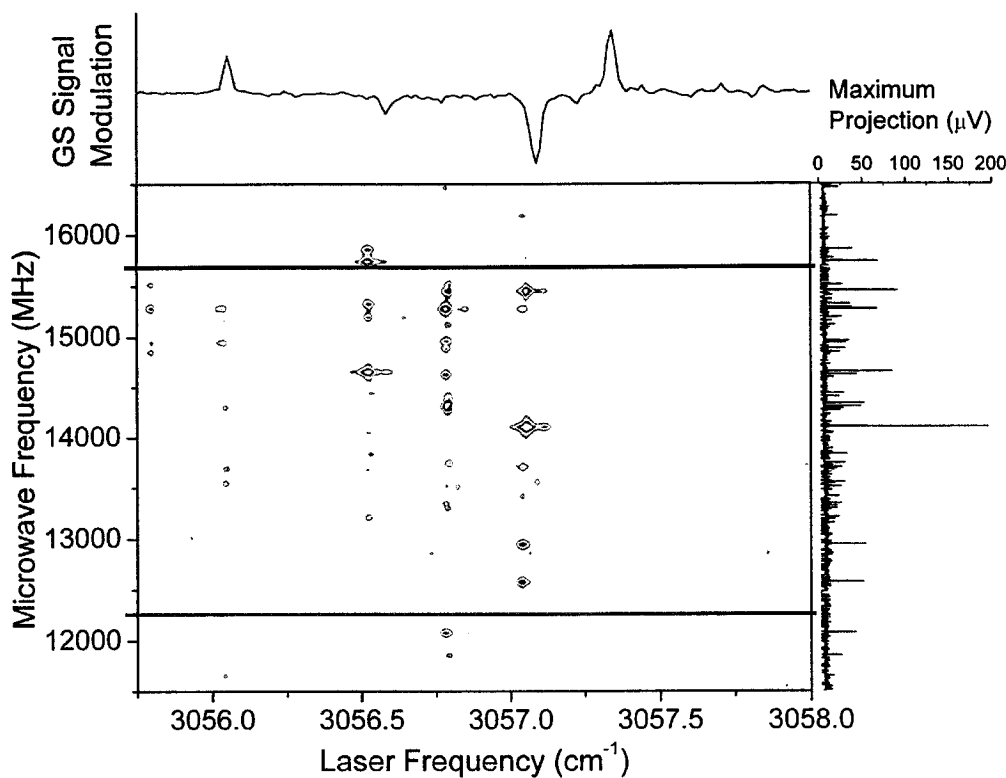


**Figure 11.12.** The rotational spectrum of CPCA in the vibrationally excited state shown is above as a contour plot for the region near 3057 cm<sup>-1</sup> for excitation out of the *cis* conformer. The bottom axis corresponds to the laser position in wavenumbers while the left axis corresponds to microwave frequency in MHz. The red and blue lines mark the ground state positions of the *trans* and *cis* 2<sub>02</sub>-1<sub>01</sub> transitions, respectively. The upper panel shows the IR-CP-FTMW double resonance spectrum for the *cis* conformer along the 1-D slices of the ground state microwave transitions, ie the ground state depletion spectra. The right panel shows the maximum peak height along the microwave axis at all laser positions, collapsing the x-axis to a single 1-D microwave spectrum.

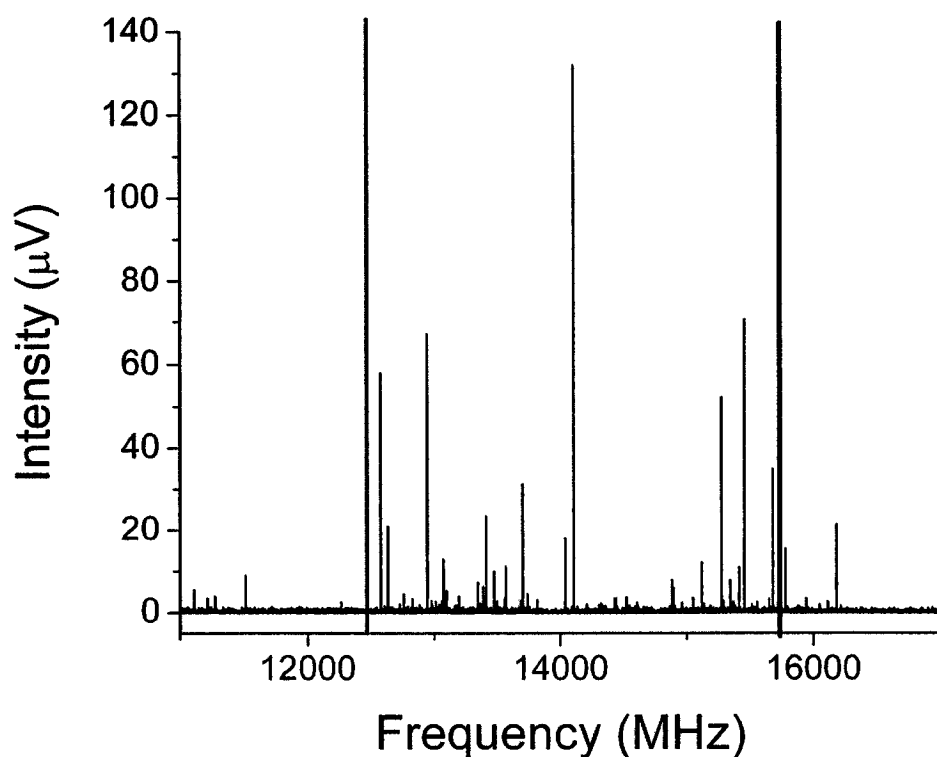


**Figure 11.13.** The above plot illustrates the rotational spectrum recorded in the vibrationally excited state with the laser frequency fixed to  $3057.08 \text{ cm}^{-1}$  and performing 10,000 signal averages.

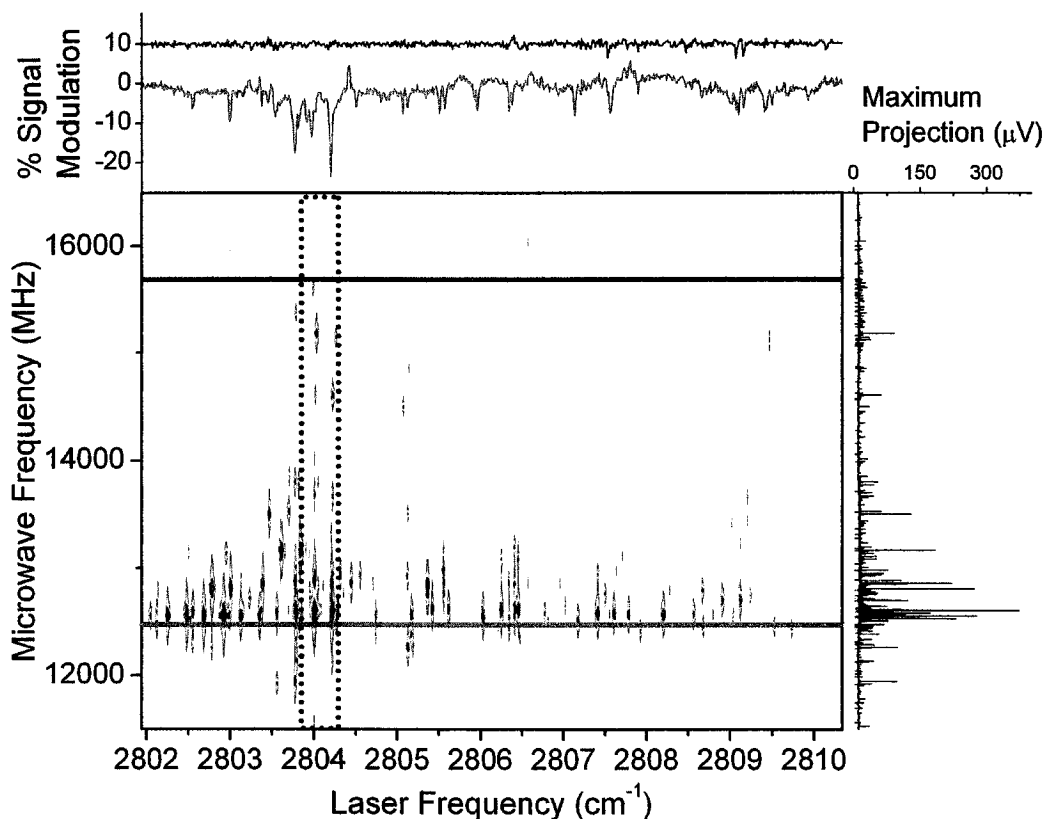


**Figure 11.14** The rotational spectrum of CPCPA in the vibrationally excited state shown is above as a contour plot for the region near  $2804\text{ cm}^{-1}$  for excitation out of the *trans* conformer. The bottom axis corresponds to the laser position in wavenumbers while the left axis corresponds to microwave frequency in MHz. The red and blue lines mark the ground state positions of the *trans* and *cis*  $2_{02}-1_{01}$  transitions, respectively. The upper panel shows the IR-CP-FTMW double resonance spectrum for the *cis* and *trans* along the 1-D slices of the ground state microwave transitions, ie the ground state depletion spectra. The right panel shows the maximum peak height along the microwave axis at all laser positions, collapsing the x-axis to a single 1-D microwave spectrum.

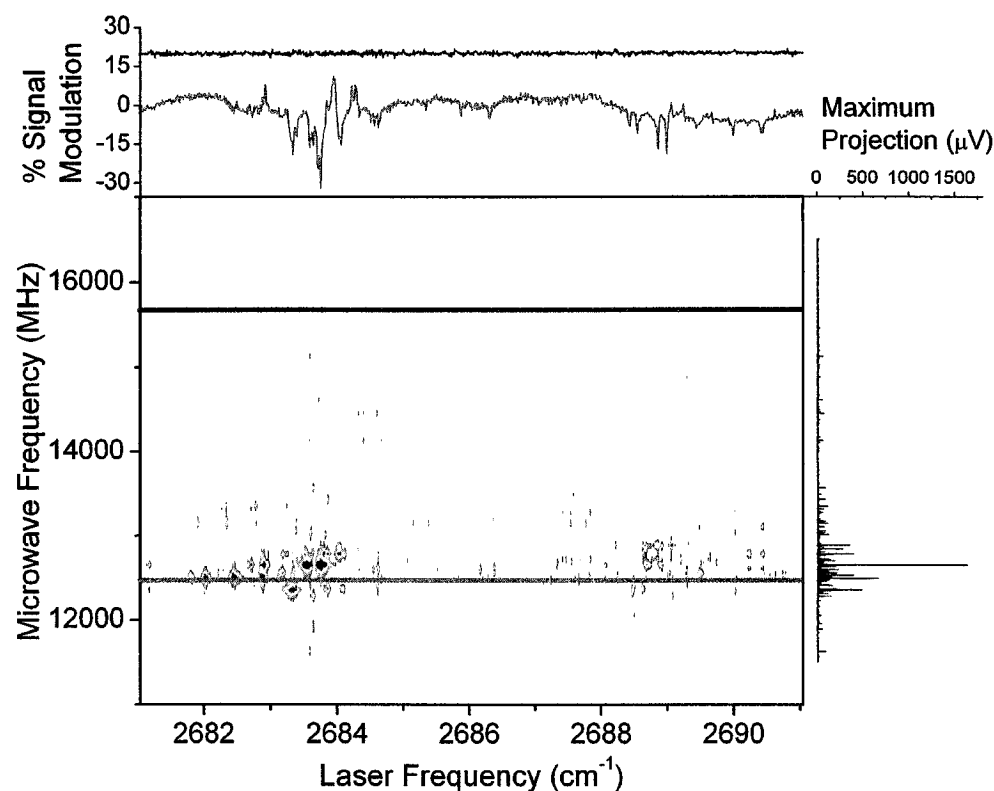


**Figure 11.15** The rotational spectrum of CPCPA in the vibrationally excited state shown is above as a contour plot for the region near  $2684 \text{ cm}^{-1}$  for excitation out of the *trans* conformer. The bottom axis corresponds to the laser position in wavenumbers while the left axis corresponds to microwave frequency in MHz. The red and blue lines mark the ground state positions of the *trans* and *cis*  $2_{02}-1_{01}$  transitions, respectively. The upper panel shows the IR-CP-FTMW double resonance spectrum for the *cis* and *trans* along the 1-D slices of the ground state microwave transitions, ie the ground state depletion spectra. The right panel shows the maximum peak height along the microwave axis at all laser positions, collapsing the x-axis to a single 1-D microwave spectrum.

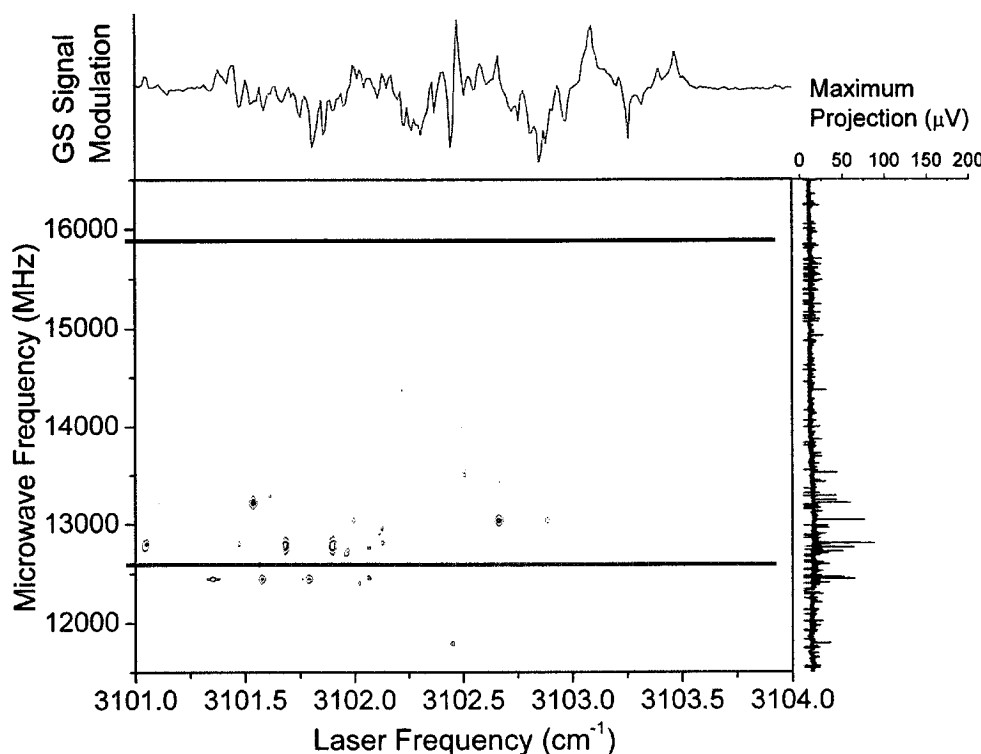


**Figure 11.16.** The rotational spectrum of CPCA in the vibrationally excited state shown is above as a contour plot for the region near  $3102\text{ cm}^{-1}$  for excitation out of the *trans* conformer. The bottom axis corresponds to the laser position in wavenumbers while the left axis corresponds to microwave frequency in MHz. The red and blue lines mark the ground state positions of the *trans*  $2_{02}-1_{01}$  transitions, respectively. The upper panel shows the IR-CP-FTMW double resonance spectrum for the *trans* along the 1-D slices of the ground state microwave transitions, ie the ground state depletion spectra. The right panel shows the maximum peak height along the microwave axis at all laser positions, collapsing the x-axis to a single 1-D microwave spectrum.

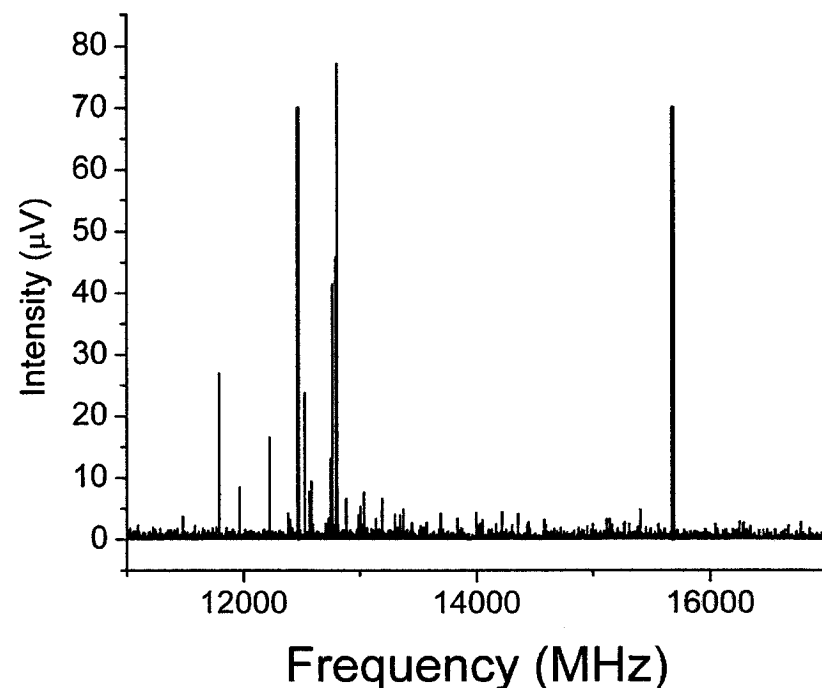


**Figure 11.17.** The above plot illustrates the rotational spectrum recorded in the vibrationally excited state with the laser frequency fixed to  $3101.97 \text{ cm}^{-1}$  and performing 10,000 signal averages.

With excitation out of the *trans* conformer at 2804 cm<sup>-1</sup> there is a greater number of transitions in the vicinity of the *trans* conformer than the *cis*, but for excitation out of the *cis* conformer at 2823 cm<sup>-1</sup> (Figure 11.8) there is a nearly equal number of transitions in the vicinity of the *cis* and *trans* conformers.

The interpretation of these results is puzzling given the form of the potential surface in Figure 11.3. The *cis* and *trans* conformational minima are predicted to lie close in energy ( $\Delta E = 46$  cm<sup>-1</sup>, ZPE corrected), which is confirmed by previous ground state microwave measurements.<sup>11</sup> The possibility of the *trans* conformer lying below the barrier to internal rotation is unlikely given that the experimentally determined barrier heights are at 1500-1600 cm<sup>-1</sup>.

The excited state rotational spectra represent an ensemble of molecular eigenstates reflecting the average bath-bath coupling across a single IR band feature. Therefore the product yields reflect the average strength of the bath-bath coupling within a single IR band that spans two extremes. In the strong mixing limit (*cis* 2824 cm<sup>-1</sup> band) the quantum yields reflect the nascent population ratios predicted by the ratio of the state densities at that energy, while the weak mixing limit (*trans* 2684 cm<sup>-1</sup> band) no isomerization is observed. The low state density (~ 0.5 states/cm<sup>-1</sup>) of above-barrier torsional levels that connect the *cis* and *trans* conformers are a likely cause for the observed isomerization dynamics. The proximity to a delocalized “coupling” level can then account for the observed fluctuations in the excited state spectra. The *cis* levels populated by the laser following relaxation could be fortuitously resonant with an above

barrier level, leading to a strong coupling picture, while the *trans* levels are remote from the above barrier levels in energy space leading to a weak coupling picture.

The current study probes an interesting regime of the potential surface just above the barrier to isomerization. The use of FTMW spectra allows the experimentalist to observe reaction dynamics and consequent change in molecular shape, thereby providing a detailed probe of isomerization reactions.

### Reference List

1. Nesbitt, D. J.; Field, R. W., *J.Phys.Chem.* **1996**, *100*, 12735-12756.
2. Lehmann, K. K.; Scoles, G.; Pate, B. H., *Annu.Rev.Phys.Chem.* **1994**, *45*, 241-274.
3. Keske, J. C.; McWhorter, D. A.; Pate, B. H., *Int.Rev.Phys.Chem.* **2000**, *19*, 363-407.
4. Pate, B. H., *J.Chem.Phys.* **1998**, *109*, 4396-4406.
5. Pate, B. H., *J.Chem.Phys.* **1999**, *110*, 1990-1999.
6. Keske, J. C.; Pate, B. H., *Annu.Rev.Phys.Chem.* **2000**, *51*, 323-353.
7. Douglass, K. O.; Dian, B. C.; Brown, G. G.; Johns, J. E.; Nair, P. M.; Pate, B. H., *J.Chem.Phys.* **2004**, *121*, 6845-6854.
8. Anderson, P. W., *J.Phys.Soc.Japan* **1954**, *9*, 316-339.
9. Kubo, R.; Tomita, K., *J.Phys.Soc.Japan* **1954**, *9*, 888-919.
10. Frisch, M. J., Trucks, G. W., Sclegel, H. B., Scuseria, G. E., Robb, M. A., Cheeseman, J. R., Zakrzewski, V. G., Montgomery, J. A. Jr., Stratmann, R. E., Burant, J. C., Dapprich, S., Millam, J. M., Daniels, A. D., Kudin, K. N., Strain, M. C., Farkas, O., Tomasi, J., Barone, V., Cossi, M., Cammi, R., Mennucci, B., Pomelli, C., Adamo, C., Clifford, S., Ochterski, J., Petersson, G. A., Ayala, P. Y., Cui, Q., Morokuma, K., Malick, D. K., Rabuck, A. D., Raghavachari, K., Foresman, J. B., Cioslowski, J., Ortiz, J. V., Baboul, A. G., Stefanov, B. B., Liu, G., Liashenko, A., Piskoz, P., Komaromi, I., Gomperts, R., Martin, R. L., Fox, D. J., Keith, T., Al-Laham, M. A., Peng, C. Y., Nanayakkara, A., Challacombe, M., Gill, P. M. W., Johnson, B., Chen, W., Wong, M. W., Andres, J. L., Gonzalez, C., Head-Gordon, M., Replogle, E. S., and Pople, J. A. Gaussian 98, Revision A.7. Gaussian, Inc., Pittsburgh PA . 1998.
11. Volltrauer, H. N.; Schwendeman, R. H., *J.Chem.Phys.* **1971**, *54*, 260-267.
12. Durig, J. R.; Feng, F.; Little, T. S.; Wang, A.-Y., *Struct.Chem.* **1992**, *3*, 418-428.
13. McIlroy, A.; Nesbitt, D. J., *J.Chem.Phys.* **1990**, *92*, 2229-2243.
14. Cupp, S.; Lee, C. Y.; McWhorter, D.; Pate, B. H., *J.Chem.Phys.* **1998**, *109*, 4302-4315.
15. Baer, T.; Hase, W. L. *Unimolecular Reaction Dynamics: Theory and Experiments*; Oxford University Press: New York, 1996.

## Chapter 12

### Concluding Remarks

Throughout this thesis several new techniques based on Fourier transform methods have been presented to perform the experimental steps of dynamic rotational spectroscopy (DRS). New techniques using cavity FTMW and the CP-FTMW spectrometers have demonstrated the high sensitivity required to perform DRS.

A completely new technique for acquiring rotational spectra has been developed that is factor of 18 faster than the previous most sensitive technique. This advancement has completely changed the way dynamical experiments are approached because of the speed at which new systems can be studied. This speed enhancement of the CP-FTMW spectrometer has been used to perform dynamical measurements on the fly as the laser scans. For measuring rotational spectra over a large bandwidth the CP-FTMW spectrometer is the method of choice. Additionally, the speed, sensitivity, and accurate relative intensities of the CP-FTMW spectrometer will have advantages as an analytical technique.

For monitoring a single rotational frequency the cavity FTMW spectrometer has significant advantages from its high Q cavity which enables extremely high sensitivity in only a few averages (~10 typical). This complementary aspect of the cavity FTMW spectrometer is used to measure the species selective rotationally resolved IR spectrum in which new background-free methods have been developed. This technique has the advantage of a rapid scan rate and spectral simplification because it is a double resonance technique. The background-free ground state depletion method provides nearly a factor

of ~10 signal-to-noise improvement over the previous ground state depletion method and enables this technique to be competitive with other double resonance techniques.<sup>1-4</sup>

### Future Experiments

In the very near future the CP-FTMW spectrometer will be upgraded by implementing 90 degree off axis parabolic mirrors to allow for greater broadcast and collection efficiency. Preliminary tests indicate that signal enhancements of 2-4 are possible. Additionally, for pure rotational spectra a coaxially oriented nozzle arrangement will be implemented which will allow for much longer  $T_2$  time as has been shown for cavity FTMW spectrometer.<sup>5</sup> The longer  $T_2$  will allow for longer gate duration and subsequently narrower lineshapes in the frequency domain which is important for precisely determining the center frequency of the rotational transition. A preliminary experiment of this effect is illustrated in Figure 12.1 for epifluorohydrin.<sup>6</sup>

Future dynamics experiments will take advantage of the CP-FTMW technique to investigate dimer dissociation dynamics or other species with dissociation lifetimes on the order of the  $T_2$  (microseconds). The aim of these experiments will be to vibrationally excite a van der Waals complex and observe the resulting dynamics such as isomerization or bond breakage. This will create a time evolving FID. By performing the Fourier transform at specific time intervals the dynamics of the molecule can be probed as a function of time.

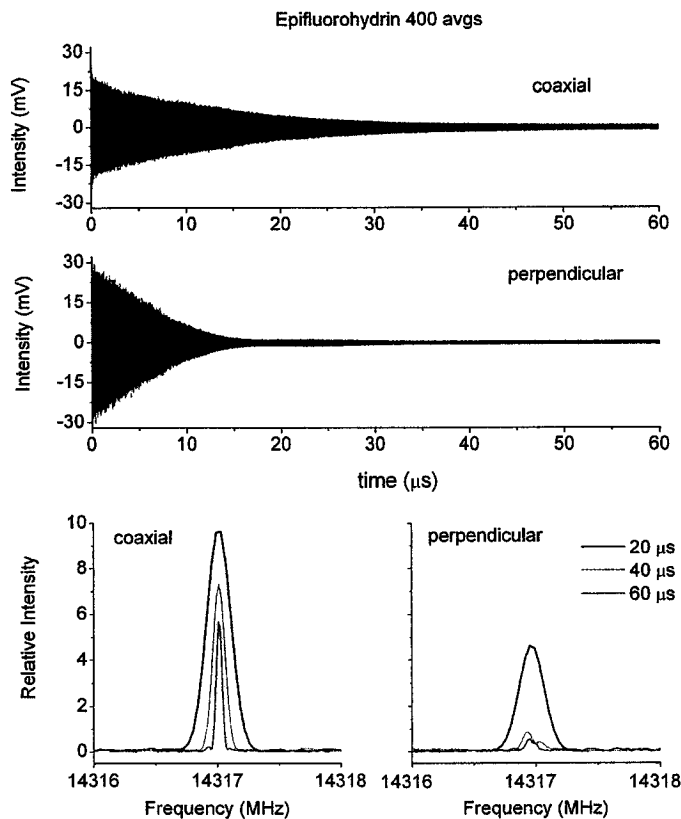


**Figure 12.1** The above figure illustrates the broadband rotational FID of epifluorohydrin with coaxial nozzle and perpendicular nozzle to microwave arrangement. The resulting Fourier transform using gate durations of 20, 40, and 60  $\mu$ s is illustrated in the lower panels for a single rotational transition ( $1_{11} - 0_{00}$ ) of the lowest abundant conformer of epifluorohydrin at 14316.9740 MHz. The spectra were acquired using the CP-FTMW spectrometer with 400 signal averages.

## Reference List

1. Lehmann, K. K.; Coy, S. L., *J.Chem.Phys.* **1984**, *81*, 3744-3745.
2. Lipert, R. J.; Colson, S. D., *Chem.Phys.Lett.* **1989**, *161*, 303.
3. Berden, G.; Meerts, W. L.; Kreiner, W., *Chem.Phys.* **1993**, *174*, 247-253.
4. Dian, B. C.; Longarte, A.; Winter, P. R.; Zwier, T. S., *J.Chem.Phys.* **2004**, *120*, 133-147.
5. Grabow, J. U.; Stahl, W., *Z.Naturforsch* **1990**, *45a*, 1043-1044.
6. Brown, G. G.; Dian, B. C.; Douglass, K. O.; Geyer, S. M.; Pate, B. H., *J.Mol.Spectrosc.* **2006**, *238*, 200-212.